Progressive linear kinematic source inversion method and its perspectives towards the uncertainty quantification.

Hugo Samuel Sanchez Reyes

To cite this version:

Hugo Samuel Sanchez Reyes. Progressive linear kinematic source inversion method and its perspectives towards the uncertainty quantification.. Volcanology. Université Grenoble Alpes, 2019. English. NNT : 2019GREAU026 . tel-02458031

HAL Id: tel-02458031
https://tel.archives-ouvertes.fr/tel-02458031

Submitted on 28 Jan 2020

Communauté
UNIVERSITÉ Grenoble Alpes

THÈSE

Pour obtenir le grade de

DOCTEUR DE LA COMMUNAUTÉ UNIVERSITÉ GRENOBLE ALPES

Spécialité : Terre Solide (CETSOL)

Arrêté ministériel : 25 mai 2016

Présentée par

Hugo Samuel SANCHEZ REYES

Thèse dirigée par **Jean VIRIEUX**, Enseignant chercheur
et codirigée par **Ludovic METIVIER**, chercheur, CNRS

préparée au sein du **Laboratoire Institut des Sciences de la Terre**
dans **l'École Doctorale Terre, Univers, Environnement**

Inversion cinématique progressive linéaire de la source sismique et ses perspectives dans la quantification des incertitudes associées

Progressive linear kinematic source inversion method and its perspectives towards the uncertainty quantification.

Thèse soutenue publiquement le **28 octobre 2019**,
devant le jury composé de :

Monsieur LUIS RIVERA
Professeur, Université de Strasbourg, Président
Monsieur ALDO ZOLLO
Professeur, Université de Naples Frédéric II, Rapporteur
Monsieur CARL TAPE
Professeur Associé, Université d'Alaska Fairbanks, Rapporteur
Madame FRANÇOISE COURBOULEX
Directrice de Recherche, CNRS Délégation Côte d'Azur, Examinatrice
Monsieur JEAN VIRIEUX
Professeur Émérite, Université Grenoble Alpes, Directeur de thèse

To my mother, family and friends

Acknowledgements

I would like to express my deepest gratitude to my supervisors, friends and family; without all the great support from them, the work presented in this PhD dissertation could have not been performed.

First of all, I would like to thank my supervisor Prof. Jean Virieux. Thank you ever so much for all the support during my Master and PhD training. I am grateful for the opportunities and support that you always offered me regarding my special needs as a visually impaired person and my desire to continue my academic career. I consider you as a very kind and great person besides the amazing researcher you are. Thanks a lot to you and also to Ludovic Métivier for all your support, comments, advices and scientific discussions that we could have during these four years of training. In addition, I would like to thank Romain Brossier and the members of the SEISCOPE Consortium (Marwan Irnaka, Julien Thurin, Pengliang Yang, Philippe Le Bouteiller, Paul Wellington, and many other colleges) for the fruitful scientific discussions, computational exchange and guidance that you provide me during my PhD training.

I would like to thank also to Josué Tago. His work and ideas allowed me to start this work. Thanks a lot for your help, advices and all the training that you provided me.

My most grateful thanks go also to my mother Evangelina Reyes. You are the best mother I could dream of. All my achievements, work and efforts are dedicated to you and inspired by your hard work to bring up me and my brother in the difficult situations we were.

Thanks also to Ekaterina Kazachkina, for all your support and patience. Without our constant conversations and your great tolerance to be far from each other I could not have worked comfortably during these four years. I would like to thank you for all the nice adventures we had during this period of time. I will always be grateful and you will have my sincere affection for all what we lived together.

I am totally grateful to the Institut des Sciences de la Terre, to the Université Grenoble Alpes, to the Centre National de la Recherche Scientifique (CNRS) and to the French Government, as well as to the Universidad Nacional Autónoma de México (UNAM) and to the Consejo Nacional de Ciencia y Tecnología (CONACyT). The work here presented was funded and supported by all these institutions.

Finally, I would like to thank to all my friends: Jorge Jara, Jesús Piña, Ariana Astorga, Claudia Aristizabal, Gökhan Aslan, Marco Salcedo, Yacine, Maureen, the Ecuadorian Crew, all my friends at ISTerre, and many others that I can not mention or it will take me more than four pages. Thanks a lot to everyone for your support and friendly "bonjours“.

Grenoble, le 18 juillet 2019

Résumé

La caractérisation des tremblements de terre est un domaine de recherche primordial en sismologie, où l'objectif final est de fournir des estimations précises d'attributs de la source sismique. Dans ce domaine, certaines questions émergent, par exemple : quand un tremblement de terre s'est-il produit? quelle était sa taille? ou quelle était son évolution dans le temps et l'espace? On pourrait se poser d'autres questions plus complexes comme : pourquoi le tremblement s'est produit? quand sera le prochain dans une certaine région? Afin de répondre aux premières questions, une représentation physique du phénomène est nécessaire. La construction de ce modèle est l'objectif scientifique de ce travail doctoral qui est réalisé dans le cadre de la modélisation cinématique. Pour effectuer cette caractérisation, les modèles cinématiques de la source sismique sont un des outils utilisés par les sismologues. Il s'agit de comprendre la source sismique comme une dislocation en propagation sur la géométrie d'une faille active. Les modèles de sources cinématiques sont une représentation physique de l'histoire temporelle et spatiale d'une telle rupture en propagation. Cette modélisation est dite approche cinématique car les histoires de la rupture inférées par ce type de technique sont obtenues sans tenir compte des forces qui causent l'origine du séisme.

Dans cette thèse, je présente une nouvelle méthode d'inversion cinématique capable d'assimiler, hiérarchiquement en temps, les traces de données à travers des fenêtres de temps évolutives. Cette formulation relie la fonction de taux de glissement et les sismogrammes observés, en préservant la positivité de cette fonction et la causalité quand on parcourt l'espace de modèles. Cette approche profite de la structure creuse de l'histoire spatio-temporelle de la rupture sismique ainsi que de la causalité entre la rupture et chaque enregistrement différé par l'opérateur. Cet opérateur de propagation des ondes connu, est différent pour chaque station. Cette formulation progressive, à la fois sur l'espace de données et sur l'espace de modèle, requiert des hypothèses modérées sur les fonctions de taux de glissement attendues, ainsi que des stratégies de préconditionnement sur le gradient local estimé pour chaque paramètre du taux de glissement. Ces hypothèses sont basées sur de simples modèles physiques de rupture attendus. Les applications réussies de cette méthode aux cas synthétiques (Source Inversion Validation Exercise project) et aux données réelles du séisme de Kumamoto 2016 (Mw=7.0), ont permis d'illustrer les avantages de cette approche alternative d'une inversion cinématique linéaire de la source sismique.

L'objectif sous-jacent de cette nouvelle formulation sera la quantification des incertitudes d'un tel modèle. Afin de mettre en évidence les propriétés clés prises en compte dans cette approche linéaire, dans ce travail, j'explore l'application de la stratégie bayésienne connue comme Hamiltonian Monte Carlo (HMC). Cette méthode semble être l'une des possibles stratégies qui peut être appliquée à ce problème linéaire sur-paramétré. Les résultats montrent qu'elle est compatible avec la stratégie linéaire dans le domaine temporel présentée ici. Grâce à une estimation efficace du gradient local de la fonction coût, on peut explorer rapidement l'espace de grande dimension des solutions possibles, tandis que la linéarité est préservée. Dans ce travail, j'explore la performance de la stratégie HMC traitant des

cas synthétiques simples, afin de permettre une meilleure compréhension de tous les concepts et ajustements nécessaires pour une exploration correcte de l'espace de modèles probables. Les résultats de cette investigation préliminaire sont encourageants et ouvrent une nouvelle façon d'aborder le problème de la modélisation de la reconstruction cinématique de la source sismique, ainsi, que de l'évaluation des incertitudes associées.

Abstract

The earthquake characterization is a fundamental research field in seismology, which final goal is to provide accurate estimations of earthquake attributes. In this study field, various questions may rise such as the following ones: when and where did an earthquake happen? How large was it? What is its evolution in space and time? In addition, more challenging questions could be addressed: why did it occur? When is the next one in a given area? In order to progress in the first list of questions, a physical description, or model, of the event, is necessary. The investigation of such model (or image) is the scientific topic I investigate during my PhD in the framework of kinematic source models. Understanding the seismic source as a propagating dislocation that occurs across a given geometry of an active fault, the kinematic source models are the physical representations of the time and space history of such rupture propagation. Such physical representation is said to be a kinematic approach because the inferred rupture histories are obtained without taking into account the forces that might cause the origin of the dislocation.

In this PhD dissertation, I present a new hierarchical time kinematic source inversion method able to assimilate data traces through evolutive time windows. A linear time-domain formulation relates the slip-rate function and seismograms, preserving the positivity of this function and the causality when spanning the model space: taking benefit of the time-space sparsity of the rupture model evolution is as essential as considering the causality between rupture and each record delayed by the known wave propagation operator different for each station. This progressive approach, both on the data space and on the model space, does require mild assumptions on prior slip-rate functions and preconditioning strategies on the slip-rate local gradient estimations. These assumptions are based on simple physical expected rupture models. Successful applications of this method to a well-known benchmark (Source Inversion Validation Exercise 1) and to the recorded data of the 2016 Kumamoto mainshock ($M_w = 7.0$) illustrate the advantages of this alternative approach of a linear kinematic source inversion.

The underlying target of this new formulation will be the future uncertainty quantification of such model reconstruction. In order to achieve this goal, as well as to highlight key properties considered in this linear time-domain approach, I explore the Hamiltonian Monte Carlo (HMC) stochastic Bayesian framework, which appears to be one of the possible and very promising strategies that can be applied to this stabilized over-parametrized optimization of a linear forward problem to assess the uncertainties on kinematic source inversions. The HMC technique shows to be compatible with the linear time-domain strategy presented here. This technique, thanks to an efficient estimation of the local gradient of the misfit function, appears to be able to rapidly explore the high-dimensional space of probable solutions, while the linearity between unknowns and observables is preserved. In this work, I investigate the performance of the HMC strategy dealing with simple synthetic cases with almost perfect illumination, in order to provide a better understanding of all the concepts and required tuning to achieve a correct exploration of the model space. The results from this preliminary investigation are promising and open a new way of tackling the kinematic source reconstruction problem and the assessment of the associated uncertainties.

⠠⠁⠃⠎⠞⠗⠁⠉⠞ (braille version)

⠠⠞⠓⠑ ⠑⠁⠗⠞⠓⠟⠥⠁⠅⠑ ⠉⠓⠁⠗⠁⠉⠞⠑⠤
⠗⠊⠵⠁⠞⠊⠕⠝ ⠊⠎ ⠁ ⠋⠥⠝⠙⠁⠍⠑⠝⠞⠁⠇
⠗⠑⠎⠑⠁⠗⠉⠓ ⠋⠊⠑⠇⠙ ⠊⠝ ⠎⠑⠊⠎⠍⠕⠤
⠇⠕⠛⠽⠂ ⠺⠓⠊⠉⠓ ⠋⠊⠝⠁⠇ ⠛⠕⠁⠇ ⠊⠎
⠞⠕ ⠏⠗⠕⠧⠊⠙⠑ ⠁⠉⠉⠥⠗⠁⠞⠑ ⠑⠎⠞⠊⠤
⠍⠁⠞⠊⠕⠝⠎ ⠕⠋ ⠑⠁⠗⠞⠓⠟⠥⠁⠅⠑ ⠁⠞⠤
⠞⠗⠊⠃⠥⠞⠑⠎⠲ ⠠⠊⠝ ⠞⠓⠊⠎ ⠎⠞⠥⠙⠽
⠋⠊⠑⠇⠙⠂ ⠧⠁⠗⠊⠕⠥⠎ ⠟⠥⠑⠎⠞⠊⠕⠝⠎
⠍⠁⠽ ⠗⠊⠎⠑ ⠎⠥⠉⠓ ⠁⠎ ⠞⠓⠑
⠋⠕⠇⠇⠕⠺⠊⠝⠛ ⠕⠝⠑⠎⠒ ⠺⠓⠑⠝ ⠁⠝⠙
⠺⠓⠑⠗⠑ ⠙⠊⠙ ⠁⠝ ⠑⠁⠗⠞⠓⠟⠥⠁⠅⠑
⠓⠁⠏⠏⠑⠝⠦ ⠠⠓⠕⠺ ⠇⠁⠗⠛⠑ ⠺⠁⠎ ⠊⠞⠦
⠠⠺⠓⠁⠞ ⠊⠎ ⠊⠞⠎ ⠑⠧⠕⠇⠥⠞⠊⠕⠝ ⠊⠝
⠎⠏⠁⠉⠑ ⠁⠝⠙ ⠞⠊⠍⠑⠦ ⠠⠊⠝ ⠁⠙⠙⠊⠤
⠞⠊⠕⠝⠂ ⠍⠕⠗⠑ ⠉⠓⠁⠇⠇⠑⠝⠛⠊⠝⠛
⠟⠥⠑⠎⠞⠊⠕⠝⠎ ⠉⠕⠥⠇⠙ ⠃⠑ ⠁⠙⠙⠤
⠗⠑⠎⠎⠑⠙⠒ ⠺⠓⠽ ⠙⠊⠙ ⠊⠞ ⠕⠉⠉⠥⠗⠦
⠠⠺⠓⠑⠝ ⠊⠎ ⠞⠓⠑ ⠝⠑⠭⠞ ⠕⠝⠑ ⠊⠝
⠁ ⠛⠊⠧⠑⠝ ⠁⠗⠑⠁⠦ ⠠⠊⠝ ⠕⠗⠙⠑⠗
⠞⠕ ⠏⠗⠕⠛⠗⠑⠎⠎ ⠊⠝ ⠞⠓⠑ ⠋⠊⠗⠎⠞
⠇⠊⠎⠞ ⠕⠋ ⠟⠥⠑⠎⠞⠊⠕⠝⠎⠂ ⠁ ⠏⠓⠽⠤
⠎⠊⠉⠁⠇ ⠙⠑⠎⠉⠗⠊⠏⠞⠊⠕⠝⠂ ⠕⠗ ⠍⠕⠤
⠙⠑⠇⠂ ⠕⠋ ⠞⠓⠑ ⠑⠧⠑⠝⠞⠂ ⠊⠎ ⠝⠑⠤

⠉⠑⠎⠎⠁⠗⠽⠲ ⠠⠞⠓⠑ ⠊⠝⠧⠑⠎⠞⠊⠛⠁⠞⠊⠕⠝
⠕⠋ ⠎⠥⠉⠓ ⠍⠕⠙⠑⠇ ⠶⠕⠗ ⠊⠍⠁⠛⠑⠶ ⠊⠎
⠞⠓⠑ ⠎⠉⠊⠑⠝⠞⠊⠋⠊⠉ ⠞⠕⠏⠊⠉ ⠠⠊ ⠊⠝⠤
⠧⠑⠎⠞⠊⠛⠁⠞⠑ ⠙⠥⠗⠊⠝⠛ ⠍⠽ ⠠⠏⠓⠠⠙ ⠊⠝
⠞⠓⠑ ⠋⠗⠁⠍⠑⠺⠕⠗⠅ ⠕⠋ ⠅⠊⠝⠑⠍⠁⠞⠊⠉
⠎⠕⠥⠗⠉⠑ ⠍⠕⠙⠑⠇⠎⠲ ⠠⠥⠝⠙⠑⠗⠤
⠎⠞⠁⠝⠙⠊⠝⠛ ⠞⠓⠑ ⠎⠑⠊⠎⠍⠊⠉
⠎⠕⠥⠗⠉⠑ ⠁⠎ ⠁ ⠏⠗⠕⠏⠁⠛⠁⠞⠊⠝⠛ ⠙⠊⠎⠤
⠇⠕⠉⠁⠞⠊⠕⠝ ⠞⠓⠁⠞ ⠕⠉⠉⠥⠗⠎ ⠁⠉⠗⠕⠎⠎
⠁ ⠛⠊⠧⠑⠝ ⠛⠑⠕⠍⠑⠞⠗⠽ ⠕⠋ ⠁⠝ ⠁⠉⠞⠊⠧⠑
⠋⠁⠥⠇⠞⠂ ⠞⠓⠑ ⠅⠊⠝⠑⠍⠁⠞⠊⠉ ⠎⠕⠥⠗⠉⠑
⠍⠕⠙⠑⠇⠎ ⠁⠗⠑ ⠞⠓⠑ ⠏⠓⠽⠎⠊⠉⠁⠇ ⠗⠑⠤
⠏⠗⠑⠎⠑⠝⠞⠁⠞⠊⠕⠝⠎ ⠕⠋ ⠞⠓⠑ ⠞⠊⠍⠑
⠁⠝⠙ ⠎⠏⠁⠉⠑ ⠓⠊⠎⠞⠕⠗⠽ ⠕⠋ ⠎⠥⠉⠓
⠗⠥⠏⠞⠥⠗⠑ ⠏⠗⠕⠏⠁⠛⠁⠞⠊⠕⠝⠲ ⠠⠎⠥⠉⠓
⠏⠓⠽⠎⠊⠉⠁⠇ ⠗⠑⠏⠗⠑⠎⠑⠝⠞⠁⠞⠊⠕⠝ ⠊⠎
⠎⠁⠊⠙ ⠞⠕ ⠃⠑ ⠁ ⠅⠊⠝⠑⠍⠁⠞⠊⠉
⠁⠏⠏⠗⠕⠁⠉⠓ ⠃⠑⠉⠁⠥⠎⠑ ⠞⠓⠑ ⠊⠝⠤
⠋⠑⠗⠗⠑⠙ ⠗⠥⠏⠞⠥⠗⠑ ⠓⠊⠎⠞⠕⠗⠊⠑⠎
⠁⠗⠑ ⠕⠃⠞⠁⠊⠝⠑⠙ ⠺⠊⠞⠓⠕⠥⠞ ⠞⠁⠅⠊⠝⠛
⠊⠝⠞⠕ ⠁⠉⠉⠕⠥⠝⠞ ⠞⠓⠑ ⠋⠕⠗⠉⠑⠎ ⠞⠓⠁⠞
⠍⠊⠛⠓⠞ ⠉⠁⠥⠎⠑ ⠞⠓⠑ ⠕⠗⠊⠛⠊⠝ ⠕⠋
⠞⠓⠑ ⠙⠊⠎⠇⠕⠉⠁⠞⠊⠕⠝⠲

⠠⠊⠝ ⠞⠓⠊⠎ ⠠⠏⠓⠠⠙ ⠙⠊⠎⠎⠑⠗⠞⠁⠞⠊⠕⠝⠂
⠠⠊ ⠏⠗⠑⠎⠑⠝⠞ ⠁ ⠝⠑⠺ ⠓⠊⠑⠗⠁⠗⠤
⠉⠓⠊⠉⠁⠇ ⠞⠊⠍⠑ ⠅⠊⠝⠑⠍⠁⠞⠊⠉
⠎⠕⠥⠗⠉⠑ ⠊⠝⠧⠑⠗⠎⠊⠕⠝ ⠍⠑⠞⠓⠕⠙
⠁⠃⠇⠑ ⠞⠕ ⠁⠎⠎⠊⠍⠊⠇⠁⠞⠑ ⠙⠁⠞⠁
⠞⠗⠁⠉⠑⠎ ⠞⠓⠗⠕⠥⠛⠓ ⠑⠧⠕⠇⠥⠞⠊⠧⠑

⠞⠊⠍⠑ ⠺⠊⠝⠙⠕⠺⠎⠲ ⠠⠁ ⠇⠊⠝⠑⠁⠗
⠞⠊⠍⠑⠤⠙⠕⠍⠁⠊⠝ ⠋⠕⠗⠍⠥⠇⠁⠞⠊⠕⠝
⠗⠑⠇⠁⠞⠑⠎ ⠞⠓⠑ ⠎⠇⠊⠏⠤⠗⠁⠞⠑ ⠋⠥⠝⠤
⠉⠞⠊⠕⠝ ⠁⠝⠙ ⠎⠑⠊⠎⠍⠕⠛⠗⠁⠍⠎⠂ ⠏⠗⠑⠤
⠎⠑⠗⠧⠊⠝⠛ ⠞⠓⠑ ⠏⠕⠎⠊⠞⠊⠧⠊⠞⠽ ⠕⠋
⠞⠓⠊⠎ ⠋⠥⠝⠉⠞⠊⠕⠝ ⠁⠝⠙ ⠞⠓⠑ ⠉⠁⠥⠤
⠎⠁⠇⠊⠞⠽ ⠺⠓⠑⠝ ⠎⠏⠁⠝⠝⠊⠝⠛ ⠞⠓⠑
⠍⠕⠙⠑⠇ ⠎⠏⠁⠉⠑⠒ ⠞⠁⠅⠊⠝⠛ ⠃⠑⠝⠑⠋⠊⠞
⠕⠋ ⠞⠓⠑ ⠞⠊⠍⠑⠤⠎⠏⠁⠉⠑ ⠎⠏⠁⠗⠎⠊⠞⠽
⠕⠋ ⠞⠓⠑ ⠗⠥⠏⠞⠥⠗⠑ ⠍⠕⠙⠑⠇ ⠑⠧⠕⠤
⠇⠥⠞⠊⠕⠝ ⠊⠎ ⠁⠝ ⠑⠎⠎⠑⠝⠞⠊⠁⠇ ⠁⠎
⠉⠕⠝⠎⠊⠙⠑⠗⠊⠝⠛ ⠞⠓⠑ ⠉⠁⠥⠎⠁⠇⠊⠞⠽
⠃⠑⠞⠺⠑⠑⠝ ⠗⠥⠏⠞⠥⠗⠑ ⠁⠝⠙ ⠑⠁⠉⠓
⠗⠑⠉⠕⠗⠙ ⠙⠑⠇⠁⠽⠑⠙ ⠃⠽ ⠞⠓⠑ ⠅⠝⠕⠺⠝
⠺⠁⠧⠑ ⠏⠗⠕⠏⠁⠛⠁⠞⠊⠕⠝ ⠕⠏⠑⠗⠁⠞⠕⠗
⠙⠊⠋⠋⠑⠗⠑⠝⠞ ⠋⠕⠗ ⠑⠁⠉⠓ ⠎⠞⠁⠞⠊⠕⠝⠲
⠠⠞⠓⠊⠎ ⠏⠗⠕⠛⠗⠑⠎⠎⠊⠧⠑ ⠁⠏⠏⠗⠕⠁⠉⠓⠂
⠃⠕⠞⠓ ⠕⠝ ⠞⠓⠑ ⠙⠁⠞⠁ ⠎⠏⠁⠉⠑ ⠁⠝⠙
⠕⠝ ⠞⠓⠑ ⠍⠕⠙⠑⠇ ⠎⠏⠁⠉⠑⠂ ⠙⠕⠑⠎
⠗⠑⠟⠥⠊⠗⠑ ⠍⠊⠇⠙ ⠁⠎⠎⠥⠍⠏⠞⠊⠕⠝⠎
⠕⠝ ⠏⠗⠊⠕⠗ ⠎⠇⠊⠏⠤⠗⠁⠞⠑ ⠋⠥⠝⠉⠞⠊⠕⠝⠎
⠁⠝⠙ ⠏⠗⠑⠉⠕⠝⠙⠊⠞⠊⠕⠝⠊⠝⠛ ⠎⠞⠗⠁⠤
⠞⠑⠛⠊⠑⠎ ⠕⠝ ⠞⠓⠑ ⠎⠇⠊⠏⠤⠗⠁⠞⠑ ⠇⠕⠉⠁⠇
⠛⠗⠁⠙⠊⠑⠝⠞ ⠑⠎⠞⠊⠍⠁⠞⠊⠕⠝⠎⠲ ⠠⠞⠓⠑⠎⠑
⠁⠎⠎⠥⠍⠏⠞⠊⠕⠝⠎ ⠁⠗⠑ ⠃⠁⠎⠑⠙ ⠕⠝
⠎⠊⠍⠏⠇⠑ ⠏⠓⠽⠎⠊⠉⠁⠇ ⠑⠭⠏⠑⠉⠞⠑⠙
⠗⠥⠏⠞⠥⠗⠑ ⠍⠕⠙⠑⠇⠎⠲ ⠠⠎⠥⠉⠉⠑⠎⠎⠋⠥⠇
⠁⠏⠏⠇⠊⠉⠁⠞⠊⠕⠝⠎ ⠕⠋ ⠞⠓⠊⠎ ⠍⠑⠞⠓⠕⠙
⠞⠕ ⠁ ⠺⠑⠇⠇⠤⠅⠝⠕⠺⠝ ⠃⠑⠝⠉⠓⠍⠁⠗⠅
⠶⠠⠎⠕⠥⠗⠉⠑ ⠠⠊⠝⠧⠑⠗⠎⠊⠕⠝ ⠠⠧⠁⠇⠊⠙⠁⠞⠊⠕

⠎⠓⠕⠺⠎ ⠞⠕ ⠃⠑ ⠉⠕⠍⠏⠁⠞⠊⠃⠇⠑ ⠺⠊⠞⠓
⠞⠓⠑ ⠇⠊⠝⠑⠁⠗ ⠞⠊⠍⠑⠤⠙⠕⠍⠁⠊⠝ ⠎⠞⠗⠁⠤
⠞⠑⠛⠽ ⠏⠗⠑⠎⠑⠝⠞⠑⠙ ⠓⠑⠗⠑⠲ ⠠⠞⠓⠊⠎
⠞⠑⠉⠓⠝⠊⠟⠥⠑⠂ ⠞⠓⠁⠝⠅⠎ ⠞⠕ ⠁⠝
⠑⠋⠋⠊⠉⠊⠑⠝⠞ ⠑⠎⠞⠊⠍⠁⠞⠊⠕⠝ ⠕⠋ ⠞⠓⠑
⠇⠕⠉⠁⠇ ⠛⠗⠁⠙⠊⠑⠝⠞ ⠕⠋ ⠞⠓⠑ ⠍⠊⠎⠋⠊⠞
⠋⠥⠝⠉⠞⠊⠕⠝⠂ ⠁⠏⠏⠑⠁⠗⠎ ⠞⠕ ⠃⠑ ⠁⠃⠇⠑
⠞⠕ ⠗⠁⠏⠊⠙⠇⠽ ⠑⠭⠏⠇⠕⠗⠑ ⠞⠓⠑ ⠓⠊⠛⠓⠤
⠙⠊⠍⠑⠝⠎⠊⠕⠝⠁⠇ ⠎⠏⠁⠉⠑ ⠕⠋ ⠏⠗⠕⠃⠁⠤
⠃⠇⠑ ⠎⠕⠇⠥⠞⠊⠕⠝⠎⠂ ⠺⠓⠊⠇⠑ ⠞⠓⠑
⠇⠊⠝⠑⠁⠗⠊⠞⠽ ⠃⠑⠞⠺⠑⠑⠝ ⠥⠝⠅⠝⠕⠺⠝⠎
⠁⠝⠙ ⠕⠃⠎⠑⠗⠧⠁⠃⠇⠑⠎ ⠊⠎ ⠏⠗⠑⠎⠑⠗⠤
⠧⠑⠙⠲ ⠠⠊⠝ ⠞⠓⠊⠎ ⠺⠕⠗⠅⠂ ⠠⠊ ⠊⠝⠤
⠧⠑⠎⠞⠊⠛⠁⠞⠑ ⠞⠓⠑ ⠏⠑⠗⠋⠕⠗⠍⠁⠝⠉⠑
⠕⠋ ⠞⠓⠑ ⠠⠓⠠⠍⠠⠉ ⠎⠞⠗⠁⠞⠑⠛⠽
⠙⠑⠁⠇⠊⠝⠛ ⠺⠊⠞⠓ ⠎⠊⠍⠏⠇⠑ ⠎⠽⠝⠤
⠞⠓⠑⠞⠊⠉ ⠉⠁⠎⠑⠎ ⠺⠊⠞⠓ ⠁⠇⠍⠕⠎⠞
⠏⠑⠗⠋⠑⠉⠞ ⠊⠇⠇⠥⠍⠊⠝⠁⠞⠊⠕⠝⠂ ⠊⠝
⠕⠗⠙⠑⠗ ⠞⠕ ⠏⠗⠕⠧⠊⠙⠑ ⠁ ⠃⠑⠞⠞⠑⠗
⠥⠝⠙⠑⠗⠎⠞⠁⠝⠙⠊⠝⠛ ⠕⠋ ⠁⠇⠇ ⠞⠓⠑
⠉⠕⠝⠉⠑⠏⠞⠎ ⠁⠝⠙ ⠗⠑⠟⠥⠊⠗⠑⠙ ⠞⠥⠤
⠝⠊⠝⠛ ⠞⠕ ⠁⠉⠓⠊⠑⠧⠑ ⠁ ⠉⠕⠗⠗⠑⠉⠞
⠑⠭⠏⠇⠕⠗⠁⠞⠊⠕⠝ ⠕⠋ ⠞⠓⠑ ⠍⠕⠙⠑⠇
⠎⠏⠁⠉⠑⠲ ⠠⠞⠓⠑ ⠗⠑⠎⠥⠇⠞⠎ ⠋⠗⠕⠍
⠞⠓⠊⠎ ⠏⠗⠑⠇⠊⠍⠊⠝⠁⠗⠽ ⠊⠝⠧⠑⠎⠤
⠞⠊⠛⠁⠞⠊⠕⠝ ⠁⠗⠑ ⠏⠗⠕⠍⠊⠎⠊⠝⠛
⠁⠝⠙ ⠕⠏⠑⠝ ⠁ ⠝⠑⠺ ⠺⠁⠽ ⠕⠋
⠞⠁⠉⠅⠇⠊⠝⠛ ⠞⠓⠑ ⠅⠊⠝⠑⠍⠁⠞⠊⠉
⠎⠕⠥⠗⠉⠑ ⠗⠑⠉⠕⠝⠎⠞⠗⠥⠉⠞⠊⠕⠝
⠏⠗⠕⠃⠇⠑⠍ ⠁⠝⠙ ⠞⠓⠑ ⠁⠎⠎⠑⠎⠤

⠍⠑⠝⠞ ⠕⠋ ⠞⠓⠑ ⠁⠎⠎⠕⠉⠊⠁⠞⠑⠙
⠥⠝⠉⠑⠗⠞⠁⠊⠝⠞⠊⠑⠎⠲

Contents

General introduction

Earthquake characterization

The planet Earth is a very active physical system. Since the humanity started to live in society, building houses, towns and any other kind of important infrastructure, we have been puzzled by earthquakes and the phenomenon that produces them. For instance, the ancient Greek society built some temples and cities over the places that they knew were previously hit by earthquakes, as it was believed that these sites held spiritual powers. On the other hand, according to Chinese and Japanese historical records, we know that several instruments have been used in the study of earthquakes for over eighteen hundred years. Nowadays, thanks to the work of many scientists and the advances of technology, we know that earthquakes are very frequent physical phenomena. The importance of studying these phenomena relies on the significant energy release that they represent and the possible destructive impact on the human activities that they can have.

The formal study of earthquakes and their causes has significantly evolved from the end of the nineteenth century up to our days. In the beginning, before that the mechanisms behind earthquakes were studied, the scientists tried to determine the location and the origin time of earthquakes. Once it was possible to estimate, with some limitations, these two fundamental features, seismologists showed the interest to measure the size of earthquakes. At that time, it was essential to determine this size to associate it with the possible impacts that future earthquakes could have on society as well as to answer related scientific questions such as: When and where did an earthquake happen? How large was it? What is its evolution in space and time? Why did it occur? When is the next one in a given area? Some of the first seismologists started proposing different strategies to characterize earthquakes according to an estimate of their sizes. Through history, several scales and parameters have been used to perform this characterization. Some of the most significant ones are the ones known as **intensity**, **magnitude** and **moment**.

Different scales: intensity, magnitude and moment

Intensity scale: One of the first features that have been used to characterize any strong motion (regardless of its cause) was the intensity of the ground motion. The intensity is rather a qualitative (often subjective) measurement of the motion experienced during an important shaking event. A given intensity level is determined based on the observed effects of the shaking at a given location. For instance, in 1873 the Rossi–Forel intensity scale was one of the first scales to propose ten levels of intensity used to describe these effects: going from level I (perceived only by instruments) to level X (great disasters). After, in 1883 the Italian volcanologist Giuseppe Mercalli introduced the first version of his intensity scale which, in the following years, became very famous and constantly used all around the world. Another example of this subjective measurement scale is the first Japanese Meteorological Agency (JMA) intensity scale (proposed in 1984) where the strength of the observed shaking had to be associated to one of the four increment levels: bi (微, faint), jaku (弱, weak), kyo (強, strong), and retsu (烈, violent). Back in time, the intensity scales were aimed at categorizing earthquakes according to the shaking felt at some location, which is generally driven by the seismic energy released by an earthquake. Nowadays, we know that other important features, such as site effects, can impact the perceived shaking. However, earthquakes differ in how much of their energy is radiated as seismic waves. In addition, the seismic waves do not radiate homogeneously in all directions: an earthquake that can generate a violent shaking at a given place can be also appreciated as a weak shaking at another location. Therefore, the intensity level given to an earthquake, might not be the most accurate and objective intrinsic measurement to categorize earthquakes or the energy released by them, but rather a local perception of the effects caused by the shaking.

Magnitude scale: The subjectivity and strong variability of the intensity measurements arose in the scientific community the desire of defining a scale able to rate earthquakes according to their energy release, independently of the perceived effects, which may be very different form one particular location to another. It was Richter (1935) who first proposed a magnitude scale that was able to categorize some earthquakes in terms of the estimated total energy released. This scale, which is now known as *local magnitude*), is based on seismometric, and other related data, measurements taken at close distances from the seismic sources (and not based on subjective observations). It has to be noted that, such measurements rely on the assumption that the location of the source generating the shaking has to be approximately known. The magnitude, contrary to the intensity, results from a direct measurement of the waves recorded in a seismogram. The idea behind this link is that, once the wave amplitudes are corrected for the decrease with distance due to the geometrical spreading and attenuation, a large wave amplitude should be related to the importance or size of the earthquake. Taking into account this expectation, different scales, based on different wave amplitudes (e.g. body waves or surface waves) were also proposed. These magnitude scales are able to discriminate between large, moderate, and small shaking events. These scales were preferred over the intensity scales to rate the earthquake sizes, mainly because these scales are completely based on direct instrumental indications, feature that reduces significantly the uncertainties and subjectivity related to personal estimates or the accidental circumstances of the reported effects.

At the beginning of the nineteenth century, when not many seismometers were deployed, it was believed that a direct observation from a single instrument could be enough to establish which level of a given magnitude scale corresponded to a given earthquake size. However, as it happened regarding the intensity scales, the energy released by earthquakes radiate unequally in different azimuths from its origin. Consequently, a unique observation (e.g. using only one instrument), provided a limited proxy of the earthquake size and energy released. In addition, the larger shocks distribute differently the energy among frequency bandwidths from what is done by the weaker events. Therefore, a magnitude derived from a direct observation from a single instrument (e.g. a recorded wave amplitude), is not enough to establish an accurate estimation of the energy released, and of the earthquake magnitude. Therefore, those magnitude scales only provided a particular comparison of the amplitude of certain wave packets produced at a given distance and frequency band. Such feature prevented to relate the estimated magnitudes to a physical property of the earthquake, such as the size or its energy released. In that context, the work from Gutemberg and Richter (1956) was the first attempt to relate the estimated magnitudes (computed form the surface waves) to the radiated energy. However, it was not until the

70s that a new magnitude scale could provide a better characterization of earthquakes.

Seismic moment and the moment magnitude scale: The static, or scalar, seismic moment is the best single measure of the size or energy released that we can provide to characterize a given earthquake. This measurement takes into account the rigidity of the medium, the average seismic dislocation, and the area where the rupture takes place. Such measurement, contrary to the previous ones, attempts to take into account effects due to the geometrical spreading, the radiation pattern and possible attenuation, which makes possible a better estimation of the energy released. At the end of the 70s, the work from Hiroo Kanamori (Kanamori, 1977) and Thomas Hanks (Hanks and Kanamori, 1979) made possible to define a different magnitude scale, which is based on this measure of the energy released. Nowadays, the seismic moment and the moment magnitude is a source attribute that seismologists estimate routinely in order to provide an average evaluation of the importance of an earthquake. In addition, it is known that the energy radiated during an earthquake varies in time and space, and that such variations can be represented by a source time function. Such time and space history can be studied and modeled through the analysis of the observed shaking generated by the earthquake. Those models, can then be used to characterize and the events, their effects and the possible causes behind the whole phenomenon.

Several years have passed since those times when the earthquake characterization was based on the hypocentral location, the origin time and the seismic moment (and estimated magnitudes). Nowadays, the seismological community is able to estimate these, and many other, source attributes automatically. In this context, one of the current fields of research that seismologists keep exploring is the modeling of the time-space history of the seismic rupture. Such representation of the time-space rupture history is understood as a physical model of the rheology failure that occurs over a domain (essentially a surface), which induces the emission of the mechanical waves that are recorded at the Earth's surface where we live.

Different strategies and approaches can be used to infer such physical models. For instance, one possible approach is to construct a **static model** of the source. Such approach tries to model the seismic rupture in terms of the final dislocation that could have occurred, along an active fault, to explain the observed permanent offsets at the surface. However, the static approach lacks of a temporal history of the seismic rupture, and it only provides a final picture of the possible occurred dislocation. Another approach, in which this PhD dissertation is focused, is the **kinematic modeling**. In such approach, the time and space history of the seismic rupture is inferred from the analysis of the temporal evolution of the observed displacement field, or any other derived observable. This approach is denoted as a **kinematic** approach because the inferred rupture models are obtained without taking into account the forces and physical laws that cause and control the seismic rupture. In contrast, if instead of providing just a description of the phenomenon, a rupture model is built based on some physical laws (e.g. laws of friction) is able to explain the observed displacement field, then that model is said to be obtained from a **dynamic approach**.

The final goal of any rupture model is the better understanding of the physical phenomena behind earthquakes. In reality, these models try to answer some of the following questions: Where did the rupture start? Which are the segments of an active fault that were active during an earthquake? Which were the regions that exhibited the maximum dislocation? Why did those regions present larger dislocations? How did the dislocation was distributed across the fault geometry? Was the rupture limited by some other geological structure? How fast did the seismic rupture propagate? These are some of the basic questions, that essentially represent a description of the seismic source. That physical model can come from the static, kinematic or dynamic approaches. It is believed that, by answering these questions, any improvement in the characterization of the seismic rupture history will allow us to better understand the physics behind earthquakes. In addition, being able to understand these phenomena would improve our knowledge of the whole seismic cycle and, as a consequence, of the associated hazard inherent to the strong shaking generated by some large earthquakes.

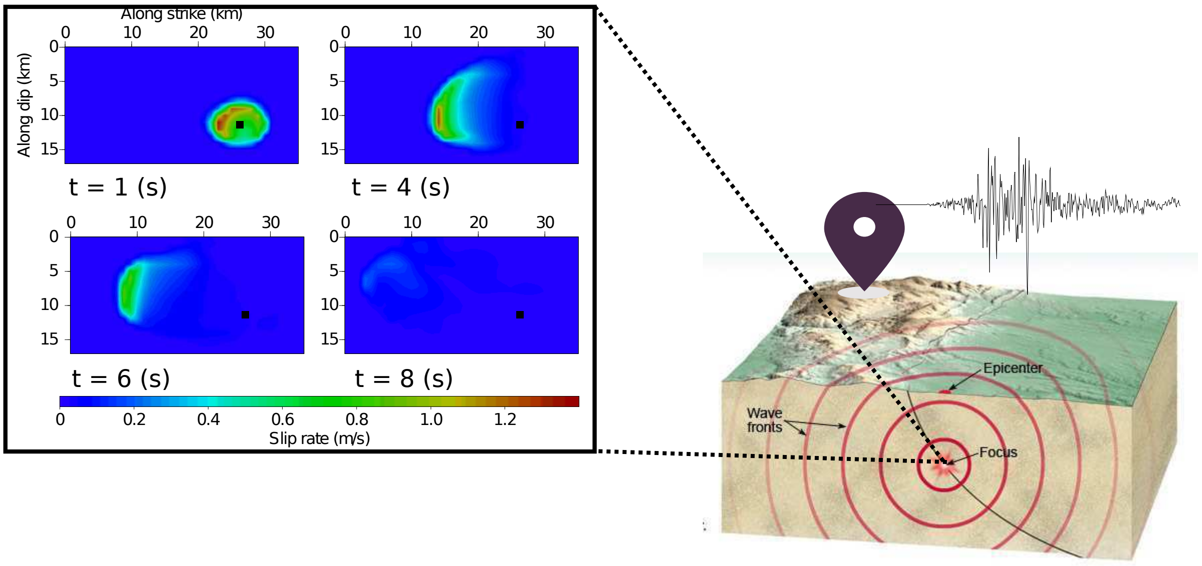

Figure 1: Schematic view of the time-space history of a seismic rupture. On the right, it is illustrated how the waves, generated by an earthquake, travel through the Earth's interior up to the surface where we can record them as seismograms. On the left, a close-up to the time and space history of the seismic source originating the waves recorded as seismograms is presented. The evolution of the seismic source is presented as snapshots at different times (1, 4, 6 and 8 seconds) across the space where it takes place.

Context

The complexity of inferring a seismic source history

A precise reconstruction of the seismic source history is, however, a very challenging task, if possible. The location of the earthquake sources is usually at a significant depth below the Earth's surface (tens to hundreds of kilometers). Down there, the physical conditions, such as temperature and density, might play an important role during the occurrence of an earthquake. Unfortunately, the conditions at such depths have never been directly observed. In addition, all the information about the density or wave velocity of the subsurface structure, where waves travel through before being recorded on the surface, is limited and based on indirect measurements. Therefore, it can be recognized the intrinsic difficulties of inferring the source history of a given earthquake based only on the observations acquired at such distances from their origin and with the lack of information and biased assumptions.

Furthermore, in addition to all what we do not know, current active faults or tectonic boundaries are usually not well instrumented. In other words, the acquisition systems recording the waves generated by seismic sources are not well distributed (Figure 2). As a consequence, all what is inferred about the source is biased by our partial observations of the phenomenon. This geometrical problem has to do with the fact that most of the earthquakes take place in tectonic regimes where receivers might

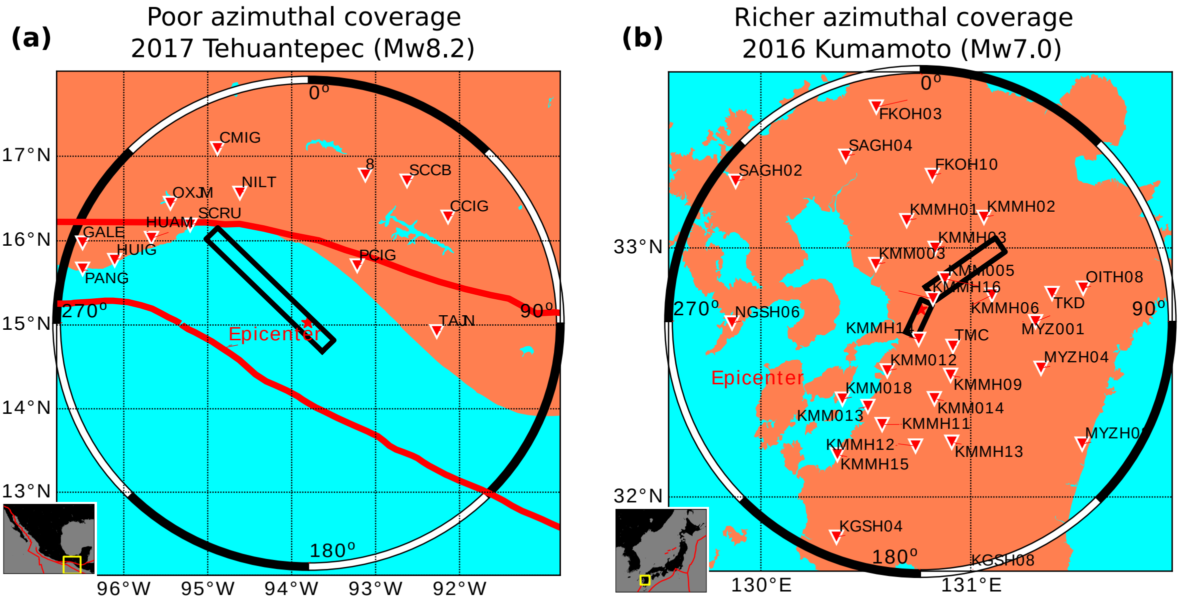

Figure 2: Comparison of the azimuthal coverage of two modern regional acquisition systems recording large earthquakes in 2016 and 2017. (a) Poor receiver azimuthal coverage recording the 2017 (M_W8.2) Tehuantepec Mexico earthquake. (b) Richer azimuthal coverage recording the 2016 (M_W7.0) Kumamoto Japan earthquake. Notice that in (a) receivers are only between $\approx 290^o$ to 115^o, while in (b) receivers are all around the assumed fault planes. In both panels, the red star, the solid black lines and the solid red lines represent the epicenter, the surface projection of the fault planes where the rupture is believed to occur and the tectonic plate boundaries.

not be distributed ideally around the earthquake source under investigation. This common problem in seismology, known as lack of illumination, is something that we also have to consider.

Assumptions and the way they shape our results

Many assumptions have to be taken in order to be able to propose a source model. Some of them are related to the geometry of the problem. For instance, the way in which fault plane orientation is defined. Is the fault plane flat or rough? can the source be described by a single fault segment (Figure 2a) or do we need more? (Figure 2b). The geometrical assumptions are not usually discussed or further investigated. Recently Ragon et al. (2018) discussed the impact of uncertainties related to a given fault geometry on the static slip inversion problem. However, there has been less discussion of this impact on kinematic approach. Therefore, the assumed fault geometries are still based on the observed evolution of the surrounding aftershock activity, that is believed to take place along the fault plane producing the main large earthquake. This uncertainty in the fault geometry makes useless to consider complex geometeries, and we therefore focus on more simple instances such as planar faults on which the dislocation is to be modeled without considering any hypothetical friction law.

Other fundamental assumptions are the ones related to the description of the medium where the waves, generated by the seismic source, travel until reaching the receivers. The seismic source reconstruction is strongly based on the waves recorded on the surface by accelerometers, seismometers, GPS, or other type of sensors. Therefore, everything that is inferred from these recordings will depend on the

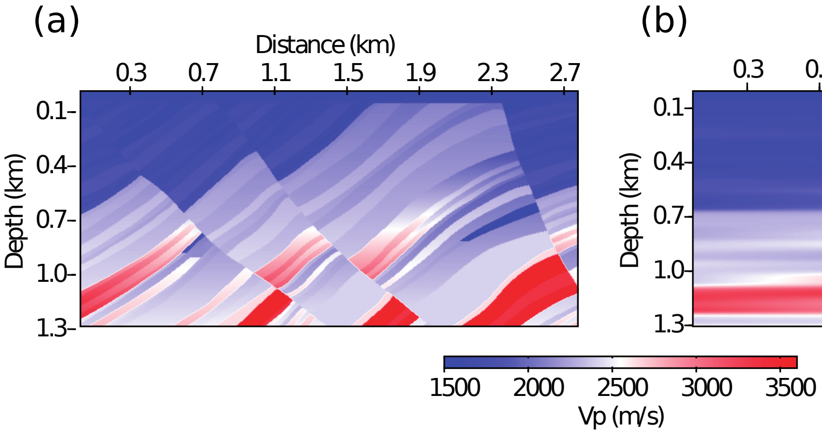

Figure 3: Comparison between (a) a realistic complex P-wave velocity model and (b) a simplified model obtained by a linear distance weighted interpolation in the x-direction between two 1D layered profiles and then gently smoothed. This comparison illustrates how far an assumed simplified subsurface velocity model can be from a realistic one. Modified from Asnaashari (2013).

velocity structure of the subsurface that we use for the wave propagation modeling (Figure 3). Consequently, it is of great importance to keep in mind that the reconstructed rupture histories are impacted, to some extent, by the assumed velocity-density structures. Depending on the range of frequencuies where the inferred rupture model is to be constructed, and the local knowledge of the subsurface structure, the assumed velocity-density structure can go from simple 1D layered media to more complex 3D heterogeneous models, which can possibly account for anisotropy and attenuation. However, we are still limited by the lack of accurate knowledge of the real structures present in the Earth's subsurface. Consequently, any inaccurate assumed velocity-density structure can be also source of errors and uncertainties during the source reconstruction process. This limitation will guide us using low-frequency content of records for which uncertainties on the velocity-density structure have less impact on the source reconstruction.

Finally, other common assumption has to be made according to the way we believe or the way we decide to model what is happening at the source location. For example, if at some position on the source the energy of the rupture is released during one single event, or if it happens during two, three or more episodes. Each of these assumptions necessarily shape the way we conceive the seismic rupture and the results we can obtain using a certain method based on those assumptions.

The purpose of this work

To date, several methodologies are available to perform the reconstruction of the source history. Each of them are based on different assumptions and formulations. This diversity of methodologies and, consequently, of results, highlights the importance of assessing the uncertainties on the reconstructed source models. Therefore, the purpose of this work is to provide a new kinematic source inversion technique which:

- preserves the linearity between the source history and the recorded observations,
- incorporates temporal causality relating a given radiation and the associated slip-rate evolution, whatever is the propagation time delay observed at receivers,
- promotes and opens perspectives in the uncertainty quantification for such models.

In order to achieve all these goals, in this thesis I present a new way to reconstruct the seismic source history that allows a time progressive analysis of the recorded wavefield. Such innovative strategy is based on a linear time-domain formulation of the forward problem. In order to be able to reconstruct physically plausible source models under this formulation, I incorporate the temporal causality by progressively assimilating the recorded seismograms to hierarchically infer the slip-rate evolution. In addition, I include model regularization and gradient preconditioning strategies to the inversion process. Such stabilizing techniques are the ones in charge of injecting the expected physics that the provided kinematic models need to respect. In addition, thanks to the whole methodological development here presented, I am able to explore the promising application of a Bayesian approach, known as Hamiltonian Monte Carlo (HMC) strategy, to assess the uncertainties of the proposed kinematic models.

Outline of this PhD dissertation

In this manuscript, I present my work following this organization:

- In Chapter 1, I present a general introduction to the kinematic source inversion problem. In addition, I provide a state-of-the-art related to this research field. Furthermore, I explain what are the main difficulties that the current strategies applied to reconstruct the source history face, which provides my motivation to introduce the new methodology at the core of this manuscript.
- In Chapter 2, I describe some of the available numerical methods that can be used to precompute the necessary wave propagation information that is required by the whole development presented in the following chapters. In this chapter, I explain how to compute the stress-state tensor from the solution to wave propagation equation that can be obtained from either boundary of domain methods. In addition, I discuss why for some cases the low frequency approach and the assumption of 1D layered media is a suitable choice to model the wave propagation to be used for the source reconstruction.
- In Chapter 3, I introduce the new hierarchical time kinematic source inversion technique. In this chapter, I present also a general strategy to include any type of prior information and regularization terms into the inversion scheme. In addition, I explain how it is possible to perform either a standard inversion of complete recordings or a progressive-time-window source inversion. In this chapter, I also illustrate the performance of this new method by applying it to well-known benchmarks (the Source Inversion Validation) (Mai et al., 2016). I also provide a conclusion discussing on results, methodological perspectives and numerical experiences gained after tackling the synthetic benchmarks.
- In Chapter 4, I apply the new inversion strategy presented in Chapter 3 to the real dataset of the 2016 (M_w7.0) Kumamoto earthquake. First, I present the source-receiver geometry assumed for this earthquake, as well as the assumed 1D layered medium used for the computation of the stress-state tensor. Then, I provide a brief description of the inversion exercises that are carried out in

order to c calibrate all the parameters required by the inversion strategy. After, I summarize the results obtained from the inversion of the real dataset for this earthquake. In addition, I provide a final conclusion about the application of the inversion strategies when tackling a real earthquake.

- In Chapter 5, I change from the deterministic point of view from Chapters 3 and 4 to a stochastic approach of the problem. First, I provide the fundamental theory and basic concepts related to Bayesian inference. In this chapter, I focus my research on the estimation of the posterior probability density by exploring the space of probable solutions using an efficient Bayesian strategy known as the Hamiltonian Monte Carlo strategy. To do that, I reformulate the inverse problem that I present in Chapters 3 and 4. In this chapter, I demonstrate the suitability of the HMC strategy to tackle the kinematic source inversion problem by applying it to two simple synthetic cases. I also discuss some conclusions and perspectives for this new strategy as well as its limitations.
- Finally, in the last chapter of this manuscript, I provide general conclusions about the theoretical and computational development of this work. In addition, I supply several perspectives of all the work here presented.

Chapter 1

Kinematic source imaging

Contents

1.1 Introduction

In this chapter, I present my personal overview of the fundamental theory to understand the kinematic source inversion problem and its complexity. In order to do so, I present the history of this research field. In addition, the content of this first chapter provides the reasons why I decide to choose a linear time-domain adjoint-based formulation to tackle this problem among all the possible frameworks.

The outline of this chapter is the following:

- In Section 1.2, I recall the fundamental equations and theory underlaying the source imaging problem. In this section, I also present the earthquake source problem when considering a ponctual source. Then, I shall consider the continuous problem of an extended finite source defined on a surface and relate this approach to the discrete computational formulation needed to tackle real applications.

- In Section 1.3, I detail the different formulations that can be used to state this problem: either a linear or a non-linear formulation as well as the possible choices to work either in the time-, frequency- or wavelet-domains. This section aims at describing the assumptions behind each of these choices, and present their advantages and limitations. This description is given through a historical review of some of the strategies that have been proposed in the available literature.

- In Section 1.4, I explain the complexity of the problem and why there is a large variability of results among the authors working on a given single earthquake. I shall explain the significant trade-off between the parameters involved in this problem and the importance of assessing their uncertainties.

- Finally, in Section 1.5, I conclude giving the reasons why I decide to use a linear time-domain adjoint-based inversion strategy to tackle this problem. Such strategy is the one that is used in the next chapters of this work.

1.2 Theory

1.2.1 Representation theorem

In this chapter, and across all the other chapters, the following convention is used: non-underlined symbols represent scalars, single underlined are vectors, and double underlined are matrices.

Let me start citing what is known as the uniqueness theorem in seismology (Aki, 1968; Udías, 1991). The displacement field $\underline{u}(\underline{x}, t)$ throughout the volume $\underline{B}$ with surface $\underline{S}$ is uniquely determined after time t_0 by the initial displacement $\underline{u}_0$ and the velocity values at t_0 throughout $\underline{B}$ (initial conditions) and by values at all times $t > t_0$ of:

1) the body forces and heat supplied throughout $\underline{B}$,

2) the traction $\underline{T}$ over any part $\underline{S}_1$ of $\underline{S}$,

3) the displacement over the remainder $\underline{S}_2$ of $\underline{S}$, with $\underline{S} = \underline{S}_1 + \underline{S}_2$.

From this theorem it is possible to introduce what in seismology is known as the representation theorem. This theorem is a mathematical form that allows to determine the displacement field $\underline{u}(\underline{x}, t)$, at the general location $\underline{x}$ and time t, in terms of three possible quantities that can originate the motion. These three quantities might be body forces $\underline{f}$ within $\underline{B}$, or induced tractions $\underline{T}$ or displacements $\underline{\mathcal{V}}$ over surface $\underline{S}$. Using Einstein index summation convention, this can be mathematically written as follows,

$$\begin{aligned} u_n(\underline{x},t) = &\int_{-\infty}^{\infty} d\tau \int\int\int_{\underline{B}} f_i(\underline{\xi},\tau) G_{in}(\underline{x},t;\underline{\xi},0) d\underline{B}(\underline{\xi}) \\ &+ \int_{-\infty}^{\infty} d\tau \int\int_{\underline{S}} G_{in}(\underline{x},t;\underline{\xi},0) T_i(\underline{v}(\underline{\xi},\tau),\underline{\eta}) \\ &- \mathcal{V}_i(\underline{\xi},\tau) c_{ijkl} \eta_j G_{kn,l}(\underline{x},t;\underline{\xi},0) d\underline{S}(\underline{\xi}). \qquad i,j,k,l,n \in [1,2,3], \end{aligned} \tag{1.1}$$

where $\tau = 0$ and $\underline{\xi}$ represent the source time and location vector, respectively, $\underline{\eta}$ is the normal vector to the surface over which the traction $\underline{T}$ is applied or the displacement $\underline{\mathcal{V}}$ occurs, c_{ijkl} is the associated component of the stiffness tensor $\underline{\underline{c}}$ containing the properties of the medium, and $\underline{\underline{G}}$ is a second order tensor that contains all the information of the waves propagating from the source to the receiver. $\underline{\underline{G}}$ is a very important tensor, known as Green functions, which represents the displacement field due to a punctual impulsive force that is applied on a given direction. Therefore, I use G_{in} to denote the n-component of the displacement field that is due to a unitary force applied on the i-th direction, and $G_{in,l}$ is its spatial partial derivative with respect to ξ_l-axis direction, $\partial G_{in}/\partial\xi_l$. Notice that the vector $\underline{\mathcal{V}}(\underline{\xi},\tau)$, hereafter denoted as slip-rate vector, has three directions and a time history $\underline{\mathcal{V}}(\underline{\xi},\tau) = [\mathcal{V}_x(\underline{\xi},\tau), \mathcal{V}_y(\underline{\xi},\tau), \mathcal{V}_z(\underline{\xi},\tau)]$. It is worth to mention that, assuming that the Earth's surface acts similarly as a homogeneous boundary condition on $\underline{S}$, then $\underline{\underline{G}}$ follows a reciprocal relationship for source and receiver coordinates. This space-time reciprocity is represented as follows

$$G_{nm}(\underline{\xi},\tau,\underline{x},t) = G_{mn}(\underline{x},-t,\underline{\xi},-\tau) \qquad m,n \in [1,2,3] \tag{1.2}$$

Taking into account this reciprocity (equation (1.2)) and the fact that faulting sources are understood as a given dislocation or relative motion between two or more blocks, equation (1.1) can be reduced. To do that, let me simplify the faulting source to a dislocation ocurring between two blocks. Those blocks are separated by a 2D spatial surface $\underline{\Sigma}$ with two sides $\underline{\Sigma}^+$ and $\underline{\Sigma}^-$ (see Figure 1.1). Then, the displacement measured at each side of $\underline{\Sigma}$ is the relative displacemenent of one block with respect to the other. Those motions are represented as $\underline{\mathcal{V}}(\underline{\xi},\tau)_{\underline{\Sigma}^+}$ on one side of $\underline{\Sigma}$ and $\underline{\mathcal{V}}(\underline{\xi},\tau)_{\underline{\Sigma}^-}$ on the other side. Such displacement discontinuity (i.e. faulting slip) can then be mathematically denoted by $[\underline{\mathcal{V}}(\underline{\xi},\tau)]$ for $\underline{\xi}$ on $\underline{\Sigma}$, and refers to the difference $\underline{\mathcal{V}}(\underline{\xi},\tau)_{\underline{\Sigma}^+} - \underline{\mathcal{V}}(\underline{\xi},\tau)_{\underline{\Sigma}^-}$ (see Figure 1.1 for a graphic illustration). By ignoring all the possible induced tractions related to this displacement, as well as possible body forces (assumption which cancels two out of three terms from equation (1.1)), the displacement field $\underline{u}(\underline{x},t)$ is only due to the faulting source. Consequently, the representation theorem (equation (1.1)) is conveniently reduced to,

$$u_n(\underline{x},t) = \int_{-\infty}^{\infty} d\tau \int\int_{\underline{\Sigma}} [\mathcal{V}_i(\underline{\xi},\tau)] c_{ijkl} \eta_j G_{nk,l}(\underline{\xi},t-\tau;\underline{x},0) d\underline{\Sigma}, \tag{1.3}$$
$$i,j,k,l,n \in [1,2,3]$$

where the indices represent

i : components of the dislocation vector

j : components of the normal vector

n : components of the recorded displacement

k : direction of the Green function

l: direction of the derivation of the Green function

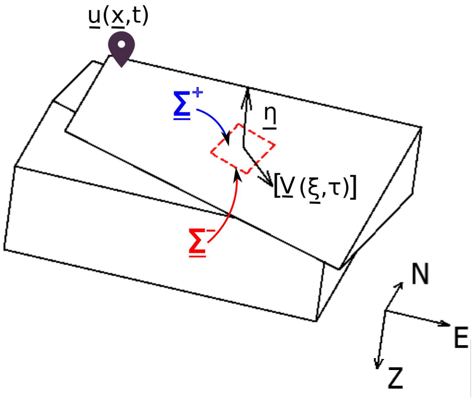

Figure 1.1: Schematic view of a dislocation between two blocks. The blocks are separated by a 2D spatial surface $\underline{\Sigma}$ that has a positive $\underline{\Sigma}^+$ and a negative $\underline{\Sigma}^-$ side. The unitary normal vector to surface $\underline{\Sigma}$ is represented by $\underline{\eta}$ and the amplitude and direction of the dislocation is denoted by vector $\underline{V}$. Notice that this dislocation is the source of the motion that is recorded at location $\underline{u}(\underline{x}, t)$. The directions along the North, East and depth are also represented in this figure.

The equation (1.3) describes the linear relation between the slip-rate $\underline{\mathcal{V}}(\underline{\xi}, \tau)$ and the particle velocity at any time and position in the medium $\underline{u}(\underline{x}, t)$, once the expression $\underline{\underline{G}}(\underline{\xi}, t - \tau; \underline{x}, 0)$ contains all the terms of the wave propagation solution: near-, far- and intermediate-fields. The term $c_{ijkl}\eta_j G_{nk,l}(\underline{\xi}, t - \tau; \underline{x}, 0)$ in equation (1.3) corresponds to a tensor constructed by the **traction vectors per unit impulse** at the fault coordinate $\underline{\xi}$, due to a point force applied in the l-th direction at the observer location $\underline{x}$. This tensor is also known as the **stress-state tensor** and it is very important for all what is presented in Chapters 3, 4 and 5. Therefore, I detail its computation in Chapter 2. Let me then assume in this chapter that this term is known.

The equation (1.3) has been massively used for many years by seismologist all around the world to estimate the wavefield radiated from earthquakes (e.g. Burridge and Knopoff, 1964; Aki, 1968; Hartzell and Helmberger, 1982; Hartzell and Heaton, 1983; Archuleta, 1984; Cohee and Beroza, 1994; Cotton and Campillo, 1995; Ji et al., 2002a; Gallovic and Imperatori, 2014; Fan et al., 2014; Somala et al., 2018). In this framework, this equation corresponds to the **forward problem**, which consists in computing the synthetic seismograms $\underline{u}(\underline{x}, t)$ given a kinematic model $\underline{\mathcal{V}}(\underline{\xi}, \tau)$. This equation has the following very interesting properties:

- Slip or slip-rate on the fault $[\underline{V}(\underline{\xi}, \tau)]$ is enough to determine displacements at any $\underline{x}$ location.
- No boundary conditions on $\underline{\Sigma}$ are needed for the Green function G_{nk}. In other words, for the propagating waves $\underline{\Sigma}$ is transparent.
- Fault motion, which may be complicated and which form might be difficult to determine $[\underline{V}(\underline{\xi}, \tau)]$, thanks to the linear relation, is completely independent from the wave propagation information contained in $\underline{\underline{G}}$.

1.2.2 Source geometry

The source geometry is very important. In equation (1.3) this information is represented by the vector $\underline{\eta}$. This vector is normal to the surface where the dislocation happens. It is necessary to first introduce the strike ϕ and dip δ angles (Figure 1.2) to define this vector. The strike angle ϕ is measured horizontally

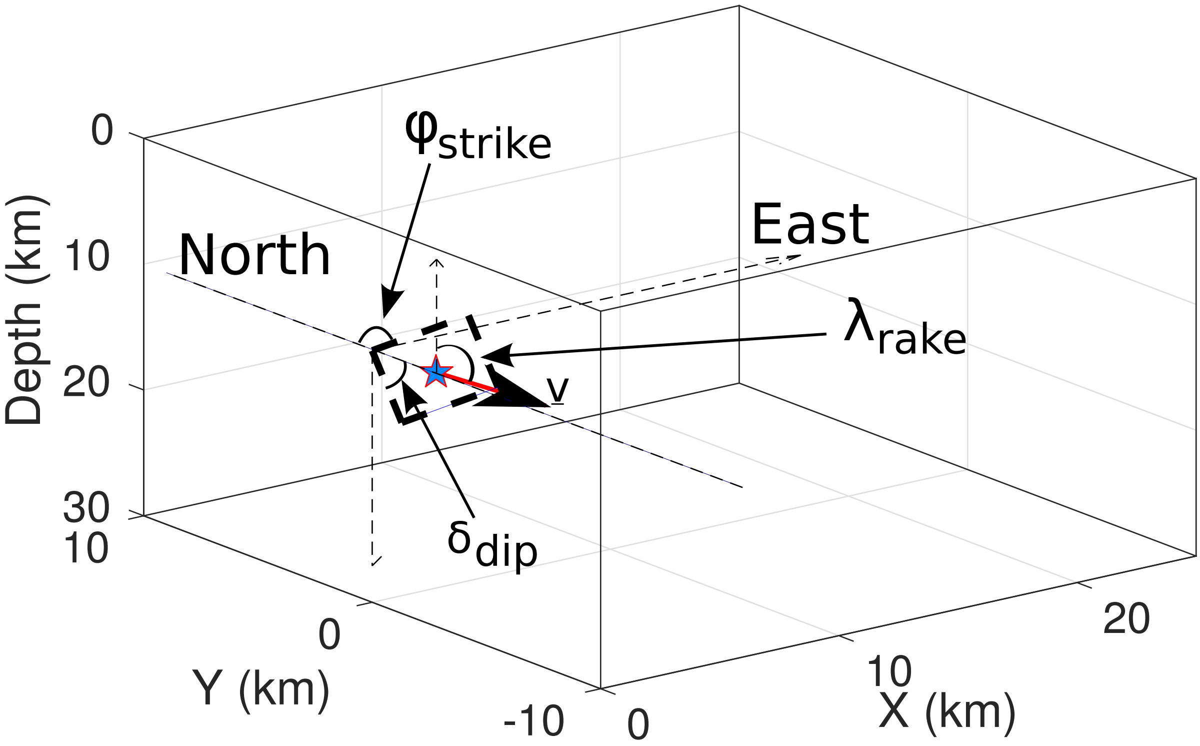

Figure 1.2: Illustration of a faulting source geometry. The strike ϕ and dip δ angles describing the faulting plane $\underline{\Sigma}$ are represented. This geometry will be considered as given. A third angle exists related to dislocation direction: the so-called rake angle λ which could be reconstructed. Notice that even if the slip vector is a 3D vector, it lies on the 2D faulting geometry.

with respect to the North and it is the orientation angle of the faulting plane. This angle is measured clockwise. The dip angle measures the inclination of the faulting plane with respect to an horizontal surface (Stein and Wysession, 2003). Using these two angles the normal vector to the dislocating surface is defined as

$$\underline{\eta} = \begin{bmatrix} -\sin\delta\sin\phi \\ -\sin\delta\cos\phi \\ \cos\delta \end{bmatrix}, \tag{1.4}$$

A third angle, the so-called rake angle λ, which is related to the dislocation direction is also very important. Its value can be reconstructed from the relation existing between the dislocation occuring along the dip and strike directions. However, the rake angle can also be assumed as a known or fixed geometrical value that is inferred from preliminary analysis. It is as well worth mentioning that a fault can have opening motion, such that the slip vector is not in the fault plane. The angle, α, which is used to represent the deviation of the slip vector from the faulting plane can be calculated directly from the moment tensor eigenvalues (Tape and Tape, 2013; Dufumier and Rivera, 1997, e.g).

1.2.3 Point source

The point source is a particular case where the double integral over the surface $\underline{\Sigma}$ from equation (1.3) is assumed to be well approximated by a single point that lies over the surface that it represents. To some extent, we assume that the rupture happens at an infinitesimal surface with size $\Delta\Sigma = \Delta\xi_\phi \Delta\xi_\delta$, where $\Delta\xi_\phi$ and $\Delta\xi_\delta$ are small distances along the strike and dip directions at the source location $\underline{\xi}$. Therefore, and using the index summation convention, equation (1.3) can be reduced to,

$$u_n(\underline{x}, t) = \left[\int_{-\infty}^{\infty} [\mathcal{V}_i(\tau)] c_{ijkl} \eta_j G_{nk,l}(\underline{x}, t-\tau; \underline{\xi}, 0) d\tau\right] \Delta\Sigma. \qquad i, j, k, l, n \in [1, 2, 3] \tag{1.5}$$

Equation (1.5) is a simpler form that we can use to first analyze, at a single source position, the time history of the dislocation and the possible parametrizations that can be used to represent it. Under this assumption, the three components of the slip-rate vector evolve in time. In order to ease the understanding of this time evolution of the slip-rate vector, let me represent this vector as the multiplication of its modulus and a unitary vector,

$$\underline{\mathcal{V}}(\underline{\xi}, \tau) = |\underline{\mathcal{V}}(\underline{\xi}, \tau)| \begin{bmatrix} \hat{\mathcal{V}}_x(\underline{\xi}, \tau) \\ \hat{\mathcal{V}}_y(\underline{\xi}, \tau) \\ \hat{\mathcal{V}}_z(\underline{\xi}, \tau) \end{bmatrix}. \tag{1.6}$$

In the real world, the shape of the function describing the time evolution of the slip-rate modulus is unknown. As mentioned by Tinti et al. (2005), several laboratory experiments investigating the behavior of rocks failure when they are subjected to high pressures and temperatures (trying to emulate the same conditions present in an earthquake) suggest that the shape of this function is close to the one illustrated in Figure 1.3 (solid red line) (see the experiment driven by Ohnaka and Yamashita, 1989). In fact, the shape of this function is defined by the physics underlying the earthquake rupture process. Such complex faulting system can be scaled down to a simple faulting geometry on which a friction law (i.e. dynamic modeling) mimicks the complexity of the earthquake rupture process. On the contrary, the kinematic slip-rate description encapsulates the possible physical causes of the real earthquake. However, for a better physical understanding, one has to consider dynamic modeling related to failure criteria and stress loading. One may infer such quantities by analyzing the reconstructed slip-rate as well as other quantities (Mikumo and Yagi, 2003) or by inverting for these parameters directly from records (Peyrat et al., 2004): however, this is not the purpose of my work. In Figure 1.3, two different time evolutions are illustrated. The first one (solid black line), is the slip (cumulative displacement) which monotonic increment grows as τ increases. The final constant value where this cumulative curve stops increasing is known in seismology as the **final slip**. The second one (solid red line), is the first derivative of that slip time history with respect to time. That first temporal derivative is the **slip-rate** time history.

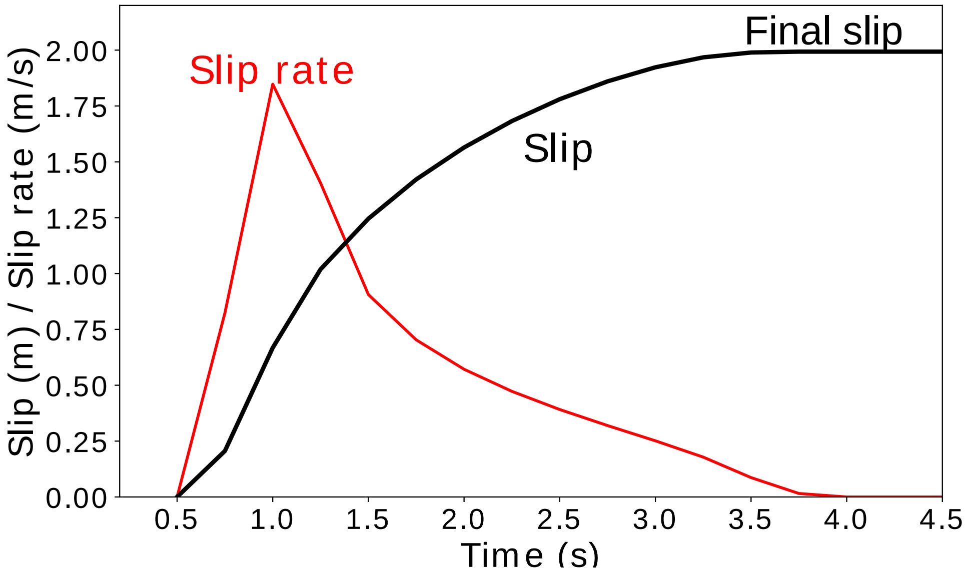

Figure 1.3: Slip (solid black line) and slip rate (solid red line) time functions. The time histories in this plot represent an idealized Yoffe-type (Tinti et al., 2005) time evolution of the amplitude of the slip rate vector and its first primitive with respect to time.

Several mathematical models have been proposed to describe either the slip or the slip-rate time histories. For instance, Cotton and Campillo (1995) use a hyperbolic tangent function to represent the slip time history,

$$S(\underline{\xi},\tau) = \int_0^{\tau} |\mathcal{V}(\underline{\xi},\tau)| d\tau = \frac{1+\tanh((\tau + r/2)(r/2))}{2r}, \qquad 0 < \tau < r \tag{1.7}$$

while Ji et al. (2002a) prefers to define it as a sine function.

$$S(\underline{\xi},\tau) = \int_0^{\tau} |\mathcal{V}(\underline{\xi},\tau)| d\tau = \frac{\tau}{r} - \frac{\sin((2\pi\tau)/r)}{2\pi}, \qquad 0 < \tau < r \tag{1.8}$$

where τ denotes the running time and r corresponds to the total time that lasts the motion (Figure 1.4a). This time duration is known as **rise time**, and it is defined as the total time which is required by a particle, located at the source location, to reach its final position after the faulting. Other authors prefer to work defining the slip-rate time function. For instance, Wald and Heaton (1994) and Archuleta (1984) define the slip-rate function as a triangle, which unequal side has a length in time corresponding to the rise time. Other authors, such as Hsieh et al. (2016), prefer to define the slip rate time history through a piece-wise function,

$$|\mathcal{V}(\underline{\xi},\tau)| = \begin{cases} \frac{1}{\tau^{\alpha\beta}}\left[1-\cos\left(\frac{\pi t}{\tau_s^{\alpha\beta}}\right)\right], & 0 < \tau < \tau_s^{\alpha\beta}, \\ \frac{1}{\tau^{\alpha\beta}}\left[1+\cos\left(\frac{\pi(\tau_s^{\alpha\beta}-t)}{\tau_e^{\alpha\beta}}\right)\right], & \tau_s^{\alpha\beta} < \tau < \tau_e^{\alpha\beta}, \\ 0, & \tau > \tau_s^{\alpha\beta} \end{cases} \tag{1.9}$$

where $\tau_s^{\alpha\beta}$ is known as the duration of the starting-phase (time taken by a particle to reach maximum slip), and $\tau_e^{\alpha\beta}$ is called the end-phase time that is the duration between maximum slip rate and the end of slip. Thus, the total rise time is given as $\tau^{\alpha\beta} = \tau_s^{\alpha\beta} + \tau_e^{\alpha\beta}$ (see Figure 1.4b).

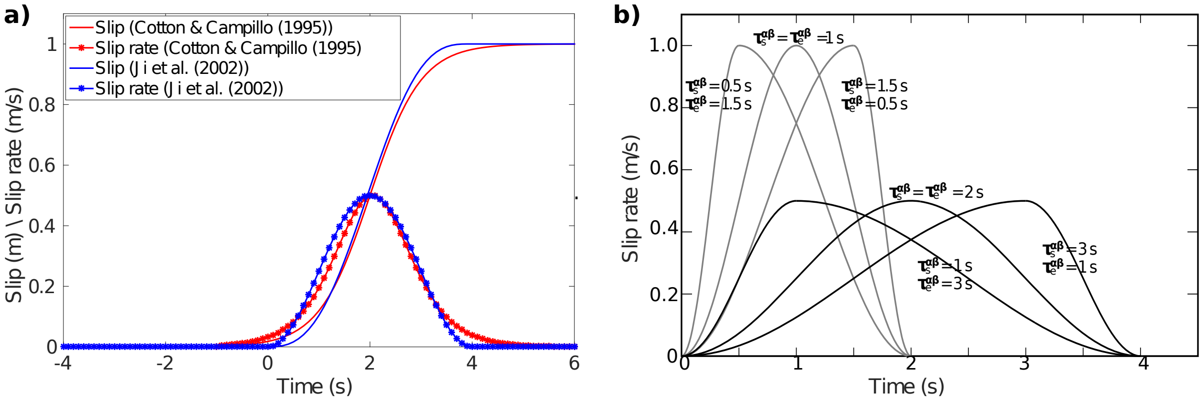

Figure 1.4: Illustration of different models to represent the slip and slip rate time histories. a) Comparison between the slip and slip rate time histories of the models proposed by Cotton and Campillo (1995) (red lines) and Ji et al. (2002a) (red lines). For the panel a) the rise time used is $r = 4$ seconds (from equations (1.7) and (1.8)). b) Compares several slip rate functions, with different starting and ending phases, which can be represented by the piece-wise function from equation (1.9).

However, in reality the slip (or the slip-rate) function does not follow a general form. In fact, a critical review provided by Beresnev (2003) illustrate that some of the most simple functions representing the slip-rate function (e.g. triangle or boxcar functions) can impact all what we can infer from the source time history.

More recently, Tinti et al. (2005) proposed a more physical meaningful slip and slip-rate functions which, compared to the sine, hyperbolic tangent or triangles, are more complex (see Figure 1.3). Besides all the possible functions that can be used to described these time histories, seismologist have agree on the fact that these functions have at least three general features that can inject some physical information in the rupture history. The first is the rupture time, which tells us at what time the faulting starts. The second is the rise time, which is interpreted as the duration of the motion. The third is the final slip, which is the final value of the slip function or the total area under the slip-rate function. When more complex functions are used, as the one proposed by Tinti et al. (2005), it is also necessary to provide two more parameters that describe the acceleration and deceleration of the motion.

While **the observed seismograms are linearly related to the slip-rate time history**, the reduced number of **parameters describing the source history do not map linearly into the slip-rate function**. Consequently, these reduced number of parameters used to described the slip, or the slip-rate, function are also not linearly related to the observations (see Figure 1.3). In particular, the parameters determining the timing of the rupture (i.e. the rupture time and the rise time) are the ones causing the nonlinearity. This was first highlighted by Archuleta (1984) and Olson and Anderson (1988). They noticed that, the rupture time nonlinearity disappears when these two parameters are fixed to expected values. This fact is widely known nowadays, but the use of this assumption to study real earthquakes may bias strongly the search for a solution.

Before extending the problem from the simple point source case to a finite source, let me summarize some important features. The time history of the slip-rate time history is linearly related to the recordings observed at any receiver location. The shape of the slip or the slip-rate functions can be defined through a reduced number of parameters: 1) starting time, 2) maximum amplitude, 3) duration, and others like 4) acceleration and 5) deaceleration (Figure 1.5). However, these parameters are non-linearly related to slip or slip-rate functions. Therefore, these parameters have a non-linear relationship with the observed wavefield at the receivers. Thus, special care must be taken when using this reduced number of parameters to described the rupture history.

1.2.4 Finite source

In reality, the point source approximation is not enough to caracterize must of the large earthquakes, or small events when they are observed from very close distances. Therefore, the surface integral (from equation (1.3)) must be computed and one can proceed with different discretization strategies related to the underlying meshing. Before doing so, let me summarize the scientific improvement over the last tenths of years.

The studies by Haskell (1964, 1966, 1969) are some of the first works devoted to investigate the radiated energy and the associated displacements induced by a finite source. In his first study Haskell (1964), showed that a finite source presenting shear faulting can be equivalently represented by a sequence of double-couple point sources distributed over the fault plane. Later in Haskell (1969), using this assumption of a distribution of double-couple point sources, the author computed the displacement, particle velocity, and acceleration waveforms recorded at near field distances from a synthetic finite source presenting unilaterally shear faulting. Certainly, these studies are the backbone of the forward modeling of synthetic seismograms associated with any given finite source model, and consequently, to infer the time-space source history of a given earthquake. His contribution to seismology allows to establish a discrete form of the surface integral present in equation (1.3).

Nowadays, practically all the forward and inverse techniques that can be found in the literature assume this distribution of point sources across the finite fault surface to represent the shear faulting. This discrete representation is not only used by researchers working on the kinematic source inversion problem, but also by seismologists investigating the static component (permanent offset) of the coseismic displacement due to earthquakes (e.g. Simons et al., 2002; Wang et al., 2003) or by other phenomena such as slow slip events (e.g. Radiguet et al., 2011).

The principal idea behind this discrete representation is to deploy across the fault surface, which length and orientation are previously defined, a finite number of point sources. Each of these point sources has its own slip and slip-rate time history. The ensemble of all the slip or slip-rate time histories across the whole spatial distribution forms the time-space history that we want to reconstruct. Ideally, the time history of each spatial node (point source) should exhibit a similar behavior as its neighbors, a condition which implies spatial coherence. The design of the discrete grid of point sources representing the fault can be simple (standard equally space along strike and dip directions), or very complex and unstructured (see Appendix C). Any discrete evaluation of the surface integral based on various formulations such as trapezoidal or Simpson's rules over grids is acceptable as long as such numerical computation is honoring the wave propagation and the rupture description specified in the forward modeling.

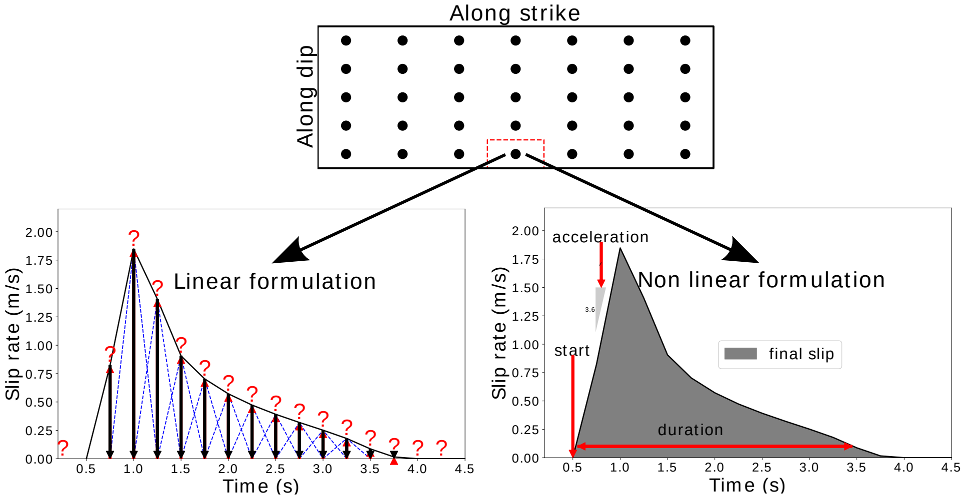

Figure 1.5: Comparison between the linear and non linear representations of the time history of the seismic source. (a) Shows the spatial discretization of the fault geometry in several nodes of support. (b) and (c) illustrate the different parametrizations of the time history of the rupture at a single spatial node. In (b) every time sample of the slip rate function is an unknown. In (c) the function is described by only four parameters: starting time, duration, final slip and acceleration, the decay of the function is controlled by the duration and a fixed decay rate.

1.3 Strategies to tackle the kinematic source inversion problem

The earthquake source reconstruction is a problem with a long history in seismology. In this section, I provide a chronological non-exhaustive overview of some of the most relevant strategies that have been proposed to tackle this problem. First, I start with the linear multiple time-window method (Olson and Apsel, 1982; Hartzell and Heaton, 1983). Then, I mention the linear source deconvolution method (Kikuchi and Kanamori, 1982, 1986, 1991). After, I mention the linear and non-linear frequency approaches (Archuleta, 1984; Steidl et al., 1991; Cotton and Campillo, 1995). Finally, I end this section reviewing more recent techniques that use the wavelet domain to decomposed the observed seismograms (Ji et al., 2002b; Hsieh et al., 2016; Hao et al., 2017), and other strategies such as the adjoint-state method to solve the inverse problem (Fan et al., 2014; Somala et al., 2014). Let me then start with this review.

1.3.1 Linear multiple time-window inversion method

The first two studies attempting to reconstruct the rupture time-space history (from the kinematic point of view) of an earthquake based on the inversion of a real data set are the ones published by Olson and Apsel (1982) and by Hartzell and Heaton (1983). Both works formulate the source reconstruction as a least-squares problem in the time domain, where the strong motion recordings observed at the Earth's surface are used to infer the time-space slip distribution on an assumed fault geometry. For both studies, the chosen parametrization is defined by a discrete grid dividing the fault surface into a finite number of segments where the rupture is allowed to occur during a chosen deterministic number of separated time intervals (multiple time-windows). Each time interval is separated from the next one by an equal time interval and the instant of time when they act is previously determined based on an expected rupture speed that is defined by trial an error exercises. Comparing the two works (that are applied to the same earthquake: 1979 Imperial Valley), the principal difference is that the work from Hartzell and Heaton (1983) considers a much finer space discretization (more unknowns) and that they also include the contribution of teleseismic phases that are jointly inverted together with the strong motion recordings.

Important conclusions were obtained from these first studies on the kinematic source inversion problem. The inverse problem is unstable and regularization is required to obtain stable physical solutions. Both studies recognize that several different constraints could be assumed and implemented. Some of these constraints are adopted and tested not only by these authors but by many other researchers. For instance, some of these constraints consider: 1) moment minimization, 2) spatial coherence through smoothing operators, 3) filtering of singular values and 4) positivity constraints.

Another important conclusion from these studies is that there is not a unique solution to the source reconstruction problem. Many slip or slip-rate time-space histories can fit the data equally well and the differences between the solutions correspond to the unstable component of the problem which is not determined by any of the available data (strong motion recordings or teleseismic phases at that time). The legacy of these first studies continues until now. Many authors have applied in the last three decades the concepts and theory developed by these authors to study the time-space history of many earthquakes: Wald and Heaton (1994); Cohee and Beroza (1994); Horikawa et al. (1996); Thio et al. (2004); Kubo et al. (2016); Asano and Iwata (2016); Okuwaki and Yagi (2017) are just some of the studies that have used, discussed and improved this multiple time-window strategy.

1.3.2 Linear time-domain source deconvolution method

Another branch of inversion strategies developed to tackle the source reconstruction problem are the linear time-domain deconvolution methods. These strategies emerged at the same time as the multiple time-window strategies. The pioneering works by Kikuchi and Kanamori (1982, 1986, 1991) are the studies that illustrate the possibility of extracting a source history, formed by a multiple shock sequence, through a progressive deconvolution of complex teleseismic body waves (see Figure 1.6).

The principle of these methods, is the fact that an earthquake source can be represented as a sequence of multiple shocks occurring across the fault surface (see panels a) and b) in Figure 1.6). Then, the main characteristics of the sub-shock in the sequence can be determined through a least-squares formulation where the height and the onset time of each shock is related to the misfit between observed and synthetic wavefields. The reconstruction of the sub-shock sequence is carried out iteratively in such a way that after the first N iterations, the heights and onset times of the first N largest shocks are obtained, and the source time function is determined as the sum of all the shocks. This causal deconvolution allows to retrieve the sub-shocks according to their amplitude importance. At each iteration of this deconvolution process, the misfit between synthetic and observed waveforms (in a least-squares sense) is decreased. For instance, as the largest shocks are deconvolved the misfit illustrated in panels c) and d) of Figure 1.6 is reduced.

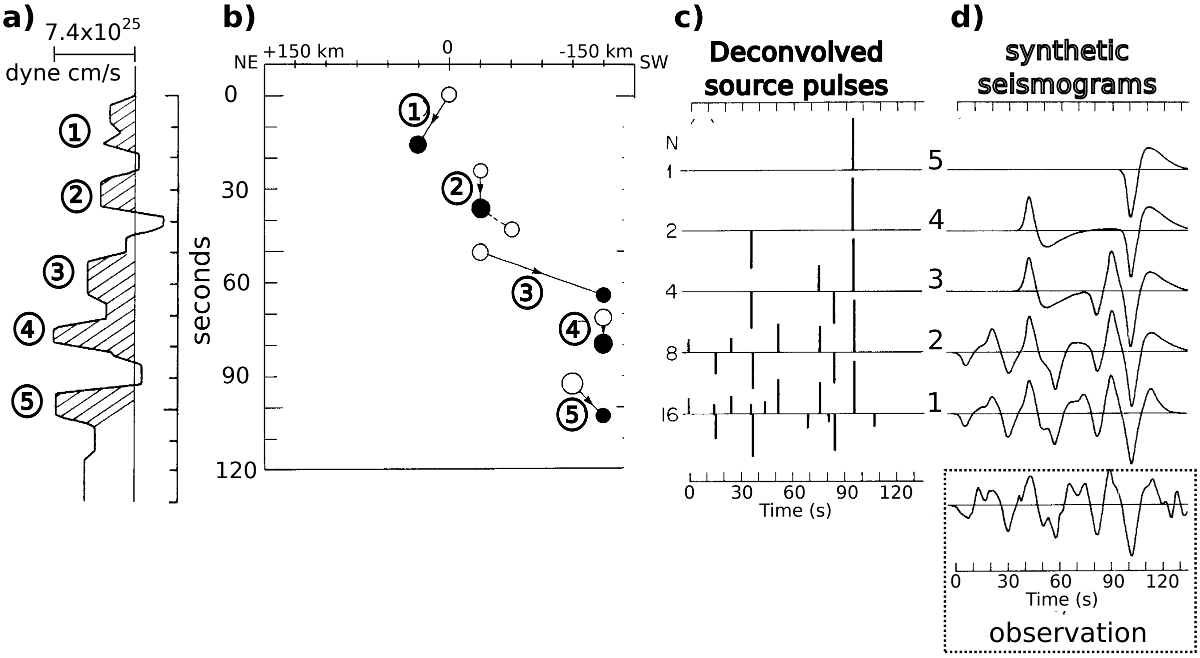

Figure 1.6: Illustration summarizing the linear time-domain source deconvolution method. a) Multiple shock sequence representing the source history obtained through this method for the 1976 Guatemala earthquake. b) Location (along the NE-SW direction) and time of the 11 largest source pulses obtained by the multi-station deconvolution process. Open and closed circles show positive and negative pulses, respectively. The numbers in b) corresponds to the ones in a) and c). In c), the progressive deconvolution process of the body waves observed in d) is shown. Notice that, as shown in c), this process deconvolves progressively the larger pulses first. Modified from Kikuchi and Kanamori (1982).

However, in their first work (Kikuchi and Kanamori, 1982), the method was limited to the assumption that all the shocks in the sequence have the same fault mechanism (strike, dip and rake angles). Another limitation is that the point source sequence was defined along an horizontal source line (at the same depth), which prevented any along dip variation. Such assumptions were successively being relaxed in the following works (Kikuchi and Fukao, 1985; Kikuchi and Kanamori, 1986, 1991). Unfortunately, as the strategy from Kikuchi and Kanamori's work became more and more sophisticated, they found that their strategy was often unstable due to the complex parameter ambiguity. In other words, they recognized the existing trade-off between the subevent timing, the possible fault mechanisms combinations and the allowed locations. Such trade-off was not surprising as it was previously observed by Hartzell and Heaton (1983); Olson and Apsel (1982), but their work showed that the deconvolution source strategies suffer from the same ill-posedness as the other methods. This feature demonstrated that the time-space ambiguity is intrinsic to the physical problem and not to the inversion strategy.

Nevertheless, I would like to recover from the discussion of Kikuchi and Kanamori (1982) an important phrase where another possible strategy to formulate this inverse problem is introduced. In that work, they mention that an alternative approach to solve this inverse problem might be to design a linear inverse filter of the impulse response as devised by **?**. They also mention that, the source time function can be obtained by convolution of this filter with the observed record. Finally, they add that the inversion in that way is straightforward since no assumptions are needed for the source time function, but, a certain criterion has to be defined to identify the individual events. This criterion, as I shall present in Chapters 3 and 4, is related to the spatial and temporal causality that exists between the source history and the recorded wavefield. These ideas are further discussed in the following chapters.

1.3.3 Linear and non-linear frequency-domain methods

Some important conclusions were depicted from the first studies that attempted to reconstruct the source history under a time domain formulation (Hartzell and Heaton, 1983; Olson and Apsel, 1982; Archuleta, 1984): this problem is very ill-posed and under-determined. In addition, at that time, the computational power and limited memory capacity were also significant obstacles to solve very large system of equations as the one related to this inverse problem. One of the workarounds proposed to get over some of these limitations was to carry out all the computations in the frequency domain. Then, another family of strategies tackling this problem in the frequency domain entered into the scene. One of the first studies applying this approach, as well as discussing its limitations was Olson and Anderson (1988). In that study, the spatial slip distributions related to independent frequency bands were obtained through a temporal deconvolution of the amplitude spectrum of the observed strong motions related to the rupture history. This different approach, greatly reduced the necessary computational effort by the simplification of operations in the frequency domain: allowing even finer grids to describe the fault surface and allowing a more accurate approximation of the continuous equation used to compute the synthetic observations. In the frequency domain, the continuous form of the representation theorem (used to compute synthetic seismogrmas) becomes simpler as the time convolution becomes a multiplication between the source history and the wave propagation information for a given frequency f. Then, using Einstein's index summation convention, equation (1.3) in the frequency domain is rewritten as,

$$u_n(\underline{x}, f) = \int\int_{\underline{\Sigma}} [\mathcal{V}_i(\underline{\xi}, f)] c_{ijkl} \eta_j G_{nk,l}(\underline{\xi}, f; \underline{x}, f) d\underline{\Sigma} \qquad (1.10)$$
$$i, j, k, l, n \in [1, 2, 3]$$

At the same level of importance that equation (1.3) has to the time-domain approaches, equation (1.10) establishes the linear relationship between the source and the observed wavefield for a determined frequency band. An important remark is that under the frequency approach it is possible to proceed from low frequency (large scale features) to high frequency (details of the source history) by progressively sweeping different frequency bands. Certainly, this frequency sweep can be performed as well in the time-domain by designing increasing frequency-band filtered data. However, the first techniques applying this strategy were the ones formulating the problem in the frequency-domain.

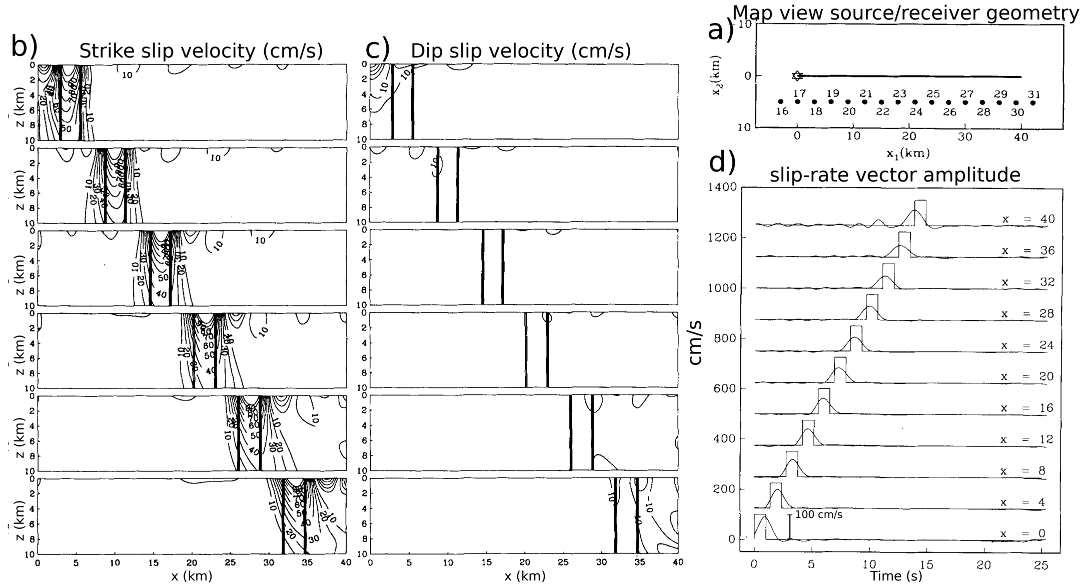

Figure 1.7: Summary of the reconstructed source history obtained using the linear frequency domain strategy for a pure stike-slip rupture synthetic case (modified from Olson and Anderson (1988)). a) Map view of source and receiver geometry: fault-parallel receiver deployment. b) and c) represent the time evolution of the pure strike-slip and dip-slip components of the slip velocity vector (contours in cm/s), respectively. The synthetic test has only pure strike-slip motion, the vertical lines in the dip-slip panels are only used as reference. d) Time evolution of the amplitude of the slip-rate vector at several nodes at a depth of z =3 km and at $x_1 = [0, 4, 8, 12, 16, 20, 24, 28, 32, 36, 40]$ km. Notice the non-zero dip-slip components in c) as well as the deviations from the solution in b) (constant value of 100 cm/s inside the vertical solid lines).

However, even if this approach overcomes difficulties as the computational cost or the necessary assumption of defining a prior rupture velocity (not required under the frequency domain), the authors recognize an important trade-off between the spectral amplitude of slip at a point on the fault and the local phase velocity of the slip propagation (Olson and Anderson, 1988). The evolution of the slip-rate that is presented in Figure 1.7) is an example of this feature. Certainly, this is the frequency domain equivalent to the time-space ambiguity that was previously observed by Olson and Apsel (1982); Hartzell and Heaton (1983) and described in detail by Archuleta (1984). In addition, that study did not tackle a real data set and its validity remained only in the field of synthetic tests.

Some years later, Hartzell (1989); Cotton and Campillo (1995) applied the frequency domain approach to invert real data sets (each one using different strategies and parametrizations). However, the strategies proposed by Cotton and Campillo (1995) and Hartzell (1989), contrary to the ones from Olson and Anderson (1988), were based on non-linear parametrizations of the time-space source history. Such parametrizations have a non-linear relationship between the observations and the unknowns. In general, these strategies described the source history in terms of the local final slip, the rupture time and the rise time. The straightforward advantage of this model description is the drastic reduction of the number of unknowns. The number of unknown reduces from the tens of thousands used by Olson and Anderson (1988) to hundreds used by Hartzell (1989) and Cotton and Campillo (1995). For instance, following Cotton and Campillo (1995), under this non-linear frequency approach, the strong motion at a given frequency band, ω, due to a certain dislocation can be computed through the following discrete equation

$$u_i(\underline{x},\omega) = \sum_{k=1}^{n} a_k \exp[-i\omega t_k] u_{ki}(\omega) S_k[R_k,\omega]. \tag{1.11}$$

where u_{ki} represents the ground motion for a unit constant slip on the discrete fault node k with a previously defined source mechanism, $\underline{x}$ is the receiver location, ω is the angular frequency, k is the fault node index, a_k is the amplitude of the slip function, t_k is the rupture time and S_k is the source function which in turn depends on R_k the local rise time. As previously described in Section 1.2.3, the slip function $S_k[R_k,\omega]$ can be chosen from several type of functions as the ones in equations (1.7) or (1.8). The fact is that, using this approach, the total set of unknowns or parameters to be found is given as

$$\underline{p}^{(i)} = [a_1, a_2, \ldots a_n, t_1, t_2, \ldots t_n, R_1, R_2, \ldots R_n]^T, \tag{1.12}$$

which is different from the linear approach that was presented by Olson and Anderson (1988).

It can be also distinguished that, compared to the strategy from Olson and Anderson (1988), the approaches from Cotton and Campillo (1995) and Hartzell (1989) consider a regularization term, which depends on a prescribed initial model. However, due to the non-linearity and the hard constrain on the shape of the slip function, this initial model can strongly impact the resulting source model.

Another important contribution from the works of Cohee and Beroza (1994); Cotton and Campillo (1995) is the estimation of the resolution matrix for this problem. This resolution matrix showed a significant reduction of the resolution power to retrieve the slip from the deeper zones along the fault (Figure 1.8). This feature of the problem has been observed by several authors Olson and Anderson (1988); Mendoza and Hartzell (1989); Steidl et al. (1991); Cohee and Beroza (1994).

More recently, with the arrival of the massive geodetic measurements to study the surface deformation associated to earthquakes, Hernandez et al. (1999) proposed a combined strategy to try to mitigate the non-uniqueness of the solution to the source reconstruction problem. In that study, the authors used Synthetic Aperture Radar (SAR) measurements of the coseismic surface deformation to first study the static component of the coseismic displacement due to an earthquake. Such static offsets are fundamentally associated to the lowest frequency, where the time history of the source is disregarded. The main idea of this approach was to use this massive interferometric data to improve the solutions provided by the analysis of GPS and strong motion data. To answer these questions, the authors considered a frequency domain approach based on the strategy proposed by Cotton and Campillo (1995). Applying such strategy was a consistent way to tackle the problem: SAR and GPS measurements can be used to invert the zero frequency content (static coseismic displacement) of the motion while the strong motions can be analyzed through the independent inversion of the data contained in other frequency bands. That way of analyzing these two different data sets to reconstruct the source history is denoted as the two-steps kinematic source inversion strategy and it is an example of the strategies that invert the available data through a frequency sweep: analyzing the available data progressively from the low- to the high-frenquency content.

This two-step inversion strategy demonstrated that the use of geodetic data can be used to constrain, to some extent, the final slip at some regions on the fault (e.g. at shallow depths if the fault reaches the surface). However, at depth the resolution is poorer, and several models with completely different characteristics can fit, with the same accuracy, the geodetic and strong motion data sets.

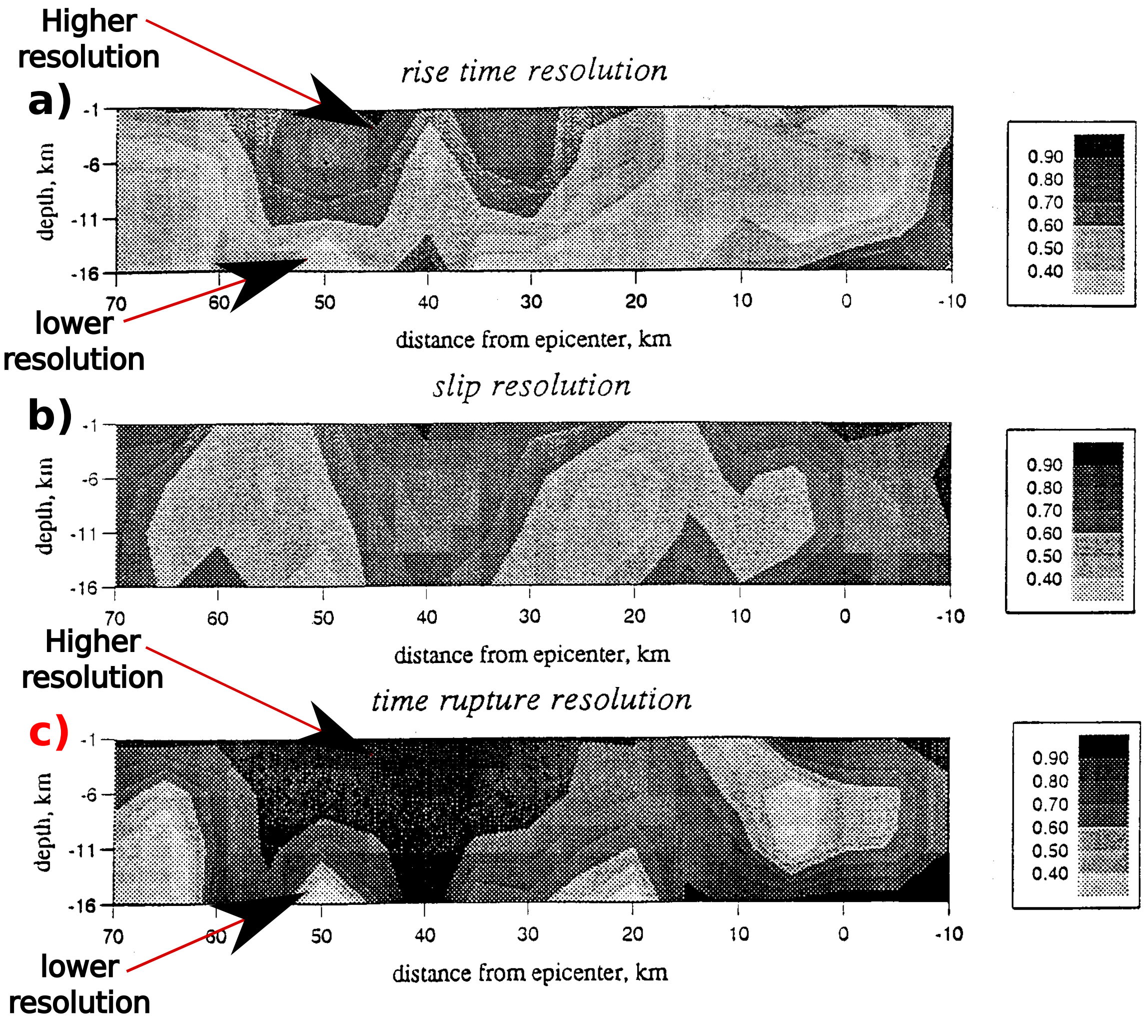

Figure 1.8: Resolution maps across the fault plane geometry for the 1992 Landers earthquake (modified from Cotton and Campillo (1995). The maps are for the a) rise time, b) slip amplitude and c) rupture time. Notice that shallower values are closer to 1 (well-resolved) while the deeper ones are significantly smaller.

1.3.4 Nonlinear time-domain strategies

Not only non-linear frequency approaches were proposed in this field. Simultaneously to the work of the authors above mentioned, other non-linear approaches in the time domain were also proposed. (Archuleta, 1984; Hartzell, 1989; Steidl et al., 1991; Liu and Archuleta, 2004; Emolo and Zollo, 2005) are some of the strategies and studies that applied the non-linear formulation of the problem in the time domain. Most of these studies are based on the iterative solution to the non-linear least-squares problem described by Tarantola and Valette (1982).

In the time domain the inversion process has to find an optimal time-space source history that explains correctly the data with a given frequency content (i.e. from 0.05 to 1.0 Hz). In the time domain this means that several parts of the recordings have to be fit simultaneously during one iteration of the linearized system that has to be solved under this approach. This feature can be problematic due to the difference in amplitude of the several wave packets (within a variety of frequency bands) that are present in a seismogram.

Another important difference between the non-linear time and frequency domain approaches is that the inclusion of physical constraints, such as causality, spatial coherence or positivity, are not easy to be incorporated in the frequency domain. In contrast, in the time domain they can be straightforwardly included into the system of equations to be solved for the source reconstruction.

Regardless of the use of frequency or time domain approaches, a solution obtained under the non-linear formulation can have a particular feature that may be required at one local minimum of the misfit function, but this feature can be entirely absent at another minimum which provides an equally good fit to the data.

1.3.5 Non-linear wavelet-domain method

Another interesting strategy proposed by Ji et al. (2002a) is the non-linear wavelet time-domain approach. In that work the authors promoted the use of a non-linear formulation and where the comparison between observed and synthetic seismograms is carried out in the wavelet domain (i.e. the wavelet decomposition is used to analyze the data).

One of the well-known problems of reconstructing the source history based on the inversion of the available observables (seismograms, accelerograms or geodetic information), is the definition of a correct weighting that balances the contributions of each data type. For instance, regarding only the inversion of seismograms, most of the strategies formulate the inverse problem as an optimization problem of a misfit function defined by the point-by-point L2-norm difference between observed and synthetic waveforms. This way of defining the misfit function already implies an unbalanced contribution between the information of high and low frequency content inside the recordings. For instance, the recordings for moderate to large earthquakes (M_w>6) have a predominant low-frequency content (below 0.2 Hz). Therefore, a correct balance between the low- (overall picture of the source history) and the high-frequency (detailed rupture characteristics) content have to be taken into account. As previously mentioned, changes in the slip amplitude or the velocity of the propagating rupture front can generate strong high-frequency content (Madariaga, 1977; Bernard and Madariaga, 1984).

To try to mitigate this problem, studies such as those proposed by Mendoza and Hartzell (1988); Wald et al. (1996) handle separately some phases with different frequency content. However, the strategy proposed by Ji et al. (2002a), introduces a different approach to measure the misfit between observed and synthetic wavefields. Instead of using the time or frequency domains, this strategy decomposes first the wavefields, using a wavelet transform, into many wave packets containing different frequencies and inverting them separately. Therefore, the authors use the Meyer Yamada Wavelet (MYW) (introduced to seismology by Yomogida, 1994), to decompose the seismograms into several wave packets to be used in the inversion process.

Once the seismograms are decomposed, a certain weight can be given to the wave packets representing the small-scale (high-frequency). These weights balance the contributions from the low and high frequency content. In addition, the misfit function used by this strategy is composed of two parts.

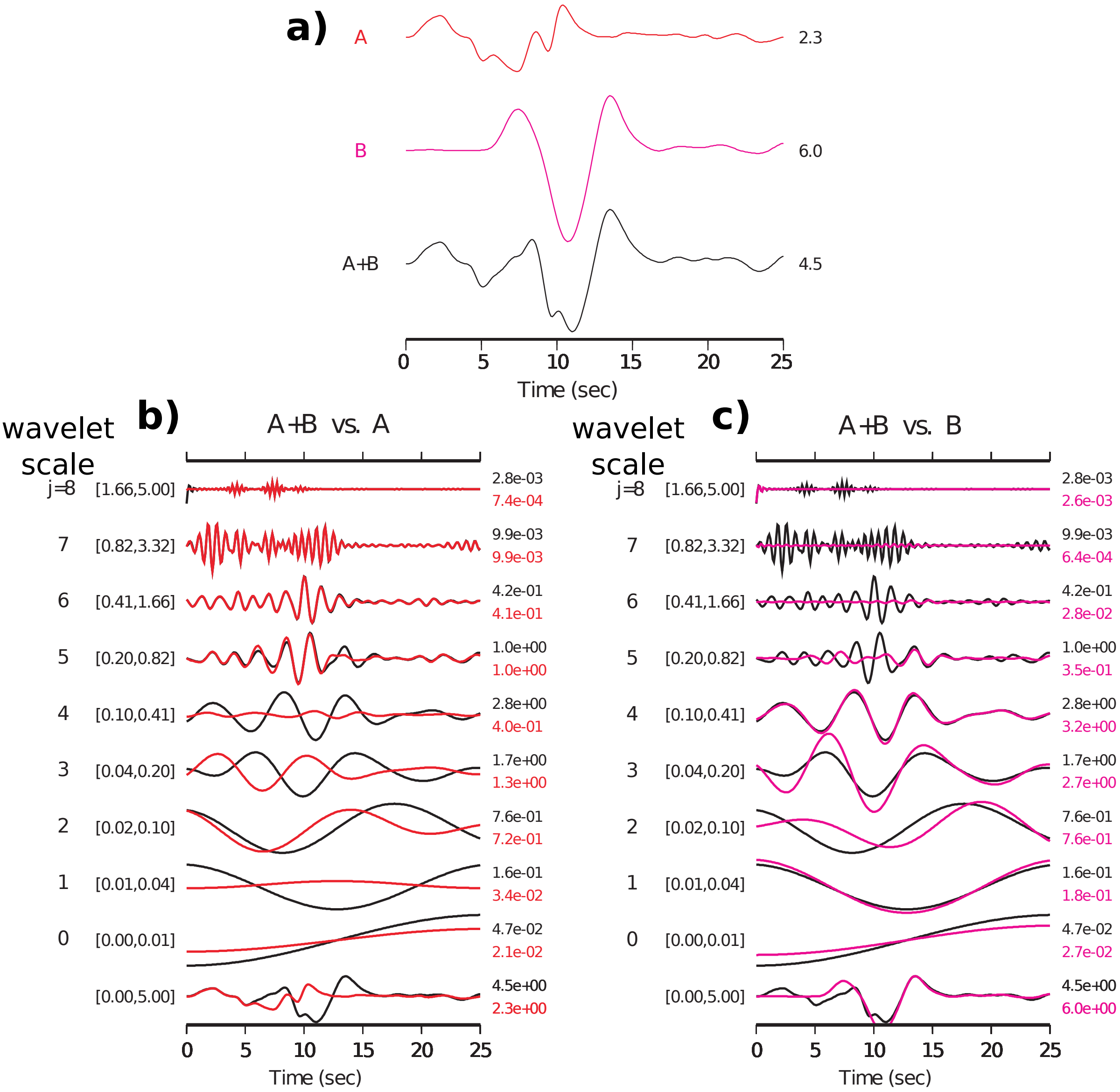

Figure 1.9: Illustation of how a time series (black line in a)) composed by two events (A solid red line in panel a)) and (B solid magenta line in panel a)) is decomposed into the different wavelet scales. Panels b) and c) show the comparison between events: A versus A+B (panel b)) and B versus A+B (panel c)) at different wavelet scales. Notice how at high frequencies, $j \geq 5$, the wavepackets A and A+B are well separated from event B, which is better represented at scales $j < 5$. On the right of each trace (in panel b) and c)) the peak values are given in mm/s, while the associated frequency band is presented on the left between parenthesis.

The first part is in charge of measuring the misfit of the low frequency information (using the L1 and the L2 norms between observed and synthetic wave packets). On the other hand, the second part measures the misfit of the high frequency content according to correlative function (suggested by Sen and Stoffa (1991)), which is more focused on the signal shape and less sensitive to the signal amplitudes, which is more suitable for the high frequency content. Such combined misfit function provides a multiscale approach to retrieve the source slip history.

Apart from this completely different way to analyze the data and to measure the misfit between observed and synthetic wavefields, Ji et al. (2002a) assumed a non-linear formulation of the problem. Consequently, as it has been mentioned before, the parameters used to describe the source history are the local slip amplitude, the rake angle, the rise time, and the rupture velocity (rupture times). Finally, the solution to the non-linear inverse problem is found using a version of the simulated annealing algorithm known as heat-bath (Rothman, 1986).

The first work that applied this technique to the real data set of the 1999 Hector Mine, California, earthquake (Ji et al., 2002a) considered only teleseismic phases and GPS data as data sets as well as a simple 1D layered media. More recently, other authors (e.g. Hsieh et al., 2016; Hao et al., 2017), have extended this technique to efficiently account for the computation of near-field strong motion recordings in complex 3D media. However, all the strategies based on this methodology suffer from the same problem as any other non-linear formulation of the problem: the shape of the slip or slip-rate functions are constrained to follow a specific shape. This particular feature does not allow to have very complex time histories (that earthquakes might have).

1.3.6 Linear adjoint-based inversion methods

Finally, to end with this review of some of the strategies available to tackle this problem, I would like to mention two recent strategies that are based on the adjoint state method. These two strategies are the ones proposed by Fan et al. (2014) and Somala et al. (2018). The adjoint method is a technique used to solve linear or non-linear problems through a local estimation of the gradient of the misfit function with a reduced computational effort (Plessix, 2006). The estimated gradient is then used to improve the model iteratively through any iterative gradient-based minimization method (e.g. steepest-descent, conjugate gradient, etc.) (Nocedal, 1980). This local optimization approach is known to be computationally more efficient than other conventional techniques.

While these two strategies are based on the use of the same local optimization technique, the first (Fan et al., 2014) states all the inversion process in the frequency domain. On the contrary, Somala et al. (2018), prefers the time domain. Both works show impressive results in terms of the resolution power, as well as their computational efficiency. Regarding the improvements that these two works represented in this field, I can mention the following. Somala et al. (2014) and Somala et al. (2018) demonstrated that the adjoint-based strategy is able to handle very efficiently much larger datasets (thousands of receivers) than previous techniques. They used this ability to handle large datasets to try to answer questions related to the resolution capacity that denser arrays can have in the near future to retrieve source attributes such as the rise time and the rupture velocity. On the other hand, the technique from Fan et al. (2014), present improved results compared to its closest predecessor technique (Olson and Anderson, 1988). The strategy presented by them considers regularization terms (e.g. slip-rate positivity and spatial coherence constraints), which were not investigated by the work from Olson. In addition, thanks to the convex optimization tools used by Fan, their inversion strategy does not require the inversion of any large and complex matrix. The strategy proposed by them, as well as the one from the work by Somala et al. (2018), can handle very large datasets.

However, these strategies have some drawbacks that I would like to discuss. First, the work from Fan et al. (2014) does not take into account the causal behavior of the rupture. Even if this strategy is able to incorporate regularization terms into their frequency domain scheme (a difficult task to do), the frequency domain approach completely disregard the causality of the problem. Inverting each frequency-band independently can certainly reduce the problem size. Nevertheless, this independent inversion can be strongly affected by the time-space-amplitude ambiguity if no physical constraints (as upper and lower rupture time limits) are considered. For instance, in their work, Fan et al. (2014), they discuss the fact that the reconstructed time-space source history obtained by their method presents negative values. These negative values might come from the time-space-amplitude ambiguity: negative slip-rate values at some instant and position compensate other large values at a different time and space. In this first work, Fan et al. (2014), the authors explore constraints related to the smoothness of the solution, as well as the incorporation of prior knowledge of the expected solution (e.g. no slip occurs at the fault boundaries). Even though the results obtained by this strategy are quite impressive, the authors recognize that this lack of causality and positivity are some of the weakness of this strategy.

On the other hand, the work from Somala et al. (2018) and Somala et al. (2014), is more devoted to present the whole theory behind the application of the adjoint-state method to solve this problem under a time domain formulation. In addition, the authors discuss the resolution power of the rise time, which is a very important source attribute that is still poorly resolved by current acquisition system around seismogenic zones. However, as in Fan et al. (2014), the causality and positivity of the solution is disregarded by their work. This is due to the fact that the representation of the seismic signals in the frequency domain lacks of the information about what happens before and after. In terms of model regularization, that has been largely discussed and found to be necessary to stabilize the inverse problem, Somala et al. (2014, 2018) only mention that they assumed as an implicit regularization the fact that they stop the optimization process after a fixed number of iterations: no smoothing, moment minimization, limits of rupture propagation, or any other physical constrain is investigated. Certainly, the goal of these works was not to explore different ways to improved the results provided by their adjoint-based linear time-domain approach but to explore the resolution power that new denser acquisition systems can have in the future to solve this inverse problem.

1.4 Kinematic source imaging uncertainties

Regardless of the chosen strategy to tackle the kinematic source inversion problem, the non-uniqueness of the solution is a fact we must face when doing source reconstruction. In general, I can say that, for a given earthquake the number of the available models fitting to some extent the data is equal or greater to the number of researchers working on that earthquake (see as an example Figure 1.10). Many authors have extensively worked to overcome this problem. For instance, Minson et al. (2013) introduced a complete Bayesian framework to infer finite fault static (permanent offsets) and kinematic (space-time histories) models using a non-linear formulation of the problem (solving for slip amplitudes and rupture times). Other works (Beresnev, 2003; Duputel et al., 2012, e.g.), stress out the importance of providing source inversion results with a realistic error analyses, and with a formal assessment of the model uncertainties.

Certainly, the non-uniqueness of the solution to this problem is related to several things. The first one is related to our poor knowledge of the velocity-density structures that are used to simulate the wave propagation that is then used to infer the source parameters. Some work has been done in order to assess and take into account the possible impact that this limited knowledge can have on the source inversion (Yagi and Fukahata, 2011; Hallo and Gallovič, 2016, e.g). The second source of uncertainties is related to all the simplistic geometrical assumptions that we used to describe the fault surfaces where the rupture occurs. Usually, simple models with one, two or even three different fault segments with prescribed geometries (strike and dip angles) are used to represent the complex surfaces where the

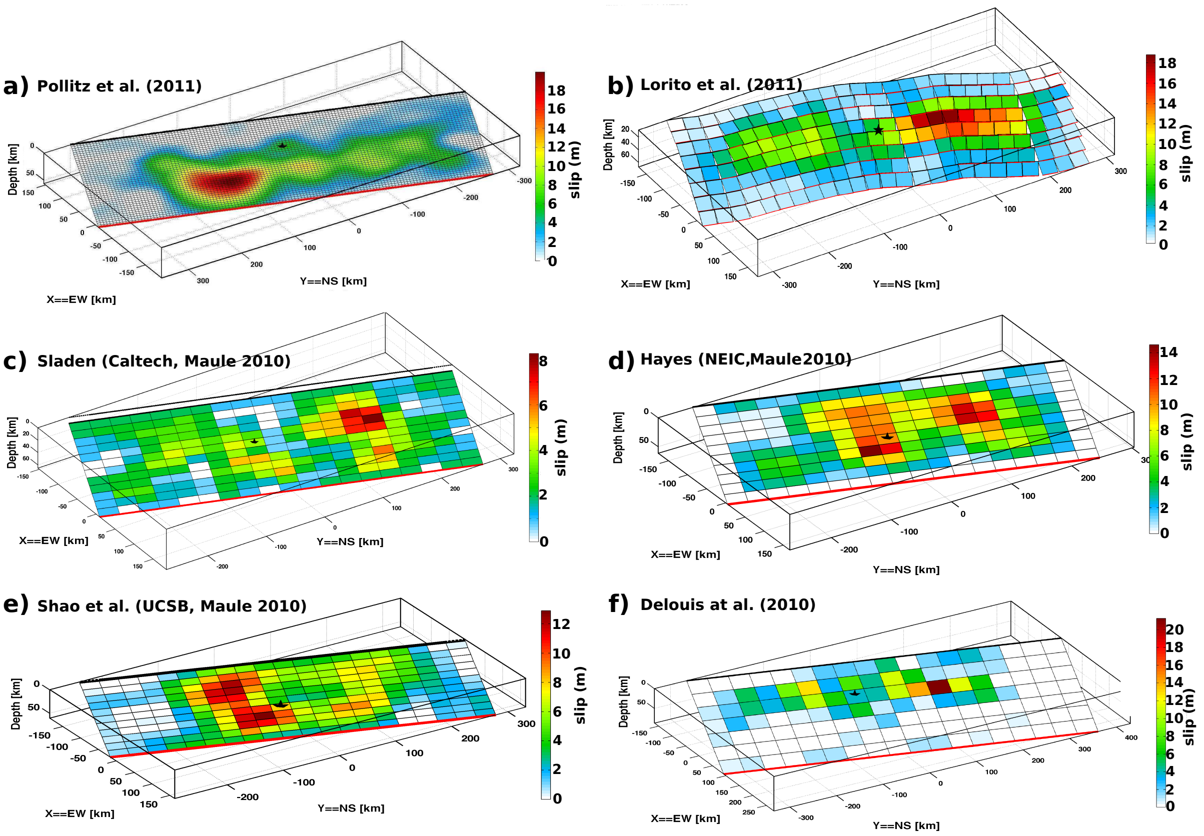

a) Pollitz et al. (2011)

b) Lorito et al. (2011)

c) Sladen (Caltech, Maule 2010)

d) Hayes (NEIC,Maule2010)

e) Shao et al. (UCSB, Maule 2010)

f) Delouis at al. (2010)

Figure 1.10: Comparison of six different source models (only final slip is shown) for the 2010 (M_w8.8) Maule, Chile, earthquake. The title on the top left of each panel provides the reference to the work where each of the models were obtained. For illustration purposes, every panel has its own color bar (slip in m). Notice the large variation of the solutions and geometries. The material used in this figure is taken from the SRCMOD website urlhttp://equake-rc.info/srcmod.

faulting takes place. Recently, Ragon et al. (2018) presented a framework which allows to account for the uncertainties of fault geometry into the static source inversion, but the extension of this strategy to the kinematic inversion problem might not be straightforward. The third source of uncertainties is related to the common non-linear description of the source time-space history. In reality, we do not know exactly what is the shape slip or the slip-rate functions. Some physical experiments (e.g. Ohnaka and Yamashita, 1989) suggest that an impulsive shape with an initial phase of acceleration and a longer phase of deceleration might be a good approximation. However, this is still an unknown. Razafindrakoto and Mai (2014) for instance, presents a work where they investigate the impact of the uncertainties of the assumed source time functions, as well as the unknown velocity-density structure, into the kinematic source inversion problem. Moreover, another source of uncertainty must be due to the poor coverage of the active faults given the current receiver acquisition systems surrounding them, which prevents a correct inference of the seismic rupture. In addition, all the available data used to study earthquakes has a significant level of noise that might not be completely removed by the digital filters.

1.4.1 Time-space-amplitude ambiguity

The term time-space-amplitude ambiguity is used to denote that the available observations produced by the waves generated by a certain amount of shear slip occurring at some position on the fault and at a given time instant, can be explained by another amount of shear motion happening in a different time and position. These other equivalent rupture models form the null-space of the problem. This feature of the finite source modeling problem has been observed practically by every researcher working in this field and several strategies have been proposed to overcome this ambiguity. While some of these equivalent rupture models remain physically possible, others can be easily discarded by looking at their unphysical behavior. This feature is the most fundamental obstacle for accurate kinematic source reconstructions (phenomenological description). This intrinsic time-space ambiguity could be overcome if we were able to adequately inject the prior information we have on the physics of the rupture problem. However, injecting it raises the problem of how to formalize it mathematically, how to inject it in practice in the inversion scheme, and of course how to ensure its validity. This obstacle imprints a particular time-space-amplitude ambiguity in the source reconstruction problem. For instance, Olson and Apsel (1982) mentions that many distributions of slip fit the data at the same level of accuracy, however, some of the differences in the solutions can correspond to the unconstrained component of the problem, which is not determined by the data. In addition, it has been demonstrated that significant changes in the rupture velocity produce seismic radiation just as slip itself does (Madariaga, 1977; Bernard and Madariaga, 1984). Furthermore, Archuleta (1984) and Steidl et al. (1991) mentioned that the kinematic source modeling implies a trade-off between the slip amplitude, the rupture velocity (speed allowing the rupture to move from one node to its neighbors), and the duration of the rupture (rise time). This is certainly due to the missing rupture physics in the formulation of the problem.

In order to illustrate this time-space-amplitude ambiguity an example of this phenomenon is presented in Figure 1.11. In that example four different time-space source histories that follow the same slip direction are illustrated. The first source (src_1) (blue star in panel (a)) occurs at time $t = t_1$ and its time history is represented as a Gaussian curve (solid blue line) in panel (b). The corresponding seismogram observed at the Earth's surface (inverted yellow triangle in panel (a)) corresponding to that first source is represented with the blue solid line in panel (c). The second source (src_2) (orange star in panel (a)), occurs at time $t = t_2$ and its time history (yellow solid line in panel (b)) and its associated seismogram (yellow solid line in panel (c)) are also illustrated. So far src_1 and src_2 have been considered to be independent from each other. The third case assumes that src_1 and src_2 occur one after the other (being $t_1 < t_2$). According to the forward modeling, this third case implies a new source time history (solid black line in panel (b)) that is described as the sum of src_1 and src_2 and which corresponding seismogram is the sum of the seismograms generated by src_1 and src_2 (black line in panel (c)) (linearity is preserved between the source and the observations). However, I include a fourth case that occurs at time $t = t_1$ and which amplitude is the double of src_1 (dashed black line in panel (b)). As you can see in the panel (c) of Figure 1.11, the seismogram from the fourth case (dashed black line) and the one obtained as the sum of src_1 and src_2 are very similar. Without knowing the fact that two events occur and that $src_1 1$ happens before than src_2 (i.e. causality), it would be very difficult to infer which of the two sources ($src_1 + src_2$ or $2 \times src_1$) causes the seismogram (solid black line) in panel (c)).

The simple example presented in this subsection, where concepts such as rupture velocity, rise time and variations of the slip direction are almost neglected, illustrates the difficulty of trying to reconstruct the source history due to the time-space-amplitude ambiguity inherent to the problem. This ambiguity has been observed since the very first studies related to this research field. However, most of the

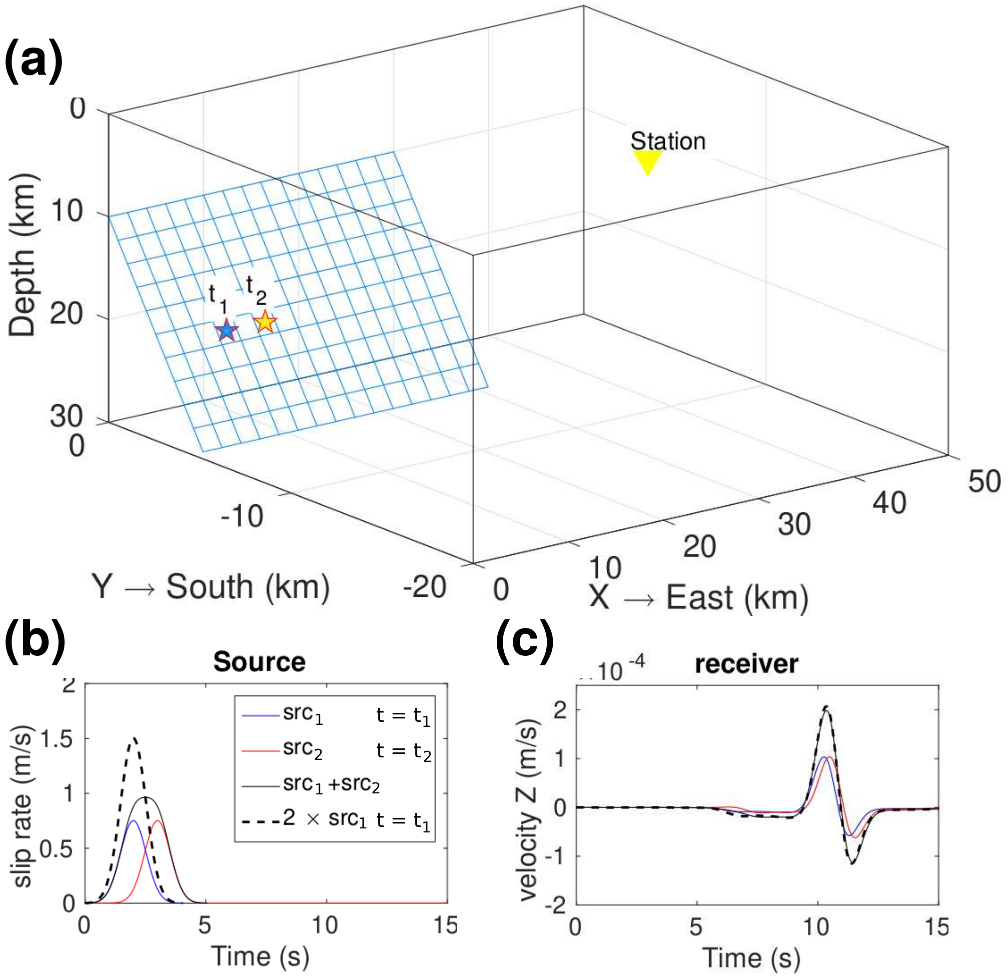

Figure 1.11: Illustration of the time-space-amplitude ambiguity between the source and the observed seismograms. Panel (a) illustrates the location of two fault nodes accross a finite source (src_1 blue star and src_2 yellow star). Panel (b) shows the time histories of src_1 occurring at $t = t_1$ (solid blue line) and source src_2 at $t = t_2$ (solid red line), both are Gaussian curves. In panel (b) other two sources are illustrate: $src_1 + src_2$ (solid black line) is the some of these two sources and $2 \times src_1$ (dashed black line) is the same as src_1 but multiplied by a factor of two. Panel (c) shows the seismograms (vertical component) observed at the receiver position of each of the four source shown in panel (b). More details are given in the main text.

available strategies proposed to infer the time-space source history from the observed wave fields do not take into account this feature. These strategies mainly rely on the fact that, having a large number of observations along a wide range of azimuths is enough to overcome this problem. Nevertheless, it is only recently that observations in a wide range of azimuths are available in some regions. For other seismogenic regions, as in subduction zones or close to blind active faults, the range of observations remains limited. The strategy that I present in Chapters 3 and 4 takes into account the causal behavior of the rupture in order to mitigate this ambiguity.

1.5 Conclusion

Why a linear time-domain formulation?

Regarding all the possible strategies, domains, misfit functions, and regularization constraints, in this work I study the rupture kinematics using a time-domain adjoint-based approach. The reasons why I decide to work under this framework are several. First, as it has been implicitly assumed by some strategies as the multiple time-window (Olson and Apsel, 1982; Hartzell and Heaton, 1983) and the source deconvolution methods (Kikuchi and Kanamori, 1982), the time-domain allows a hierarchical data analysis. This analysis, can be used to enforce a causal behavior of the reconstructed rupture models through a data and model time-windowing technique (as it has been demonstrated by Kolb et al. (1986) when imaging geological structures). Moreover, the time-domain formulation allows a simple incorporation of required regularization terms, which might be significantly more complex to include under a frequency- or wavelet-domain formulation. In addition, I decide to solve the problem following a quasi-Newton minimization technique, where the gradient of the least-squares misfit function is computed following the adjoint state strategy. This methodology has demonstrated an increased computational efficiency compared to previous approaches.

Therefore, in Chapter 3 I discuss more about the application of this time-domain adjoint-based approach to the kinematic source inversion problem. Moreover, in that chapter I present an inversion strategy that incorporates the causality of the rupture into the analysis of the observed wavefields. In addition, in Chapter 4 I present an application of this new inversion strategy to a real data set (for the 2016 Kumamoto earthquake). This real data application illustrates the use of the adjoint-based strategies to real earthquakes, as the works from Fan et al. (2014) and Somala et al. (2014, 2018) did not apply their strategies to invert real data sets. Finally, in Chapter 5 I show how, in a synthetic example, the local gradient of the misfit function can be used to perform an efficient investigation of the model space, which allows the assessment of the uncertainties of the reconstructed source histories.

To end this chapter, let me recall that the representation theorem has two fundamental parts: 1) the source history and 2) the wave propagation information. The representation theorem allows us to consider each of these part separately. So far in this chapter, I have only discussed about some of the different strategies to reconstruct the source history assuming that the Green functions (wave propagation information) are known. Therefore, in the following chapter I discuss about how the necessary wave propagation information can be independently computed of the source reconstruction problem.

Chapter 2

Wave propagation and its impact on source modeling

The following chapter is inspired on the work presented by Bouchon and Aki (1977); Bouchon et al. (1989); Coutant (1989); Tago et al. (2012); Marcial (2017) and by the collaborative work that I could have with Dr. Contreras-Zazueta, Dr. Tago and Prof. Bouchon during my PhD training.

Contents

2.1 Introduction

Many formulations and numerical methods can be used to solve the wave equation and to simulate the wave propagation through several media under different conditions. The right choice has to be made according to the characteristics of the medium we want to work with as well as the goals of the study to be performed. For instance, some methods might be more suitable than others to simulate the wave propagation through strongly heterogeneous media. Therefore, before deciding to work with one or another method it is very important to identify the main characteristics of the medium and the Advantages and limitations of each of the different methods when they are applied to that specific configuration.

In general, the different techniques used to simulate the wave propagation can be subdivided into three main categories: 1) asymptotic approaches, 2) domain methods and 3) boundary methods. As a brief summary of these three different approaches, it can be said the following.

Ray tracing (or asymptotic) techniques: This first group relies on asymptotic expansions for waves with an assumed small wavelength with respect to the size of the medium heterogeneities (i.e. high frequency approach). These techniques are suitable when the wave propagation problem can be significantly simplified and the use of geometric techniques is satisfactory enough. These techniques have two principal steps: 1) find the source-receiver path that follows the corresponding wave (ray) and 2) estimate the intensity of the propagating field along each of the rays. Several works and techniques have used this approach to study the wave propagation in simple 1D layered media as well as in 2D and 3D idealized structures (e.g. Lee and Langston, 1983; Madariaga, 1984; Červený, 1985a,b; Sánchez-Sesma et al., 1988; Virieux, 1991). However, an implicit problem of the ray tracing approach is the fact that the diffraction phenomenon can not be taken into account (Červený, 1985b). Another issue of these approaches is that they can not tackle the incidence of inhomogeneous waves (*e. g.* Rayleigh or evanescent waves). A detailed explanation of these techniques can be found in the works of (Červený, 2001) and Chapman (2004).

Domain Methods: This group, also known as direct or volumetric methods, is formed by techniques that rely on a discrete representation of the physical domain (medium of propagation) where the wave equation, between two neighboring discrete elements, has to be solved (Figure 2.1). This type of numerical methods can simulate the propagation of complete wavefields through the whole medium for successive time intervals. The main advantage of these techniques is their capacity to deal with very complex media. However, even if the system of equations to be solved by these methods can be sparse, their main disadvantage is their high computational cost and memory requirements. The different methods belonging to this group can be subdivided into three main categories: 1) finite difference approaches, 2) pseudospectral methods and 3) finite element methods (Igel, 2017).

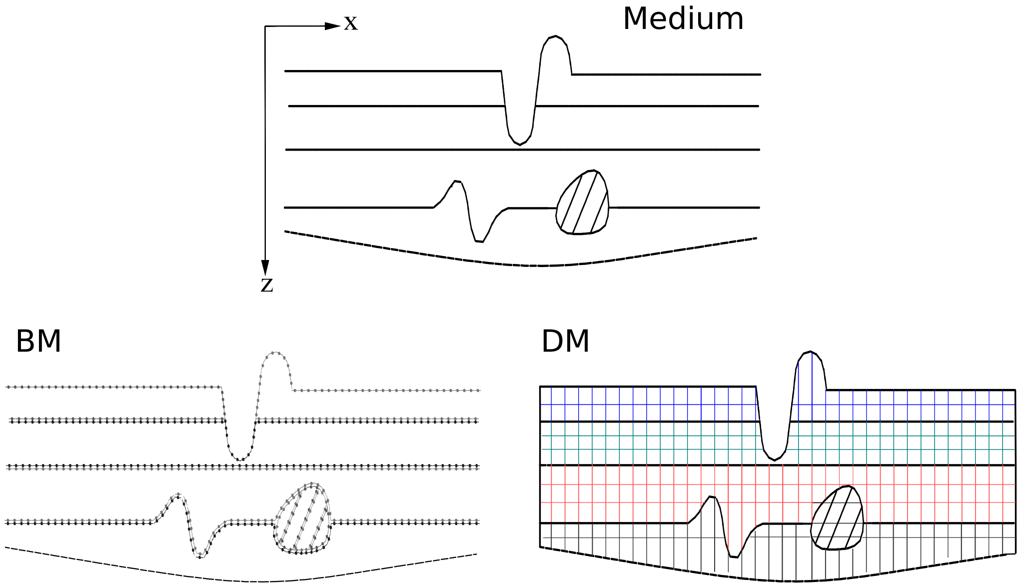

Figure 2.1: 2D Profile view of the difference between the assumed discretization for Boundary Methods (BM) and Domain Methods (DM). BM need to solve with an integral method using Green functions for homogeneous infinite space inside the defined regions to give a solution at the supporting nodes located at the two sides along the boundaries (dots located at the boundaries of specific regions in the left bottom panel). DM solve the wave equation at every node/element belonging to the grid that discretizes the whole physical domain (nodes are located at every line junction in the right bottom panel).

Boundary Methods: This last group is formed by methods that discretize only the boundaries of relevant regions in the medium and they use Green functions representing the wave propagation inside these regions to reconstruct the numerical solution at a given location (Figure 2.1). The boundary methods are based on three main techniques: 1) the use of complete systems of solutions (Herrera and Gourgeon, 1982), 2) the representation of the wavefield in the discrete wave number (Aki and Larner, 1970; Bouchon and Aki, 1977), and 3) the use of integral equations (Brebbia, 1980). The main advantage of these methods is their efficiency (i.e. very fast computation). However, they are limited to work only with media that can be represented by a combination of honogeneous regions (sequence of layers or intrusions with specific geometrical shapes).

In this chapter, I discuss about how the necessary wave propagation information needed to image an earthquake source can be estimated from the simulations provided by three numerical methods I have worked with during my PhD. Two out of these three methods belong to the group of the boundary methods, while the third is a domain method. After, I shall discuss why, a low frequency approximation (common in the source reconstruction field), is the most suitable choice to mitigate the impact that a wrong estimation of this information (in high frequencies) can have on the source reconstruction.

Outline This chapter is organized as follows:

- In Section 2.2, I explain how the solutions to the wave equation provided by three different numerical methods: the Discontinuous Galerkin Finite Element Method (Etienne et al., 2010; Tago et al., 2012), a recently published hybrid Integral Boundary Element method (Perton et al., 2016; Marcial, 2017) and a modified version of the well-known Discrete Wave Number (AXITRA; Bouchon and Aki, 1977; Bouchon, 1981; Coutant, 1989) which is also a boundary integral method, are used to build a bank of stress-state tensors that can be used to reconstruct a kinematic source model of a given earthquake. In addition, I provide some comparisons between the estimations provided by these three different methods.
- In Section 2.3, I discuss about the implications of using a low frequency approximation to the solution of the wave equation. I shall point out why this approximation is valid for the type of configurations that are usually assumed when a source reconstruction is to be performed.
- Finally, in Section 2.4 I provide a conclusion on how to choose the most suitable numerical method to be used to build the necessary information to perform a kinematic earthquake source reconstruction taking into account the characteristics of the medium properties and the goals of the reconstruction.

2.2 Building the stress-state tensor for earthquake imaging

The stress-state tensor derived from Green functions: As it is mentioned in Chapter 1, one of the principal ingredients of the representation theorem (equation (1.3)) is the tensor formed by the vectors of traction per unit impulse. This tensor is also known as the **stress-state tensor** $\underline{\underline{\mathcal{T}}}(\underline{\xi}, t-\tau; \underline{x}, 0)$. This term of the representation theorem, that is written as $c_{ijkl}\eta_j G_{nk,l}(\underline{\xi}, t-\tau; \underline{x}, 0)$ in equation (1.3) using Einstein index summation convention (please see Chapter 1 for more details), is independent of the time-space source history. The columns of this tensor contain the traction vectors per unit impulsive, which can be derived from the estimated solution to the wave equation (i.e. Green functions). The Green functions are the displacement solution to the wave equation when impulsive forces are applied on the Earth's surface (at the receiver location) and which induced motion is recorded at the fault surface (at the source position). Therefore, this tensor is defined as,

$$\underline{\underline{\mathcal{T}}}(\underline{\xi}, t-\tau; \underline{x}, 0) = \begin{bmatrix} \underline{\underline{\sigma}}^{(x)}(\underline{\xi}, t-\tau; \underline{x}, 0)\underline{\eta} \\ \underline{\underline{\sigma}}^{(y)}(\underline{\xi}, t-\tau; \underline{x}, 0)\underline{\eta} \\ \underline{\underline{\sigma}}^{(z)}(\underline{\xi}, t-\tau; \underline{x}, 0)\underline{\eta} \end{bmatrix}^T , \tag{2.1}$$

where $\underline{\underline{\sigma}}^{(n)}(\underline{\xi}, t-\tau; \underline{x}, 0)$ is the stress tensor induced at $\underline{\xi}$ and time $t-\tau$ by a unitary force applied at the $\underline{x}$ and time 0 along the direction denoted by the superscript $n \in [x, y, z]$, and $\underline{\eta}$ is the normal vector to the fault surface representing the source geometry (as described in equation (1.4)). In other words, the columns of the stress-state tensor $\underline{\underline{\mathcal{T}}}$ are the corresponding traction vectors per unit impulse. These traction vectors depend on the elastic properties of the medium, used for the wave propagation simulation as well as for the stress estimation (through constitutive laws), and on the geometry of the fault plane. In addition, because the traction is independent of the rupture process, it can be determined before the source investigation (Archuleta, 1984; Zhao et al., 2006). Unfortunately, this stress-state tensor is not a common output of the wave propagation simulators. Consequently, in this section I describe how the results from some wave propagation methods (e.g. boundary and domain techniques) can be used to build this very important stress-state tensor.

2.2.1 Modified DWN Method

The Discrete Wavenumber (DWN) method is a boundary integral technique. This strategy is well known by its efficiency and accuracy dealing with wave propagation in stratified media. An uncountable number of seismologists have used this method to tackle problems such as seismic exploration, earthquake seismology, microseismicity studies, modeling of regional and near field seismograms, and many more. Its efficiency and low computational requirements rely on the way the radiated wave field generated by a given source is represented through a spatial periodic array of virtual sources. At the same time, this method relies on the Fast Fourier Transform (FFT) in order to compute efficiently the partial derivatives involved in the wave equation. In this method, the use of the cylindrical coordinate system (r, θ, z with the generating source location as the center of the system) is more convenient than the Cartesian one as the periodic source representation can be done through virtual sources located according to concentric circles around the real source. Such virtual source representation allows a more efficient computational implementation. Then, once the radiation is described as the summation of waves propagating with discrete wavenumbers, the next thing to deal with are the effects of reflections and refractions caused by the layering structure. In order to take into account these phenomena, every reflection and transmission coefficient is estimated for each plane wave arriving to the interfaces of abrupt changes of the material properties, and all the contributions are summed up. This summation can be efficiently performed by calculating the reflectivity and transmissivity matrices of the layered medium (Bouchon, 2003; Kennett and Kerry, 1979).

Using this method, as described by Bouchon (2003), the solution to the linear elastic wave equation for homogeneous isotropic media,

$$\mu \frac{\partial^2 u_i}{\partial x_j \partial x_j} + (\lambda + \mu) \frac{\partial^2 u_j}{\partial x_i \partial x_j} + f_i = \rho \frac{\partial^2 u_i}{\partial t^2}, \qquad i, j \in [x, y, z] \tag{2.2}$$

assumption where my work is developed, can be obtained from the combination of the compressional and rotational potential wavefields,

$$\underline{u} = \nabla \phi + \nabla \times (\nabla \times \psi \underline{\hat{e}}_z) + \nabla \times \chi \underline{\hat{e}}_z, \tag{2.3}$$

where $\underline{\hat{e}}_z$ is the unitary vector along the z direction, and ϕ, ψ and χ are the compressional and the two rotational potential fields respectively. For a point source, $\underline{F} = [F_x,\ F_y,\ F_z]$, these potentials are given as,

$$\begin{aligned}\phi(r,\theta,z;\omega) =& \frac{1}{2L\rho\omega^2}\Bigg[\text{sign}(z)F_z\sum_{n=0}^{N}k_nJ_0(k_nr)e^{-iv_n|z|}\\ &-i(F_x\cos\theta+F_y\sin\theta)\sum_{n=0}^{N}\frac{k_n^2}{v_n}J_1(k_nr)e^{-iv_n|z|}\Bigg] \qquad (2.4)\\ \psi(r,\theta,z;\omega) =& \frac{1}{2L\rho\omega^2}\Bigg[-iF_z\sum_{n=0}^{N}\frac{k_n}{\gamma_n}J_0(k_nr)e^{-i\gamma_n|z|}\\ &+\text{sgn}(z)(F_x\cos\theta+F_y\sin\theta)\sum_{n=0}^{N}J_1(k_nr)e^{-i\gamma_n|z|}\Bigg] \qquad (2.5)\\ \chi(r,\theta,z;\omega) =& i\frac{(F_y\cos\theta-F_y\sin\theta)}{2L\rho\beta^2}\sum_{n=0}^{N}\frac{1}{\gamma_n}J_1(k_nr)e^{-i\gamma_n|z|} \qquad (2.6)\end{aligned}$$

with

$$\gamma_n = \sqrt{\frac{\omega^2}{\beta^2}-k_n^2}, \qquad \text{Im}(\gamma_n)<0, \qquad v_n = \sqrt{\frac{\omega^2}{\alpha^2}-k_n^2}, \qquad \text{Im}(v_n)<0,$$

and,

$$\text{sgn}(z) = \begin{cases}1, & \text{if}\, z>0,\\ -1, & \text{if}\, z<0,\end{cases}$$

where ρ is the density, α and β are the compressional and shear wave velocities, k_n is the nth wavenumber, ω is the associated angular frequency and, J_0 and J_1 are the Bessel functions of zero and first orders, respectively. In the cylindrical coordinate system, the displacement field $\underline{u} = [u_r, u_\theta, u_z]^T$ in a homogeneous isotropic elastic medium can be estimated from these potential fields as follows (Muller, 1985),

$$u_r = \frac{\partial \phi}{\partial r} + \frac{\partial^2 \psi}{\partial r \partial z} + \frac{1}{r}\frac{\partial \chi}{\partial \theta}, \tag{2.7}$$

$$u_\theta = \frac{1}{r}\frac{\partial \phi}{\partial \theta} + \frac{1}{r}\frac{\partial^2 \psi}{\partial \theta \partial z} - \frac{\partial \xi}{\partial r}, \tag{2.8}$$

$$u_z = \frac{\partial \phi}{\partial z} - \frac{\partial^2 \psi}{\partial r^2} - \frac{1}{r}\frac{\partial \psi}{\partial r} - \frac{1}{r^2}\frac{\partial \psi}{\partial \theta^2}. \tag{2.9}$$

The use of the reflectivity and transmissivity matrices, defined for the layered medium, together with equations (2.7), (2.8) and (2.9), form the fundamental concepts behind the DWN method.

One of the most popular computational implementations of this numerical method is AXITRA. Three versions of AXITRA are available in the website of Prof. Olivier Coutant `https://www.isterre.fr/annuaire/pages-web-du-personnel/olivier-coutant`. However, none of these versions provide the stress-state tensor (equation (2.1)) that is required by the inversion strategy that I present in Chapter 3. Therefore, in order to have access to this tensor, I had to implement some modifications to one of the available versions of this numerical method.

The original version of AXITRA that I modified is the one able to compute the displacement field induced by applied single forces. This version of AXITRA provides as output the displacement field in cylindrical coordinates $\underline{u} = [u_r, u_\theta, u_z]^T$. Therefore, the first thing to do is a geometrical transformation that allows to know the displacement field in Cartesian coordinates $\underline{u} = [u_x, u_y, u_z]^T$. This transformation is performed in the following way,

$$\begin{bmatrix} u_x \\ u_y \\ u_z \end{bmatrix} = \begin{bmatrix} \cos\theta & \sin\theta & 0 \\ \sin\theta & -\cos\theta & 0 \\ 0 & 0 & 1 \end{bmatrix} \begin{bmatrix} u_r \\ u_\theta \\ u_z \end{bmatrix} \tag{2.10}$$

where θ is the angle describing the position of the receiver with respect to the source location (which is the origin of the cylindrical coordinate system).

Once the displacement field (in Cartesian coordinates) is known, the stress tensor $\underline{\underline{\sigma}}$ can be derived. In order to do that, the constitutive equation relating stress and strain for linearly elastic materials (*Hooke's law*) is used. Thus,

$$\sigma_{ij} = \lambda \mathrm{Tr}(\underline{\underline{e}})\delta_{ij} + 2\mu e_{ij}, \qquad i, j \in [x, y, z] \tag{2.11}$$

remembering that $\mathrm{Tr}(\underline{\underline{e}}) = e_{11} + e_{22} + e_{33}$, that δ_{ij} is Kronecker's delta and that the strain tensor $\underline{\underline{e}}$ is given by the spatial partial derivatives of the displacement field,

$$\underline{\underline{e}} = \begin{bmatrix} \frac{\partial u_x}{\partial x} & \frac{1}{2}\frac{\partial u_x}{\partial y}\frac{\partial u_y}{\partial x} & \frac{1}{2}\frac{\partial u_x}{\partial z}\frac{\partial u_z}{\partial x} \\ \frac{1}{2}\frac{\partial u_y}{\partial x}\frac{\partial u_x}{\partial y} & \frac{\partial u_y}{\partial y} & \frac{1}{2}\frac{\partial u_y}{\partial z}\frac{\partial u_z}{\partial y} \\ \frac{1}{2}\frac{\partial u_z}{\partial x}\frac{\partial u_x}{\partial z} & \frac{1}{2}\frac{\partial u_z}{\partial y}\frac{\partial u_y}{\partial z} & \frac{\partial u_z}{\partial z}. \end{bmatrix}. \tag{2.12}$$

Computationally, the spatial derivatives of the displacement field can be evaluated through any finite difference scheme. In the method here proposed, I use a first order central difference scheme that needs to evaluate the displacement field at six points around the location where the values of the stress tensor are to be computed (see Figure 2.2). These six locations are far from the point of interest by a distance Δh measure along the three directions of the Cartesian space. The value of such step can impact the accuracy of the approximation of the estimated derivative. Therefore, the corresponding spatial derivatives are estimated as

$$\begin{aligned}
\frac{\partial u_x}{\partial x} &= \frac{u_x(x+\Delta h, y, z) + u_x(x-\Delta h, y, z)}{2\Delta h} \\
\frac{\partial u_x}{\partial y} &= \frac{u_x(x, y+\Delta h, z) + u_x(x, y-\Delta h, z)}{2\Delta h} \\
\ldots &= \qquad \ldots \\
\frac{\partial u_z}{\partial z} &= \frac{u_z(x, y, z+\Delta h) + u_z(x, y, z-\Delta h)}{2\Delta h}.
\end{aligned} \tag{2.13}$$

It can be seen that, using equations (2.10), (2.11), (2.12) and (2.13), the stress tensor $\underline{\underline{\sigma}}$ can be computed from the original version of AXITRA. Finally, the stress-state tensor can be easily computed through a multiplication of this stress tensor by the unitary normal vector to the fault surface $\underline{\eta}$ (equation (2.1)). Because this proposed strategy to compute the stress-state tensor relays on a mixure between the well-known DWN and a Finite Difference (FD) scheme, hereinafter I refer to this approach as the FD-DWN method.

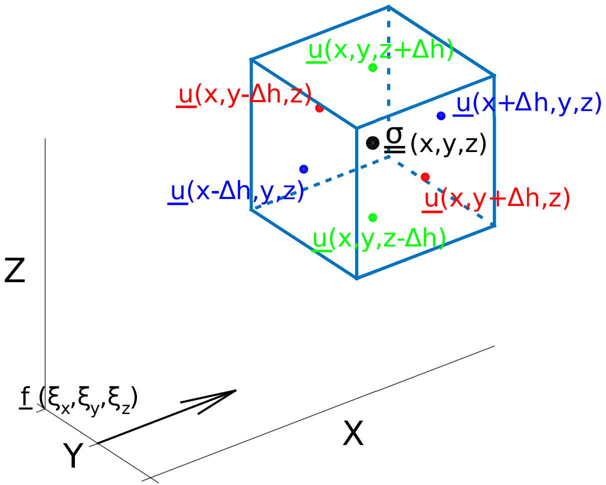

Figure 2.2: Illustration of the necessary six locations where the displacement field $\underline{u} = [u_x, u_y, u_z]^T$ needs to be estimated in order to evaluate the stress tensor $\underline{\underline{\sigma}}$ at the position of interest through a first order central difference scheme. The stress field in this figure is induced by an impulsive force applied in the x direction (black arrow) at the source location $\underline{\xi}$.

2.2.2 The hybrid IBEM-DWN

The Indirect Boundary Element Method (IBEM-DWN) that I present here is the one introduced by Perton et al. (2016) and Marcial (2017). This method, compared to other IBEM approaches, allows the simultation of the elastic wave propagation in complex configurations: embedded regions with homogeneous isotropic elastic material properties with irregular boundaries inside half spaces or 1D layered structures are possible. Therefore, this method can deal with more complex media than the FD-DWN above mentioned.

The Boundary Element Methods (BEM) are based on the representation theorem of Somigliana (Sánchez-Sesma and Campillo, 1991). In the classic formulation of BEM the field of displacement $\underline{u}$ and stress $\underline{\underline{\sigma}}$ generated by a source within a region limited by surface S, can be expressed through an integral representation of the wave equation. Such representation is an inhomogeneous linear differential equation. If the inhomogeneous term of the equation is set as unitary (a delta function), it is said that the nucleus of this integral equation is a Green function: displacement field induced by a unitary force. In order to evaluate this Green function, the BEM place sources on or very close to the surface limiting the medium of propagation and establish that the wave field produced by these sources must fulfill the boundary conditions on that same surface. In contrast, in the indirect formulation of this approach (IBEM; Sánchez-Sesma and Campillo, 1991), one intermediate step in which a density of auxiliary forces which are distributed along the boundaries of the regions of interest are calculated. These forces have to verify the corresponding boundary conditions: null tractions at the free surface and continuity of tractions and displacements across interface between materials with different properties. In the indirect formulation, the total wavefield is constructed as the sum of two terms: 1) the diffracted field, which is built from the auxiliary forces and whose amplitudes are to be determined, and 2) the incident field. The amplitude of the auxiliary forces is found by solving a set of equations that are formed once the boundary conditions are established at the discrete elements distributed along the surfaces. The diffracted wavefield at each of these boundary elements is constructed using the integral representation of the auxiliary forces, which conforms a determined linear equation system which dimension depends on the number of elements, the length of the boundary and the corresponding condition to fulfill. Gaffet and Bouchon (1991) and Sanchez-Sesma and Luzon (1995), are the first studies to extend the BEM and the IBEM techniques, respectively, to study complex 3D media.

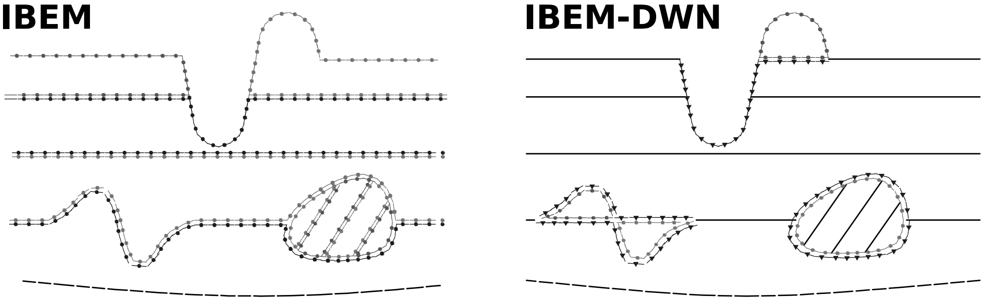

Figure 2.3: Illustration of how the IBEM and the IBEM-DWN strategies discretize the interfaces inside the medium to solve it through the integral formulation of the wave equation. For the IBEM the points on the surfaces illustrate the locations where the amplitude of the auxiliary forces used to build the diffraction field have to be determined. For the IBEM-DWN the points are located only at the irregular boundaries as the use of Green functions (estimated through the DWN method) already considered the diffraction field from the regular stratified regions.

The idea behind the use of an hybrid method where the IBEM can be mixed with the above described DWN method is the following. The formulation of the IBEM can be adapted to use Green functions that already contain the diffraction field generated at the free surface and any stratified structure. These Green functions can be efficiently estimated by the DWN method, while the solution to the integral equation can be limited only to the boundaries with irregular geometries (see Figure 2.3). This hybrid technique allows to reduce the dimension of the linear system related to the amplitude of the auxiliary forces at the irregular boundaries as well as an acceleration of the computational cost thanks to the DWN.

The details of the mathematical development of the equations used to tackle complex geometries like the one shown in Figure 2.3 for 3D configurations are given in Marcial (2017), and the reader is invited to consult this complete description. Here, I shall only insist on the fact that under simple configurations, the equation governing the total displacement field $\underline{u}(\underline{x}, \underline{x}_s, \omega)$, where ω is the angular frequency, due to a force applied at $\underline{x}_s = [x_s, y_s, z_s]^T$ is given as the sum of the direct incident field in the absence of surface S, $\underline{u}^0(\underline{x}, \underline{x}_s, \omega)$, and the diffracted field by the surface, $\underline{u}^d(\underline{x}, \underline{x}_s, \omega)$),

$$\underline{u}(\underline{x}) = \underline{u}^0(\underline{x}) + \underline{u}^d(\underline{x}), \tag{2.14}$$

where the incident term exists only if $\underline{x}_s$ lives inside V: $\underline{x}$ and $\underline{x}_s$ coexist in the same region.

The IBEM-DWN provides as a solution the displacement and traction fields following a complex set of equations and it is not the purposes of this work to describe it. The reader needs to keep in mind, however, that this displacement field can be used to obtained the stress tensor (as it is described by equations (2.11), (2.12), and (2.13)). The stress tensors are the ones required to estimate the stress-state tensor needed by the earthquake source reconstruction that I shall present in the following chapters. Compared to the DWN, the hybrid IBEM-DWN is able to handle more complex geometries than the simple 1D layered structured. Moreover, when there is no intrusion of any complex structure, the solution must be as accurate as the semi-analytical one provided by the DWN as there is no need to use the IBEM.

My work related to the IBEM-DWN was to collaborate with its creators during the last stage of its development. I contributed to the work from Dr. Perton and Dr. Contreras-Zazueta with several exercises of callibration. These exercises allowed them to calibrate the solutions provided by the IBEM-DWN. My tasks consisted of proposing the exercises, going from simple homogeneous half spaces to complex media. Then, I had to provide, using the above mentioned FD-DWN and/or the Discontinuous Galerkin Finite Element Method (DG-FEM), the solution to the displacement and traction fields that the IBEM-DWN team had to use to calibrate the IBEM-DWN. As a result from this collaboration, the results from the IBEM-DWN are now calibrated, without mentioning that my knowledge about this type of boundary methods was enriched.

2.2.3 The DG-FEM

This last strategy belongs to the group of Domain methods. For this method, the solution to the elasto-dynamic equation system (Virieux, 1986; Ben Jemaa et al., 2009) is evaluated through a Discontinuous Galerkin Finite-Element Method (DG-FEM) formulation with Convolutional Perfectly Matched Layer (CPML) (Etienne et al., 2010). The CPML is used to ensure that the absortion of the waves, reaching the artificial boundaries of the computational domain, is performed without causing any reflection at these boundaries. The system that is solved by DG-FEM is written as follows,

$$\begin{aligned} \rho \partial_t \underline{v} &= \sum_{\theta \in [x,y,z]} \partial_\theta \underline{\underline{\mathcal{M}}}_\theta \underline{\sigma} + \underline{f}, \\ \underline{\underline{\Lambda}} \partial_t \underline{\sigma} &= \sum_{\theta \in [x,y,z]} \partial_\theta \underline{\underline{\mathcal{N}}}_\theta \underline{v} + \underline{\underline{\Lambda}} \partial_t \underline{\sigma}_0, \end{aligned} \tag{2.15}$$

with the particle velocity and stress vectors defined as,

$$\begin{aligned} \underline{v} &= [v_x,\, v_y,\, v_z]^T, \\ \underline{\sigma} &= [\tau,\, \tau',\, \tau'',\, \sigma_{xy},\, \sigma_{xz},\, \sigma_{yz}]^T, \end{aligned} \tag{2.16}$$

where

$$
\begin{aligned}
\tau &= \frac{1}{3}(\sigma_{xx} + \sigma_{yy} + \sigma_{zz}), \\
\tau' &= \frac{1}{3}(2\sigma_{xx} - \sigma_{yy} - \sigma_{zz}), \\
\tau'' &= \frac{1}{3}(-\sigma_{xx} + 2\sigma_{yy} - \sigma_{zz}),
\end{aligned}
\tag{2.17}
$$

$\underline{\underline{\mathcal{M}}}_\theta$ and $\underline{\underline{\mathcal{N}}}_\theta$ for $\theta \in [x, y, z]$ are six real constant matrices (see Etienne et al. (2010) for details) and $\underline{\underline{\Lambda}}$ is a diagonal matrix containing the Lamé parameters

$$
\underline{\underline{\Lambda}} = \text{diag}\left(\frac{3}{3\lambda + 2\mu}, \frac{3}{2\mu}, \frac{3}{2\mu}, \frac{1}{2\mu}, \frac{1}{2\mu}, \frac{1}{2\mu}\right). \tag{2.18}
$$

The DG-FEM approach is able to provide an approximation to $\underline{v}$ and $\underline{\sigma}$ at any location inside the whole discretized domain through the following nodal form (Hesthaven and Warburton, 2008),

$$
\begin{aligned}
\hat{\underline{v}}_i(\underline{x}, t) &= \sum_{j=1}^{d_i} \underline{v}_{ij}(\underline{x}_j, t)\varphi_{ij}(\underline{x}), \\
\hat{\underline{\sigma}}_i(\underline{x}, t) &= \sum_{j=1}^{d_i} \underline{\sigma}_{ij}(\underline{x}_j, t)\varphi_{ij}(\underline{x}),
\end{aligned}
\tag{2.19}
$$

where i is the element number of the domain, $\underline{x}$ represents the spatial coordinates inside the element where the field has to be evaluated, and t is the time. d_i is the number of nodes or degrees of freedom (see Figure 2.4) associated with the interpolating Lagrangian polynomial basis function φ_{ij} relative to the jth node located at position $\underline{x}_j$ (Etienne et al., 2010).

As an advantage, over some other methods, the DG-FEM is an $h - p$ adaptable technique: the element sizes and the order of the polynomial functions used to approximate the numerical solution can vary locally, while other Finite-Element Methods (such as Finite Difference) can rely only on grid refinements to improve the estimated solution. In addition, contrary to other Domain Methods, the DG-FEM does not require continuity of the basis functions representing the wavefield between neighboring elements. Therefore, discontinuities in the seismic wavefield, (*e. g.* fluid–solid interfaces) (Etienne et al., 2010) can be better represented using this approach. Inherent to this implicit discontinuity, the completely local operators that DG-FEM uses allows a straightforward parallel implementation as well as the use of different order of approximation for each element according to desired accuracy level in specific regions (see Figure 2.4).

However, as it can be seen in equations (2.16) and (2.17), not all the six independent components of the stress tensor $\underline{\underline{\sigma}}$ are provided by DG-FEM as part of the solution vectors. Therefore, in my work, I had to include to this numerical method the following change of variables to obtain the remaining three independent components of the stress tensor,

$$
\begin{aligned}
\sigma_{xx} &= \tau + \tau' \\
\sigma_{yy} &= \tau + \tau'' \\
\sigma_{zz} &= \tau - \tau' - \tau''.
\end{aligned}
\tag{2.20}
$$

Once these three independent components of the stress tensor $\underline{\underline{\sigma}}$ are estimated, the stress-state tensor can be computed following equation (2.1). This stress-state tensor is the wave propagation information that will be required by the source reconstruction strategy that I present in the following chapters.

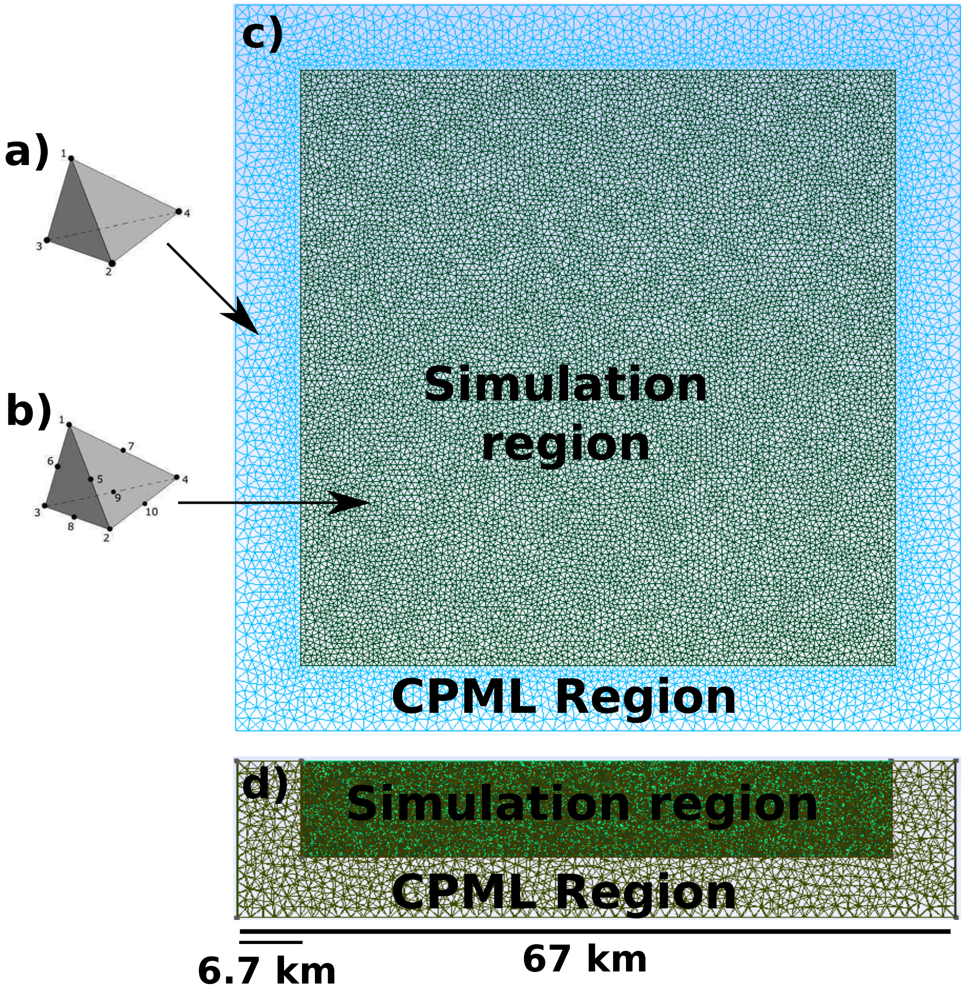

Figure 2.4: Illustration of the tetrahedral geometry of the elements used by DG-FEM to discretize the medium. The number of degrees of freedom associated to two different orders of approximation are shown for: a) first order (P_1, 4 DOF) and B) second order (P_2, 10 DOF). c) and d) offer map and profile views of a simple mesh used for a wave propagation simulation using DG-FEM. The characteristic length of the tetrahedral elements used inside the simulation and CPML regions are different. The element sizes were significantly increased for illustration purposes.

2.2.4 Numerical validation

Before I present the numerical exercises used in this section to compare the solution from the three above mentioned methods, I would like to emphasize the following statement. For any kinematic source reconstruction strategy, precomputed Green functions or stress-state tensors (depending on the chosen version of the representation theorem to work with) are required. This precomputed wave propagation information is independent of the source history to be reconstructed and it does not depend on the method used to compute it.

The validation of results is a very important when dealing with different numerical methods. Therefore, I present two numerical validation exercises where the six components of the stress tensor are computed using the three different methods presented in the previous section: FD-DWN, IBEM-DWN and DG-FEM. For both validations, the time history of the amplitude of the force applied along any of the three directions of the space $[x, y, z]$ is a Gaussian shape function with $2\sigma = 0.5$ seconds and with an area under the curve equal to 1 (see Figure 2.5a,b). The first exercise considers the propagation inside a homogeneous isotropic elastic half space with P and S wave velocities $\alpha = 5.72$ km/s, $\beta = 3.3$ km/s and a density $\rho = 2.6$ g/cm^3. The second case assumes a stratified layered medium with the physical properties described in Table 2.1 (this medium is the same as the one used for the numerical exercises presented in Chapters 3 and 4).

Table 2.1: Velocity-density structure used for the computation of the stress tensors of the second case presented in this section. This structure is the same as the one used in the next sections 3.3 and 3.4.

Depth (km)	V_P (km/s)	V_S (km/s)	Density (g/cm^3)
0.0	4.8	2.6	2.3
2.0	4.8	2.6	2.3
2.0	5.5	3.1	2.5
4.8	5.5	3.1	2.5
4.8	6.2	3.6	2.7
18.0	6.2	3.6	2.7
18.0	6.8	3.8	2.8
24.0	6.8	3.8	2.8
>24.0	8.0	4.62	3.2

Table 2.2: Sources and receiver locations used for the computation of the stress tensors in the two exercises presented in this section.

# source	x (km)	y (km)	z (km)
1	0	0	0
2	40	40	0
3	-40	40	0
4	-40	-40	0
5	40	-40	0
# receiver	x (km)	y (km)	z (km)
1	0	0	15

For both cases, I assumed the same configuration of sources and receivers. The sources (unitary forces) are applied at the center and at 4 positions of a cross array of 40 km. Each of these 4 positions are 40 km far from the center of the array (Figure 2.5c and Table 2.2). All the forces are applied at the free surface ($z = 0$ km). The location of the receiver is exactly below the center of the array at z=15 km. The source-receiver configuration of these two exercises is shown in Figure 2.5c.

In order to use the DG-FEM, a mesh of 67 [x-direction] $\times 67$ [y-direction] $\times 25$ [z-direction] km is designed. The smallest characteristic length (at the shallowest layer of the stratified medium) is $\approx$ 220 km. The characteristic length used in the CPML region is $\approx$ 670 km. A total number of 4,123,610 tetrahedral elements is used to discretize the whole domain. The same mesh is used for the first homogeneous case.

The time history of the stress fields compared in Figure 2.6 and Figure 2.7 are filtered to account for frequencies below 2 Hz (a zero-phase butterworth of 1st order was applied to all of the traces).

The three different methods provide very similar results. However, in both cases, DG-FEM presents some spurious oscillations on the traces σ_{xy} and σ_{yz}. This spurious oscillations can be related to some numerical noise propagating in the medium or it can be associated to the location at which the source and receiver are located (both positions share the same y-coordinate).

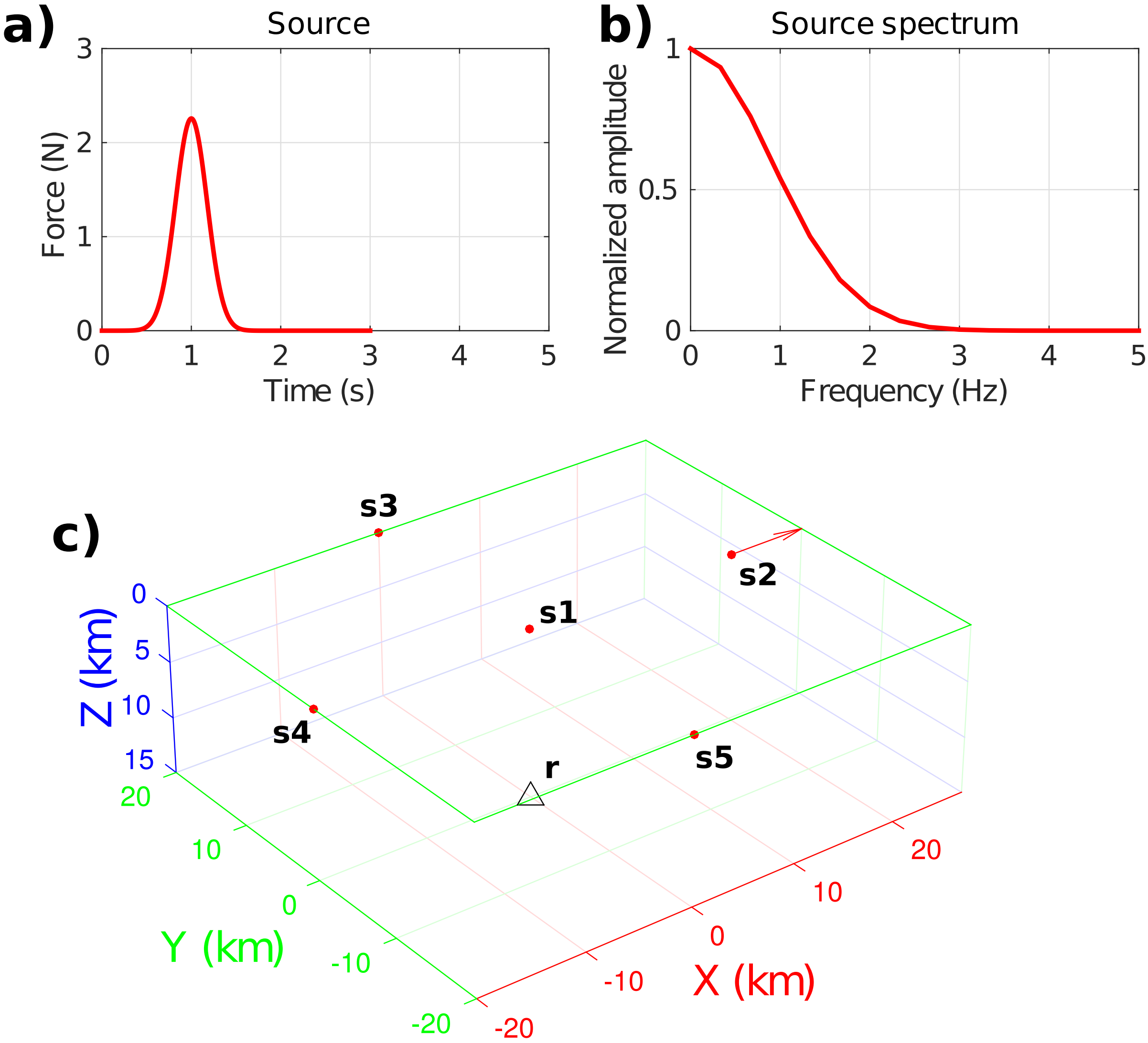

Figure 2.5: a) Time history and b) amplitude spectrum of the unitary force applied to compute the Green functions and the stress tensors with the three methods: FD-DWN, IBEM-DWN and DG-FEM. c) Shows the source-receiver configuration: dots represented the locations where the sources are applied and the triangle illustrate the location of the receiver where the stress tensor is computed. The arrow in c) illustrates the direction of a force applied along the x direction at the source location number 2.

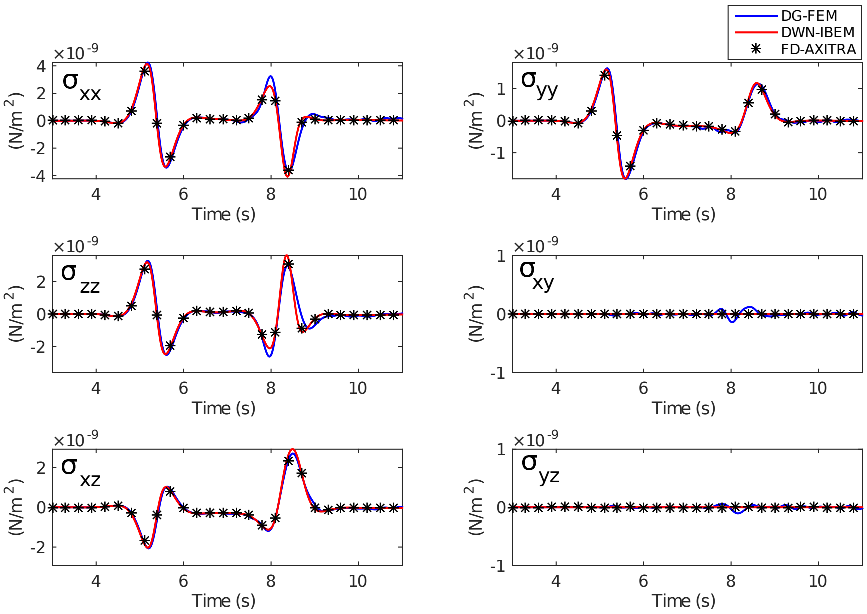

Figure 2.6: Comparison of the six independent components of the stress tensor computed using the three methods previously described: FD-DWN (black lines), IBEM-DWN (blue lines) and DG-FEM (red lines). This comparison is done for the first case: waves propagating in an homogeneous isotropic elastic medium with $\alpha = 5.72$, $\beta = 3.3$ km/s and $\rho = 2.6$ g/cm^3. The unitary force is applied along the x direction at the position $[40, 40, 0]$ km and it is recorded at $[0, 0, 15]$ km (see Figure 2.5).

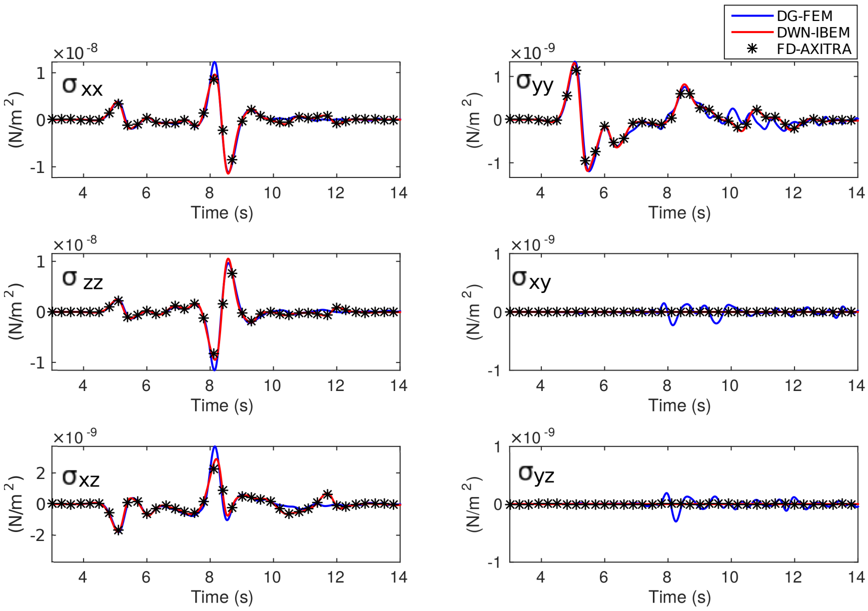

Figure 2.7: Comparison of the six independent components of the stress tensor computed using the three methods previously described: FD-DWN (black lines), IBEM-DWN (blue lines) and DG-FEM (red lines). This comparison is done for the second case: waves propagating in a 1D layered isotropic elastic medium with the velocity-density structure described in Table 2.1. The unitary force is applied along the x direction at the position $[40, 40, 0]$ km and it is recorded at $[0, 0, 15]$ km (see Figure 2.5).

2.3 Why a low frequency approximation

Nowadays, one important question and challenge in this field is to understand and to account for the effects that heterogeneous complex media can have into the reconstructed earthquake source models. The estimation of Green functions, and stress tensors, is currently possible even when dealing with very complex media. However, such simulations can represent a significant computational cost. In addition, we have to keep in mind that improvemnts on the source reconstruction can be only ensured if the 3D velocity models are correct enough to have a proper estimation of the wavefields. However, most of the time we face limitations to have accurate wavefield estimations due to the lack of knowledge about the heterogeneities present in the subsurface.

It is certain that, at the Earth's crust, where earthquakes ocurred, the structure is highly heterogeneous in several scales. However, as demonstrated by some authors (e.g. Capdeville and Guillot, 2009; Capdeville et al., 2010), relatively accurate wave simulations can be obtained assuming simpler equivalent medium configurations instead of the highly complex and computational costly realistic media. This is possible due to the natural way in which the waves are sensitive to the medium where they propagate. In other words, the seismic wavefield, considered in a certain frequency range, could be well-approximated by another one that propagates through an equivalent effective medium of the real structure. The question how waves are sensitive to the medium and how simpler equivalent media can be used to obtain accurate wave propagation simulations with less computational requirements is a whole research field known as medium homogenization. For elastic waves and Earth Sciences, the pioneering work by Yann Capdeville (e.g. Capdeville and Guillot, 2009; Capdeville et al., 2010; Capdeville and Marigo, 2013; Capdeville and Cance, 2015; Capdeville and Métivier, 2018) are important references in this field.

As I mentioned in the previous section, the wave propagation is not a problem that has to be solved simultaneously to the source reconstruction problem. All the wave propagation information can be computed and stored before performing any source inversion. Consequently, the computational cost is not actually the main problem of obtaining accurate and trustful wave propagation simulations. The main question regarding the wave propagation problem in the source inversion field is related to a correct medium structure setup that can accurately reproduce, to some extent and under a given frequency range, the response of the real heterogeneous medium. In order to answer if simple assumptions (for instance 1D layered media) can be used for a correct source reconstruction, it is necessary to recall that most of the source studies are limited to the analysis of frequency contents below 1 Hz, where most of the source energy is radiated. This implies the existance of a minimal wavelength of the wavefield radiated by earthquakes that propagates through the complex medium. This minimal wavelength that can be observed under this low frequency approach is given as $\lambda_{min} = V_{min}/f_{max} = V_{min}/(1Hz)$. Considering this low frequency approach, the propagating wavefield might be, in many cases, completely insensitive to structures that are much smaller than λ_{min}. It is then, in these cases, where the 1D layered medium will be enough accurate to serve us for problems such as the source reconstruction.

At higher frequencies (>2 Hz), it is clear that the 1D layered medium assumption is a very naive and incorrect representation of an equivalent medium to the more complex heterogeneous real structures. Some of the exercises presented by Capdeville et al. (2010), showed that such naive models (e.g. just smooth versions of the real structures) do not provide an accurate prediction of the ground displacement. When the solution obtained in such low wavenumber models is compared to the ones that are expected in more realistic complex media, important differences in first arrival times, coda, amplitude errors and phase time shifts can be certainly expected. However, these differences are mostly relegated to much higher frequency bands than the ones used for the source reconstruction. For instance, a phase time shift of 0.1 seconds (that can be expected as the result from an incorrect medium setup) can be of great importance for a seismogram with a frequency content up to 15 Hz: several phases could be misinterpreted. On the other hand, the same 0.1 second phase time shift will be insignificant for a signal which frequency content is below 1 Hz. Another way to see that the 1D layered approach is accurate enough to tackle the source reconstruction problem is that, as mentioned by Hsieh et al. (2016) and Ozgun Konca et al. (2013), a velocity medium with 3D structural variations of up to 5% does not lead to significant degradation of the reconstructed source models. Therefore, if a given 1D layered medium does not differ significantly (more than 5%) from a more complex 3D structure, this assumption will be still acceptable for our purposes.

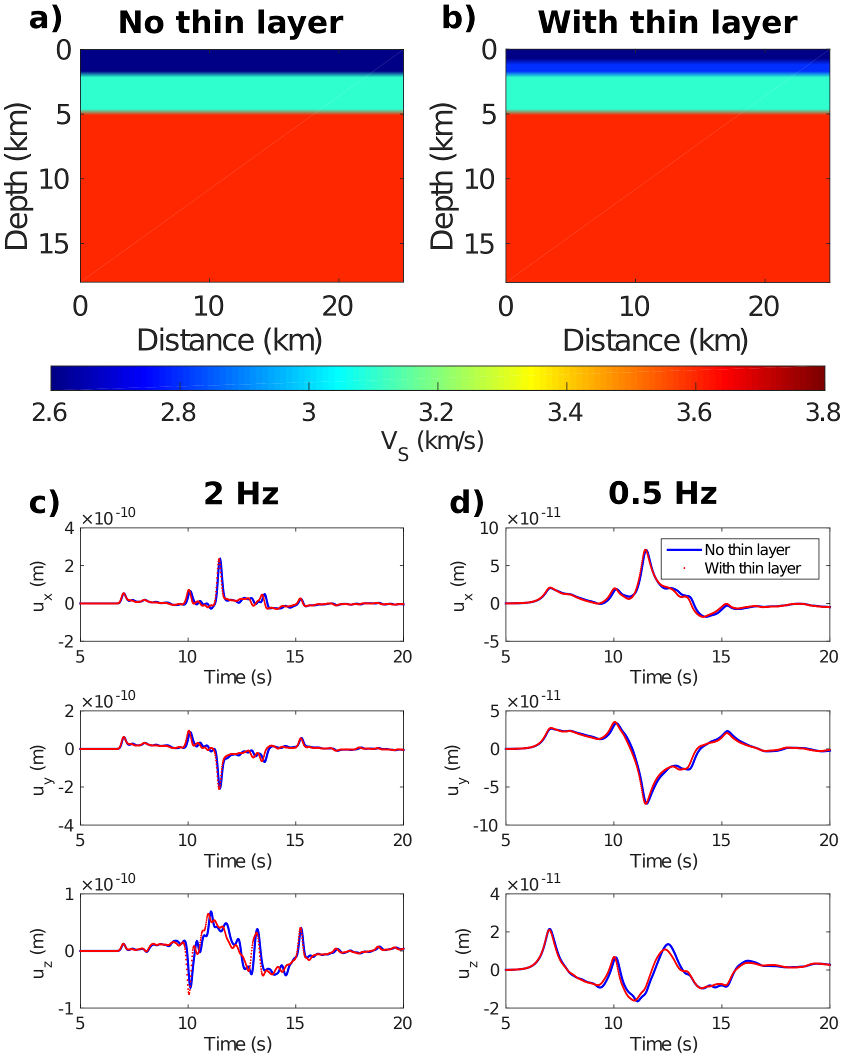

Figure 2.8: Illustration of two 1D layered media: a) with thick layers and b) with two thin shallow layers. Panels c) and d) compare the displacement field $[u_x, u_y, u_z]$ for frequencies ≤ 2 and ≤ 0.5 Hz recorded for the waves propagating across medium a) (blue lines) and medium b) (red lines). The displacement field is recorded at $[34,\ 31,\ 0]$ and its generated by a unitary force applied along the x direction at $[56.5,\ 56.0,\ 10]$ and $t = 1$. The time history of the force is a Gaussian curve with $2\sigma = 0.5$ seconds, centered at $t = 1$ seconds and a unitary area under the curve. The thin layer is influential at frequencies (wavelengths) corresponding to its thickness.

As an example, in panels c) and d) of Figure 2.8 I offer a comparison between the Green functions (displacement field components: u_x, u_y, u_z) recorded at the receiver location $[34,\ 31,\ 0]$ km due to a force applied along the x direction at the coordinates $[56.5,\ 56.0,\ 10]$ km. The Green functions are estimated using two different 1D layered media: Figure 2.8a illustrates a layered structure that is visible to waves with 2 or 0.5 Hz, while 2.8b has two shallow thin layers that are more visible for wavefields with frequency contents higher than 2 Hz than for the ones below 0.5 Hz. This difference can be noticed comparing the red and the blue lines in panes c) and d). Therefore, in terms of Green functions estimation, both models in Figure 2.8 produce similar responses at frequencies lower than 0.5 Hz. Consequently, at that frequency range of study, the responses estimated at the coarse layered medium are expected to be close to the one produced by a real medium embedding small heterogeneities. The differences, between both media, might be at the noise level. Furthermore, in order to perform a source reconstruction at such high frequencies requires, for any numerical method, of a detailed knowledge of the subsurface velocity structure, which is not often the case.

2.4 Conclusion

In this chapter, I present some of the strategies that can be used to simulate the wave propagation in simple and complex media. I would like to highlight that, any strategy (respecting its own limitations) can be used to accurately compute the necessary wave propagation information required to perform a source inversion. As long as these techniques can provide the corresponding Green function solution, the stress-state tensor can be efficiently computed. In my work, I use undistinguishably any of these three techniques presented in this chapter. The important point to stress out is the fact that the choice of the method to be used depends on the type of structure model that needs to be handled (1D vs 3D models). In this chapter, I present three numerical methods, however, many more strategies can be used for the same purpose. For instance, the work by Romano et al. (2014) used a Finite-Element Method called Abaqus to study the coseismic deformation from the 2011 Tohoku earthquake, while Emolo and Zollo (2005) used a ray tracing approximation to compute the Green functions required to study the 1989 Loma Prieta earthquake.

It is very important to highlight that the source reconstruction problem does not require to solve simultaneously the wave propagation. Therefore, the computational cost of estimating Green functions is not really an issue as this is an offline computation. Therefore, the important point regarding the Green function computation is the selection of a numerical method that can provide a correct and accurate approximation. For instance, if the real 3D medium where the simulation has to be performed can be well approximated by a simple 1D structure, the best choice is to use boundary element methods, which are accurate and more efficient than other methods dealing with those configurations. Domian methods, such as the DG-FEM, would be the best choice if the complex structure can not be well represented by a simple 1D structure and if its heterogeneties strongly impact the wave propagation prediction.

It is certain that the velocity structure impacts the results from a kinematic source inversion. The better we know them, and the better we can model these structures and the way waves propagate through them, can reduce their influence in the infered source models. However, nowadays our knowledge of the complex geological structures present in the subsurface remains very limited. In the specific source inversion problem, the information considered to reconstruct the source history is usually constrained to the low frequency bands, where most of the energy radiated by earthquakes propagates. Taking into account our limited knowledge of the Earth's subsurfacce and our interest in the low frequency content, it is reasonably accurate to use 1D velocity-density assumptions. Finally, it is for these reasons that in most of the cases I prefer to build the Green functions using boundary element methods, which offer a simpler, faster and cheaper way of estimating them.

Now that I have presented some of the strategies that can be used to pre-compute the wave propagation information required to perform an earthquake source reconstruction, I shall present in the next chapter the linear time-domain strategy that I propose to reconstruct the source history. This strategy tries to incorporate most of the advantages of the techniques presented in Chapter 1. In addition, its design and constraints are thought to mittigate some of the obstacles mentioned by the authors working in this field (e.g. poor resolution at depth and non-causal behavior of the solutions). All this is performed based on the pre-computed bank of stress-state tensors that was detailed in this chapter.

Chapter 3

The progressive time-space kinematic source inversion

The material presented in this chapter has been written based on the following work:

- Sánchez-Reyes, H., Tago, J., Métivier, L., Cruz-Atienza, V., Contreras-Zazuerta, M., and Virieux, J. (2016). An evolutive quasi-real-time source inversion based on a linear inverse formulation. *2016 AGU Fall Meeting*.
- Sánchez-Reyes, H., Tago, J., Métivier, L., Cruz-Atienza, V., and Virieux, J. (2018). An evolutive linear kinematic source inversion. *Journal of Geophysical Research: Solid Earth*, 123.
- Jouanny, S., Sánchez-Reyes, H., Virieux, J., Métivier, L. (2018). Inversion cinématique pour une source sismique. Master 1 Géophysique 2017/2018 Rapport de Stage. Université Grenoble Alpes

---

Contents

3.1 Introduction

Nowadays, kinematic source parameters are routinely obtained for any moderate to large earthquake (events with $M_w \geq 5.5$) by geological services and research institutes around the world (*e.g.* the USGS in the USA or the NIED in Japan). Efforts have been made to develop fast and automated inverse methods (e.g. Ji et al., 2002a; Diao et al., 2016; Hsieh et al., 2016) to provide a kinematic source model few minutes after an earthquake has occurred. However, for the reconstruction of the spatio-temporal distribution of the slip on a prescribed fault geometry, these approaches consider all available recorded data to be inverted altogether. In seismology, source modeling strategies preserving the causality could drastically take benefit of the natural time ordering of records. Moreover, assessing uncertainties on the estimated quantities is crucial as illustrated by the great variability of recovered slip models for recent earthquakes, as illustrated in Section 1.4, or looking at recent source models such as the ones proposed for the large Tohoku earthquake (Ide et al., 2011; Koper et al., 2011; Lay et al., 2011; Suzuki et al., 2011; Satake et al., 2013). In order to move towards imaging while recording as well as on-line uncertainty quantification, a kinematic source inversion method based on a linear time-dependent formulation is a key ingredient for allowing progressive-time-windowing source analysis. The development presented in this chapter has as main purpose to introduce such technique.

In terms of data fitting, the kinematic source inversion is a procedure used to infer, from any set of seismological observations (seismograms, geodesy, ground motion recordings), a spatio-temporal representation of the rupture history. The development presented in this chapter illustrates such methodological investigation. This inverse problem can be stated as a least-squares problem, where finding an optimal spatio-temporal slip-rate distribution, on a given fault geometry, minimizing the differences between observed and computed seismograms is the goal. Chapter 1 provides an overview of this minimization problem and a summary of several strategies that have been proposed to solve it. However, the solution of this ill-posed inverse problem is non-unique (e.g. Hartzell, 1989; Cohee and Beroza, 1994; Wald and Heaton, 1994; Cotton and Campillo, 1995; Hernandez et al., 1999; Minson et al., 2013) and, according to current acquisition systems surrounding active faults, this problem is highly underdetermined in most cases, in spite of its rather simple formulation as a linear inverse problem.

Since Haskell (1964, 1966) has promoted the idea of describing the seismic rupture as a finite sequence of breaking subevents, many strategies have been applied to solve this inverse problem. Ide (2007) provides a complete historical review on the evolution of these strategies. According to their features, these strategies can be divided into two main categories. On the one hand, we recognize those that are based on a linear inverse formulation linking linearly the spatio-temporal slip-rate distribution as parameters and the synthetic seismograms predicting observations (e.g. Hartzell and Heaton, 1983; Olson and Anderson, 1988; Wald et al., 1990; Gallovic and Imperatori, 2014; Fan et al., 2014; Somala et al., 2018). This linear formulation may lead to a significant number of parameters in the model space often composed of a 2D fault surface and a time axis. On the other hand, model reduction strategies could be used by prescribing a different parametrization driven by physical understanding of the seismic rupture process, such as slip-rate direction, rupture velocity, rise time (duration) and local maximum slip-rate amplitude. While the linear relationship between the observations and the slip-rate amplitude remains true, the slip-rate history becomes a non-linear function of the parameters controling the starting time of the sliding (rupture velocity) and its duration (rise time) making the forward computation non-linear (e.g. Archuleta, 1984; Hartzell, 1989; Steidl et al., 1991; Cotton and Campillo, 1995; Hernandez et al., 1999; Ji et al., 2002a; Liu and Archuleta, 2004; Shao et al., 2011; Hsieh et al., 2016). This inverse formulation with a significant reduction of unknown parameters greatly stabilizes the inversion procedure but prevents the simple use of linear algebra tools, especially for uncertainty quantification. Even if the problem might not seem to be strongly nonlinear, and therefore an iterative linearization could be reasonable, the uncertainty quantification remains dependent of the local solution.

The ill-posedness of the problem while keeping a linear formulation requires dedicated strategies which are investigated in this chapter. For example, a progressive-time-windowing strategy introduces a data-driven hierarchy, illustrated nicely by previous studies of source deconvolution (Kikuchi and Kanamori, 1982, 1986, 1991). In addition to such strategy, model-driven regularization should be added while preserving the linear relation between model parameters and data. In this chapter, I propose a time-domain kinematic source inversion strategy based on the adjoint-state method which honors causality and which preserves a linear inverse formulation as promoted by Fan et al. (2014) and Somala et al. (2014). Prior knowledge of the rupture and standard physically plausible regularization terms are key elements of this time-domain implementation and can be efficiently introduced while still taking benefit of the causality of the seismic rupture. The related expansion of the model space, following the increase of recorded time, will introduce as well a way to stabilize the inversion while preserving the linear relation.

Outline The outline of this chapter is the following:

- In section 3.2, I introduce the new hierarchical time kinematic source inversion technique. I present also a general strategy to include any type of prior information and regularization terms into the inversion scheme. Then, I explain how it is possible to perform either a standard inversion of complete recordings or a progressive-time-window source inversion.
- In section 3.3, I illustrate the performance of this new method by applying it to a well known synthetic case (the Source Inversion Validation exercise 1 (SIV1) (Mai et al., 2016).
- In section 3.4 I increase the difficulty by applying this method to the Source Inversion Validation exercise 2a (SIV2a).
- Finally, in section 3.5 I conclude this chapter providing a discussion on results, methodological perspectives and numerical experiences gained after tackling these two benchmarks.

3.2 Methodological description

In this section, I first describe the **forward problem**. Then, I set up the **inverse problem** of reconstructing the slip-rate history from the observed seismograms. The inverse problem is formulated as a least-squares problem where the solution is found through the minimization of a misfit function. A local optimization based on the estimated gradient of the misfit function, with respect to the slip-rate parameters, is in charge of performing this minimization. Therefore, I discuss the related **gradient computation** that is needed to solve the inverse problem. In addition, I describe how to consider model constraints for stable reconstructions.

3.2.1 Forward problem

In this work the following convention is used: non-underlined symbols represent scalars, single underlined are vectors and double underlined are matrices.

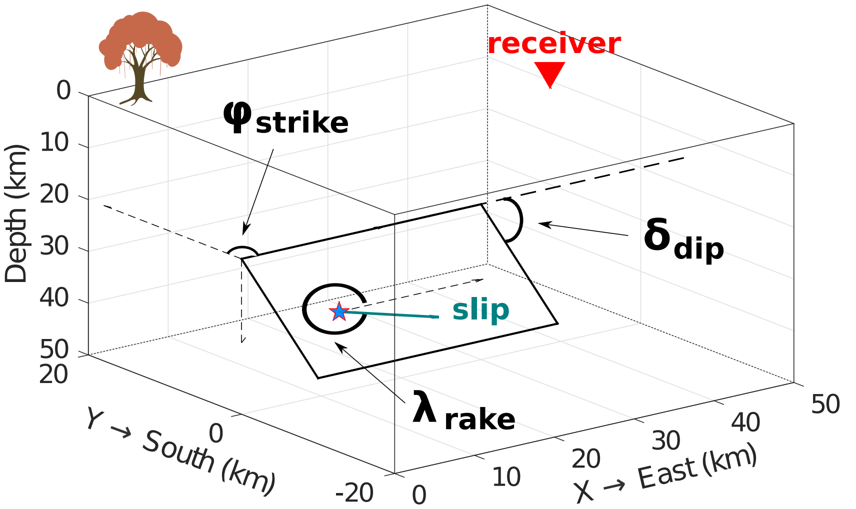

Figure 3.1: Schematic representation of the fault geometry. Strike, dip and rake angles are represented.

The source geometry is defined by a 2D surface, $\Sigma(\underline{\xi})$, embedded in a 3D known medium (Figure 3.1). The fault position vector $\underline{\xi}$ is defined over this 2D planar surface, which in turn is specified by strike ϕ and dip δ directions known prior to the slip inversion. More complex surfaces could be assumed if needed: the normal vector to the surface may vary along the fault surface. However, in this work I assumed that a planar surface assumption is a decent approximation with actual available data and it will simplified the notation. The forward problem is the computation of velocity recordings $\underline{v}(\underline{x}, t) = [v_x, v_y, v_z]^T$, at any receiver location $\underline{x} = [x_x, x_y, x_z]^T$ and time t during the interval $[t_1, t_2]$, given a certain spatio-temporal slip-rate distribution $\underline{\mathcal{V}}(\underline{\xi}, \tau)$, occurring at the position $\underline{\xi}$ and at a rupture time $\tau \in [\tau_1, \tau_2]$. Using an indicial notation, where subscripts are used along with the Einstein summation convention, the representation theorem (Burridge and Knopoff, 1964; Archuleta, 1984; Aki and Richards, 2002) can be used to compute a synthetic velocity field as a double integral over the 2D fault surface and the time window through the following expression

$$v_n(\underline{x}, t) = \int_{\tau_1}^{\tau_2} d\tau \iint_{\Sigma} \mathcal{V}_i(\underline{\xi}, \tau) \mathcal{T}_{ni}(\underline{x}, t; \underline{\xi}, 0) d\Sigma(\underline{\xi}), \qquad n, i \in [x, y, z] \tag{3.1}$$

where the stress-state tensor $\mathcal{T}_{ni}$ is deduced from Green functions computed in the 3D known medium, as described in Chapter 2 Section 2.2. However, I assume that there is no opening mode during an earthquake and, therefore, the slip-rate vector lies along the fault surface, which is supposed to be continuous, allowing the definition of normal and tangential vectors at least locally. Consequently, the general slip-rate vector $\underline{\mathcal{V}} = [\mathcal{V}_x, \mathcal{V}_y, \mathcal{V}_z]^T$ can be represented by only two components V_ϕ and V_δ along the local strike (ϕ) and dip (δ) directions respectively (Figure 3.1). Moreover, in my work, the fault surface is assumed to be a plane with a constant unitary normal vector. Using this description of the fault geometry (δ, ϕ and $\underline{\eta}$), a reduction of the slip-rate vector from the cartesian coordinate system (3 unknowns) to a strike and dip coordinate system (2 unknowns) can be done through the followin linear transformation,

$$\underline{\mathcal{V}}(\underline{\xi}, t) = \begin{bmatrix} \cos\phi & \eta_y \sin\phi \\ \sin\phi & -\eta_z \cos\phi \\ 0 & \eta_y \cos\phi - \eta_x \sin\phi \end{bmatrix} \begin{bmatrix} V_\phi(\underline{\xi}, t) \\ V_\delta(\underline{\xi}, t) \end{bmatrix}, \tag{3.2}$$

$$= \underline{\underline{\mathcal{P}}}_{3\times 2} \quad \underline{V}_{2\times 1}(\underline{\xi}, t) \tag{3.3}$$

or, in cases where the rake angle (λ) is assumed as known, such reduction can be done to a single scalar (1 unknown) controlling the vector amplitude along the assumed orientation,

$$\underline{\mathcal{V}}(\underline{\xi},t) = \begin{bmatrix} \cos\lambda\cos\phi + \sin\lambda\cos\delta\sin\phi \\ -\cos\lambda\sin\phi + \sin\lambda\cos\delta\cos\phi \\ \sin\lambda\sin\delta \end{bmatrix} V_s(\underline{\xi},t), \tag{3.4}$$

$$= \underline{\underline{\mathcal{P}}}_{3\times 1} \qquad V_{1\times 1}(\underline{\xi},t). \tag{3.5}$$

Therefore, in a general way, this reduction can be written as $\underline{\mathcal{V}}_{3\times 1}(\underline{\xi},t) = \underline{\underline{\mathcal{P}}}_{3\times n}\underline{V}_{n\times 1}(\underline{\xi},t)$ with $n = 2$ or $n = 1$, and vector $\underline{\eta} = [-\sin\delta\sin\phi,\ -\sin\delta\cos\phi,\ \cos\delta]^T$ (Stein and Wysession, 2003). Notice that by choosing parameters V_s and λ as unknowns, the inverse problem would have become non-linear, while the parameter set (V_ϕ, V_δ) preserves the linear property. Therefore, in this work the rake angle (λ) is never treated as a parameter to be inverted during this work and it will be only an attribute for which hard or soft constraints have to be designed.

For the complete description of the integral representation, the components of the stress-state tensor, $\underline{\underline{\mathcal{T}}}(\underline{x},t-\tau;\underline{\xi},0)$, are detailed as

$$\underline{\underline{\mathcal{T}}}(\underline{x},t;\underline{\xi},0) = \begin{bmatrix} \underline{\underline{\sigma}}^{(x)}(\underline{x},t;\underline{\xi},0)\underline{\eta} \\ \underline{\underline{\sigma}}^{(y)}(\underline{x},t;\underline{\xi},0)\underline{\eta} \\ \underline{\underline{\sigma}}^{(z)}(\underline{x},t;\underline{\xi},0)\underline{\eta} \end{bmatrix}^T, \tag{3.6}$$

where $\underline{\underline{\sigma}}^{(n)}(\underline{x},t;\underline{\xi},0)$ is the stress tensor induced at $\underline{x}$ and time t by a unitary force applied at the $\underline{\xi}$ and time $\tau = 0$ along the direction denoted by the superscript $n \in [x,y,z]$. In other words, the columns of the stress-state tensor $\underline{\underline{\mathcal{T}}}$ are formed by the corresponding unitary traction vectors.

Finally, thanks to the reciprocity property of Green functions and the specified linear transformation, the forward problem (3.1) can be rewritten as the following expression

$$v_n(\underline{x},t) = \int_{\tau_1}^{\tau_2} d\tau \iint_{\Sigma} \mathcal{P}_{ik}\, V_k(\underline{\xi},\tau)\, \mathcal{T}_{in}(\underline{\xi},t-\tau;\underline{x},0)d\Sigma(\underline{\xi}),$$
$$n,i \in [x,y,z] \text{ and } k \in [\phi,\delta] \text{ or } k \in [\lambda], \tag{3.7}$$

which is the continuous integral form of our forward problem. Einstein summation convention is again used as in equaiton (3.1). Contrary to (3.1), in equation (3.7) the unitary force used to compute $\underline{\underline{\mathcal{T}}}$ is now located at the receiver position and the stress-state tensor is estimated on the fault plane. Regardless of the number of receivers and the number of nodes used to discretized the fault plane, the strategy of precomputing the stress-state tensor will favor the formulation (3.7) instead of (3.1).

This continuous representation of the forward problem can be discretized and computed through the trapezoidal rule implying a continuous trilinear interpolation in time and space of the slip-rate function. Appendix 3 provides a detailed expression for the discrete form of equation (3.7). It is important to highlight that any method for computing $\underline{\underline{\mathcal{T}}}$ is suitable (e.g. see Section 2.2), as long as tensor values could be stored at points on the source plane for each receiver as proposed by Zhao et al. (2006); Hsieh et al. (2016). This off-line computation requires a sampling which should honor the physical description of the expected rupture front width and the wave propagation at the frequencies involved in the rupture reconstruction: if finer sampling is needed by the rupture physics, trilinear interpolation of these tensor components is often enough. These look-up tables are efficiently read and recovered when integrating the weighted slip-rate function. They can describe any complex 3D heterogeneous media as long as we know how to define these 3D media. For instance, my computational implementation is able to use the stress tensors estimated by boundary-integral equations (Perton et al., 2016) as well as the ones computed through a sophisticated finite-element method (Etienne et al., 2010; Tago et al., 2012) to evaluate the stress-state tensor $\underline{\underline{\mathcal{T}}}$. Similar results were obtained from both strategies when the same medium definition was assumed (see Section 2.2). This pre-computed and fixed wave propagation information will be of great importance for the progressive-time-windowing strategy because they will define the data window to be selected inside the current recorded window at each receiver location.

3.2.2 Inverse probem

Formulation: The optimal spatio-temporal slip-rate distribution will minimize the sum of squared differences between observed and synthetic time samples of seismograms. Synthetic seismograms are estimated through the discrete form of equation (3.7). The total misfit $\mathcal{C}(\underline{V})$ is composed of two terms corresponding to the data and model misfit, decomposed as follows:

$$\mathcal{C}(\underline{V}) =\mathcal{C}_{\underline{d}}(\underline{V}) + \epsilon\mathcal{C}_{\underline{m}}(\underline{V}), \tag{3.8}$$

where the hyperparameter ϵ is used to balance the influence of data and model error terms in the misfit function. The first term $\mathcal{C}_{\underline{d}}$, known as the data misfit term, is given by

$$\mathcal{C}_{\underline{d}}(\underline{V}) = \frac{1}{2}\sum_{\underline{x}}\int_t \Delta\underline{d}[\underline{V}](\underline{x},t)^T\Delta\underline{d}[\underline{V}](\underline{x},t)dt, \tag{3.9}$$

where the upperscript symbol ^{T} denotes the transpose of the vector $\Delta\underline{d}[\underline{V}](\underline{x},t)$ and $\sum_{\underline{x}}$ corresponds to a summation over all the receiver locations $\underline{x}$. In equation (3.9), the vector $\Delta\underline{d}[\underline{V}](\underline{x},t)$ is used to represent the residuals between the observed, $\underline{u}(\underline{x},t) = [u_x(\underline{x},t), u_y(\underline{x},t), u_z(\underline{x},t)]^T$ and the calculated seismograms, $\underline{v}[\underline{V}](\underline{x},t) = [v_x[\underline{V}](\underline{x},t), v_y[\underline{V}](\underline{x},t), v_z[\underline{V}](\underline{x},t)]^T$, and $[\underline{V}]$ is used to denote a dependence on a given rupture model $\underline{V}$,

$$\Delta\underline{d}(\underline{x},t) = \begin{bmatrix} u_x(\underline{x},t) - v_x[\underline{V}](\underline{x},t) \\ u_y(\underline{x},t) - v_y[\underline{V}](\underline{x},t) \\ u_z(\underline{x},t) - v_z[\underline{V}](\underline{x},t) \end{bmatrix}. \tag{3.10}$$

Recalling that $\underline{v}[\underline{V}](\underline{x},t)$ is estimated through equation (3.7). In order to takespo into account the possible available prior information regarding the data quality, or, as a way to balance the different information contained in all the available seismograms, a data weighting function can be incorporated into equation (3.9),

$$\begin{aligned}\mathcal{C}_{\underline{d}}(\underline{V}) =&\frac{1}{2}\sum_{\underline{x}}\int_t \Delta\underline{d}[\underline{V}](\underline{x},t)^T\underline{\underline{W}}_{\underline{d}}(\underline{x},t)^T\underline{\underline{W}}_{\underline{d}}(\underline{x},t)\Delta\underline{d}[\underline{V}](\underline{x},t)dt \\ =&\frac{1}{2}\sum_{\underline{x}}\int_t \Delta\underline{d}[\underline{V}]^T\underline{\underline{W}}_{\underline{d}}^T\underline{\underline{W}}_{\underline{d}}\Delta\underline{d}[\underline{V}]dt,\end{aligned} \tag{3.11}$$

being

$$\underline{\underline{W}}_{\underline{d}}(\underline{x},t) = \begin{bmatrix} w_{\underline{d}_x}(\underline{x},t) & 0 & 0 \\ 0 & w_{\underline{d}_y}(\underline{x},t) & 0 \\ 0 & 0 & w_{\underline{d}_z}(\underline{x},t) \end{bmatrix} \tag{3.12}$$

the data weighting function controling the contribution of the data residuals. In seismology, this function is often built in such a way that the weight values are related to the noise for each trace, the epicentral distances or the azimuthal coverage. Recently, Hallo and Gallovič (2016) has proposed a way to incorporate into this data weight the missing knowledge of the medium propagation using uncorrelated uncertainties based on receiver-source distances and azimuth coverage. In this work, a diagonal shape of function $\underline{\underline{W}}_{\underline{d}}(\underline{x}, t)$ is assumed with values ranging from 0 (no contribution) to 1 (full normalized contribution), scaled by a normalizing factor related to the units of the data we use in order to get an adimensional misfit term as I am going to mix different quantities in the total misfit.

The second term of the misfit function is in charge of introducing (in a least-squares sense) all available prior knowledge that we have in our hands, such as upper and lower expected rupture velocities, fault boundary slip penalization, expected shapes of the slip-rate time functions, local rake angle variability and others. This term requires two ingredients: a prior model $\underline{\hat{V}}(\underline{\xi}, \tau)$ and a model weighting function $\underline{\underline{W}}_{\underline{m}}(\underline{\xi}, \tau)$. By using $\Delta\underline{m}[\underline{V}]$ as the vector measuring the difference between a current model $\underline{V}$ and the model built based on prior information $\underline{\hat{V}}$, this model misfit term is written as the following least-squares expression

$$\begin{aligned}
\mathcal{C}_{\underline{m}}(\underline{V}) =& \frac{1}{2}\int_{\underline{\xi}}\int_{\tau} \Delta\underline{m}[\underline{V}](\underline{\xi}, \tau)^T \underline{\underline{W}}_{\underline{m}}(\underline{\xi}, \tau)^T \underline{\underline{W}}_{\underline{m}}(\underline{\xi}, \tau) \Delta\underline{m}[\underline{V}](\underline{\xi}, \tau)\, dt\, d\underline{\xi} \\
=& \frac{1}{2}\int_{\underline{\xi}}\int_{\tau} \Delta\underline{m}[\underline{V}]^T \underline{\underline{W}}_{\underline{m}}^T \underline{\underline{W}}_{\underline{m}} \Delta\underline{m}[\underline{V}]\, dt\, d\underline{\xi}
\end{aligned} \tag{3.13}$$

where $\Delta\underline{m}[\underline{V}](\underline{\xi}, \tau)$, is given as

$$\Delta\underline{m}[\underline{V}](\underline{\xi}, \tau) = \begin{bmatrix} \hat{V}_{\phi}(\underline{\xi}, \tau) - V_{\phi}(\underline{\xi}, \tau) \\ \hat{V}_{\delta}(\underline{\xi}, \tau) - V_{\delta}(\underline{\xi}, \tau) \end{bmatrix}, \tag{3.14}$$

while the model weighting function is defined as

$$\underline{\underline{W}}_{\underline{m}}(\underline{\xi}, \tau) = \begin{bmatrix} w_{\underline{m}_{\phi}}(\underline{\xi}, \tau) & 0 \\ 0 & w_{\underline{m}_{\delta}}(\underline{\xi}, \tau) \end{bmatrix}. \tag{3.15}$$

The prior model, $\underline{\hat{V}}(\underline{\xi}, \tau)$, could be any preferential model of the spatio-temporal rupture history with a given hypocenter location, rupture time, rake angle and shape of slip-rate time functions: this model is often based on a simple physical description of the possible seismic rupture. In this work, I use a model weighting function $\underline{\underline{W}}_{\underline{m}}(\underline{\xi}, \tau)$ that is not designed to consider possible neighboring links in space and time, although nothing prevents me to define other structures allowing such interactions. This further investigation is left for future work. The design of these two ingredients (prior model and its weight) must incorporate: 1) any desirable feature coming from seismic rupture models or other prior information of the event under investigation such as final surface displacements, attributes obtained from teleseismic phases or GPS measurements if they are not included in the inverted data and 2) the expected error between the running and prior models. This design will regularize the inverse problem by reducing the null-space size. This design is application-dependent, and its construction will be further detailed at the description of the case studies investigated in sections 3.3, 3.4, 4.3 and 4.4.

In order to clarify how the model weigthing function can emphasize physically meaningful models, two different examples of weighting functions and the impact they could have into the inversion process can be seen in Figures 3.3 and 3.2. For instance, we see in Figure 3.2 a time constant weighting function

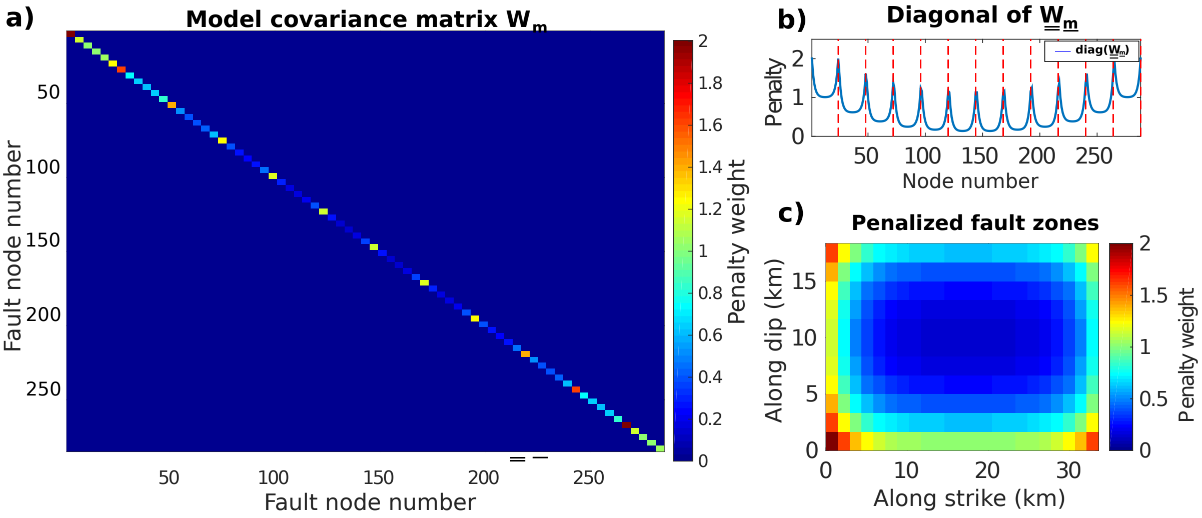

Figure 3.2: Illustration of a time constant model covariance matrix $\underline{\underline{W}}_m$ and the fault zones where the slip-rate vector is penalized thanks to this diagonal matrix. a) Schematic illustration of the penalizing diagonal covariance matrix. b) Illustrates the variation of the diagonal elements of the weighting matrix: the peak values represent the large weights given to the nodes at the edges of the fault surface. The vertical dashed lines in b) indicate the number of the nodes that are at the edge of the fault. c) Strong or weak penalized fault zones where the slip-rate is prevented or promoted, respectively. The rupture should rapidly vanish toward the fault edges. Notice that it is possible to prevent or promote the rupture at any fault zone if required by prior information.

($\underline{\underline{W}}_m(\xi, \tau)$ does not evolve in time) that promotes a vanishing slip behavior toward the edges of the defined fault plane. This boundary condition is physically reasonable, since it avoids the creation of an infinite strain at the edges and ensures that some physical mechanism allows the faulting to die down at those boundaries (as suggested by Beresnev (2003)). On the other hand, we can see in Figure 3.3 a time dependent weighting function that prevents having slip at some fault zones at time instants where it is not expected. The design of the function that we see in Figure 3.3 imprints an upper limit to the expected rupture velocity (as applied by other authors through other strategies).

It is important to highlight that, even if the design of this regularization term seems complex (designing prior model and covariance matrix together), having only one term flexible enough to include all the prior information available is very attractive. Furthermore, the design of this regularization term can be more physically meaningful if information coming from the geology, observed static displacements and/or previous studies can be translated into such prior model and its expected weight.

As for any inversion strategy with penalty/regularization terms, the adimensional hyperparameter ϵ balances the different terms contributing to the global misfit function. The choice of the amplitude of this hyperparameter has to be tuned according to a more or less arbitrary criterion, such as the L-curve analysis (Hansen, 1992) or by setting empirically this value through several trials in order to ensure that a decent data fit is performed. Another possibility, as it is done in Chapter 2, is to previously calibrate this hyperparameter through several synthetic tests performed in a configuration similar to the real-case study where a known synthetic rupture has to be reconstructed, as I discuss in Chapter 4.

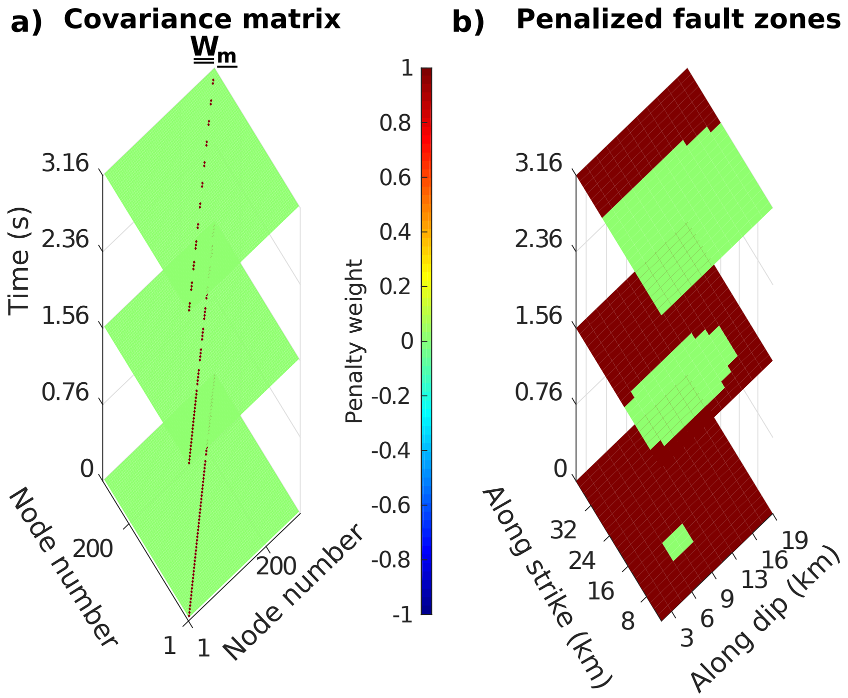

Figure 3.3: Illustration of the time evolution of a model covariance matrix $\underline{\underline{W}}_m$ and the different fault zones where the slip-rate vector is penalized at the same instants. a) Shows three snapshots (at 0, 1.56 and 3.16 seconds) of the penalizing diagonal covariance matrix. b) Illustrates how the covariance matrix maps into allowed and not allowed rupture zones across the fault plane. The rupture could not occurred before a given time in this example. Notice that it is possible to prevent future slip after a given time.

Solution through local optimization: Using equations (3.11), and (3.13) together with (3.7) I can formally state the kinematic source inversion problem as follows:

$$\begin{aligned}
\min_{\underline{V}} \quad & \mathcal{C}(\underline{V}) = \frac{1}{2}\sum_{\underline{x}} \int_t \Delta\underline{d}[\underline{V}]^T \underline{\underline{W}}_d^T \underline{\underline{W}}_d \Delta\underline{d}[\underline{V}]\, dt + \epsilon\frac{1}{2}\int_{\underline{\xi}}\int_\tau \Delta\underline{m}[\underline{V}]^T \underline{\underline{W}}_m^T \underline{\underline{W}}_m \Delta\underline{m}[\underline{V}]\, d\tau d\underline{\xi} \\
\text{s. t.} \quad & F_n(\underline{v},\underline{V}) = \int_{\tau_1}^{\tau_2} d\tau \int\int_{\underline{\xi}} \mathcal{P}_{ik}\, V_k(\underline{\xi},\tau)\, \mathcal{T}_{in}(\underline{\xi}, t-\tau; \underline{x}, 0) d\underline{\xi} - v_n(\underline{x}, t) = 0,
\end{aligned} \tag{3.16}$$

with the same index and Einstein summation convention as for equation (3.7).

It is worth mentioning that, because our forward problem is linear, the misfit function has a convex quadratic shape. Therefore, for a given set of observed seismograms, there is only one optimal spatio-temporal slip-rate distribution for which differences between observed and estimated seismograms is minimum. However, it is important to underline that, even with this formal existence of an unique optimal solution, the convergence might not be achieved for insufficient numbers of iterations depending on the shape of the misfit function. For some parameters with a rather weak (if not null) imprint in the recorded data, we may never reach the convergence. Well-distributed observations, as well as a correct knowledge of the velocity-density structure of the medium, are essential but not enough: prior information on the slip-rate model based on geological and physical understanding of the rupture process should be considered as well. As mentioned before, this inverse problem is ill-posed and most of the time highly under-determined, which makes the inclusion of regularization strategies a way to reduce the large null-space.

Gradient computation: Finding the minimum of the misfit function leads to the following Newton equation

$$\underline{\underline{\mathcal{H}}}_{\mathcal{C}(\underline{V})} \Delta \underline{V} = -\underline{\mathcal{G}}_{\mathcal{C}(\underline{V})} = -\nabla_{\underline{V}} \mathcal{C}(\underline{V}), \tag{3.17}$$

where the matrix $\underline{\underline{\mathcal{H}}}_{\mathcal{C}(\underline{V})}$ and the vector $\underline{\mathcal{G}}_{\mathcal{C}(\underline{V})}$ (the n-th component is expressed as $\mathcal{G}_n(\underline{\xi},\tau)$) represent the Hessian and the gradient of the misfit function. The model perturbation $\Delta\underline{V}$ will be added to the current model with a step length α^k estimated by the optimization procedure (Nocedal, 1980). The Hessian matrix is defined as second-order derivatives of the misfit function with respect to the slip-rate parameters. Instead of estimating the Hessian matrix (significantly more computationally expensive to estimate) in order to solve the linear system, I rely on the estimation of the gradient which will be used in an iterative procedure for solving the Newton system (3.17). In this work, I use the limited-memory BFGS quasi-Newton strategy (although steepest-descent or conjugate-gradient algorithms are possible with often more iterations) (Nocedal, 1980). Consequently, the misfit gradient is the quantity I need to compute and its estimation is efficiently performed through an adjoint-state method (Plessix, 2006). Each gradient component of the misfit can be written as

$$\begin{aligned} \mathcal{G}_k(\underline{\xi},\tau) = &\sum_{\underline{x}} \int_{t_1}^{t_2} \underline{\underline{W}}_d^T \underline{\underline{W}}_d \Delta d_n[\underline{V}](\underline{x},t) \mathcal{T}_{ni}(\underline{\xi},\tau - t;\underline{x},0)\, \mathcal{P}_{ik}^T dt \\ &+ \epsilon \left[\underline{\underline{W}}_m^T \underline{\underline{W}}_m \Delta m[\underline{V}](\underline{\xi},\tau)\right]_k \\ &n, i \in [x,y,z] \text{ and } k \in [\phi,\delta] \text{ or } k \in [\lambda], \end{aligned} \tag{3.18}$$

with the same index and Einstein summation convention as for equations (3.7) and (3.16). The first term in equation (3.18), which is the data term, is the sum of the projections of the unexplained residues at all the receivers onto the fault plane through the stress-state tensor, while the second term incorporates the prior model information. In reverse-time imaging as proposed by Fink (1993, 2008) and applied to earthquakes by Gajewski and Tessmer (2005); Larmat et al. (2006); Ishii et al. (2007) among others, projections of observations (and not the unexplained data by the current model) are performed in the 3D volume around the rupture zone or onto the 2D rupture surface tracking the spatio-temporal evolution of the rupture front. This is the same difference between migration techniques and full waveform inversion (FWI) in velocity model imaging where full observations are back-projected for migration (Claerbout, 1971; Lailly, 1983; Tarantola, 1984) while only unexplained observations are back-projected for FWI Gauthier et al. (1986); Virieux and Operto (2009). I should highlight that the computational task of estimating the data misfit gradient and the model misfit gradient is quite simple, once the stress-state tensor has been pre-computed and stored. Let me repeat that this tensor, which describes the influence of the velocity model, plays a quite important role in the reconstruction of the slip-rate by inferring the causality due to propagation while preserving the linear formulation.

In this work, the 3D space-time volume is sampled with a regular discretization along strike, dip and time ($[\phi_j, \delta_k, t_l]$) directions for the numerical estimation of the data gradient, although other discretizations are possible. Designing the discretization along these three directions is application-dependent and we shall consider here regular grids. The slip-rate values should be evaluated at each node of the spatial grid and I assume a linear continuous interpolation of the slip-rate over space (i.e. using the trapezoidal rule for the spatial integration). The regular time sampling is adapted to the frequency content of the data to be inverted. These samplings should honor the expected physical behavior of the slip-rate function in space and time to be inverted which is more restrictive than the discretization related to the propagation.

3.2.3 Standard Inversion Strategy (SIS)

The first strategy to reconstruct the time-space slip-rate distribution which handles the complete available seismic data (from initial to final recording time) for a given event will now be introduced. Hereinafter I label this first strategy the Standard Inversion Strategy (SIS).

The algorithm (1) and Figure 3.4, based on equations (3.7) and (3.18), provides the different steps necessary to perform the SIS which tentatively performs a simultaneous fitting of different wave packets recorded at the receivers: spatial/temporal leakage in the data gradient might occur as long as kinematic features of the data are fulfilled. Consequently, model gradient terms play a major role for modifying the descent direction and, therefore, stabilize the inversion.

Algorithm 1: Standard kinematic source inversion strategy using the adjoint-state method.

```
Specify source geometry, $(\underline{\xi}, \tau)$, acquisition configuration, $(\underline{x}, t)$ and pre-computed stress-state tensor $\underline{\underline{T}}$ from a velocity model (using any wave-propagator tool).
Input complete observations (3-component seismograms) at each receiver.
Initialize a zero slip-rate $\underline{V}^k(\underline{\xi}, \tau) = \underline{0}$ for $k = 1$
Design prior model $\hat{\underline{V}}$ and weighting matrix $\underline{\underline{W}}_m$.
while Convergence is not reached (iterate over k) do
    Compute $\hat{\underline{v}}^k(\underline{x}, t)$, forward modeling using $\underline{V}^k(\underline{\xi}, \tau)$ in equation (3.7).
    Estimate residues, $\Delta\underline{d}[\underline{V}^k](\underline{x}, t) = \hat{\underline{v}}^k[\underline{V}^k](\underline{x}, t) - \underline{u}(\underline{x}, t)$.
    Calculate the gradient according to equation (3.18) and evaluate $\Delta\underline{V}^k$ .
    Update the slip-rate $\underline{V}^{k+1} = \underline{V}^k + \alpha^k \Delta\underline{V}^k$, ($\alpha^k$ the step length).
```

3.2.4 Progressive Inversion Strategy (PIS)

Instead of considering the entire dataset, we may proceed in a hierarchical way taking benefit of causality by increasing the data time-windows we consider through iterations. This sweeping strategy has often been used when imaging structures (Kolb et al., 1986). A data time-windowing strategy is expected to reduce the leakage related to time-space ambiguity, by taking benefit from sparsity and causality of this rupture problem (Heaton, 1990). The preservation of a time formulation is essential in this approach. We label this strategy the Progressive Inversion Strategy (PIS).

Observations in specific time-windows defined for each receiver will be associated to a limited slip-rate time-space zone. These data time-windows are defined by the acquisition configuration with respect to the rupture surface and the velocity model described through the stress-state tensor between each point of the rupture surface and each receiver. For example, first recorded pulses are expected to come from the nucleation zone and they will impact nearest stations first. Therefore, stress-state tensors can be used for defining the data time-window of each record participating to the rupture inversion assuming a simple expansion of the active zone inside which the expected slip-rate should be.

Considering as known the hypocentral location, the origin time of the rupture and a maximum value of the rupture velocity, expected spatial zones and time intervals, where the slip-rate inversion is to be performed, can be specified through an Eikonal solver (e.g. Podvin and Lecomte, 1991). Using the pre-computed stress-state tensors, it is possible to estimate the data time-window at each receiver to be

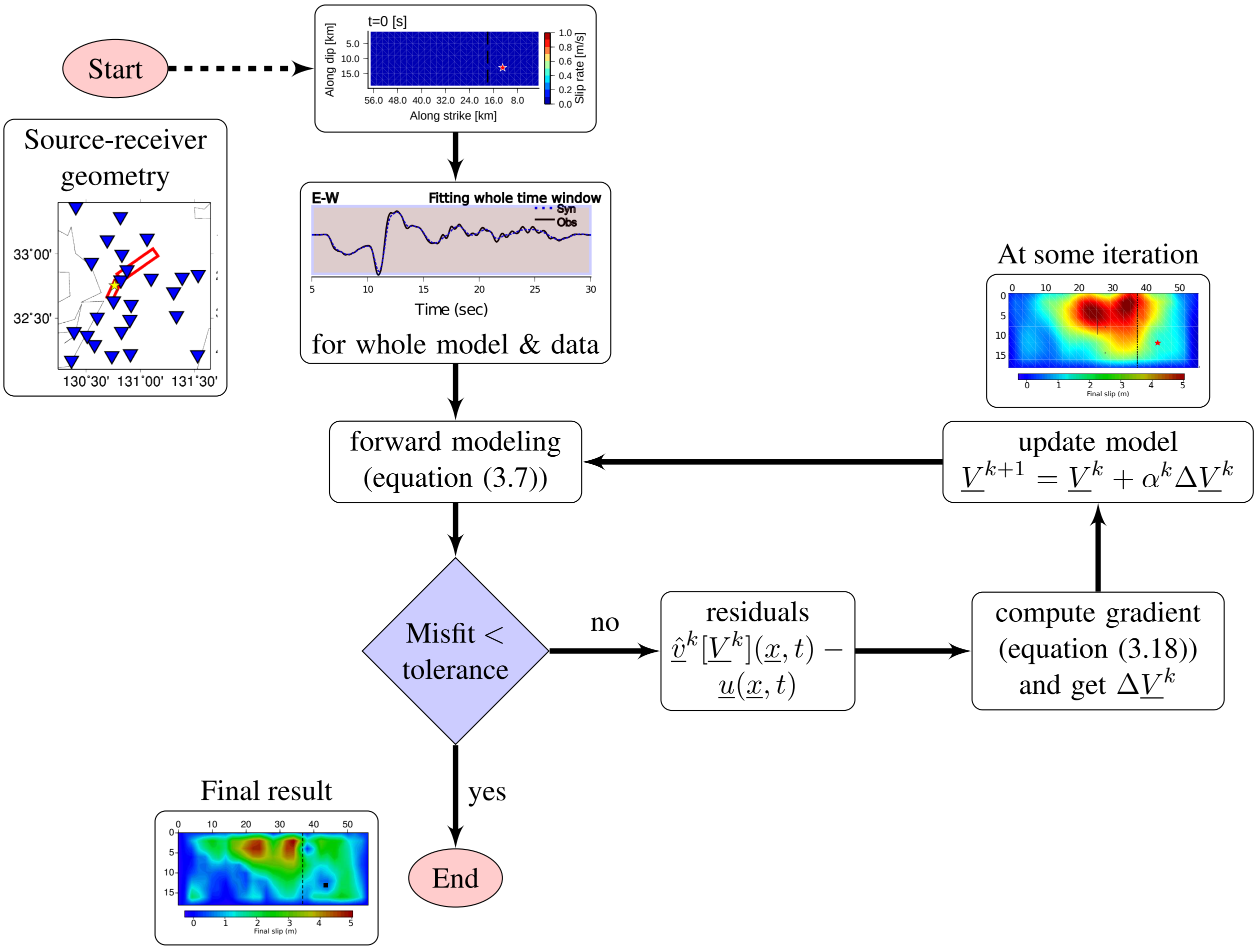

Figure 3.4: Standard Inversion Strategy (SIS) work-flow. This flow chart describes how the complete recordings are inverted through a local optimization strategy in order to reconstruct the whole time-space seismic rupture history. See Algorithm 1 for details.

involved by these selected zones and intervals (Figure 3.5). Of course, these data time-windows are specific to each receiver with the imprint of the propagation. For instance, a far-away station may have a different time-window evolution compared to a near station. All expected phases should be included in these time windows, from the fastest P-wave phases to the possible surface-wave phases. I rather use the local P-wave speed when solving the Eikonal equation to determine the limits of this growing allowed region where the rupture is expected to be. The choice of using the P-wave velocity instead of the S-wave is made in order not to miss any possible super-shear phenomena, as they may be present in several earthquakes (Bouchon et al., 2001).

Let me underline that these windows define a tight breakable region. Moreover, any time delay of converted phases is included in these time-dependent tensors, allowing a prediction of not-yet-recorded phases reducing the space-time leakage, thanks to the causality. However, in spite of this reduction of null-space size in this PIS, prior model information is still needed because this is a key element for a better injection of phenomenological description of the rupture physics which are not explicitly considered in the parametrization used.

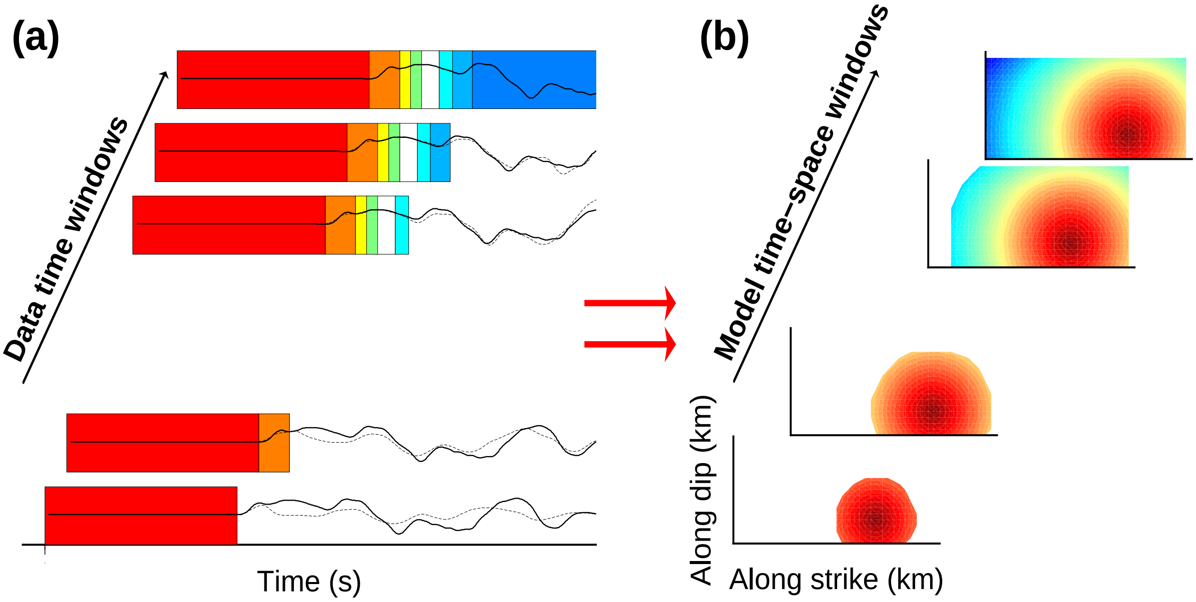

Figure 3.5: (a) The illustrated selection of increasing data time-windows is related to the temporal evolution of the seismic active zone (b). (a) Progressively increasing data time-windows are highlighted with different colors after which the data is ignored during the current iteration of the inversion process. (b) Related active space regions increase with time. At a given time, only the active zone is allowed to be used for data inversion. The same colors, ranging from red to blue, are used for data and model windows in order to enhance their relationship. Notice that, at later stages of the PIS, only the residues between observations and synthetic recordings need to be explained: a key property of causality. Solid and dashed lines represent the observed and synthetic wave fields, respectively.

This strategy leads to a slightly different algorithm compared to the previous one as described here

Algorithm 2: Progressive inversion strategy using the adjoint-state method for source imaging.

```
1: Specify source geometry, $(\underline{\xi}, \tau)$, acquisition definition, $(\underline{x}, t)$ and stress-state tensor $\underline{\underline{T}}$.
2: Input first data time-windows at each receiver.
3: Initialize zero slip-rate $\underline{V}^k(\underline{\xi}, \tau) = \underline{0}$, $k = 1$
4: Design prior model $\underline{V}_p$ and weighting matrix $\underline{\underline{W}}_m$.
5: while Final data time-window is not reached do
    5.1: Select the active fault zone and the time-window/receiver with the help of the $\underline{\underline{T}}$.
    5.2: while convergence is not reached (iterate over $k$ do
        5.2.1: Compute $\hat{\underline{v}}^k[\underline{V}^k](\underline{x}, t)$, forward modeling using $\underline{V}^k(\underline{\xi}, \tau)$ in equation (3.7).
        5.2.2: Estimate residues $\hat{\underline{v}}^k[\underline{V}^K](\underline{x}, t) - \underline{u}(\underline{x}, t)$
        5.2.3: Calculate gradient according to equation (3.18) and evaluate $\Delta\underline{V}^k$.
        5.2.4: Update slip-rate $\underline{V}^{k+1} = \underline{V}^k + \alpha^k \Delta\underline{V}^k$, ($\alpha^k$ the step length).
```

The interesting behavior of the PIS acting as a predictive deconvolution filter can be observed in Figure 3.5. Notice that, thanks to the wave propagation information stored in the stress-state tensors $\underline{\underline{T}}$, a tentative prediction of the data recorded at longer time-windows not yet considered at previous stages of the inversion process is already available from the time-space limited slip-rate reconstruction. Therefore, as the time-space source active zone grows, the new parameters have to explain only the

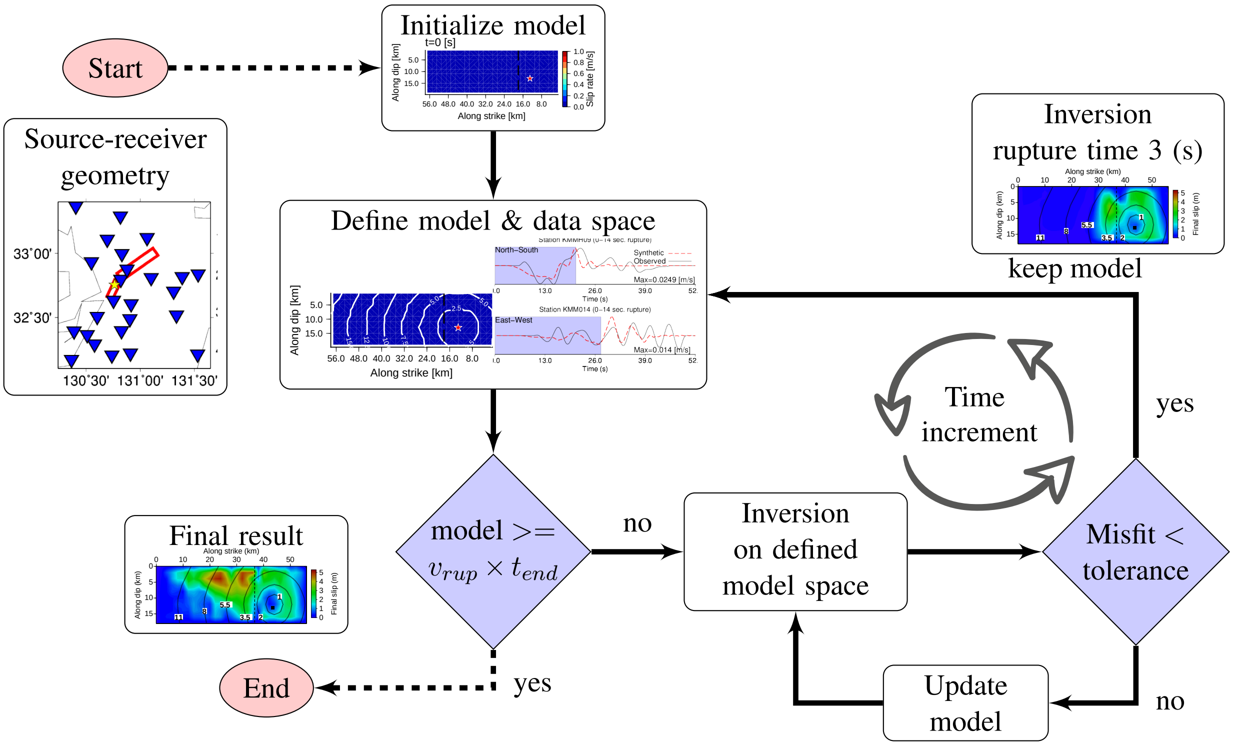

Figure 3.6: Progressive Inversion Strategy (PIS) work-flow. This flow chart describes how the PIS is able to assimilate and invert incomplete seismograms (i.e. recording time is not over) to partially reconstruct the rupture history. See Algorithm 2 for details.

not-yet-understood residues related to the new data time-windows. This progressive strategy mitigates the space-time ambiguity occurring in the SIS, thanks to the causality property of the time kinematic formulation.

3.2.5 Model regularization and model preconditioning

Besides the chosen strategy (SIS or PIS) and the regularization term, based on the model-driven gradient, we can apply a smoothing operator on the data gradient. The data-driven gradient is spatially filtered as $\underline{\mathcal{G}}^{new} = \underline{\underline{K}}\,\underline{\mathcal{G}}$, where the kernel $\underline{\underline{K}}$ represents a 2D Gaussian spatial filter based on the corresponding correlation distances along strike and dip directions of neighboring nodes. No time filtering is considered in this work. For simplification, such gradient smoothing does not require any hyperparameter setting but relies on the smoothing strategy driven by the expected features of the wanted model. This new smooth gradient is the one given to the optimization algorithm for updating the current model.

Because the acquisition is frequently deployed at the free surface while the slip-rate may vary with depth, a depth-dependent preconditioning is considered in this work, in a similar way for the compensation of illumination deficit with depth (Plessix and Mulder, 2008; Asnaashari et al., 2013; Pérez Solano, 2013). The new scaled version of the slip-rate is

$$\underline{\hat{V}} = \frac{1}{z^c}\underline{V}, \tag{3.19}$$

where z is the local node depth and c is a case-dependent constant that should be tuned. The values of this constant, as far as I have experienced, range from 0.01 to 1 in our different applications. Such model scaling turns the estimated gradient $\underline{\mathcal{G}}(\underline{\xi}, \tau)$ from equation (3.18) into a new gradient

$$\hat{\underline{\mathcal{G}}} = z^c \underline{\mathcal{G}}. \tag{3.20}$$

Another strategy could be coarsening the grid while increasing the depth (Barnhart and Lohman, 2010): I prefer to keep the meshing simple in this work. Nevertheless, as in the case of the gradient filtering, this strategy is case-dependent and a previous calibration of constant c has to be conducted on synthetic exercises before performing any inversion of real data. Similarly, the depth coarsening of the grid is case-dependent and requires numerical analysis.

3.3 Synthetic case: Source Inversion Validation exercise 1 (SIV1)

Before a possible application to real data, the verification of both approaches is essential. Thanks to a research community effort recently reviewed by Mai et al. (2016), different examples are proposed for the validation step. The Source Inversion Validation exercise 1, named SIV1, is considered in this section for which both behaviors of misfit-data term and misfit-model term are investigated as is known the exact model solution. For this validation exercise, the velocity model for wave propagation is known and the observations are noise-free: an optimistic point of view when considering real data. In other words, we are in a very favorable situation for this synthetic analysis and the obtained solutions would be the optimal ones for the undertaken approaches in real cases.

3.3.1 SIV1 Description

In the SIV1 exercise, the source geometry is a fault plane with known strike $\phi = 90^o$, dip $\delta = 80^o$ and rake $\lambda = 180^o$ (Figure 3.7b). The fault is embedded in an elastic layered isotropic medium (Figure 3.7a and Table 3.1). The dimensions of the fault are approximately 35 km along strike by 20 km along dip. The final slip, slip-rate time histories and rupture speed are heterogeneous along the fault (Figure 3.7c and 3.7d). As prior information, the location of the hypocenter, the final seismic moment ($M_0 = 1.06 \times 10^{19}\ Nm$, $M_w = 6.69$) and the fact that the rupture does not reach the surface (see Mai et al. (2016) for details) are input information aside seismograms. Forty receivers at the surface with 3-component noise-free velocity recordings (maximum resolved frequency about $\approx$ 2.5 Hz) are available in the distributed database. As it can be seen in Figure 3.7b, the 40 receivers form a satisfactory azimuthal coverage.

3.3.2 Settings: Discretization, regularization design and preconditioning strategies

Four scenarios are presented with different SIS work-flows. The first one, referred as SIS1, carries a SIS without any regularization term or prior information. The second case which will be called SIS2, applies the regularization and preconditioning strategies just described previously. For these first two cases, the rake angle is allowed to smoothly vary inside the interval $[150^o - 210^o]$. Two additional exercises, SIS1* and SIS2*, are considered where exactly the same configuration is used as for the first two exercises, but the rake angle is kept to its exact value ($\lambda = 180^o$) during the inversion.

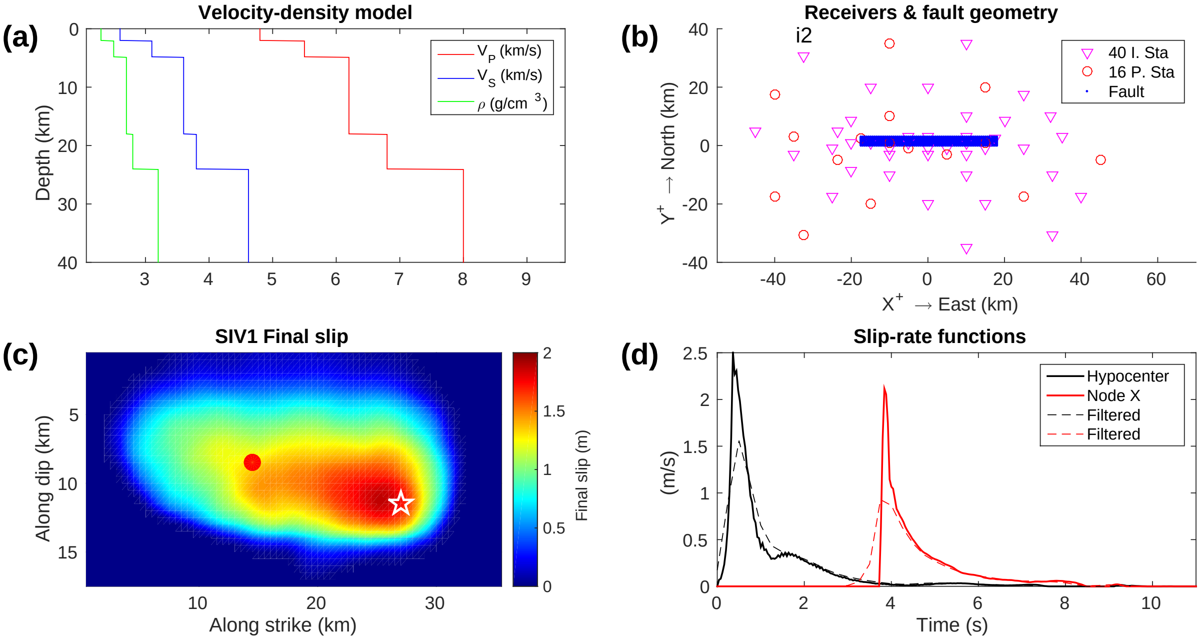

Figure 3.7: Summarized description of the SIV1. (a) Velocity-density structure of the embedding medium. (b) Surface projection of the fault geometry (2592 fault-nodes) and the locations of the 40 receivers used for the inversion (40 I. Sta) and 16 stationsare left for quality control by confronting the predicted velocity records of the inversion results to the not-used observations (16 P. Sta). (c) Final slip distribution along the fault after ≈ 10 seconds of rupture. (d) Slip-rate time functions from two different locations, at the hypocenter (black line) and far from it (red line). The slip-rate functions are from the positions represented by the star and the circle at (c). Dashed lines on panel (d) represent the slip-rate functions of the filtered version of the SIV1 ($0 - 1$ Hz) used in this work. Information taken from Mai et al. (2016).

Depth (km)	V_P (km/s)	V_S (km/s)	Density (g/cm^3)
0.0	4.8	2.6	2.3
2.0	4.8	2.6	2.3
2.0	5.5	3.1	2.5
4.8	5.5	3.1	2.5
4.8	6.2	3.6	2.7
18.0	6.2	3.6	2.7
18.0	6.8	3.8	2.8
24.0	6.8	3.8	2.8
$>$24.0	8.0	4.62	3.2

Table 3.1: Velocity-density structure used for Green function and stress-state computation for the SIV1 and SIV2a synthetic cases.

As mentioned earlier, the 3D (strike, dip and time) slip-rate model space must be discretized for accurate forward modeling on one side and for feasible inversion using a limited number of degrees of freedom. The time discretization is related to the frequency content of the data. A maximum frequency of 1 Hz is considered for this synthetic exercise. Therefore, a time sampling of the slip-rate time-space history Δt of 0.25 s corresponds to half of the Nyquist sampling. The spatial discretization is controlled by two characteristic lengths. The first one is related to the Green function and related wave propagation. The grid spacing must be a small fraction of the shortest expected wavelength, which turns out to be shorter than 1.3 km for a minimum shear velocity V_s of 2.6 km/s. The second characteristic length is related to the rupture front width. The rupture front width depends on the rise time and the rupture velocity. The spatial spacing has to sample enough the rupture front width for a continuous propagation of the rupture front. The rupture front width can be roughly estimated by multiplying the mean value of the expected rupture speed and the rise time. Thus, by considering a mean rise time of 4 s and a rupture velocity of 70% of the minimum V_s, the rupture front width will be around 7.3 km. Consequently, a spatial discretization Δx sampling of 1 km in both the strike and dip directions is selected. This choice depends essentially on the frequency range of waves considered at receivers. The choice of the discretization is crucial for the inversion: the total number of invertible parameters can be a drastic tuning strategy to control the dimension of the model space and the null space.

Figure 3.8 illustrates how a very coarse spatial discretization impacts the correct estimation of synthetic seismograms at a given receiver location when compared with those for the discretization which is recommended. Of course, a finer time and space sampling could be used at the expense of having more unknowns to be solved. Some tests were carried out in order to check that the effect of any further refinement of the spatial grid does not mean a significant improvement of the forward or inverse problems. More objective criteria should be introduced for designing the discretization such as the statistical Fisher test or a trans-dimensional analysis (Bodin et al., 2012; K. and Reetam, 2017). For this work, I did not elaborate such criterion. This sampling design is related to resolution and uncertainty investigation. Because for this exercise the solution is known, I was able to proceed this way and I found that the spatial discretization deduced from the expected minimum wavelength propagating in the medium and the estimated average rupture velocity provides a decent approximation of the needed discretization.

Taking into account this discretization setting, the synthetic exercises is set as follows. The duration of observed seismograms is 35 s for all of 120 traces with a maximum frequency of 1 Hz. For real earthquakes, the maximum frequency of the observations used for source inversion are usually lower (e.g. frequency bands between $0.025 - 0.25$ Hz or $0.025 - 0.5$ Hz). High-frequency content is sensitive to small-size heterogeneities of the medium velocity, already difficult to include in the propagation, preventing reconstruction of the corresponding slip-rate contribution for the source at these frequencies. In this exercise, the medium is exactly known but our restriction to 1 Hz might represent a more realistic situation. In order to speed up the time convolution, I decimate signals down to a sampling rate of 0.1 seconds, representing 87 % of the original dataset. Let me highlight that the slip-rate time-space history and the observed wave fields have different time sampling rates (0.25 s versus 0.1 s) but an equal frequency content up to 1 Hz. The fault geometry is represented through 36×18 nodes equally separated every 1 km along strike and dip, respectively (Figure 3.8). The total duration of the rupture is fixed to last less than 9.5 s. Therefore, the total number of parameters describing the slip-rate distribution for the first two cases is 36 [nodes along-strike] $\times 18$ [nodes along-dip] $\times 39$ [time-samples] $\times 2$ [slip-rate components] $= 50544$ when the rake angle is unknown, and half this amount 25272 when the rake angle is fixed to a given value. In contrast, the total number of observations in both cases is 141 [time-samples] $\times 120$ [traces] $= 16920$. For consistent comparison, the time-space discretization is the same for all exercises. Each of the inversion strategies has a different stopping criteria related to the time-window that they invert. For the exercises where the SIS is applied, the stopping criterion is set to a limited number of iterations (20 maximum) or a convergence tolerance equal to a normalized misfit less

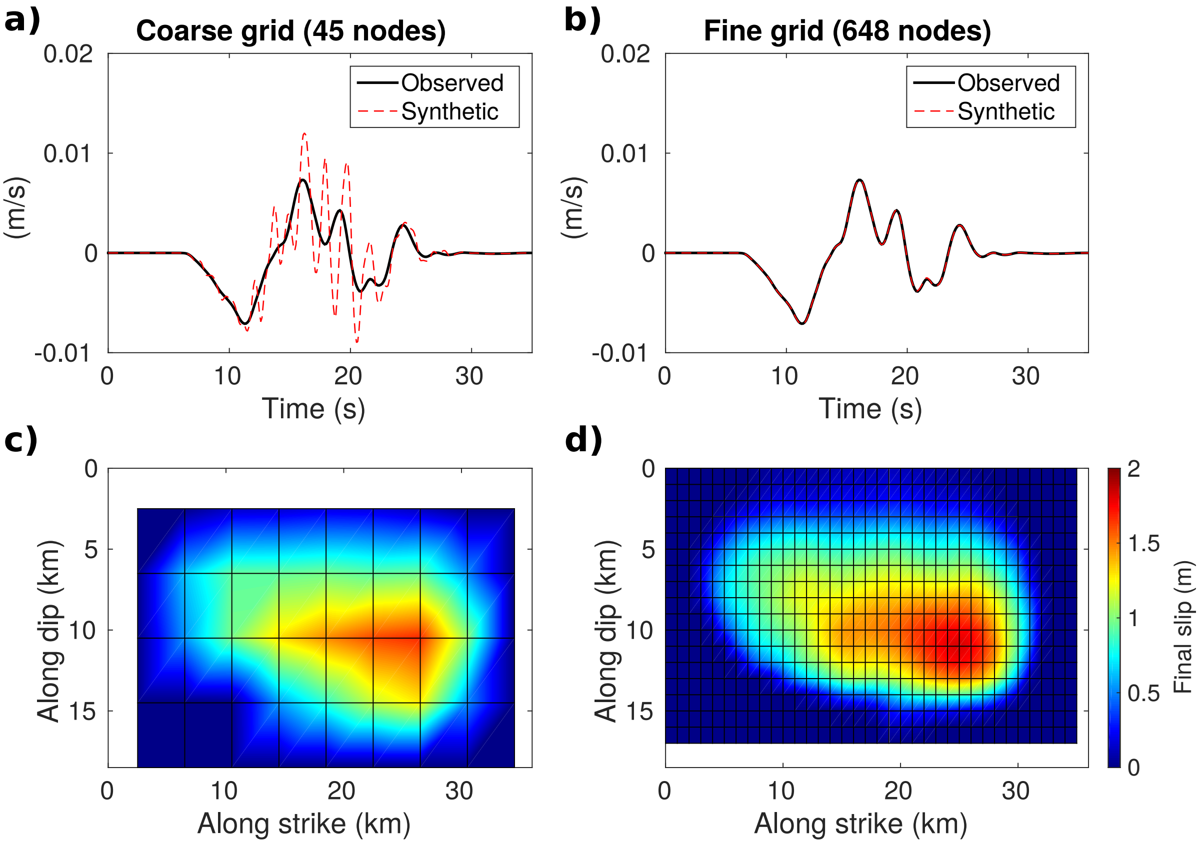

Figure 3.8: Comparison between the synthetic seismograms (panels a) and b)) produced when considering a c) coarse and a d) fine spatial discretization. c) and d) display final slip distributions for both discretizations. An incorrect coarse spatial discretization can produce spurious oscillations in the estimated synthetic wave field as shown in a). The coarse grid assumes 9 nodes along strike by 5 nodes along dip (45 total nodes) (4 km sampling) while the finer one considers 36 nodes along strike by 18 nodes along dip (648 total nodes) (1 km sampling). Both synthetic wave fields (red dashed lines) are compared with the SIV1 data set (solid black line) filtered at a maximum frequency of 1 Hz at a given receiver location. The location of all the nodes can be identified at the junctions of the grid.

than 1×10^{-2} related to the initial total data misfit $\mathcal{C}_{\underline{d}}(\underline{V})$. On the other hand, the stopping criterion for each stage of the PIS is set so that at least a certain number of iterations is performed (10 maximum) and a convergence tolerance equal to a normalized misfit less than 1×10^{-2} related to the data misfit of only the data time-window that is taken into account at that stage is ensured. These two criteria are defined in this way in order to avoid over-fitting the data when performing a large number of iterations.

The prior model, $\underline{\hat{V}}$, and weighting matrix, $\underline{\underline{W}}_m$, are incorporating the following information. The prior model is built as a rupture which starts at the known hypocentral location. The rupture front of this prior model propagates at the local shear wave velocity at the beginning of the propagation and it slows down while it goes far from the hypocenter (Figure 3.9a). The rupture times are computed through an Eikonal solver (Podvin and Lecomte, 1991) and an additional delay (ranging from 0 s to 0.5 s) is added to the calculated rupture times according to a Laplacian function in terms of the correlation distance between the different nodes in the mesh and the hypocenter location. Yoffe-type functions (Tinti et al., 2005) with 5 s of effective rise time and 0.5 s of duration of the positive acceleration are assumed. The total slip amplitude is fixed to 1.6 m at the nodes inside a central region of the fault plane and it decays exponentially while approaching the borders of the fault geometry.

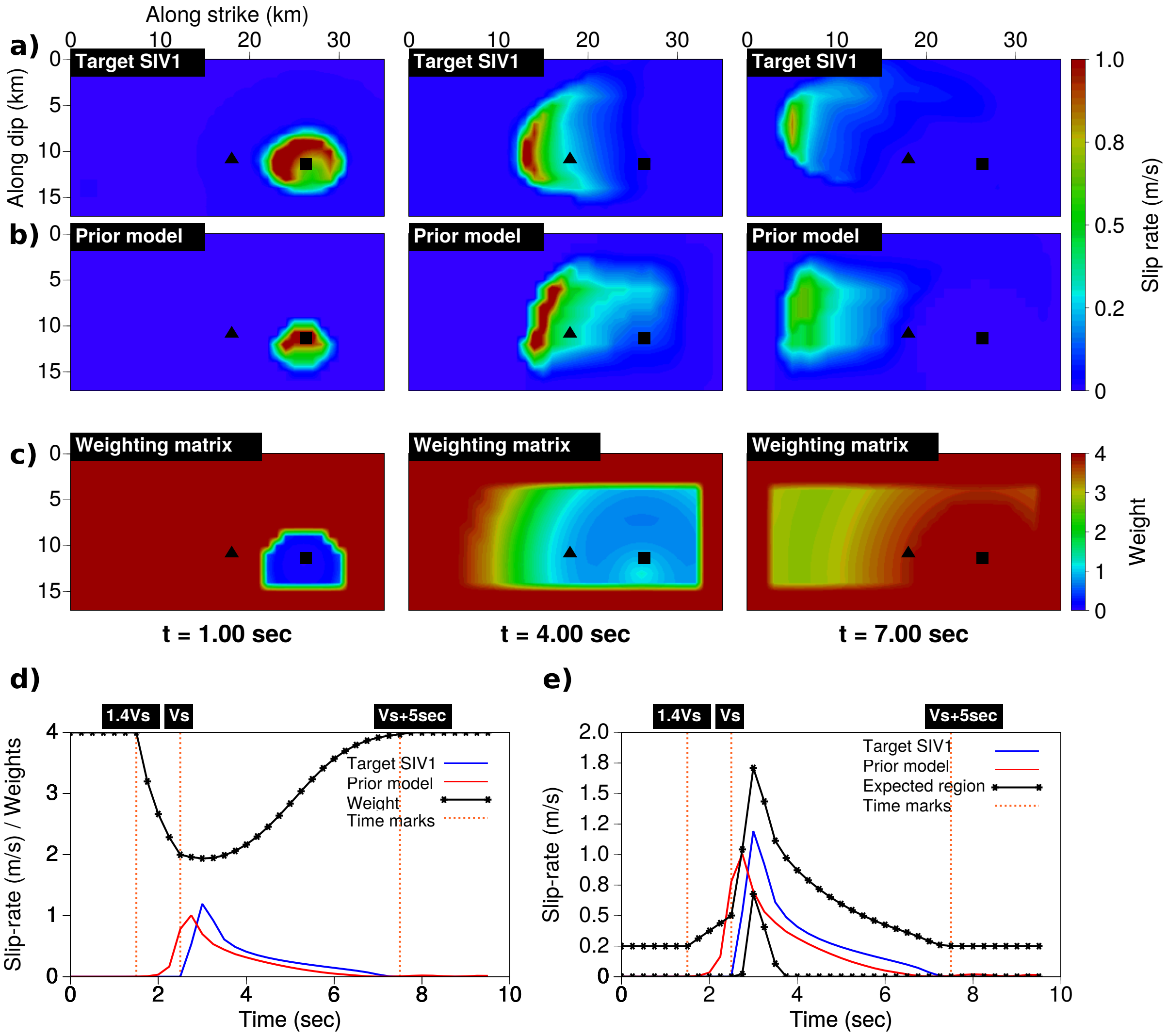

Figure 3.9: Summary of the designed prior model, $\underline{V}_p$, and weighting matrix, $\underline{\underline{W}}_m$. a) Illustration of the time evolution along the fault of the filtered version of the SIV1, b) the prior model and c) its associated weighting matrix at 1, 4 and 7 seconds of rupture (from left to right). Panels d) and e) show exactly the same comparison of the amplitude of the slip-rate functions from the filtered version of the SIV1 (blue line), the prior model (red line) and the weight time history (black line on d)). On panel e), the weight time history from panel d) is translated into the expected zone where the rupture is preferred (black line on e)). Time marks (orange dashed lines) on d) and e) illustrate the arrival times of rupture fronts propagating at speeds of $1.4V_s$ (rupture time upper limit) and V_s as well as the expected rise time (5 seconds, rupture time lower limit). The location of the fault-node at which slip-rate functions and weight time history are shown on d) and e) is represented by a black triangle on panels a) b) and c) while the hypocenter is represented by a black square. In the representation of the weighting matrices shown on panel c), the confidence on the prior model is represented by the colors ranging from blue (low confidence) to red (high confidence).

The weighting matrix $\underline{\underline{W}}_m$ is designed to emphasize to which extent model prior information is trustful. Because the prior information ensures that the rupture does not reach the surface, strong weights are given to the slip-rate difference $\underline{V} - \underline{\hat{V}}$ at shallow nodes and at those nearby the other boundaries of the predefined fault (similar to the matrix shown in Figure 3.2). Slip-rates at those nodes are set to zero initially and, therefore, any non-zero slip-rate is strongly penalized at these nodes. At the same time, the weighting matrix can also penalize any slip-rate values occurring at lower or higher rupture speed than the expected limits. For these exercises, the model weighting matrix is designed in such a way that ruptures propagating faster than 1.4 times the local shear wave velocity (V_s) are strongly penalized (i.e. rupture time upper-limit as in Figure 3.3). To prevent that a node breaks a second time or to limit the energy at that node after an expected duration of the rupture, a lower limit that penalizes any rupture happening at a given node after 5 seconds beyond the passing time rupture at that node is also included. Figures 3.9 offers a comparison between a) the slip-rate distribution to be reconstructed, b) the designed prior model, and c) the evolution of the highly penalized areas on the fault at different times of the rupture (at 1, 4 and 7 seconds). The weighting matrix is constructed based on an expected area of confidence around the prior model. At each node, the time history of the confidence grows linearly from the first expected rupture arrival and another rupture arrival propagating at V_s. Then, the confidence decays as a Gaussian curve the half-width of which lasts the expected duration of the slip-rate functions (5 s). This weighting matrix is related to physically meaningful model covariance and the global hyperparameter ϵ scales the model misfit with respect to the data misfit: this is the reason why this scaling is not integrated into the weighting matrix for making explicit this balance between data and model terms.

Let me note that the prior model is designed in such a way that information about the minimum and maximum rupture speeds, vanishing slip at the fault boundaries and expected rake angle limitations are included. Fast changes from low to high values during the time evolution of the weighting matrix represent the limits on the expected rupture velocities (Figure 3.9c). Moreover, the Yoffe-type slip-rate functions of this prior model are chosen in order to see if the inverted slip-rate functions could benefit from this prior information on the shape of the time history (Tinti et al., 2005). A comparison between target and prior model slip-rate functions, at a node far from the hypocenter, is provided in Figures 3.9d and 3.9e. A prior homogeneous final slip of 1.6 m is allowed uniformly over the breakable zone, giving equal probable contribution everywhere inside this zone. We can see in the panels of Figure 3.9 these constraints on the possible rupture process.

When regularization is activated, the depth-dependent model preconditioning and the data gradient smoothing strategies are also applied. For the depth-dependent strategy it was found that, for this receiver configuration, the optimal value of the constant c is $\approx$ 0.08. In addition, a 2D Gaussian-shape filter with a correlation distances of 3 km and 2 km along strike and dip, respectively, is applied to the data gradient at each iteration of the inversion to ensure the spatial coherence of the slip-rate distribution.

3.3.3 SIS Synthetic case SIV1

In this section, and across the whole manuscript, I use the term “final slip" to define the cumulative slip (in meters) that is reached at some location on the fault once the rupture is over (final value). On the contrary, the term ”cummulative slip" (in meters) is used to describe the slip reached at some location on the fault for a time instant that is not the final time (i.e. the rupture is not over yet and the slip can still increase). Figure 3.10 and Table 3.2 summarize the results for these four exercises by comparing their final data misfit, model misfit (resolved slip-rate functions versus filtered version of the SIV1), mean value and standard deviation of the rake angle extracted from the solutions and estimated seismic moment.

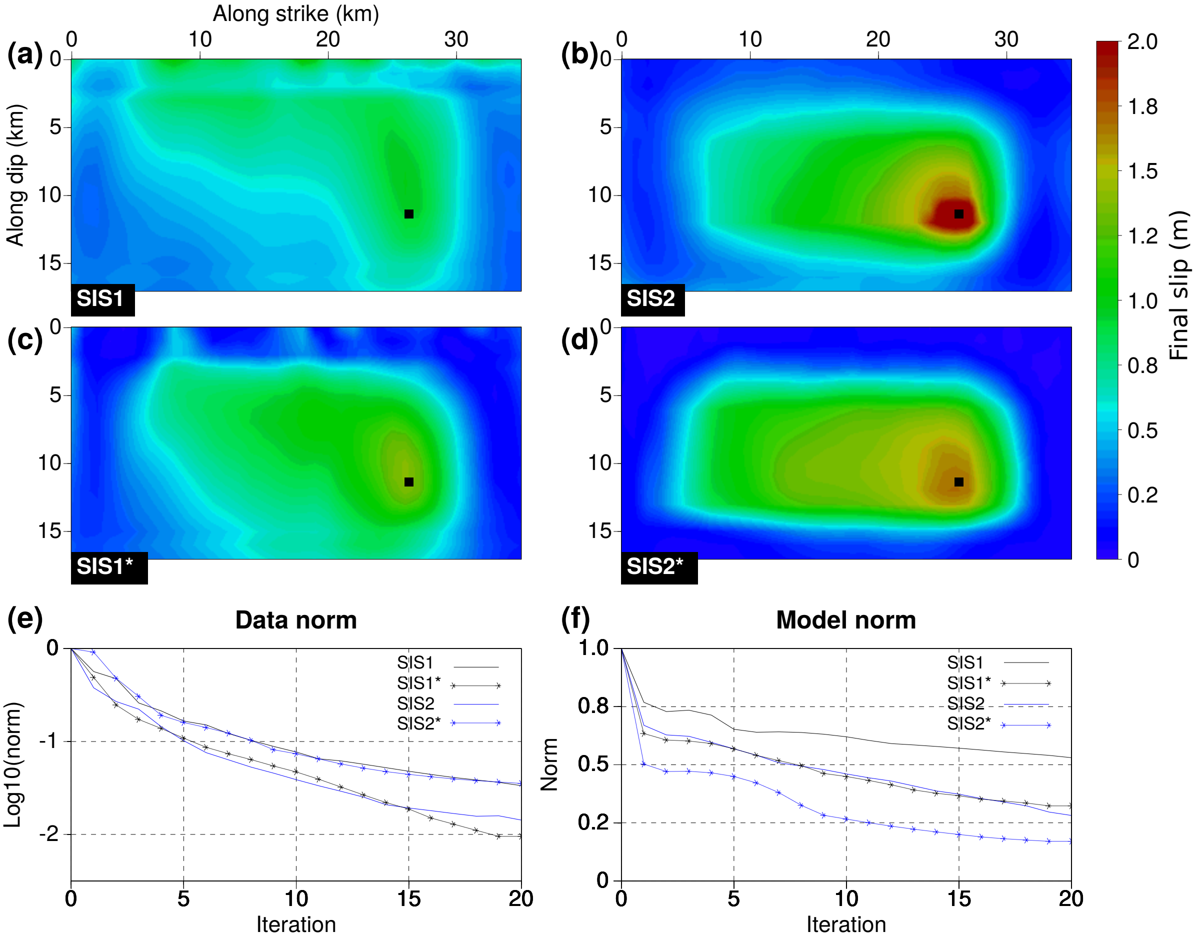

Figure 3.10: Comparison of the final slip resulting from applying the SIS with and without regularization. Results from panels (a) and (b) are obtained without assuming any rake angle (allowed to vary between 150^o-210^o). (a) comes from a SIS without regularization or preconditioning and (b) includes regularization and preconditioning. Panels (c) and (d) show the results from the SIS when the rake angle if fixed to its correct value ($\lambda = 180^o$). Panel (c) is obtained without regularization or preconditioning, while panel (d) is obtained with regularization and preconditioning. Panels (e) and (f) illustrate the evolution of the data and model L2 misfit norm through the iterative process of inversion, respectively.

As expected, when no prior information is used (except the hard limits of the expected rake angle range), time-space ambiguity will impact the fitting of the observations. As a consequence, results for the SIS1 show slip everywhere on the fault (Figure 3.10a). The configuration of SIS1 allows to correctly minimize both data and model misfit but the results are worse than for the other cases. Even without regularization, one may notice that the reconstruction is significantly improved when keeping fixed the rake angle (SIS1*). The improved results from the SIS1* correspond to the reduction of the number of invertible parameters when assuming a known rake direction instead of performing a vectorial reconstruction of the slip-rate (Figure 3.10c). However, according to Figure 3.10f, when regularization is included without strong rake constraints (case SIS2 Figure 3.10b) the reduction of the model misfit shows comparable results to the non-regularized and fixed-rake exercise (case SIS1* Figure 3.10c).

Therefore, in terms of model misfit, fixing the rake at the correct value allows an improvement comparable to the one gained when prior information is used to regularize the inversion for this synthetic exercise. Even though cases SIS1 and SIS2 over-estimate the final seismic moment (Table 3.2), they under-estimate the local final slip and slip-rate amplitudes almost everywhere, which is another consequence of the spread of the information onto a large number of parameters. Regularization terms help to decrease this time-space leakage but results are not significantly improved.

Contrary to these poor final slip estimations and slip-rate reconstructions, the exercises without fixing rake values (SIS1 and SIS2) provide a satisfactory estimation of the average rake angle (Table 3.2). Fixing the rake by considering only the slip-rate modulus as the inverted parameter is essential for reducing the number of parameters and for a significant improvement of the slip-rate reconstruction. Following this idea, a hierarchical two-step inversion scheme, where an initial inversion is performed first to infer the local rake direction of the sliding and where a second inversion with fixed rake direction inverts for the slip-rate amplitude, can be a very useful strategy. A preliminary estimation of these local directions will allow us not to over-simplify the rupture history: smooth variations of local rake angles seem to be a reasonable assumption as we do not expect drastic changes of the sliding direction in less than 1 km distance. Such two-step strategy will be of great importance when tackling real datasets. In realistic conditions, few prior information on spatial variations of the rake is available, acquisition systems are not dense enough to properly illuminate the fault and the limited knowledge of the velocity medium makes even more challenging the rake angle recovery.

Results from cases SIS1* and SIS2* (Figures 3.10c and 3.10d) illustrate the importance of prior information on the rake angle. When this information is available (for example, from focal mechanisms deduced from teleseismic phases), the inversion is able to better locate and estimate the zone of maximum slip. Even when no regularization (except the assumed fixed rake angle) is used in case SIS1*, the cross-talk between nodes decreases and the estimated maximum slip (1.4 m) reached 80% of the expected value (1.8 m). However, the exercise SIS1* still shows important slip (0.6-0.8 m) at the deepest boundary. Therefore, additional regularization and preconditioning play a complementary role for the exercise SIS2*. Results from this exercise are the best among these four exercises: the zone of maximum slip is well located and its amplitude (1.7 m) is very close to the expected one. For the case SIS2*, the whole final slip is less over-estimated than for the other three exercises and the regularization term and preconditioning strategies partially remove the slip at regions where rupture is not expected to happen. Let us underline that, without imposing any direct constraint on the seismic moment, the computed M_0 for SIS2* over-estimates by 11% the true value. However, results from SIS2* required various prior information: rake angle bounds first through a vectorial reconstruction and then by keeping it fixed, hypocenter location, free-surface vanishing slip coming from potential geological observations and expected expansion of the slip-rate surface with time.

In general, we observe that the space-time ambiguity between nodes is strongly reduced when the information of the rake is used. When regularization terms are used, both data and model misfits improve. The prior model regularization term removes exactly what is expected: slip vanishes at boundaries of the pre-defined geometry, slip-rate does not occur before the time of the pre-defined rupture time at each position and may not re-start after an expected duration if not requested by the data. As a consequence, the final slip estimation over the whole fault is better predicted. Let us now perform the same four exercises using the PIS.

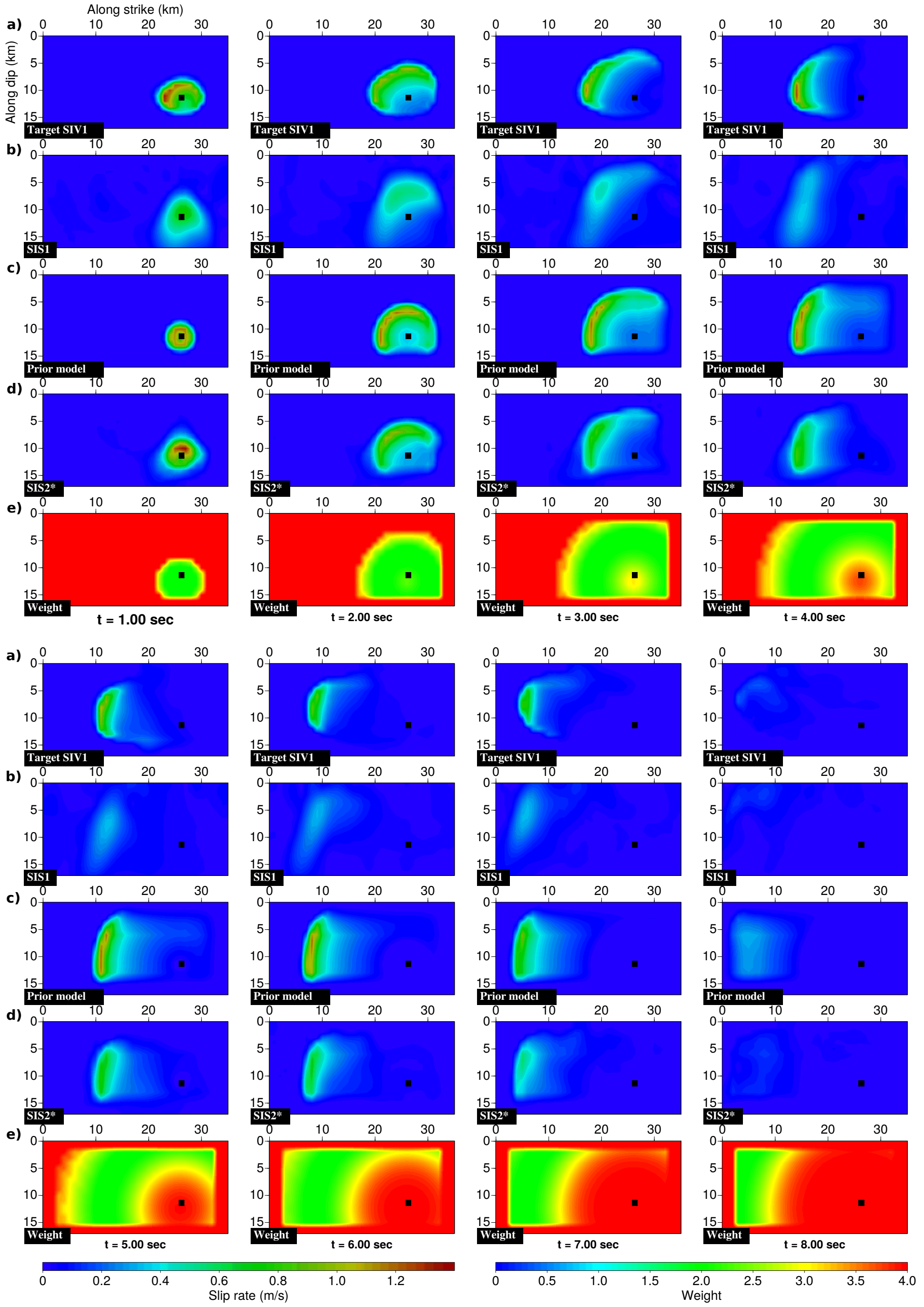

Figure 3.11: Comparison of the slip-rate evolution across the fault plane from a) the target model, b) resulting model from the SIS1 exercise (the worst according to Figure 3.10 and Table 3.2), c) the prior model, d) results from the SIS2* (preferred SIS model) and e) the weighting associated to the prior model. The model from panel b) is obtained without assuming any rake angle (allowed to vary between 150^o-210^o) or regularization/preconditioning. d) Includes regularization and preconditioning. Panels (c) and (e) show the prior model (simple concentric rupture vanishing toward the fault edges) and its associated weighting, respectively, that are used to obtain the model SIS2*. The prior information and weighting function allows to remove slip-rate at the fault boundaries and other unphysical rupture times: focusing the energy on the rupture front. The snapshots are taken at every second of the rupture history.

3.3.4 PIS Synthetic case SIV1

The following four exercises preserve the same time-space discretization, regularization configuration and preconditioning strategies of the exercises described in the previous section: here I simply substitute the acronym PIS instead of SIS, meaning that an evolutive selection of the data is going to be inverted. Exercises PIS1 and PIS2 are the two-component inversion where the rake angle is allowed to smoothly vary between $150^o - 210^o$. In the same way as before, PIS1* and PIS2* are exercises where the rake angle is fixed to its true value ($\lambda = 180^o$). These labels PIS2 and PIS2* refer to exercises where the prior information regularization term, and the depth-dependent model preconditioning and the data-gradient smoothing are applied.

The main difference between the SIS and PIS strategies is related to the data used at each stage of the inversion procedure. Different progressive time-windows are defined for mapping a limited time-space region of the source into a limited window of seismic signals. For the PIS, one has to specify these time-windows to consider at each receiver for the specific time-space source zone to be imaged. Therefore, a preliminary procedure has to be carried out to define these time-windows. By using an Eikonal solver (Podvin and Lecomte, 1991) for the wave propagation inside the velocity model, we define a concentric rupture zone starting from the hypocenter until the edges of the pre-defined fault geometry with an expected maximum rupture speed of 1.4 times the local shear wave velocity. Such over-estimation of the rupture speed prevents the concentration of energy at the hard upper-limits of the allowed time-space zone where the rupture is allowed to occur and admits possible super-shear ruptures. From these specific rupture times at each node of the fault, we define a synthetic rupture scenario by placing the beginning of generic-shape slip-rate functions at the correct rupture time for each node. Contrary to the rupture times estimated through the Eikonal solver, the shape and duration of the slip-rate functions of this synthetic rupture scenario are not crucial to correctly define the time-windows for each stage of the inversion. However, we recognize that the effective rise-time of these generic-shape slip-rate functions has to be close to the expected duration ($4 - 5$ s). An example of a concentric synthetic rupture with gaussian-shape slip-rate functions and an homogeneous final slip of 2 m is illustrated in Figures 3.12c and 3.12d. Using this synthetic rupture scenario, a direct forward modeling is performed to compute synthetic seismograms at all receiver locations. Then, we consider several progressively increasing rupture time-space zones and their corresponding incomplete seismograms computed at all receiver locations to define these time-windows specific to each receiver. By analyzing residual differences between complete and incomplete seismograms for each progressive time-space zone, we can detect the time after which residues are negligible, giving the final time we must consider for each rupture window. Figures 3.12a,b illustrates this time hashing procedure.

The wave propagation information from the pre-computed stress-state tensor allows a rough prediction of the time-windows not yet considered according to the analysis of the residues for a given inversion stage, as we can see in 3.12. As the source time-space region allowed to break spans, the incomplete prediction gets closer to the observed recording and the data time-windows extend faster. Therefore, regardless of the receiver location, the data time-windows are shorter at the beginning and their duration increases rapidly. We should mention as well that, because the inversion of the first data time-windows already provides a given prediction of the unexplained data, the following inversion stages need to explain only residues inside the new data time-windows as for iterative deconvolution (Kikuchi and Kanamori, 1991). The evolution of the misfit function is completely different from the SIS, because the data size is varying through stages. For the following exercises, nine time-space zones of the synthetic rupture are considered: they are (*i.e.* $0 - 1.0, 0 - 1.5, 0 - 2.0, 0 - 2.5, 0 - 3.5, 0 - 5.0, 0 - 7.0, 0 - 9.0$ and $0 - 10.0$ s).

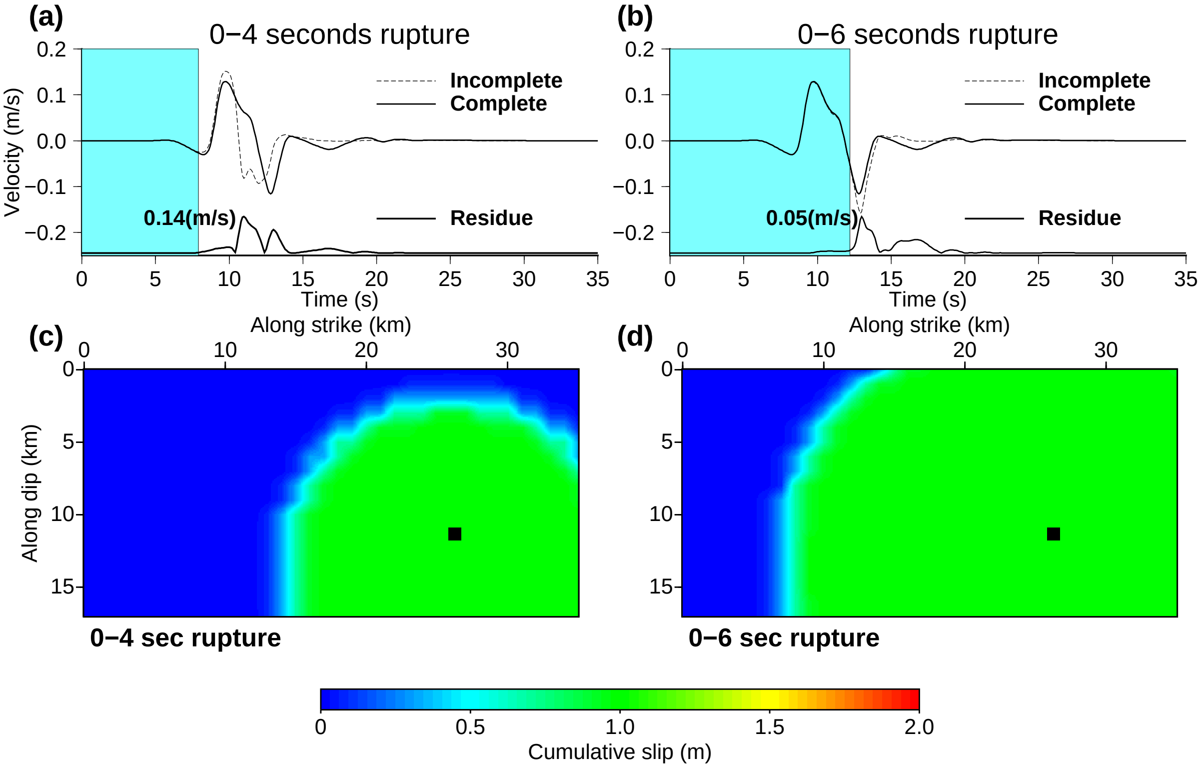

Figure 3.12: Progressively increasing data time-windows for each component at each station can be determined through the analysis of residues between complete and incomplete seismograms. On panels (c) and (d), the cumulative slip for different time-space intervals of a synthetic rupture is shown. The analysis of the residues between complete (recorded after the whole rupture of 9 seconds, solid black line) and incomplete recordings (for 4 s, and 6 s, dashed lines on (a) and (b)) define the blue time-window to be used during the PIS. The absolute residual value is plotted below traces in a different scale where the maximum value is written next to it. The black square on panels (c) and (d) represents the hypocenter location.

Finally, in order to better enforce causality into the prior information, results from every previous stage of the progressive inversion are used for updating the prior model $\underline{V}_p$ and the model weighting matrix $\underline{\underline{W}}_m$. The evolving prior model is built as an hybrid of the previous results and the initial prior model. Therefore, the slip-rate time functions from the initial prior model at the nodes that were inside the previously allowed source region are replaced by the reconstructed solution from the previous stage while the functions at the nodes outside this area are kept from the initial prior model. An additional 2D spatial smoothing (the same as the one applied to the gradient) has to be applied over the new hybrid prior model to avoid discontinuities. In order to ensure that the information from the following data time-windows do not affect considerably the results from previous inversion stages (*i.e.* to respect causality), the weighting matrix is also changed so that any difference between the current model and the hybrid prior model will be strongly penalized at the zones where the prior slip-rate functions were already replaced. I may highlight that this simple way of modifying and freezing the prior information is completely based on the causality of the phenomenon. In addition, this evolutive prior information prevents a strong influence of the prior model in the final reconstruction. In fact, this strategy reduces the impact of the initial prior model in such a way that we have to increase around 100% the value of the hyperparameter ϵ at each new inversion stage.

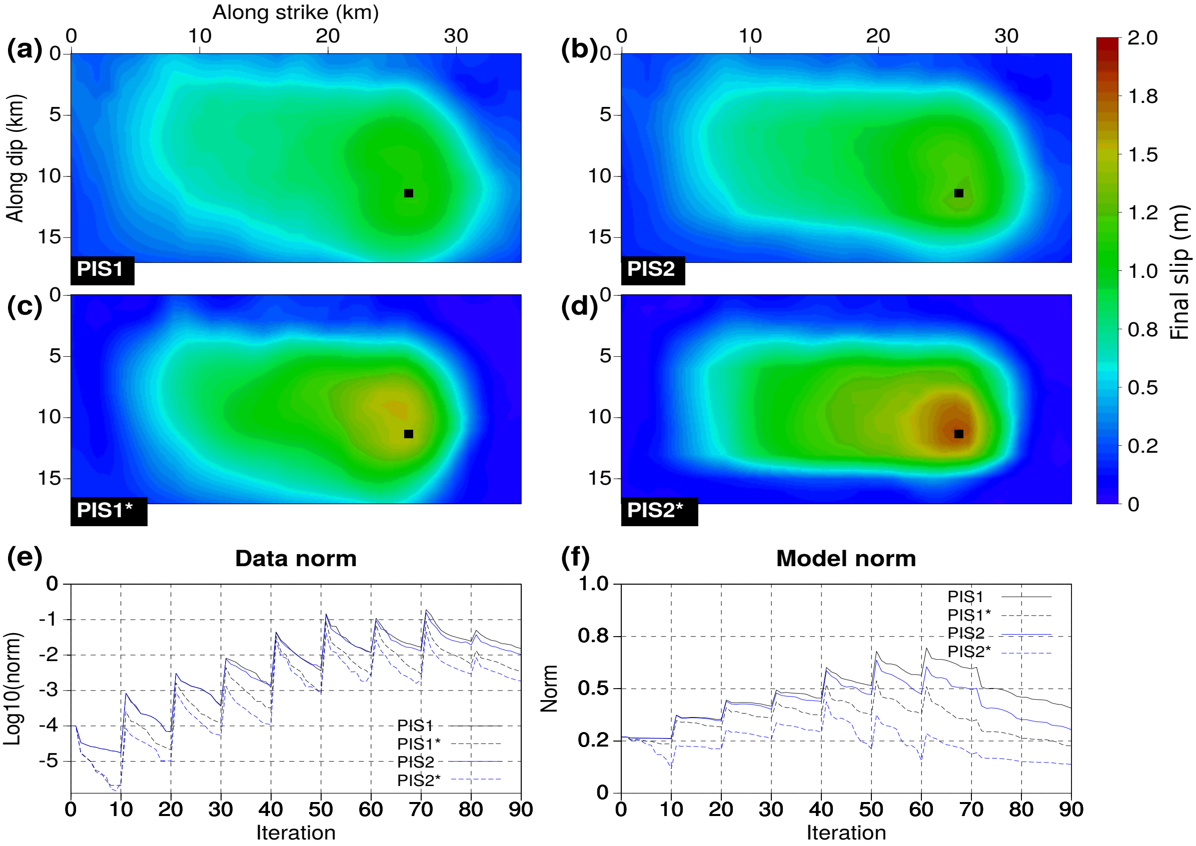

Figure 3.13: Same exercises as Figure 3.10 but applying the PIS. Results from panels (a) and (b) come from inversions that do not assume any rake angle (allowed to vary between $150 - 210^o$). Panels (b) and (a) are obtained from the PIS with and without regularization and preconditioning strategies, respectively. Panels (c) and (d) show the results from applying the PIS when the rake angle is kept fixed ($\lambda = 180^o$). Panel (c) does not consider any regularization while panel (d) applies regularization and preconditioning. Panels (e) and (f) illustrate the evolution of the data and model L2 misfit norm through the iterative process of inversion, respectively.

Once the data time-windows are defined, the progressive inversions for the four exercises follows the Algorithm 2. Due to the progressive build-up of parameters and data time-windows, the computational time of one iteration of the progressive inverse process at early stages is shorter (≈ 0.003 s) than an iteration assuming the final number of parameters to invert (≈ 0.02 s). Stopping criteria are those mentioned before for proper comparison between previous exercises.

The results from these four exercises applying the PIS without and with regularization terms are summarized in Figure 3.13 and Table 3.2. Please recall that the rake angle is always constrained in a limited range when both slip-rate components are inverted.

Compared to the results from the previous section, all the four PIS exercises fit better the data than their SIS counterparts. The saw shape of both misfit functions (Figure 3.13e,f) can be explained by the growth of the data records and the model parameters every time that new data have to be explained. We also recognize that cases PIS1 and PIS2 are able to better estimate the rake angle than the cases SIS1 and SIS2, as well as the seismic moment (Table 3.2). The PIS1 gets closer to the solution than its counterpart SIS1, decreasing its model misfit by 13% (see Figures 3.13f, 3.10f and Table 3.2). However, we do not see this amount of improvement of the data and model misfits when comparing PIS2 to SIS2. The better seismic moment estimation comes from a mitigation of the time-space ambiguity. When a SIS is carried out, even with regularization, the inversion is allowed to place values of the slip-rate at any time and at any place to enforce a better misfit reduction, which ends up with the over-estimation of the seismic moment. The improvement of the seismic moment estimation and the better rake reconstruction can be quite useful for real-earthquake applications for which the lack of information about local rake angles and the over-estimation of the seismic moment are recurrent problems.

The results from exercises where the rake angle is fixed are also closer to the solution than their SIS counterparts. Compared to SIS1*, the results from PIS1* improved $\approx 10\%$ in terms of model misfit while the data misfit is decreased by a factor three. Improvements are even more significant for the last exercise PIS2* that is the closest to the solution and to the observed data according to the misfits (Table 3.2). Furthermore, looking at the evolution of the data and model misfits of the PIS2* (Figure 3.13e,f) we recognize that, even at its maximum values, the progressive reconstruction of the slip-rate time-space history is never very far from the solution (43% model misfit) and the observed data time-window (4.5% data misfit). We interpret this feature as a correct progressive reconstruction of the rupture history.

Summarizing the results from the PIS exercises, it can be said that in general they fit better the data. The progressive introduction of the data allows an improved rake recovery, avoiding leakages of parameter values between space-time nodes. Moreover, restricting the zone of reconstruction of the slip-rate and freezing the previous results through the evolutive prior model expresses the causality feature between the slip-rate and the seismograms: phases coming from a specific zone of the source surface may arrive as energy packets with different propagation times at stations, leading to a natural hierarchy in the inversion procedure. Signals beyond the current inverted data window are already explained by the current active fault zone: only residues should be interpreted at the next stage, preventing the leakage to the next active zone, reducing drastically the spatial spread of information. We can see in Figure 3.15 an Illustration of the importance of this feature, where the cumulative slip estimated from the partially reconstructed solutions inverted from shorter data time-windows ($0-4$ and $0-7$ seconds) are shown as well as the predicted unrecorded data.

The time evolution of the reconstructed slip-rate time-space history from the best approach (exercise PIS2*) is shown in Figure 3.16. The reconstructed slip-rate shows an overall under-estimation compared to the true model. However, notice that such underestimation gets worse when the rupture front goes far from the hypocenter (snapshots at $t = 6.00$, $t = 7.00$ and $t = 8.00$ s Figure 3.16). In general, the time-space leakage of the solution is much less near the hypocenter and the origin time, thanks to the reduced number of parameters involved at earlier stages of the progressive inversion. When the progressive inversion tries to solve for nodes far away from the hypocenter, the time-space leakage increases because more parameters are considered, as for the SIS case. This is also true at the end of the rupture time history.

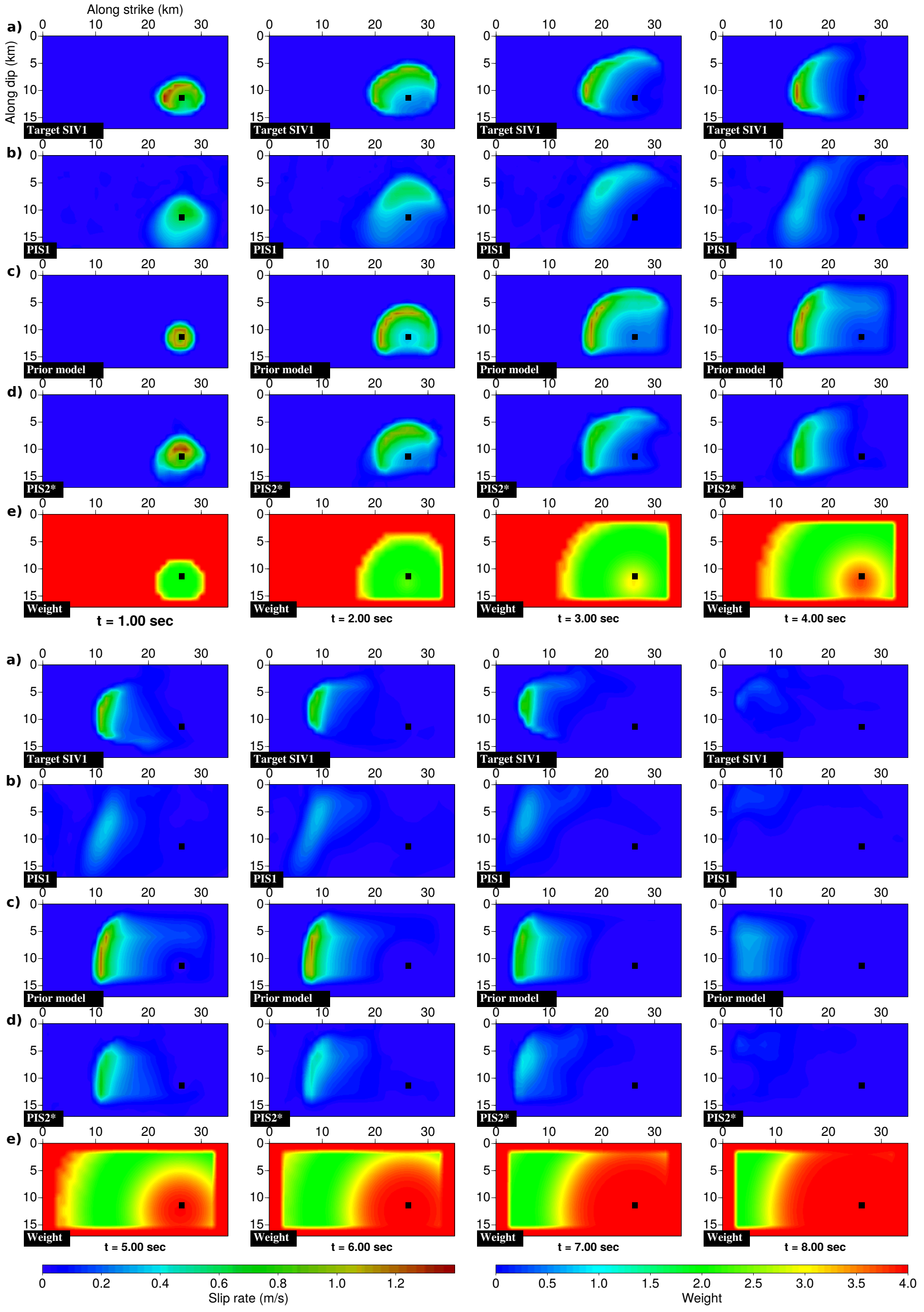

Figure 3.14: Comparison of the slip-rate evolution across the fault plane from a) the target model, b) resulting model from the PIS1 exercise (the worst PIS exercise according to Table 3.2), c) the prior model, d) results from the PIS2* (preferred PIS model) and e) the weighting associated to the prior model. The model from panel b) is obtained without assuming any rake angle (allowed to vary between 150^o-210^o) or regularization/preconditioning. d) Includes regularization and preconditioning. Panels (c) and (e) show the prior model (simple concentric rupture vanishing toward the fault edges) and its associated weighting, respectively, that are used to obtain the model PIS2*. The prior information and weighting function allows to remove slip-rate at the fault boundaries and other unphysical rupture times: focusing the energy on the rupture front. The snapshots are taken at every second of the rupture history.

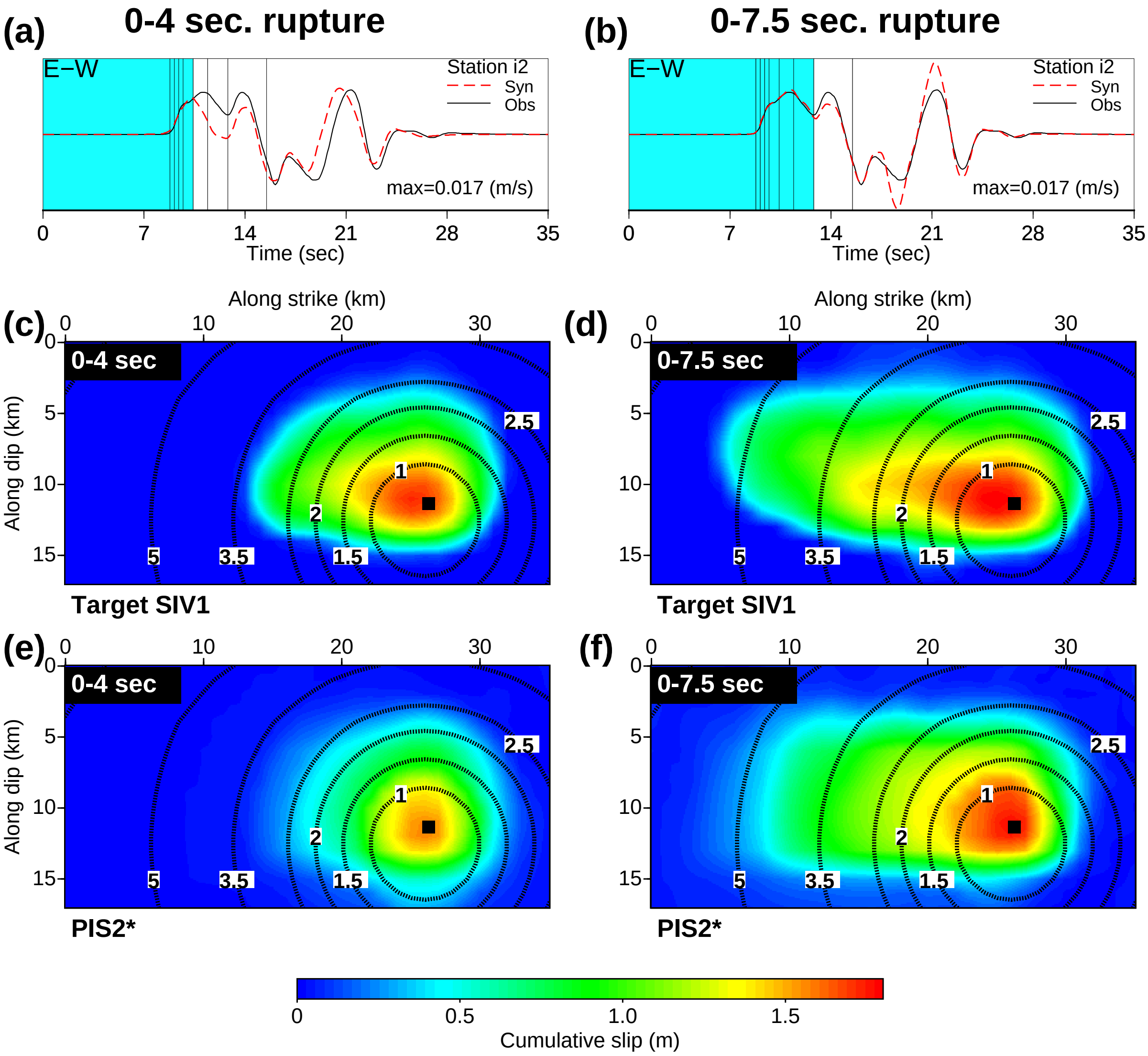

Figure 3.15: Comparison between cumulative slip distributions coming from the filtered version of the SIV1, panels (c) and (d), and the ones obtained from the PIS2*, in panels (e) and (f), which are obtained for the inversion of two different limited data time-windows illustrated in panels (a) and (b). Panels (a) and (b) show two different data time-windows used (blue colored window) at receiver location "i2" (see Figure 3.7b) to invert for the slip-rate time-space history for time intervals of $0 - 4$ s and $0 - 7.5$ s. Notice that, by inverting a small amount of data (blue colored data windows), we are able to predict waveforms that have not yet been used (data outside the colored windows) because delayed by the propagation. Dashed black lines overlaying the slip distributions illustrate the increasing allowed 2D area where the rupture is allowed to happen at every time interval ($0 - 1, 0 - 1.5, 0 - 2.0, 0 - 2.5, 0 - 3.5, 0 - 5.0, 0 - 7.0, 0 - 9.0$ s). Vertical black lines in panels (a) and (b) represent the time limit of the data time-windows for each stage of the PIS.

As a partial conclusion, we can see in Figure 3.17 a final comparison between the best results from the SIS and PIS work-flows, both applying regularization and preconditioning strategies. Results form the PIS2* spread less across the fault than the ones from the SIS2*, counter-balanced by the time evolution. In both cases, the zone of maximum slip is correctly located. However, the PIS2* seems to have a better along-strike and along-dip behavior. The improved behavior of PIS2* can be seen as well in Table (3.2) comparing data and model misfits as well as the estimated seismic moment. The SIS2* fits the target almost as well as the PIS2* (17% versus 13%) but the data misfit is 19 times larger than the one from the PIS2* (3.54% versus 0.18%) and the seismic moment is more over-estimated (11.6% versus 0.1%).

The results from both strategies are satisfactory. However, the PIS2* case is preferred, because poor acquisition design and less accurate velocity model could favor the PIS work-flow which is expected to be more robust by reducing the number of involved parameters at each inversion step. Moreover, as we can see in Figure 3.15, this strategy opens the door to quasi-real-time implementations and assimilation techniques for uncertainty estimation that were not considered in this section.

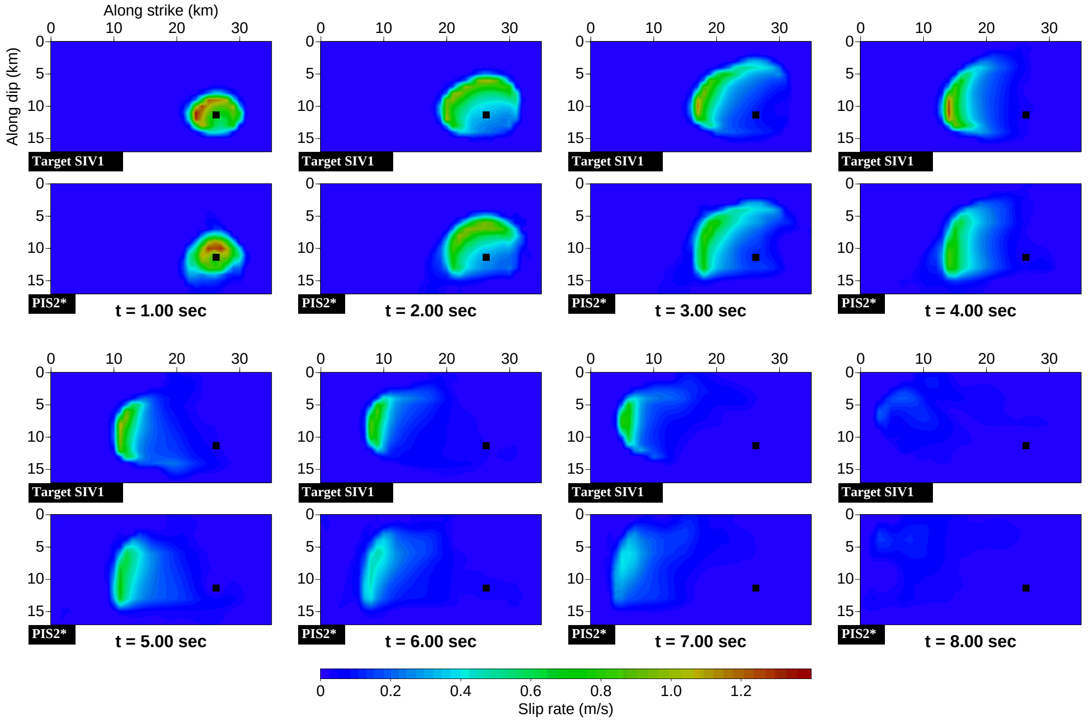

Figure 3.16: Comparison between the filtered version of the SIV1 (0-1 Hz) and the resulting slip-rate spatio-temporal distribution obtained from the PIS2*. For each snapshot, the corresponding rupture time is shown at the bottom of each snapshot couple.

Table 3.2: Summary of the results for the SIS and PIS cases applied to the filtered SIV1.

	M_0 $\times 10^{19}$(Nm)	Data misfit (%)	Model misfit (%)	Mean $\lambda \pm \sigma_\lambda$ (^{o})
SIV1-filtered	1.052			180
SIS1	1.157	3.35	53.02	186.47 ± 20.61
SIS2	1.225	1.42	28.16	181.73 ± 9.08
SIS1*	1.153	0.95	32.28	180
SIS2*	1.174	3.54	17.03	180
PIS1	1.175	1.52	40.68	182.66 ± 8.59
PIS2	1.128	1.03	30.34	181.31 ± 3.23
PIS1*	1.103	0.34	22.68	180
PIS2*	1.053	0.18	13.83	180

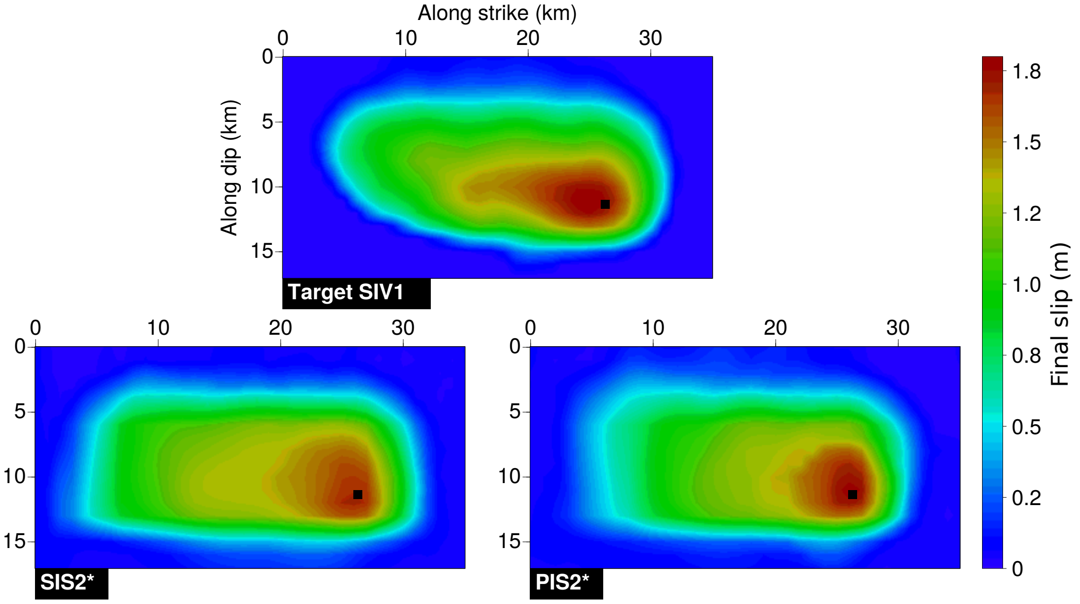

Figure 3.17: Final slip comparison between the filtered version of the SIV1 (0-1 Hz) and the solutions for the cases SIS2* (bottom left) and PIS2* (bottom right). While these two results achieve comparable final data and model misfit, the PIS2* shows a better along-strike final slip distribution. Both inversion results shifted the maximum slip zone by $\approx$ 1 km along dip direction.

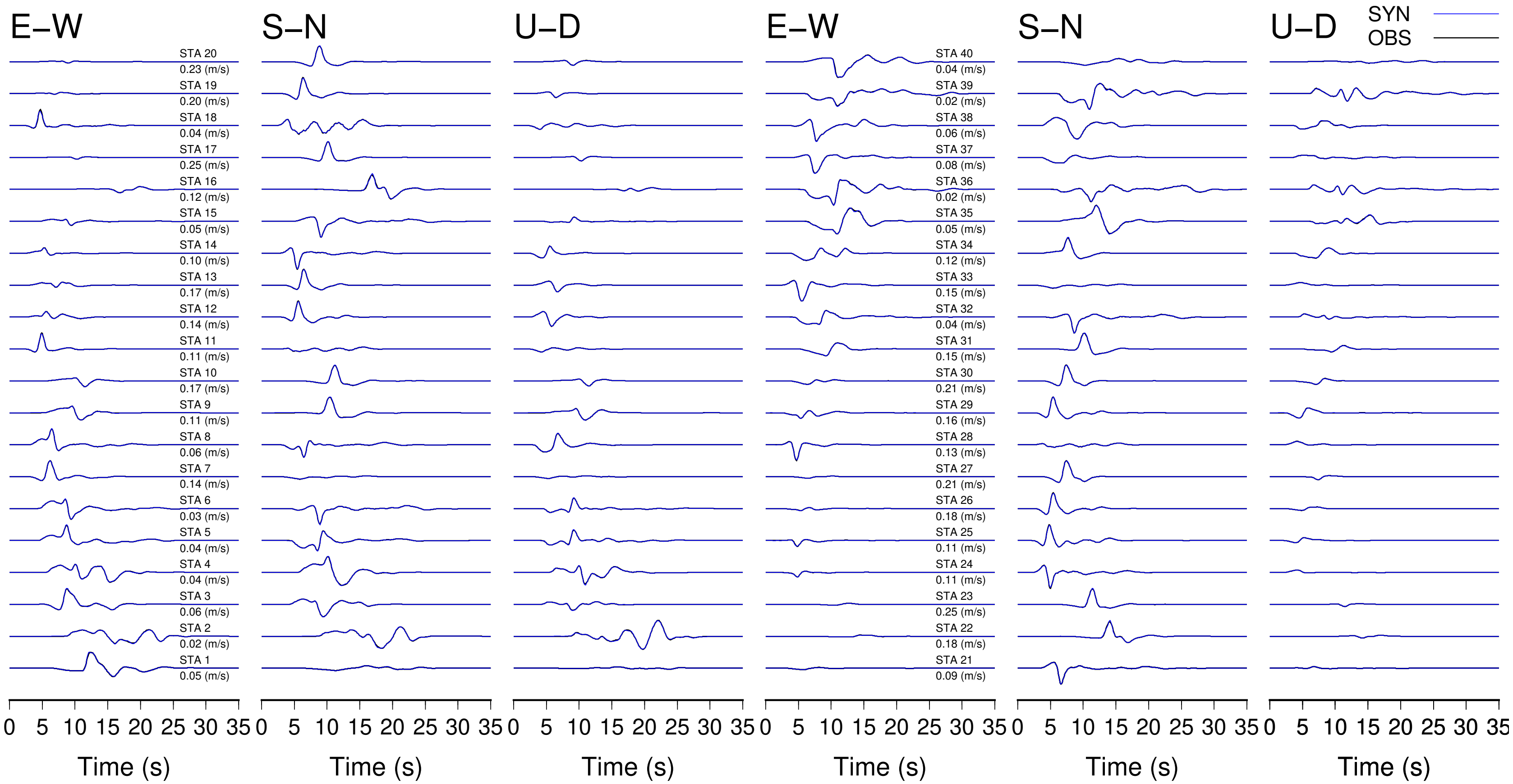

Figure 3.18: Final comparison between synthetic (solid blue line) and the observed (solid black line) seismograms for the resulting model from the PIS2* exercise. No significant difference between the waveforms can be seen. The station number and the absolute maximum amplitude observed at that receiver location (used to normalized the three traces) is written next to E-W component.

3.4 Synthetic case: Source Inversion Validation exercise 2a (SIV2a)

The material presented in this section has been written based on the work developed by Solène Jouanny during her Master 1 research internship at the Institut des Science de la Terre:

- Jouanny, S., Sánchez-Reyes, H., Virieux, J., Métivier, L. (2018). Inversion cinématique pour une source sismique. Master 1 Géophysique 2017/2018 Rapport de Stage. Université Grenoble Alpes

3.4.1 SIV2a Description

The Source Inversion Validation exercise 2a (SIV2a), is a further step in complexity compared to the previously mentioned SIV1 (Section 3.3). In contrast with the SIV1, the SIV2a slip and slip rate distributions across the fault geometry are more complex and heterogeneous (Figure 3.19b) than for the SIV1 case. Moreover, contrary to the SIV1, in this case the dip and rake angles are only approximately known, but both are constant across the fault. The dipping angle of this normal faulting exercise is $\delta \approx 45 \pm 5^o$ with a known strike angle $\phi = 90^o$ and an oblique rake $\lambda \approx 240 \pm 10$. As well as for the SIV1, in this case the rupture did not reach the surface. The fault dimensions are ≈ 40 km along strike and ≈ 20 km along dip. The estimated seismic moment is $M_0 \sim 3.5 \times 10^{19}$Nm (Mw7.0). In addition, the hypocenter location is $x = -4.57$ km; $y = -9.54$ km and a depth of $\approx -10 \pm 1$ km. Variations of the rupture velocity across the fault are also included. Finally, no detailed time history is provided for the SIV2a, only a reduced number of parameters are provided (final slip, rupture time, rise time and rake angle) at discrete positions across the fault.

For the SIV2a, the acquisition configuration and the embedding velocity-density medium are exactly the same as for the SIV1 (see Figures 3.19 3.7 and Table 3.1). As well as for the SIV1, other extra 16 sites are used as "blind prediction sites". At those sites the ground motion recordings are not used during the inversion but the waveforms are forward predicted based on the preferred source model. In addition, the SIV2a has an interesting difference with the SIV1, this case includes synthetic GPS data at the 40 receiver locations (Figure 3.19d). Even though the SIS and PIS strategies do not currently include the joint inversion of geodetic data, a forward prediction of the available GPS data is provided for the preferred solution for this exercise as a way to cross validate the results.

3.4.2 Settings: Discretization, regularization design and preconditioning strategies

The preferred discretization for all the inversion exercises of the SIV2a is the same as the one described in Section 3.3.2: a spatial node discretization of 1 km along the strike and dip directions, while the time history at each spatial node is discretized every 0.25 seconds. Under this configuration, and assuming a fixed rake angle across the fault, the source model to reconstruct has 40 [nodes along-dip] $\times$ 20 [nodes along-dip] $\times$ 65 [time-samples] = 52000 unknowns. In contrast, as well as for the SIV1, the number of observations is 141 [time-samples] $\times$ 40 [receivers] $\times$ 3 [components] $=$ 16920. Therefore, SIV2a has approximately twice the number of unknowns than the SIV1.

For the SIV2a case, four different exercises are presented. The first two exercises presented in Section 3.4.3 apply the SIS while the other two carried out in Section 3.4.4 are performed using the PIS. All these exercises assumed a fixed value of the rake angle. I prefer to consider a fixed rake value across the fault plane due to the large number of unknowns involved. All the inversion exercises here reported assumed a dipping angle of 45^o. Further investigations about the optimal dipping angle and

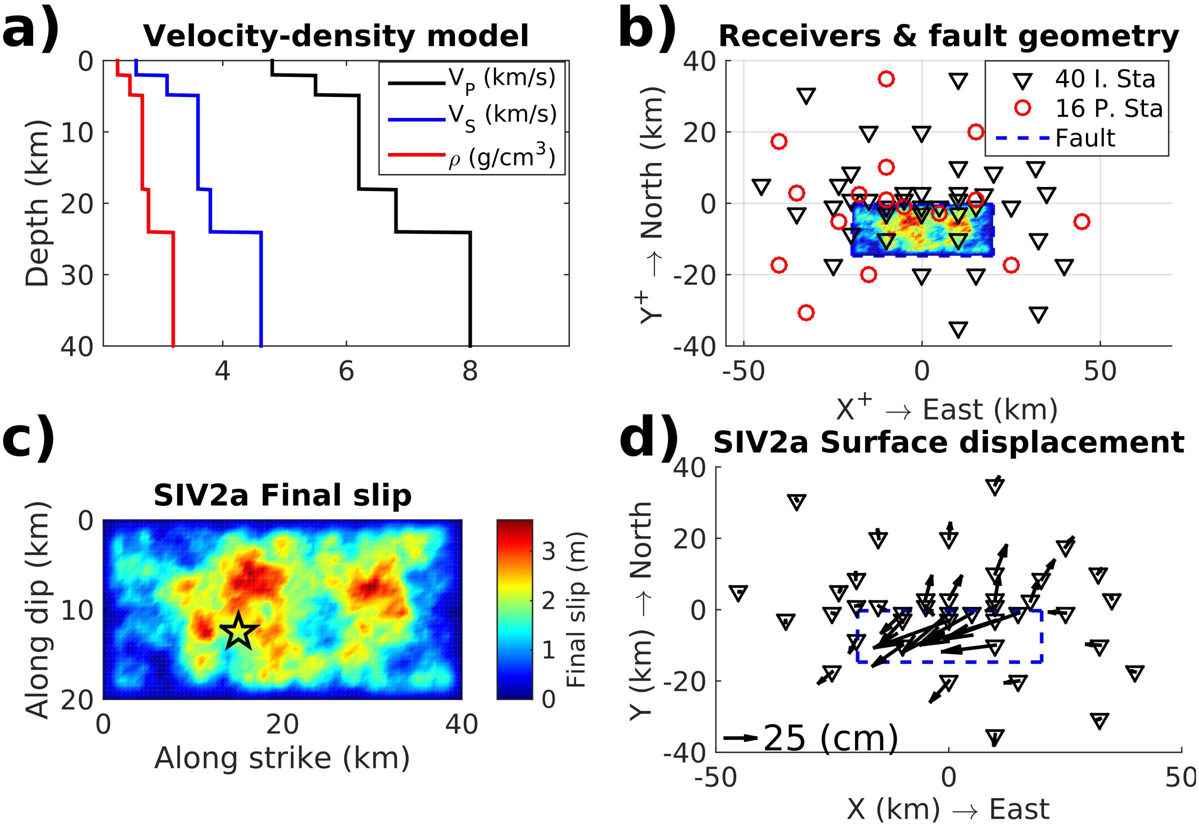

Figure 3.19: Summarized description of the SIV2a. (a) Velocity-density structure of the embedding medium. (b) Surface projection of the fault geometry (3321 fault-odes) and the locations of the 40 receivers used for the inversion (40 I. Sta) and 16 used to verify the predicted velocity recordings of the inversion results (16 P. Sta). (c) Final slip distribution along the fault after ≈ 16 seconds of rupture. (d) Surface deformation (black arrows) observed at the 40 receiver locations. Notice the normal faulting behavior well illustrated by the surface deformation. The star on panel c) represents the hypocentral location. No detailed time history is known for the SIV2a to be shown as in Figure 3.7d. Information taken from Mai et al. (2016).

the uncertainties related to this choice are left for a future work. The exercises here presented assum $\lambda = 250^o$ which is a value that was found as optimal after a grid search investigation where the final data misfit and final slip comparison between the known solution (only the final slip is provided) and the resulting models from several inversions considering fixed rake angles ranging from 230^o to 250^o were compared.

The first exercise, identified as SIS1, refers to an exercise where the SIS is applied without taking into account any model regularization or preconditioning. The second exercise, called SIS2, preserves the same configuration and inversion strategy as the SIS1 but includes model regularization and model preconditioning. The third and fourth cases are the PIS counterparts of the first two exercises. Consequently, the case PIS1 is the one where the progressive strategy is applied without any regularization or preconditioning. Finally, the PIS2 includes the model regularization and preconditioning into the progressive inversion strategy.

In order to include model regularization for cases SIS2 and PIS2 a prior model and its associated covariance matrix were designed. The prior model was constructed as a concentric rupture with an homogeneous final slip of 1.5 m and an anomalous gaussian shape zone with a maximum slip (2.3 m) far from the hypocenter: ≈ 5 km to the East of the hypocenter along the strike direction and ≈ 6 km on the updip direction (Figure 3.20). This off-hypocenter expected large slip is taken as a prior information coming from an interpretation of the observed surface displacement that exhibits a larger amplitude to the eastern end of the fault (Figure 3.19d). I expect that placing this prior zone of maximum slip at that location will reduce the overestimation of the slip near the hypocenter. As detailed in the previous Section, the amplitude of the slip rate vector of this prior model is set to rapidly vanish at the fault boundaries (see Figure 3.20). The rupture front of this prior model was set to a 70% of the local shear wave velocity and the rupture times were computed by an Eikonal solver (Podvin and Lecomte, 1991). The local slip-rate functions were assumed to be Yoffe-type with an effective rise time of 3 seconds, final slip of either 1.5 m (homogeneous part), 2.5 m (inside the gaussian anomaly) or decreasing toward the fault boundaries. The associated model weighting matrix was designed in such a way that, at the fault edges, any difference from the prior model (set to be zero at those zones) is strongly penalized. In the same way, this matrix penalizes any slip occurring before and after the time when the expected rupture front has to pass (see snapshots on Figure 3.20). These time-space limits of the expected rupture zone are obtained considering a faster rupture front propagating across the fault at 90% V_S (upper limit) and a 90% V_S + 3 seconds (lower limit). Several tests with different values for ϵ, ranging fro 5×10^{-6} to 5×10^{-4} were performed. At the end, the hyperparameter ϵ for the case SIS2 was fixed to 1×10^{-5} as it correctly balanced the regularization term and the data misfit while the resulting model was the closest (when applying the SIS) to the provided final slip distribution.

For the model preconditioning, two strategies were used. The first is related to the depth preconditioning. After several tests, the preferred value for the depth coefficient from equation 3.19 was set to $c = 0.52$. This value was determined carrying out several inversions with c-values ranging from 0 to 2 and the preferred value was selected as the one that minimized the norm between the inverted final slip distribution and the one provided as a solution. A spatial smoothing operator was also considered. A 1 × 1 km smoothing operator was applied. Longer spatial operators were also tested but the rupture was strongly blurred and the data misfit increased significantly.

For cases PIS1 and PIS2 11 time-space model and data windows were predefined before running the progressive inversion. These windows were determined as described in Section 3.2.4 and the resulting SIS2 source model was used as the reference for the estimation of the window limits (i.e. 0–0.5, 0–1.5, 0–2.5, 0–3.5, 0–4.5, 0–5.5, 0–6.5, 0–8.5, 0–9.5, 0–11.0, 0–16 seconds of rupture). Finally, for the case PIS2, the regularization is applied under the same configuration as for SIS2 but instead of using the same prior model (Figure 3.20a) I decide to use the resulting model from the SIS2 exercise (Figure 3.21f). The prior model was changed in order to incorporate some of the knowledge gained from the previous exercises. In any case, as it was shown in Section 3.3.4, the prior model has a smaller impact on the results from the progressive strategy. Finally, for case PIS2, the hyperparameter ϵ is set to increase 1.5 % at each stage of the progressive inversion (each new time window). As in Section 3.3.4, the solution from the inversion of the first data time windows is frozen by increasing significantly the model weights at those fault zones once the inversion was performed there. The increment of the weighting matrix is set to start after the inversion of the third window (0–3.5 seconds of rupture).

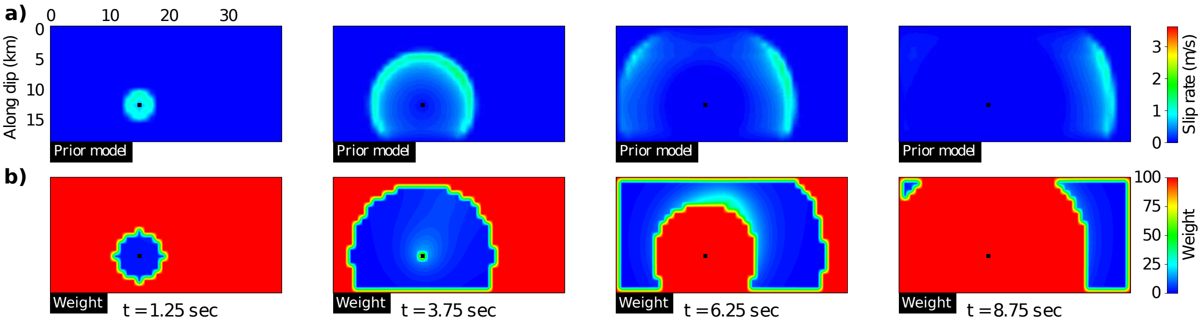

Figure 3.20: Evolution of the designed a) prior model, $\underline{V}_p$, and b) weighting matrix, $\underline{\underline{W}}_m$. These two terms are used as regularization terms during the inversion of the SIV2a. The snapshots shown for both panels are at 1.25, 3.75, 6.25 and 8.75 seconds of rupture (from left to right). The rupture front of the prior model travels at 70% of the local shear wave velocity, while the weighting matrix limits allows rupture fronts traveling at 90% V_S (upper limit) and 90% V_S + 3 seconds (lower limit). The slip-rate functions assumed for the prior model are Yoffe-type functions. The black square represents the assumed hypocentral location. Notice the strong values of the weighting matrix at the edges and at fault zones where the rupture is not expected to occurred at specific times.

3.4.3 SIS Synthetic case SIV2a

The resulting final slip from the first inversion exercise, SIS1, where the standard strategy is applied with no regularization or preconditioning are quite far from the provided final slip solution. By comparing the final slip from the SIV2a and from the SIS1 (Figure 3.21a,b), it can be seen that the slip gets concentrated at the fault boundaries. This behavior could drive us to change the fault dimensions (e.g. extending it in the updid and easter directions). However, I preferred to apply the depth preconditioning and model regularization to reduce this behavior that could be also seen as an artifact of the surface acquisition. The maximum slip from SIS1 is located at the fault boundaries and is more than two times larger (9 m) than the expected (3.6 m). For comparison purposes, the final slip distribution on Figure 3.21b is saturated up to 4 m. An interesting feature is that at the shallow west border of the fault the slip is significantly less. This can be interpreted as a continuous slip accumulation form the inversion strategy along the direction where the maximum slip occurred.

Figure 3.21d shows a reconstructed slip-rate evolution across the fault plane of the provided solution of the SIV2a. Such reconstruction is done by assuming Yoffe-type functions at each spatial node following the provided parameters in the solution: rupture time, effective rise time and final slip. Comparing the slip-rate evolution from the SIS1 and the one from the SIV2a (Figures 3.21d,e), it can be seen that the slip-rate from the SIS1 is quiet heterogeneous and that several spatial nodes break more than one time, which is unphysical. In addition, the slip-rate distribution at $t = 0$ is not null, meaning that in that model the slip is occurring before the rupture started. However, notice that the SIS1 was able to reconstruct a propagating rupture front even when no regularization was applied. Therefore, I expect that the regularization and preconditioning strategies will reduce most of these unphysical features.

In contrast with the SIS1, the results from the regularized SIS2 are closer to the final slip solution of the SIV2a. The maximum slip from SIS2 (3.9 m) is a little larger to the solution (3.6 m) and it is much less than the one from SIS1 (9 m). The SIS2 presents an attenuated final slip at the upper fault edge when it is compared to the SIS1. At the other fault boundaries the slip vanishes rapidly in agreement with the applied regularization. For the SIS2, there are still some nodes that break several times, but

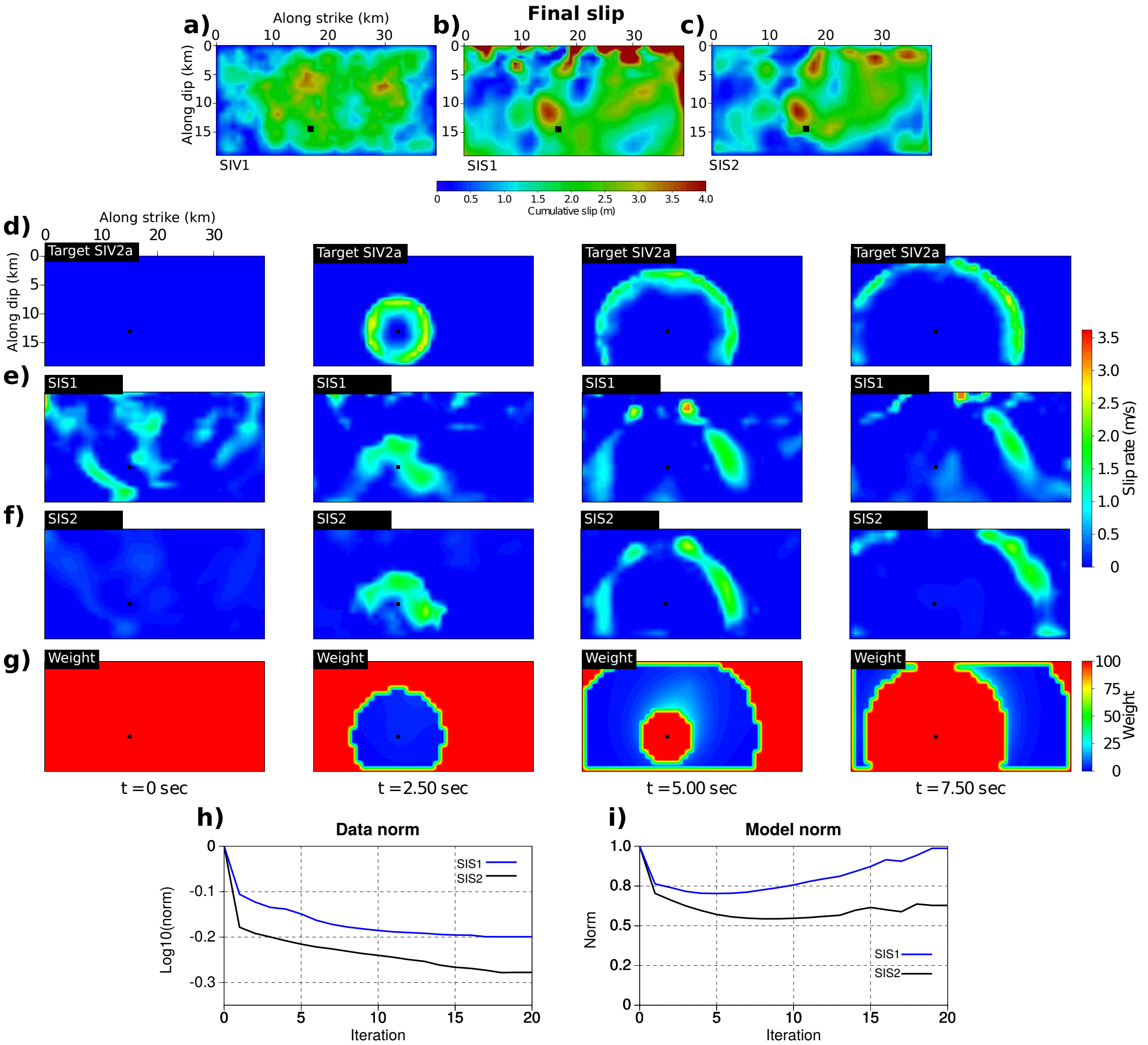

Figure 3.21: Comparison of the final slip distribution from a) the provided SIV2a solution, b) the SIS1 and c) the SIS2 inversion exercises. Snapshots of the slip-rate evolution across the fault plane of d) the reconstructed solution for the SIV2a based on the provided parameters, e) the SIS1, f) the SIS2 inversion exercises and g) the weighting matrix. On d), e) and f) the black dot represents the hypocentral location. Comparison of the h) data norm and i) model norm with respect to the reconstructed time history (not the true solution) for the SIS1 and SIS2 exercises are shown at the bottom.

the amplitude of those unphysical events is drastically reduced in contrast with the SIS1 (e.g. Figures 3.21e,f at $t = 0$). The reduction of those artifacts helped to focus most of the energy on the rupture front as shown in Figures 3.19e,f.

In terms of data and model misfit, SIS2 performed better than the SIS1. However, the conclusions drawn from the model misfit have to be taken carefully. The model misfit reported in Table 3.3 and on Figure 3.21i are based on the norm L2 between the inverted model (SIS1 or SIS2) and the reconstructed version of the SIV2a. The true time-space history from the SIV2a is unknown and this affects the estimated model norm reported. For instance, after the first 5 iterations the model norm of the SIS1 starts to increase, while the norm of the SIS2 starts increasing after the first 10 iterations (see Figure 3.21i). Consequently, a large final model norm does not necessarily guarantee results far from the true solution. In any case, the SIS2 adjusted much better the data (10% less misfit than the SIS1).

In terms of seismic moment, the SIS1 (M_0 =5.02×10^{19}Nm) overestimated the value provided in the SIV2a solution (M_0 =3.5×10^{19}Nm). This overestimation might be due to the large slip at the upper boundary (9 m) and the several times that some nodes were emitting energy during the whole rupture duration (unphysical features). The SIS2, as seen in Table 3.3, has a similar seismic moment to the expected value.

I shall now present the results from the two inversion exercises where the progressive inversion strategy is applied to the SIV2a.

3.4.4 PIS Synthetic case SIV2a

The results obtained from the progressive exercises with (PIS2) and without (PIS1) regularization and preconditioning are Summarized in Figure 3.22 and in Table 3.3. The final slip exhibited by PIS1 has a maximum slip amplitude of 7.9 m at the upper most edge of the fault (Figure 3.22b). Even if this large slip is far from the provided solution (3.6 m), it is 1 m less than the results from exercise SIS1 (9 m). The large slip at shallow depths from PIS1 follows the same behavior observed in the SIS1. However, significantly less shallow slip at the western side was found by PIS1 than by the SIS1. It is also important to notice that at t=0, the slip-rate evolution obtained from PIS1 has less amplitude than the SIS1. This significant decrement of the slip-rate amplitude at the nodes that broke several times (unphysical) impacted all the time history of the PIS1. In terms of data misfit, SIS1 and PIS1 achieved almost the same results (63.11% of SIS1 versus 63.12% of PIS1). However, the estimated seismic moment of PIS1 is much less than the one from SIS1 and it is much closer to the provided solution (see Table 3.3). Even if the reconstructed version of the SIV2a might mislead the interpretation of the model misfit evolution (Figure 3.22i), at its final iteration the model PIS1 is $\approx$ 32% closer to the SIV2a than the SIS1.

In contrast with the results from the PIS1, the time evolution of the slip-rate across the fault obtained from the exercise PIS2 exhibits less unphysical behaviors. The PIS2 has less slip at shallow depths and there is less slip-rate amplitude out of the rupture front than for the PIS1. In terms of norms, the PIS2 is the best result. However, the data and model norms from the PIS2 are only $\approx$1% and 4% better compared to the SIS2. According to the estimated seismic moments, the SIS2 model was closer to the solution, but only for $\approx$ 0.8%.

Looking at the results from the SIS2 and the PIS2 cases for the SIV2a, it is very difficult to distinguish which is the best result. Both solutions are acceptable and they just illustrate the non-uniqueness of the solution to this problem. However, it can be argued that the PIS2 has more pros than the standard strategy. The respect of the causality of the phenomenon and the Consequently available rough prediction of the future wave packets to be recorded being the most important of these advantages.

To end this section, Figures 3.23 and 3.24 show the comparison between the synthetic and observed seismograms at the 40 sites used for the inversion and at the 16 sites only used for waveform prediction. Finally, Figure 3.25 offers a comparison between the observed and predicted surface deformation estimated for the preferred final slip distribution coming from the PIS2 computed through a modified version of the code EDGRN/EDCMP (see Section 2.2 for details) from Wang et al. (2003).

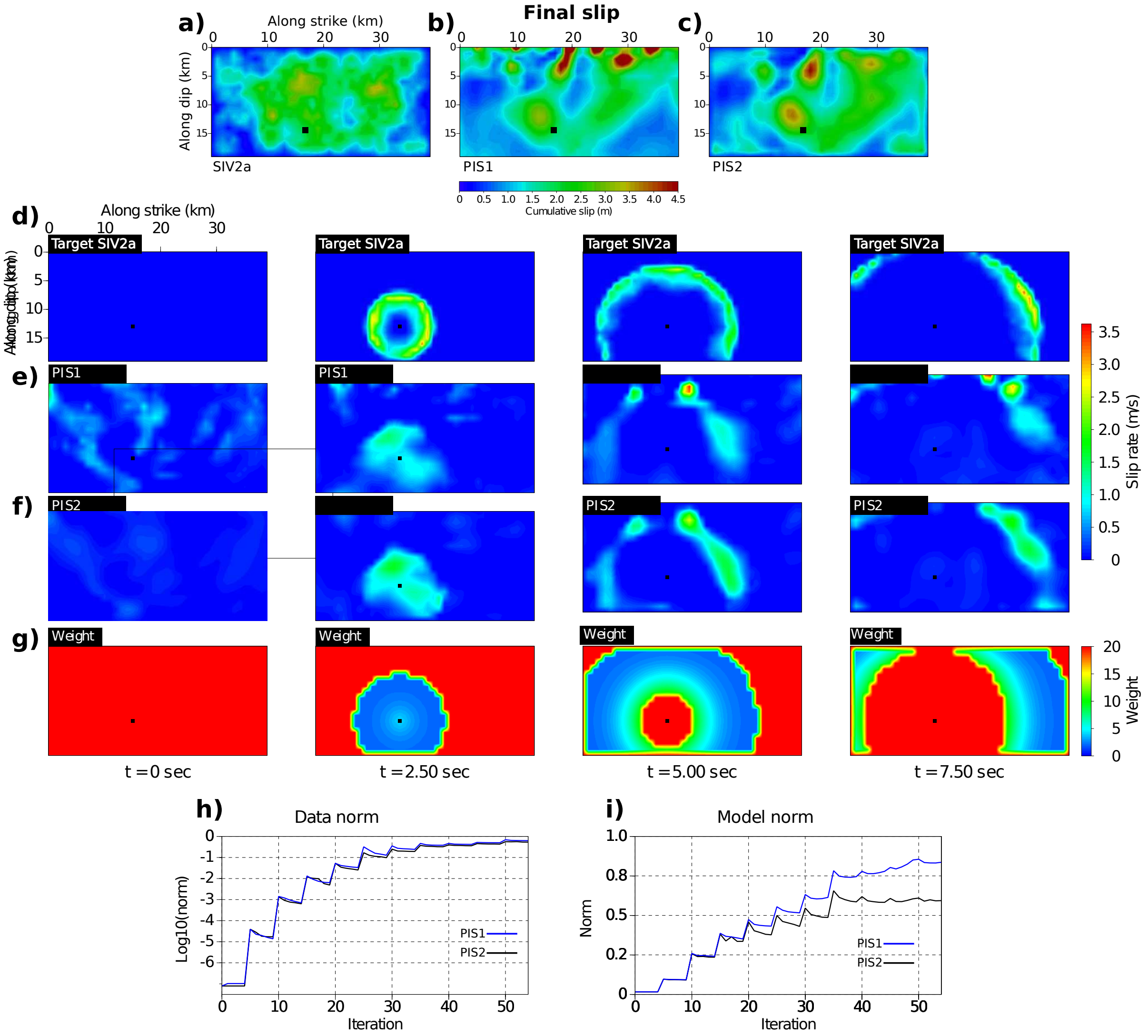

Figure 3.22: Comparison of the final slip distribution from a) the provided SIV2a solution, b) the PIS1 and c) the PIS2 inversion exercises. Snapshots of the slip-rate evolution across the fault plane of d) the reconstructed solution for the SIV2a based on the provided parameters, e) the PIS1, f) the PIS2 inversion exercises and g) the weighting matrix. On d), e) and f) the black dot represents the hypocentral location. Comparison of the h) data norm and i) model norm with respect to the reconstructed time history (not the true solution) for the PIS1 and PIS2 exercises.

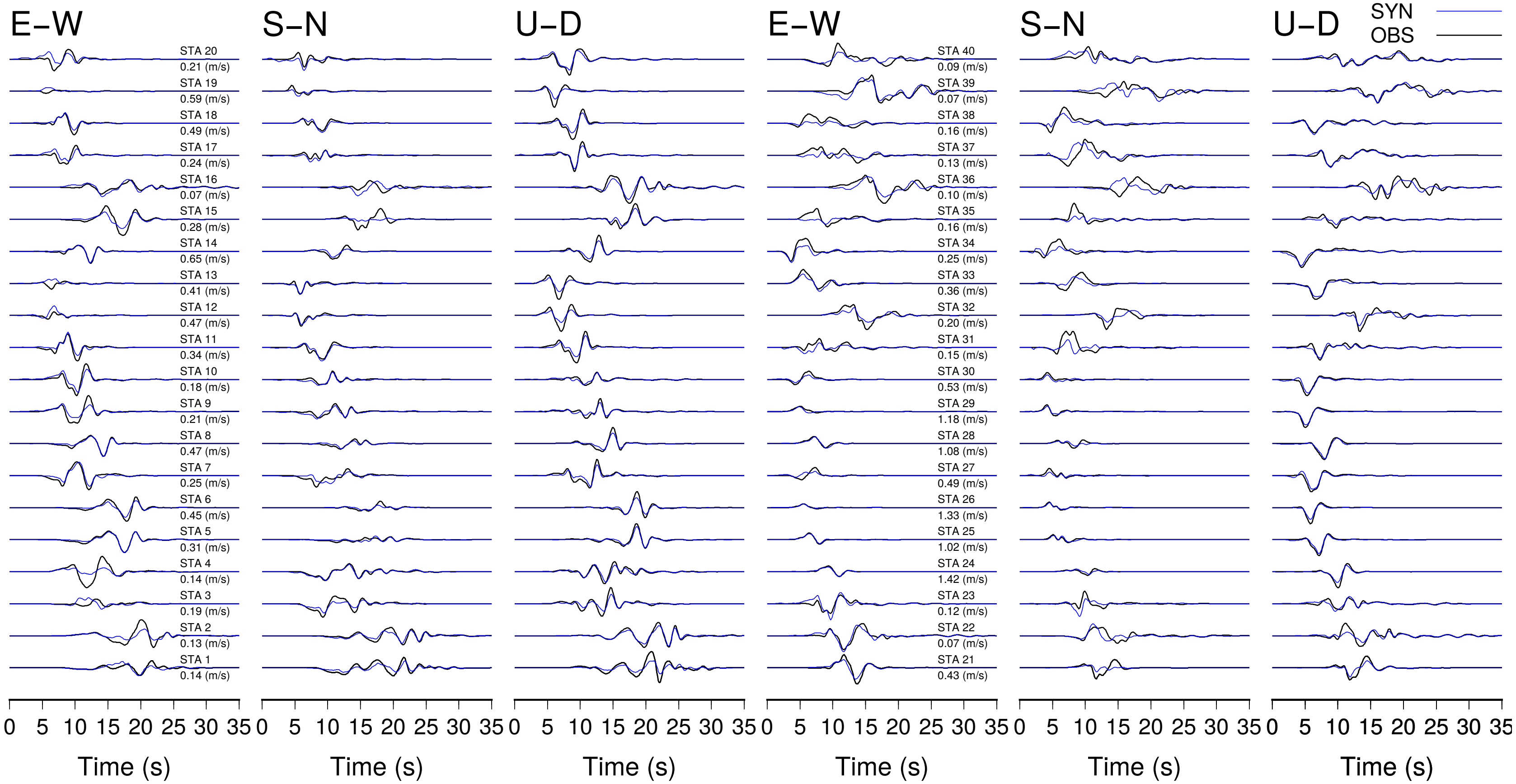

Figure 3.23: Comparison between synthetic (solid blue line) and the observed (solid back line) seismograms for the resulting model from the PIS2 for the SIV2a exercise. The station number and the absolute maximum amplitude observed at that receiver location (used to normalized the three traces) is written next to E-W component.

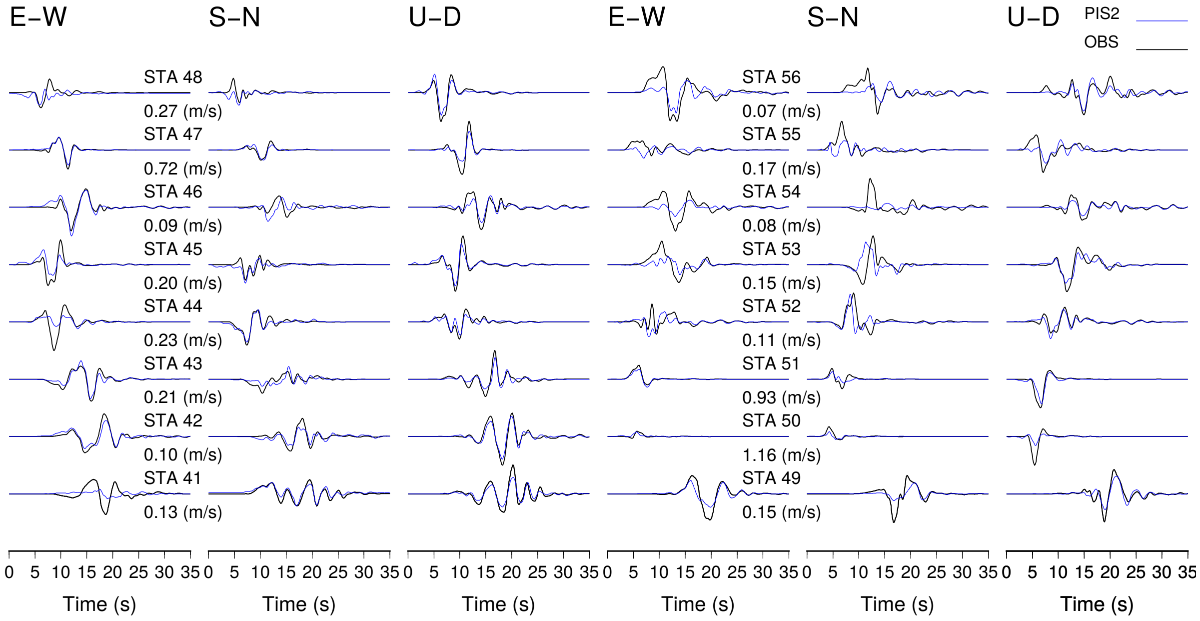

Figure 3.24: Comparison between synthetic (solid blue line) and the observed (solid black line) seismograms at the 16 sites not used for waveform inversion. This comparison is made for the seismograms corresponding to to the preferred final model PIS2 for the SIV2a exercise. The station number and the absolute maximum amplitude observed at that receiver location (used to normalized the three traces) is written next to E-W component.

Table 3.3: Results for the SIS and PIS cases applied to the reconstructed version of the SIV2a.

	M_0 $\times 10^{19}$(Nm)	Data misfit (%)	Model misfit (%)	Mean $\lambda \pm \sigma_\lambda$ (^{o})
SIV2a-reconstructed	3.54 (Mw6.96)			241.7
SIS1	5.02 (Mw7.06)	63.11	94.99	250
SIS2	3.39 (Mw6.95)	52.75	62.81	250
PIS1	3.57 (Mw6.96)	63.12	83.65	250
PIS2	3.72 (Mw6.98)	51.66	59.36	250

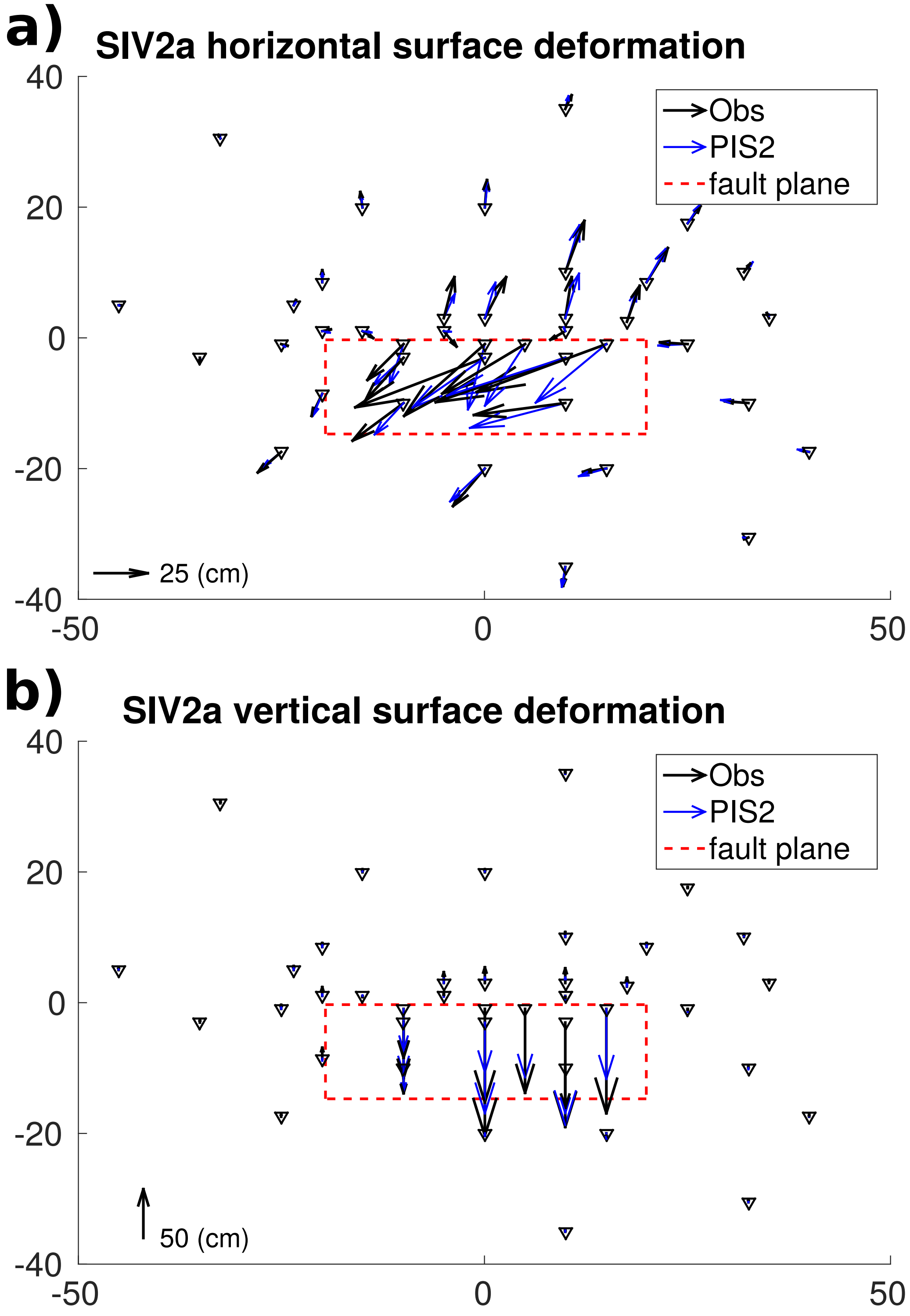

Figure 3.25: Comparison between synthetic (solid blue arrows) and the observed (solid black arrows) surface deformation resulting from the PIS2 model and for the SIV2a. a) Horizontal component and b) vertical component.

3.5 Conclusion

In this chapter, I present a new strategy to tackle the kinematic source inversion problem. The mathematical formulation is based on the linear relationship between the earthquake source time-space history and the recorded seismograms. Thanks to the pre-computed stress-state tensor (i.e. wave propagation information) and the time domain formulation of the forward problem, I show that it is possible to invert progressively increasing data time-windows. By doing that, the strategy incorporates the physical causality of the problem into the inversion strategy. In addition, due to the large number of unknowns encountered (tens of thousands), I include strategies of model regularization and preconditioning. These strategies were thought in such a way that they could incorporate physically meaningful features of the expected ruptures. Moreover, the regularization framework established is quiet flexible in order to be able to incorporate any type of prior information or physical behavior desired.

As presented in sections 3.3 and 3.4, the two strategies introduced in this chapter, the SIS and the PIS, were successfully applied to well-known synthetic benchmarks. I recognize that the PIS shows better results for both synthetic cases. However, for the SIV2a that has more uncertainties, mainly related to the source geometry, the performance of the PIS is not drastically better than the SIS. It is very important to mention that when wrong values of the rake, strike or dip angles are assumed, spurious unphysical bursts of energy start appearing away from the rupture front. This unphysical slip tries to balance the errors induced by the wrong geometrical assumptions. When the rake angle is not assumed as a fixed value, the source reconstruction is poorer due to the larger number of unknowns that this unconstrained problem represents. Therefore, a fixed-rake assumption is preferred. However, as well as for the regularization and preconditioning strategies, a prior calibration of the rake angle has to be driven before applying either the SIS or the PIS.

One of the very interesting features of the PIS is the handling of a limited number of unknowns at the different stages of the inversion. For instances, during the inversion of the first data time-windows only 30 to 60 unknowns are involved in the problem. As the time passes the number of unknowns increase rapidly. However, from a physical perspective it is acceptable to think that most of the nodes (that have not yet been broken) will exhibit a similar behavior to its closest neighbor (that already broke). Under this assumption, it is not necessary to try to explain the whole history of new node included into the inversion from scratch, but from the knowledge of its closest neighbors. In the same way, we can see in Figure 3.15 that the data assimilated in the next time-window needs to explain only the difference between the predicted and the already inverted slip-rate history.

Chapter 4

Real data application: 2016 Mw7.0 Kumamoto earthquake

The material presented in this chapter has been written based on the following work:

- Sánchez-Reyes, H., Tago, J., Métivier, L., Cruz-Atienza, V.M, and Virieux, J. (2016). An evolutive linear kinematic source inversion. *2018 AGU Fall Meeting*.
- Sánchez-Reyes, H., Tago, J., Métivier, L., Cruz-Atienza, V.M., and Virieux, J. (2017). An evolutive quasi-real-time source inversion based on a linear inverse formulation: Application to the 2016 Kumamoto mainshock (M W 7.0). *2017 IAG-IASPEI Meeting*.
- Sánchez-Reyes, H., Tago, J., Métivier, L., Cruz-Atienza, V.M., and Virieux, J. (2018). An evolutive linear kinematic source inversion. *Journal of Geophysical Research: Solid Earth*, 123.

Contents

4.1 Introduction

In this chapter, I present the results from the inversion strategies, SIS and PIS, that were presented in Chapter 3, when they are applied the mainshock of the 2016 Kumamoto earthquake sequence. Before applying these strategies to the real data set of this earthquake, I present several synthetic inversion exercises that are carried out under the same configuration of the Kumamoto mainshock in order to calibrate all the necessary parameters involved in each of the inversion strategies. Once these parameters are chosen, the SIS and the PIS are applied to the real data set of this strike-slip earthquake.

Outline The outline of this chapter is the following:

- In Section 4.2, I introduce the source geometry assumed for this earthquake and the available stations recording the associated motion. In addition, I describe the 1D layered medium used for the computation of the stress-state tensor. The assumed spatial-temporal discretization of the model to be reconstructed is also provided in this section.
- In Section 4.3, I present a brief description of the inversion exercises that were carried out in order to calibrate all the choices related to the depth preconditioning, model regularization, smoothing operator and progressive time windowing. All these exercises are performed under the same configuration that is described in Section 4.2 and the synthetic rupture model to be reconstructed is based on the solution provided by Asano and Iwata (2016) for the 2016 (Mw7.0) Kumamoto earthquake.
- In Section 4.4, I summarize the results from both, the SIS and PIS, when applied to the real data set for this earthquake. I compared these two results and I give a short discussion about why they are different.
- In Section 4.5, I provide a final conclusion about the application of these two strategies when tackling a real earthquake.

4.2 Settings: source and acquisition geometry

Source-receiver geometry

The (Mw7.0) Kumamoto earthquake occurred at 16:25:05.47 UTC on 15 April 2016 according to the National Research Institute for Earth Science and Disaster Resilience (NIED). As reported by Uchide et al. (2016) and Asano and Iwata (2016), this event has activated slips along two different fault segments of the Futagawa and Hinagu fault systems in the Kumamoto prefecture, South West Japan (Figure 4.1a). Both fault systems exhibit a dextral strike-slip motion (Uchide et al., 2016). The velocity structure used to pre-compute the stress-state tensor is taken from the results of a regional traveltime tomography presented by Uchide et al. (2016), and the values of the density for each layer are estimated by assuming a linear relationship between V_p and ρ taken from Berteussen (1977) (see Figure 4.1b and Table 4.1).

I adopt the fault plane geometry from Asano and Iwata (2016) with a longer length along the strike direction: this longer dimension is in better agreement with the geometry used by Uchide et al. (2016) (Table 4.1 and Figure 4.1). The fault geometries from these two authors were built according to the aftershock distribution and the surface trace of known active faults. Their main difference is less than 5 degrees for strike and dip angles. Segment lengths differ as well: longer fault segments are preferred in order to avoid the non-physical accumulation of slip at the boundaries.

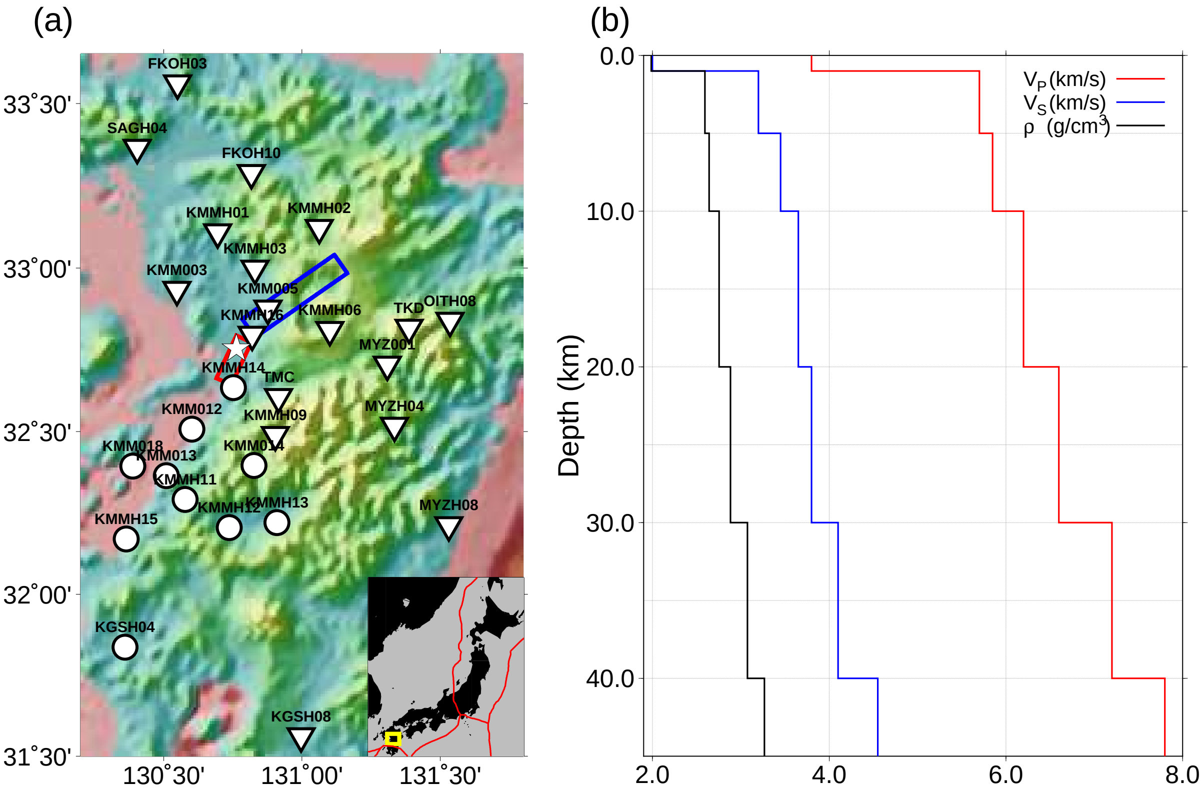

Figure 4.1: (a) Fault geometry and location of receivers recording the 2016 Kumamoto earthquake (Mw 7.0). The rectangles indicate the surface projection of the Futagawa (blue) and Hinagu (red) fault segments assumed in this work, while the white star represents the epicenter reported by the NIED. Inverted triangles are used to illustrate the location of the 19 receivers used in the inversion, while the 11 circles represent locations where waveforms are just predicted. (b) Velocity-density structure used to estimate the stress-state tensor. The velocity model was taken from Uchide et al. (2016) and the density was derived from the linear relationship between V_P and ρ presented by Berteussen (1977).

Two 3-component velocimeters from the Broadband Seismograph Network (F-net) and 28 3 component accelerometers from the strong-motion seismograph Networks (K-NET, KiK-net) have recorded this event at epicentral distances shorter than 150 km. In Section 4.3, all the 30 receiver locations are used for the synthetic exercises to calibrate the inversion parameters. In contrast, in Section 4.4 not all recordings are used in the real data inversion exercises, mainly due to the complexity of the recordings related to evident site effects at certain locations. For the K-NET and KiK-net networks, recorded accelerograms are converted from counts to acceleration, baseline corrected and integrated to particle velocity recordings. For the F-net network, the velocity recordings are deconvolved by the instrument response and baseline corrected. Then, all velocity recordings are band-pass filtered inside the window [0.025-0.25] Hz by applying a one-pass butterworth of first order. Anti-causal zero-phase filters were not used as the main idea behind the progressive inversion strategy is to benefit from causality. However, not large differences were observed in the inversion results when zero-phase filters are applied.

Compared to other recent events, the 2016 Kumamoto mainshock presents a reasonable azimuthal coverage of receivers around the active fault system (see Figure 4.2). This important feature of the acquisition system certainly enhances the resolution power in terms of source imaging. However, only the seismograms that can be satisfactorily modeled, according to the limited knowledge that we have of the velocity-denstity structure, should be considered to reconstruct the source history. By analyzing the recordings at the 30 receiver locations available, the seismograms recorded in the southwest of this region (represented by circles in Figure 4.1) show a more complex waveform than other locations at similar epicentral distances with symmetric azimuths. For instance, we can see in Figure 4.3 a comparison of the seismograms recorded at two locations close to the epicenter (KMM005 at 17 km and KMMH14 at 13 km). The comparison in Figure 4.3 shows that for two locations, following a SSN-NNE direction, the motion recorded in the southwest lasts longer and its waveform is more complex than the one from the northeast. These features can strongly impact the source reconstruction (e.g. adding spourious bursts of slip) if the assumed velocity structure is not accurate enough to model this complex wave propagation.

Table 4.1: Kumamoto fault geometry and velocity-density structure used in this work (modified from Uchide et al. (2016)).

	1^{rst} segment Hinagu	2^{nd} segment Futagawa	Depth (km)	V_P (km/s)	V_S (km/s)	ρ (g/cm^3)
Strike (ϕ)	205^o	235^o	0-1	3.80	2.00	1.98
Dip (δ)	72^o	65^o	1-5	5.70	3.20	2.59
Rake (λ)	180^o	210^o	5-10	5.85	3.45	2.64
σ_λ	$\pm 30^o$	$\pm 30^o$	$10-20$	6.20	3.65	2.75
Length (km)	18	40	$20-30$	6.60	3.80	2.88
Width (km)	20	20	$30-40$	7.20	4.10	3.07
Nodes	90	200	$40-$	7.80	4.55	3.26

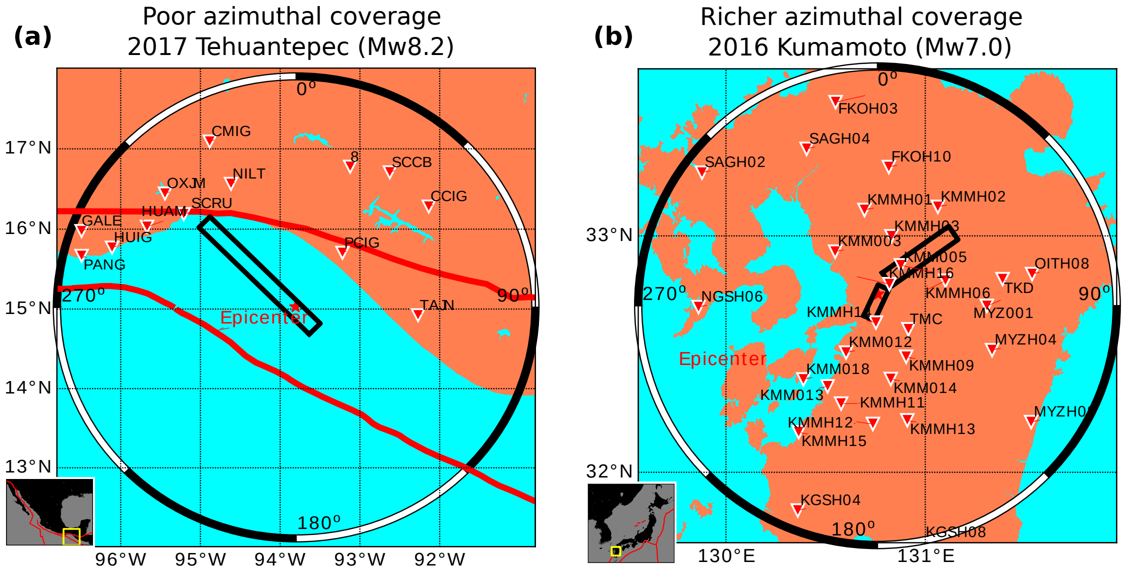

Figure 4.2: Comparison of the azimuthal coverage of two modern regional acquisition systems recording large earthquakes in 2016 and 2017. (a) Poor receiver azimuthal coverage recording the 2017 (M_W8.2) Tehuantepec Mexico earthquake. (b) Richer azimuthal coverage recording the 2016 (M_W7.0) Kumamoto Japan earthquake. Notice that in (a) receivers are only between $\approx 290^o$ to 115^o, while in (b) receivers are all around the assumed fault planes. In both panels, the red star, the solid black lines and the solid red lines represent the epicenter, the surface projection of the fault planes where the rupture is believed to occur and the tectonic plate boundaries, respectively.

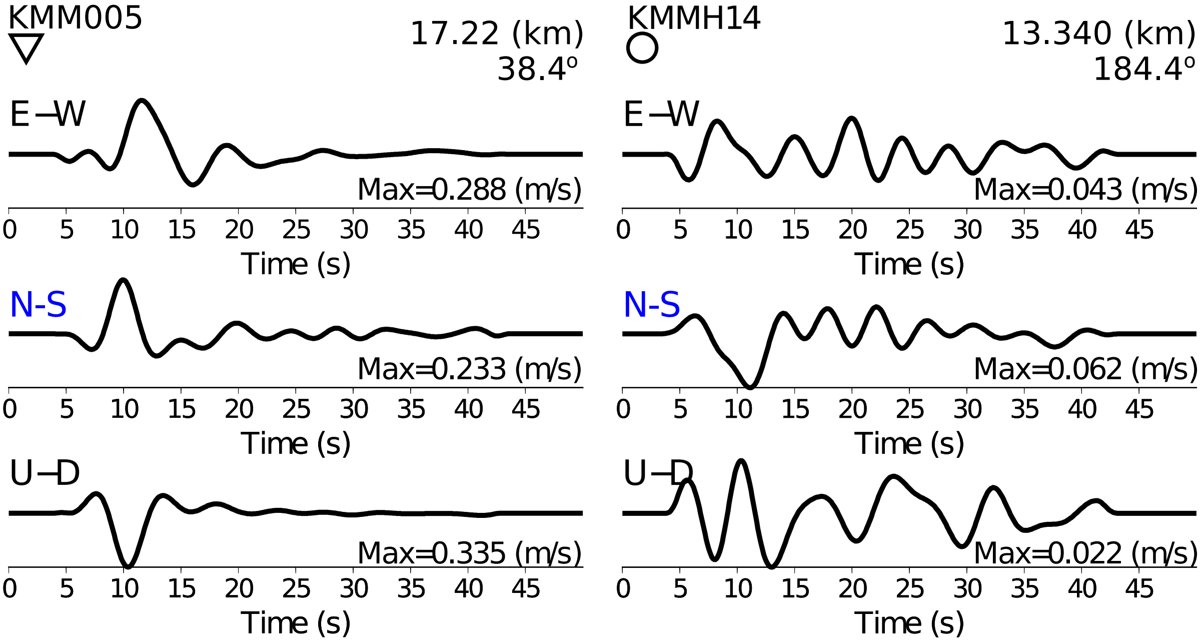

Figure 4.3: Comparison of the particle velocity recordings at two locations: KMM005 (left) and KMMH14 (right). The epicentral distance and azimuth of each location is given at the top right of each panel (see Figure 4.1). The maximum absolute amplitude of each trace is given at the bottom right of each seismogram. Notice that both locations are less than 20 km far from the epicenter. The complicated shape of the traces recorded at KMMH14 evidences a complex velocity-density structure in that direction (South-West from the epicenter). In addition, the amplitude difference (one order of magnitude) indicates the rupture direction and the existence of an important slip zone closer to KMM005 than to KMMH14. The information about the treatment of the signals can be found inside the text.

Discretization

The total fault surface was discretized in 290 nodes equally spaced every 2 km along strike and dip directions. This space discretization is in agreement with maximum frequency of 0.25 Hz that I consider. The minimal detectable rupture durations is of 4 s: the rupture speed is expected to be between 2.6 and 2.2 km/s. The duration of the rupture is expected to last less than 20 s. The time sampling rate of the slip-rate functions is set to 0.5 s which is four times shorter than the maximum sampling rate allowed according to the highest frequency limit of the observations (0.25 Hz). Observations are decimated to have samples every 0.1 s with a duration of 65 s. The number of parameters involved in the inversion is 41 [time-samples] $\times 290$ [fault-nodes] $\times 1$ [slip-rate component] $= 11890$, as I assume the rake angle as known from prior information, while the number of observations is 30 [receivers] $\times 3$ [components] $\times 131$ [time samples] $= 11790$. However, only 19 stations out of the 30 available are considered in the inversion, which decreases the number of observations to 19 [receivers] $\times 3$ [components] $\times 131$ [time samples] $= 7461$. The other remaining 11 stations are not used for the inversion due to their complexity (see Figure 4.3). However, a comparison between these complex recordings and the synthetic waveforms predicted from the preferred reconstruction of the slip-rate distribution is provided.

4.3 2016 Mw7.0 Kumamoto earthquake: synthetic case and calibration

I would like to highlight that, the exercises presented in this section have as goal to illustrate how the parameters needed to apply either the standard or progressive inversion strategy are chosen when tackling a real earthquake. Each of these exercises respect the source-receiver geometry, velocity-density medium and spatial-temporal discretization of the source model described in Section 4.2. Due to the complex behavior that a complete combination of all the regularization and preconditioning strategies can have into the inversion results, the following exercises present step-by-step the calibration of each ingredient. Therefore, in this section I present several inversion exercises that were used to determine the correct depth preconditioning (c value), smoothing operator and prior model regularization. Each of these exercises include progressively the parameters already calibrated.

The seismic source used in this section as the target model to be reconstructed is based on the inversion results to the 2016 (Mw7.0) Kumamoto earthquake reported by Asano and Iwata (2016). This solution is available at `http://sms.dpri.kyoto-u.ac.jp/k-asano/`. In order to build this source model the authors applied the multiple time-window strategy (Hartzell and Heaton, 1983; Olson and Apsel, 1982) to the real data set available for the 2016 (Mw7.0) Kumamoto earthquake. This technique relies on a linear time domain formulation that links the slip time function (not the slip-rate), described by a multiple time-window smooth ramp function, to the displacement recordings. Contrary to the progressive inversion strategy, the multiple time-window technique requires the completeness of the recordings. In addition, this technique needs to set a central value of the rupture velocity around which the slip on the other time-windows has to be determined. By using that strategy, at each of the 189 subdivision of the fault plane (described as subfaults of 2 by 2 km) the solution reports 9 amplitude values of the basis functions (smooth ramps) corresponding to each of the time windows discretizing the whole time slip history. Once the slip time-space history is reconstructed based on this knowledge, I apply the following operations to the slip distribution to build the slip-rate time-space history that is used in these calibration exercises: 1) the time-space slip history is first interpolated in time and space over a finer grid and smoothed in order to reduce the effects of the discretization, 2) the slip-rate distribution is then obtained through the time derivative of the reconstructed smoothed version of the slip evolution and 3) the information at the location of the assumed geometry for this work (described in Section 4.2) is extracted from the finer reconstructed slip-rate history. Figure 4.4 illustrates the final slip and the reconstructed slip-rate time history across the assumed geometry. In this section, this reconstructed source model is assumed as the target model to be reconstructed. Finally, through a forward modeling on the finest grid of this target model I compute the synthetic seismograms at the 30 receiver locations at the surface and I use them (without adding noise) as the real data to invert the source on the coarser grid (assumed geometry).

4.3.1 Depth preconditioning

The first strategy to be calibrated is the depth preconditioning. Due to the surface acquisition, any reconstructed source model is expected to exhibit significant slip at shallow depths. This artifact is an implicit consequence of the amplitude difference of the waves propagating along short and long source-receiver paths. I try to mitigate this implicit weighting through equations (3.19) and (3.20). Consequently, an optimal c value for these equations has to be set. To do that, I carried out several SIS exercises applying only the depth preconditioning strategy. Each exercise had a different c value ranging from 0.05 to 2.0. The optimal value among these tests is found to be $c = 0.1$. Figure 4.5 illustrates the effect of some wrong values for c as well as the result using the optimal value.

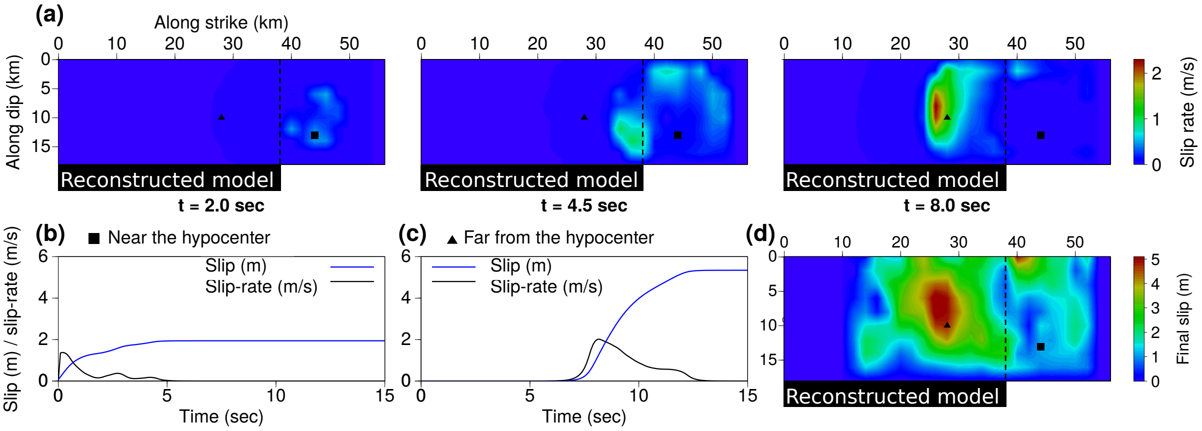

Figure 4.4: Summary of the assumed target source model built from the reconstruction and interpretation of the time-space slip inversion from Asano and Iwata (2016). Panel (a) shows the evolution of the slip-rate distribution at three different rupture times (t=2.0, 4.5 and 8.0 s from left to right). Panels (b) and (c) illustrate the reconstructed cumulative slip (blue line) and the derived slip-rate time histories (black line) at two different fault-nodes of the assumed geometry. Locations of the fault-nodes shown in panels (b) and (c) are represented by the black square and triangle on panel (a). The black square represents the hypocentral location while the triangle illustrates a location near to the zone of expected maximum slip. The vertical black dashed line indicates the division between the Hinagu (shorter) and Futagawa (longer) fault segments. Panel (d) displays the final slip distribution of the reconstructed source model.

The first thing to notice from these exercises is that even when the $c = 0$ (Figure 4.5c) the resulting final slip is not very different from the target model (Figure 4.5a). Such encouraging result means that the illumination is enough to have a satisfactory reconstruction of the main characteristics of the target. However, there is an up dip shift of the maximum slip zone as it was expected. By progressively increasing the c value it can be observed how this zone is slowly moved along the downdip direction. As a consequence of the downdip shift, all the slip across the fault increases significantly: the inverted model is forced to have more slip to compensate the geometrical spreading effect to correctly match the observed wave field. After this serie of exercises, I set $c = 0.1$ as the value to be used for any inversion using this source-receiver geometry.

4.3.2 Smoothing operator

The smoothing operator is also an important ingredient to calibrate. I apply a 2D locally variant Laplacian correlation function in order to incorporate the spatial coherence between neighboring fault-nodes. The time history of each node is not affected by any smoothing filter. Spatial smoothing filters have been largely applied in seismic exploration (Longbotham and Bovak, 1989; Claerbout, 1992; Fomel, 2002; Fehmers and Höcker, 2003) as well as in seismology (Cara, 1978; Nolet, 1987, 2008) as strategies to extract source information or to mitigate artifacts such as acquisition footprints, spatial aliasing, and coherent and incoherent noise. However, in seismic exploration more complex locally variant (sometimes anisotropic) laplacian correlation filters have been applied to effectively attenuate these effects while improving the imaging resolution when they are designed taking into account the orientation of the expected local geological structures (Hale, 2007; Guitton et al., 2012; Trinh et al., 2017; Wellington et al., 2017). In seismology, specifically in source imaging, the locally variant smoothing filters are

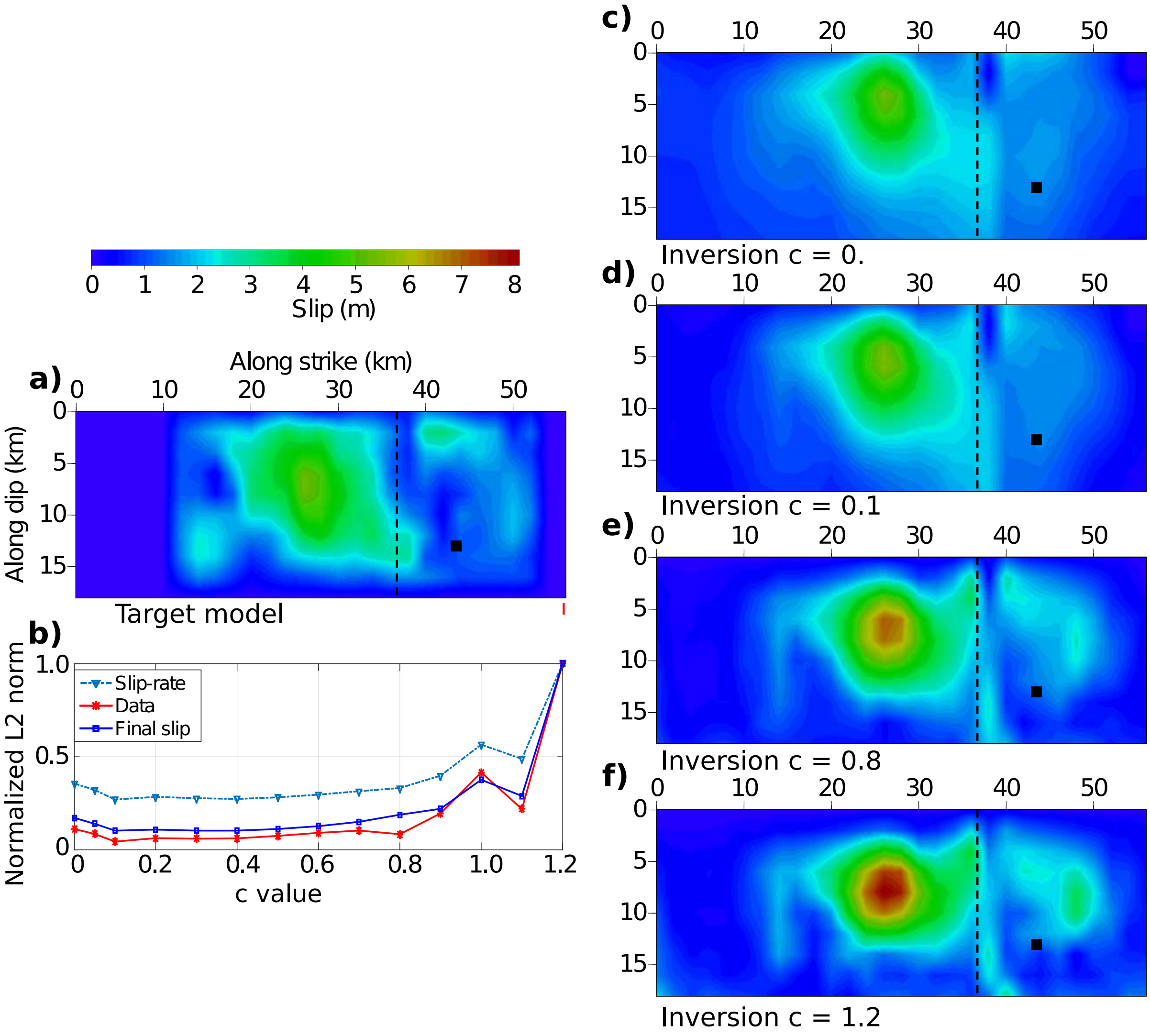

Figure 4.5: Results from the inversion exercises carried out to calibrate the depth preconditioning strategy. Panels a) c) d) e) and f) show the final slip distribution across the fault of the target model and for the inversion exercises using different c values for the depth preconditioning. b) Illustrates the normalized L2 norms between the resulting models and the target model. The preferred c value is 0.1. For illustration purposes, the norms shown in b) are normalized by the maximum value of each quantity reported by these exercises for each field: final slip, slip-rate time-space history and data. For illustration purposes, the color scale in this figure is changed due to the high values of slip obtained when $c = 1.2$.

less common and intuitive: an assumed local geometry of the propagating rupture front through time and space is necessary. Trying to incorporate this type of structure-driven spatial filters into the source imaging problem, I decide to use a local anisotropic smoothing filter instead of the one presented in Sections 3.3 and 3.4. Therefore, in this 2D case (along strike ϕ and dip δ directions), it is necessary to define a 2D correlation function $Corr_{2D}$ which will be in charge of controling the influence at the fault position (ϕ, δ) caused by another one located at (ϕ', δ'). Such correlation is given as

$$Corr_{2D}(\phi, \delta; \phi', \delta') = \frac{\alpha}{2\pi L_\phi^2} e^{-\frac{1}{L_\phi}\sqrt{(\phi-\phi')^2+\alpha^2(\delta-\delta')^2}}, \tag{4.1}$$

with

$$\alpha = \frac{L_\phi}{L_\delta}, \tag{4.2}$$

where L_ϕ and L_δ are the two different correlation lengths which are orientated along the strike ϕ and dip δ directions respectively. The term $\alpha/(2\pi L_\phi^2)$ in equation (4.1) is a normalization factor of the 2D correlation function, which means that

$$\int_{-\infty}^{\infty}\int_{-\infty}^{\infty} \frac{\alpha}{2\pi L_x^2} e^{-\frac{1}{L_x}\sqrt{(x-x')^2+\alpha^2(z-z')^2}} dx'dz' = 1. \tag{4.3}$$

In addition, if a change of the directions along which the smoothing is applied (along strike and dip directions) is required, a change of variable from (ϕ',δ') to ($\hat{\phi}'$,$\hat{\delta}'$) can be done according to the following transformation,

$$\begin{bmatrix} \hat{\phi}' \\ \hat{\delta}' \end{bmatrix} = \mathbf{R} \begin{bmatrix} \phi' \\ \delta' \end{bmatrix} = \begin{bmatrix} \cos\theta & -\sin\theta \\ \sin\theta & \cos\theta \end{bmatrix} \begin{bmatrix} \phi' \\ \delta' \end{bmatrix}. \tag{4.4}$$

which allows the rotation of the orthogonal correlation lengths in equation (4.1), that are no longer aligned with the strike and dip directions. These correlation lengths are instead rotated by some angle θ (see Figure 4.6). Using the correlation function described in equations (4.1), (4.2) and (4.4), the smoothed version of the n-th component of the gradient vector across the fault surface, here denoted as $\hat{\mathcal{G}}_n(\phi,\delta)$, is obtained through a 2D convolution operation between the local anisotropic correlation function $Corr_{2D}(\phi,\delta;\phi',\delta')$ and the n-th component of the estimated gradient $\mathcal{G}_n(\phi,\delta)$,

$$\begin{aligned} \hat{\mathcal{G}}_n(\phi,\delta) =& Corr_{2D}(\phi,\delta) \star \mathcal{G}_n(\phi,\delta) \\ =& \int_{-\infty}^{\infty}\int_{-\infty}^{\infty} Corr_{2D}(\phi,\delta;\phi',\delta')\mathcal{G}_n(\phi,\delta) d\phi' d\delta'. \qquad n \in [\phi,\delta] \end{aligned} \tag{4.5}$$

Therefore, instead of applying a 2D smoothing filter with correlation distances along fixed strike and dip directions, as in Sections 3.3 and 3.4, in this chapter I use the smoothing filter described in equation (4.5), wich allows different local correlation lengths and rotations of the principal axes of the spatial filter. It is important to mention that, the correlation function is defined all across the fault surface (ϕ,δ) in terms of correlation distances, L_ϕ and L_δ, and an angle of rotation θ. Consequently, it is necessary to define for each position on the fault (ϕ,δ) the corresponding values of correlation lengths and angle of rotation. These values defining the 2D correlation function can be roughly approximated by looking at the shape of the data gradient (at the first iteration of the SIS) or by assuming a concentric rupture front propagation across the fault surface. An illustration of the different effects between the fixed along strike and dip directions filter versus the locally rotated one can be seen in Figure 4.6. In Figure 4.6a four slip-rate spikes across the fault plane are presented, while in 4.6b and 4.6c the smoothed versions coming form the fixed and the locally variant operator are illustrated. It has to be noticed that, at each node location on the fault the two principal correlation distances and the rotation angle has to be defined in terms of the expected rupture front. In this case, I considered a 2 by 4 km correlation distance filter at all nodes with a local rotation angle that tries to follow the structure of the expected rupture front.

The Figures 4.6d,e,f show the snapshots of the target model and the two resulting slip-rate time-space histories obtained from inversion exercises using the fixed and the locally variant smoothing filters, respectively. Both exercises consider the following stopping criteria: 1) a maximum number of 20 iterations and a data misfit lower than 1 %. Once the inversion procedure passes these thresholds, I recognize that the resulting models do not significantly improved (in terms of model misfit) and the

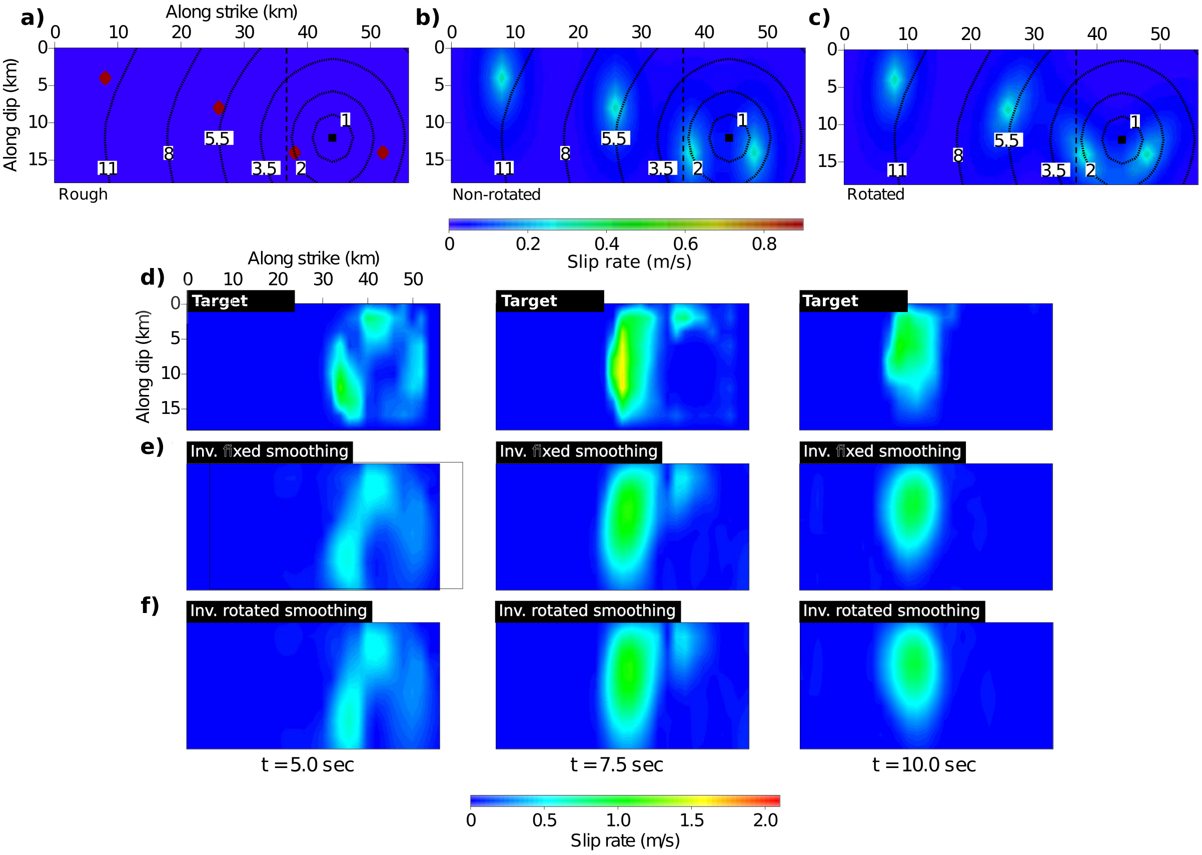

Figure 4.6: Effects of a globally fixed and a locally variant smoothing filter. a) Shows four spikes of slip-rate (1 m/s) at different location on the fault. b) and c) illustrate the effect of the two different filters to those four spikes shown in a). Notice that on c) the response to the filter has a different inclination angle (in agreement with the travel time isochrones) for each of the locations. d), e) and f) show the snapshots (at $t = 5$, 7.5 and 10 seconds of rupture from left to right) of the target model and the inversion results obtained when each of the two different filters are applied. In panels a), b) and c), the black square represents the hypocentral location, while the concentric black lines show the expected position of a rupture front traveling at the local shear wave velocity.

data misfit dicreases slowly at the cost of injecting spourious slip-rate pulses in the reconstructed source models. In terms of data and model misfit, the preferred locally variant smoothing filter performed better than the fixed one. However, the misfits were not significantly less. The data misfit for the rotated one is almost two times smaller than its non-rotated counterpart (0.929×10^{-2} for the locally variant versus 1.6×10^{-2} for the fixed). The model misfit (slip-rate L2 distance between target and resulting model) for the locally variant is $\approx 2\%$ closer to the target than the other one (18.88% versus 20.70%).

After this analysis, I set the locally variant smoothing filter to be the one to be used. This operator implies a more physically meaningful spatial coherence, even if the data and model misfits did not show a very significant improvement. In terms of the final slip distribution, I noticed a small correction of an inclination angle of the maximum zone of slip present in the results where there is no local angle rotation of the filter. This correction also improved the slip-rate evolution across the fault (not shown in figure 4.6).

4.3.3 Model regularization: prior model and associated weighting

In order to reduce the null-space size, for these synthetic tests of calibration, I consider as prior information the hypocentral location and the existence of a zone of maximum slip far from the hypocenter (not knowing its maximum value). As in previous sections, I assume that the slip vanishes rapidly toward the fault boundaries. Using this information a prior model consisting of a concentric rupture front propagating from the hypocenter to the fault boundaries at the local shear wave velocity is built. This model has an average background slip value of 1.6 m with a Gaussian anomaly of 4.4 m to the east of the hypocenter. Figure 4.7e illustrates the final slip distribution of this assumed prior model. The slip-rate time-space evolution across the fault is also shown in figure 4.5 where it is compared to the evolution of the target model. The rake angle was fixed to the value reported by Asano and Iwata (2016). The individual slip-rate time functions at each node were assumed as Yoffe-type functions with 5 seconds of effective rise time and 0.5 seconds of positive acceleration. The amplitude of the slip-rate functions were controlled by the local slip amplitude of the proposed model.

The weighting function (represented by a diagonal matrix) controlling the importance of the prior information is set to have strong values at the fault boundaries and at time-space zones that are outside of the active region (where the rupture front is expected to be). The upper limit of the rupture velocity is set to 1.2 times the local shear wave speed while the lower limit is set in such a way that the rupture at each node is promoted to have rise-times of ≈ 5 s. The estimation of the rupture times, necessary to build this weighting matrix, is carried out through the previously used 2D Eikonal solver (Podvin and Lecomte, 1991). Figure 4.7c illustrates this penalized regions controlled by the weighting matrix.

Once the prior model and weighting matrix are designed, a correct value for the hyperparameter ϵ from equations 3.13 and 3.18 has to be determined. To do that, I run several exercises with different ϵ values ranging form 5×10^{-5} to $1\ \times10^{-1}$. By choosing this range of values, at the first iteration of the SIS the model misfit term (from equation 3.8) represented from 200% to 0.1% of the initial data misfit.

Figure 4.9 summarizes the results from these calibration exercises of the prior model regularization term. As expected, when the hyperparameter is large (1×10^{-3}) the final slip distribution of the reconstructed model to be driven more by the prior model than by the observed data. Therefore, for large values of ϵ the data norm increases as well as the model norm (L2 distance of the slip-rate between target and inverted model). On the other hand, if ϵ tends to zero, the data fitting remains the same while the model norm starts to increased. Consequently, the optimal region is bounded somewhere around 2×10^{-5} and $1\ \times10^{-4}$ (see Figures 4.9e,f). From these exercises, the optimal value for the hyperparameter was fixed to 8×10^{-5} (meaning that the model misfit term is $\approx$10% of the initial data misfit).

It is interesting to see that, when $\epsilon = 8 \times 10^{-5}$, the obtained model shows a final slip distribution (Figure 4.9c) that starts to exhibit the deep and furthest zone of slip that is not visible when $\epsilon \to 0$. This feature illustrates that even if the prior model was not designed to see this zone, it helped to at least have a blurred reconstruction of that feature.

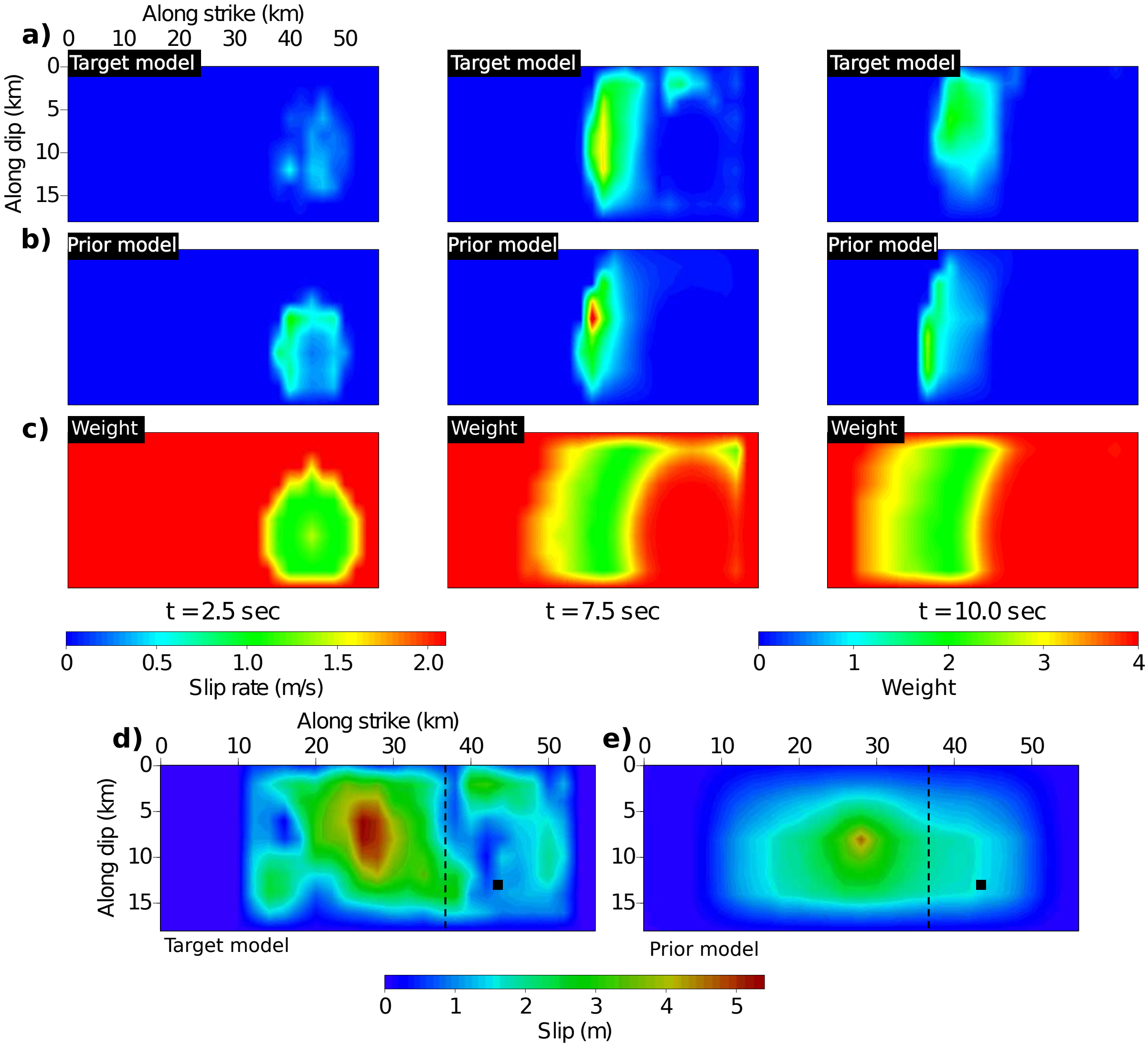

Figure 4.7: Comparison of the slip-rate evolution across the fault of a) the target model, b) the prior model, $\underline{V}_P$, and c) the weighting matrix, $\underline{\underline{W}}_m$, built for the calibration exercises. Notice that on c) the confidence on the prior model is represented by the colors ranging from blue (low confidence) to red (high confidence). A comparison between of the final slip distribution of a) the target model and b) the prior model is also provided. In all panels, the black square represents the hypocentral location while the vertical black dashed line indicates the division between the two fault segments.

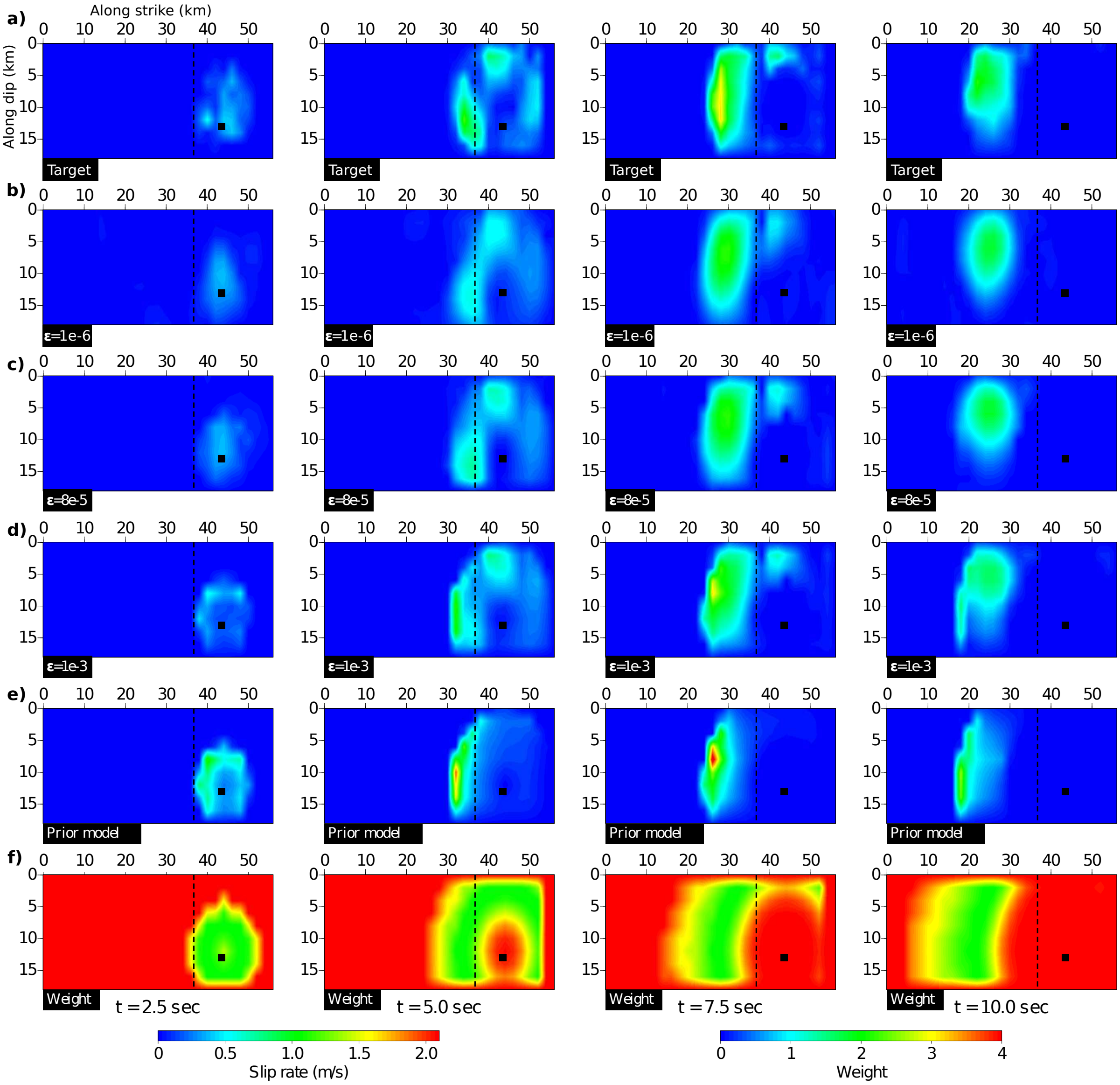

Figure 4.8: Summary of the results obtained from the exercises carried out to calibrate hyperparameter ϵ. Panels a), b), c), d), e) and f) show snapshots of the slip-rate time-space history of the target model, inverted models with different values of hyperparameter ϵ, the prior model and its associated weight respectively. The models shown in b), c) and d) have increasing values of $epsilon$: b) has almost no imprint of the prior model, c) has an optimal balance between data and prior model information and c) has a strong imprint of the prior model. In all panels, the black square represents the hypocentral location while the vertical black dashed line indicates the division between the two fault segments.

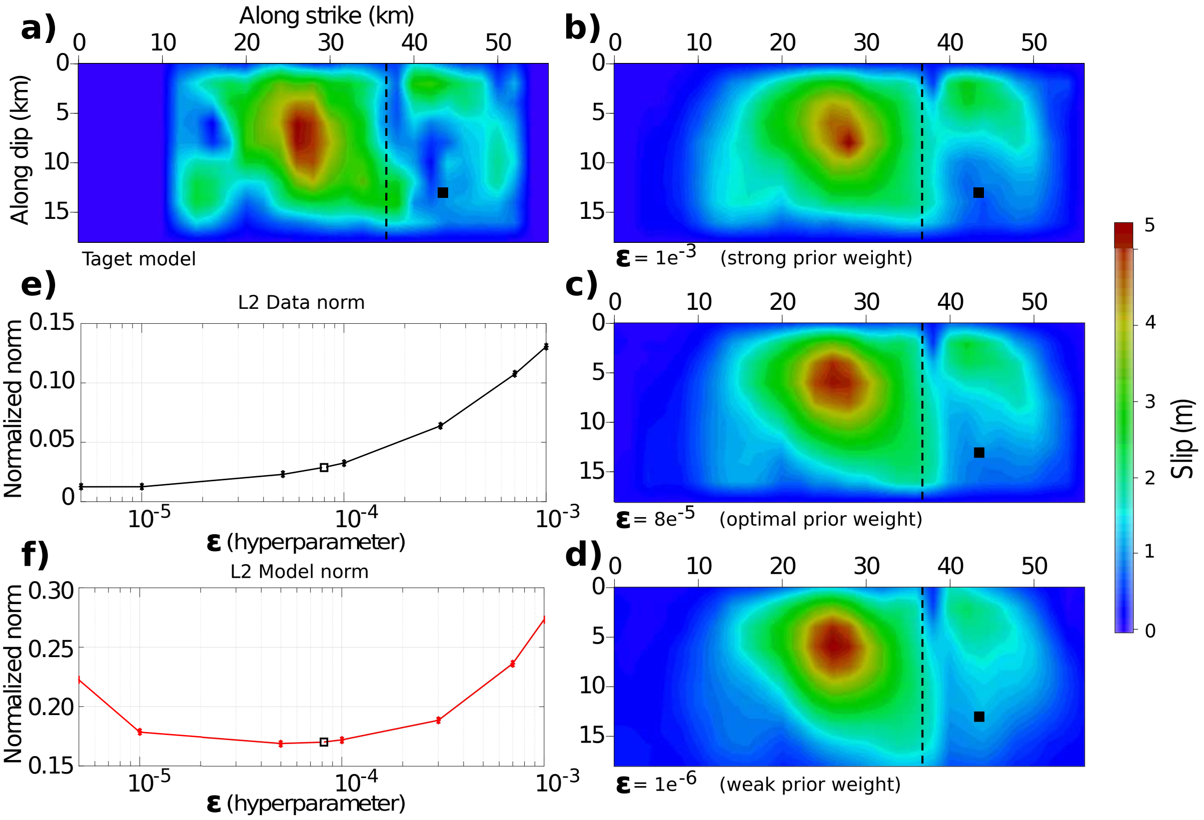

Figure 4.9: Summary of the results obtained from the exercises carried out to calibrate hyperparameter ϵ. Panels a), b), c) and d) show the final slip distributions obtained from inversions using different ϵ values. b) shows a strong prior model weighting while d) a weak one. e) and f) present the final L2 data and model norms, respectively, for each of the models obtained. The norms shown on e) and f) were normalized by the initial L2 distance for the observed data and target slip-rate evolution. The empty square on e) and f) shows the norms for the optimal value ($\epsilon = 8 \times 10^{-5}$).

4.3.4 Data and model windowing

To end this section, the data and model time-windows have also to be defined in order to apply the PIS. As it was illustrated in Section 3.3.4, the definition of the corresponding model and data time-windows for each of the inversion stages relies on a synthetic rupture time-space history and the computation of complete and incomplete seismograms related to that scenario (Figure 3.12). In this case, I use as synthetic rupture the solution proposed by Asano and Iwata (2016). Using this model eight progressive time windows are defined for the rupture history (*i.e.* $0-1.0$, $0-2.0$, $0-3.5$, $0-5.5$, $0-8.0$, $0-11.0$, $0-15.0$ and $0-20.0$ s). Then, for each of this limited model windows I analyze the residuals between the complete and incomplete seismograms and the data time-window limits were defined for each of the inversion stages. Figure 4.10 illustrate this procedure that helps to define the limits of every data time-window. With all these ingredients, either the PIS or the SIS can be carried out.

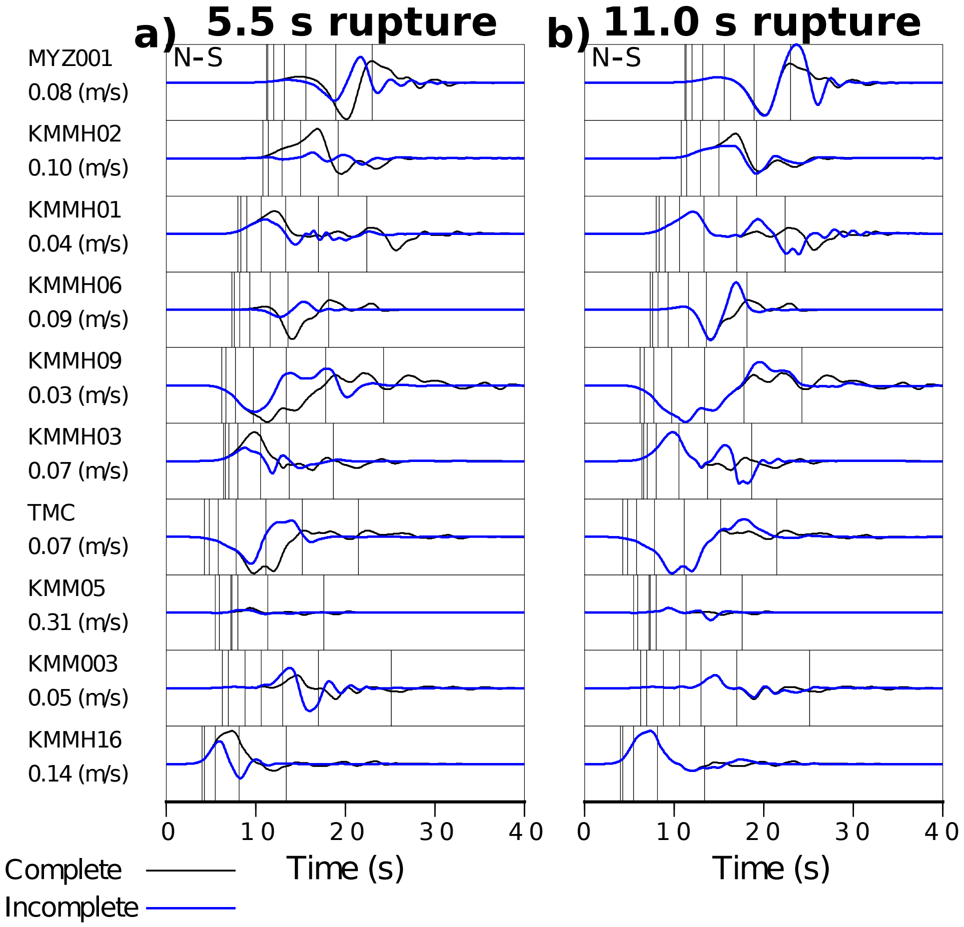

Figure 4.10: Illustration of the data time-window limits determined by comparing complete versus incomplete seismograms for two different rupture time-space windows. a) shows the comparison between the complete (solid black line) and incomplete (solid blue line) seismograms for a rupture that lasted 5.5 seconds while b) is the same comparison for a rupture that lasted 11 seconds. For every North-South trace the 8 vertical lines represent the time limits for the data windows used at each stage of PIS. Notice that in a) the difference between complete and incomplete seismograms starts after the fourth vertical line (time limit for that window of 5.5 s of rupture), while in b) this difference starts after the sixth.

Calibration summary The following is a list of the ingredients that were calibrated in this section:

1 An optimal depth preconditioning with constant $c = 0.1$.
2 A locally variant smoothing operator based on the expected rupture propagation.
3 The source model from Asano and Iwata (2016) was reconstructed and set as the prior model.
4 The weighting matrix penalizing slip at the fault boundaries and at rupture times not expected.
5 A correct balance between the model and data terms of the misfit function (controlled by ϵ).
6 Definition of the eight data and model time-windows where the PIS will be carried out.

All these parameters are the ones to be used for the inversion of the real data set of the 2016 Kumamoto earthquake. As a final illustration of all the callibration exercises, Figures 4.11 and 4.12 show how the reconstructed time-space history progressively improves when each of the ingredients, presented in this section, are taken into account.

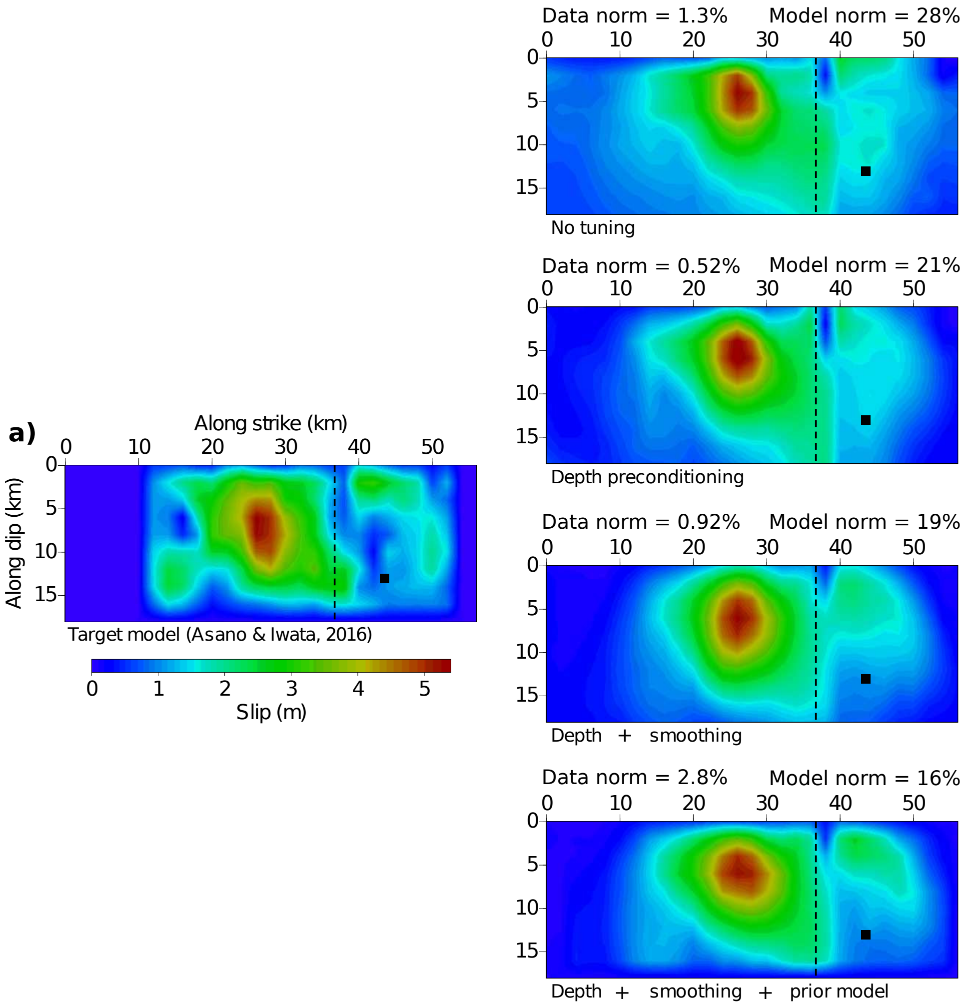

Figure 4.11: Comparison of the final slip distributions obtained after taking into account each preconditioning and regularization strategy. Panel a) illustrates the final slip of the target model to be reconstructed. The other panels illustrate the final slip distribuitons without any tuning (panel b)), only including the depth preconditioning (panel c)), with depth and smoothing preconditioning (panel d)), and with depth and smoothing preconditioning as well as prior model regularization (panel e)). Notice how the maximum slip zone is better located when the depth preconditioning is used, and how the slip at the fault boundaries is removed thanks to the model regularization. According to the data and model norms at the last iteration of each result (values shown at the top of each panel), the reconstructed models get progressively closer to the target, being e) the best even though the data norm increases $\approx 1.5\%$ compared to the model from panel b).

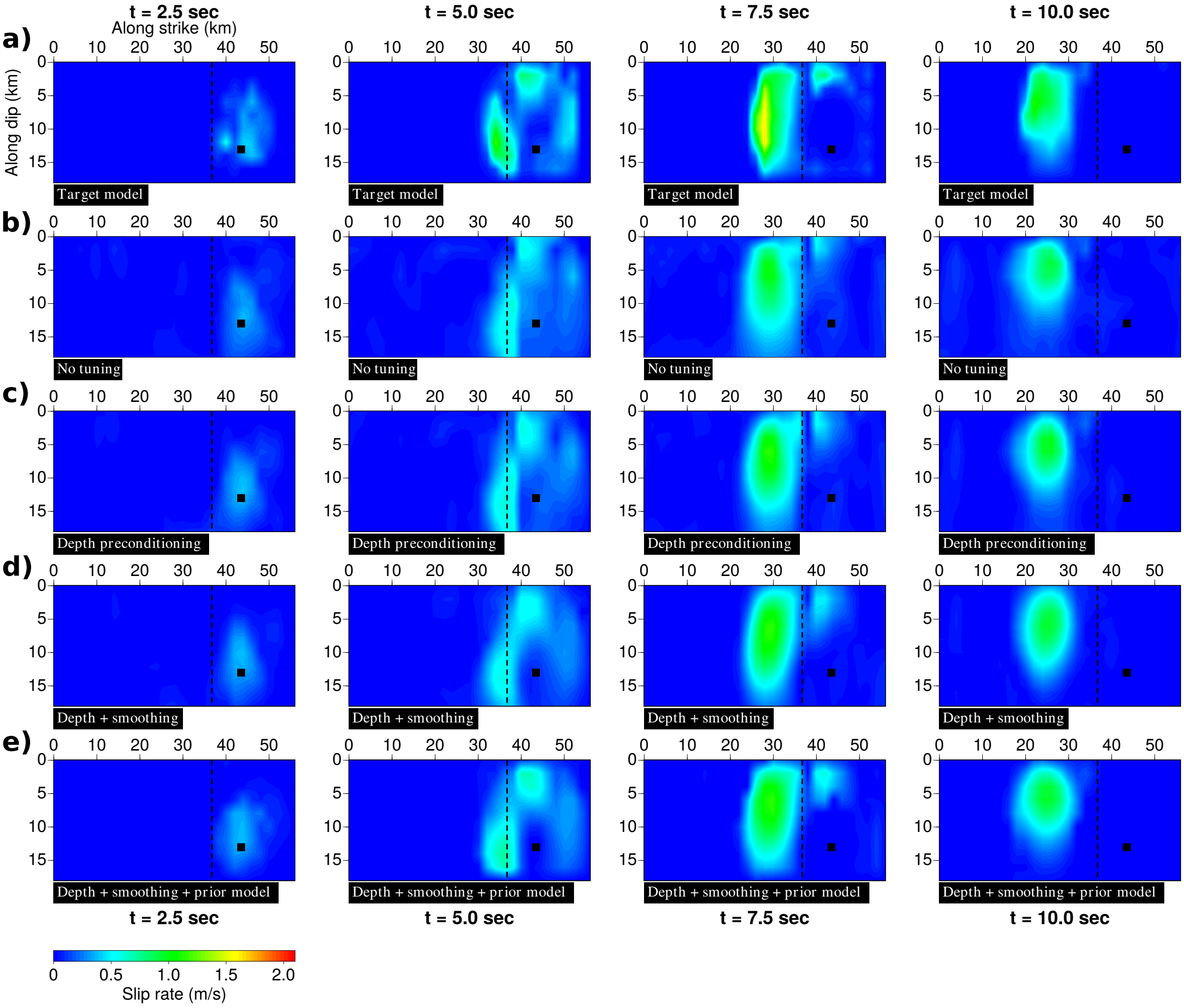

Figure 4.12: Same comparison as in Figure 4.11 but for the evolution of slip-rate time-space history. The snapshots are taken at $t = 2.5$, 5.0, 7.5 and 10.0 seconds.

4.4 2016 Mw7.0 Kumamoto earthquake: real case

For the real cases presented in this section I consider two different exercises. The first one, labeled as SIS-KUMA, assumes prior information on the rake angle to fix the relationship between the two components of the slip-rate vector. This prior information is obtained from the previous results reported by Asano and Iwata (2016). Regularization based on a prior rupture model as well as the depth-dependent and smoothing preconditioning strategies are also included for SIS-KUMA case (details are given in section 4.3). The second exercise, labeled PIS-KUMA, applies the PIS to exactly the same configuration of the SIS-KUMA case. PIS-KUMA and SIS-KUMA strategies differ only on the way the data is provided to the inversion scheme and the related evolution of the regularization term during the progressive inversion.

For each of the following exercises, the hyperparameter ϵ is set in different ways. For the SIS-KUMA case, this hyperparameter is fixed at the begining of the inversion process in a way that the contribution of the regularization term $\mathcal{C}_{\underline{m}}(\underline{V})$ corresponds to $\approx 10\%$ percent of the data term $\mathcal{C}_{\underline{d}}(\underline{V})$. With such a small initial contribution, the impact of the regularization is expected to be stronger at the final iterations where most of the data misfit has been already explained. This value of ϵ was defined based on the analysis presented in section 4.3.1, which showed that this choice ensure a decent data fit while still taking into account the prior information. For PIS-KUMA case, the hyperparameter ϵ evolves increasingly through the inversion stages. An initial contribution of 2% of the data misfit term was given to $\mathcal{C}_{\underline{m}}(\underline{V})$ and, at each of the next stages of the inversion it increased 3% more of the current $\mathcal{C}_{\underline{d}}(\underline{V})$. For instance, for the second stage of the PIS $\epsilon\mathcal{C}_{\underline{m}}(\underline{V}) = 0.05\mathcal{C}_{\underline{d}}(\underline{V})$, for the third $\epsilon\mathcal{C}_{\underline{m}}(\underline{V}) = 0.08\mathcal{C}_{\underline{d}}(\underline{V})$, and so on. At every step when a new data time-window is integrated, the prior model is updated by gathering inversion results of the previous stage. The model weighting matrix is also modified at those nodes where the prior model is replaced, so that any difference between the current model and the modified prior model is strongly penalized. This evolution of the prior model and weighting matrix enforces a causal behavior: it prevents the inversion from modifying the results already obtained to explain the new data, which have more tendency to be be mapped into the newly introduced parameters involved in the current inversion stage. That is the reason why the hyperparameter ϵ increases through the PIS procedure. Apart from this difference on the evolution of hyperparameter ϵ, the standard and progressive inversion strategies are carried out under exactly the same time-space discretization and regularization.

4.4.1 Standard versus Progressive

In general, both strategies show similar slip-rate evolutions and final slip distributions (see Figure 4.13). However, results from the SIS present a slightly larger ambiguity between the model parameters and longer durations of the rupture at several fault-nodes. For instance, the SIS-KUMA final slip distribution (Figure 4.13c) seems unclear around the hypocentral zone compared to PIS-KUMA (Figure 4.13d). Furthermore, we recognize a zone of considerably large slip at the north-east bottom of the Futagawa fault segment (left bottom in Figure 4.13c) that is absent in the PIS-KUMA results. Such result in SIS-KUMA could be caused by the time-space regularization or discretization limits. However, this slip zone is not observed in the PIS-KUMA case which does not take into account the contribution of these fault-nodes until very late inversion stages. The possible influence of this slightly larger cross-talk from SIS-KUMA case can be also seen at the higher amplitudes of its final slip distribution compared to the one from the PIS-KUMA (see Figures 4.13c,d). As in the synthetic case, the final slip distribution from SIS-KUMA case spreads through wider areas on the fault which could be an expression of the

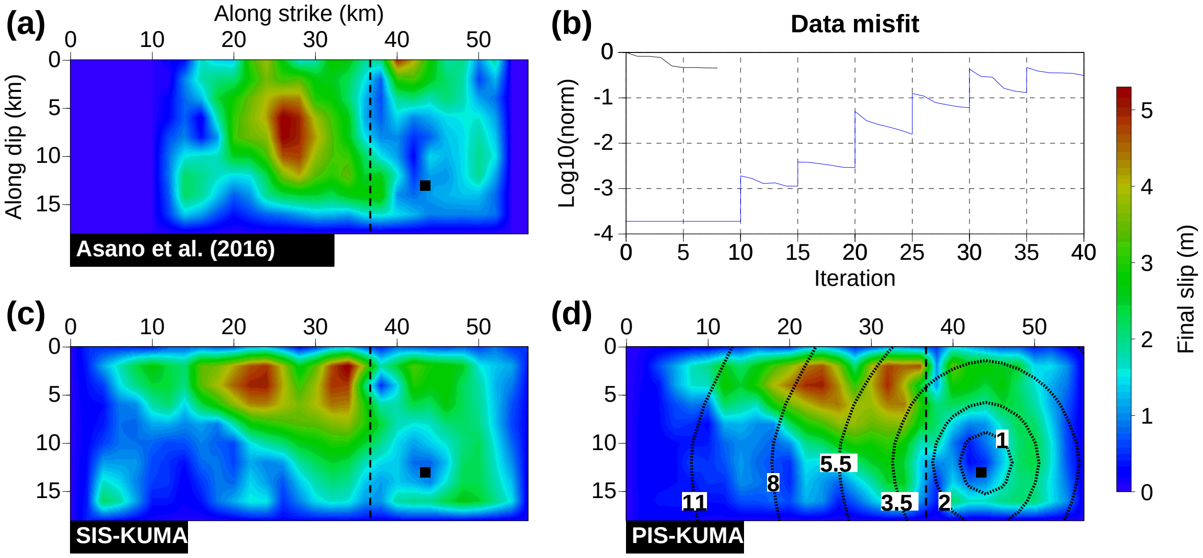

Figure 4.13: Summary of the results obtained for the 2016 Kumamoto earthquake applying the SIS and the PIS. Panels (a), (c) and (d) show the final slip distributions from the prior model, SIS-KUMA and PIS-KUMA, respectively. Panel (b) shows comparison of the data misfit evolution (L2 norm) of the two inversion strategies. On panels (a), (c) and (d), the vertical black dashed line represents the boundary between the two defined fault segments while the black square represents the hypocentral location. Both strategies coincide in the overall shape of the final slip. See text for details.

inversion leakage. For instance, results from PIS-KUMA case exhibit less slip near the hypocenter and at the furthest maximum slip patch while still resolving well enough the seismic moment and the data misfit (Table 4.2). As a consequence of this behavior, the SIS-KUMA case overestimates the seismic moment (Table 4.2). On the contrary, results from the PIS2-KUMA seem better spatially constrained around some fault zones and the estimated seismic moment is closer to the one reported by the NIED.

In terms of data misfit (regarding only the inverted data), SIS-KUMA case achieves better results as the final data misfit is 2% less than the misfit from the PIS-KUMA case. However, this better fit of the data might be the consequence of having this wider space-time domain, allowing leakage between nodes. When the SIS-KUMA inversion is performed, more degrees of freedom can be used to fit the data even if strongly penalized. Therefore, the reduction of the data misfit for SIS-KUMA case is ensured in the least-squares sense. The PIS-KUMA case does not fit the data as well as the SIS-KUMA one (34% of data misfit) but the evolution of the number of inverted parameters is rather different. Figure 4.17 shows a comparison between observed seismograms (solid black line) and inverted seismograms (blue dashed line) for the PIS-KUMA case, corresponding to bottom traces. Top traces (solid black for observed ones and dashed red for synthetic ones) are not used during the inversion and their waveforms are very similar to the predicted ones by the slip-rate reconstruction illustrated in Figure 4.14. While the fit of inverted data is better for SIS-KUMA case (not shown in Figure 4.17), the prediction of traces not used during the inversion for the SIS-KUMA case shows later large oscillations on several recordings. These oscillations lead us to think that the SIS-KUMA inversion over-fits the observed data, inducing these spurious oscillations for predictions of unused signals: this is not the case for the PIS-KUMA inversion. Figure 4.15 illustrates these later oscillations at one of the 11 locations used for waveform prediction: a good quality-control criterion.

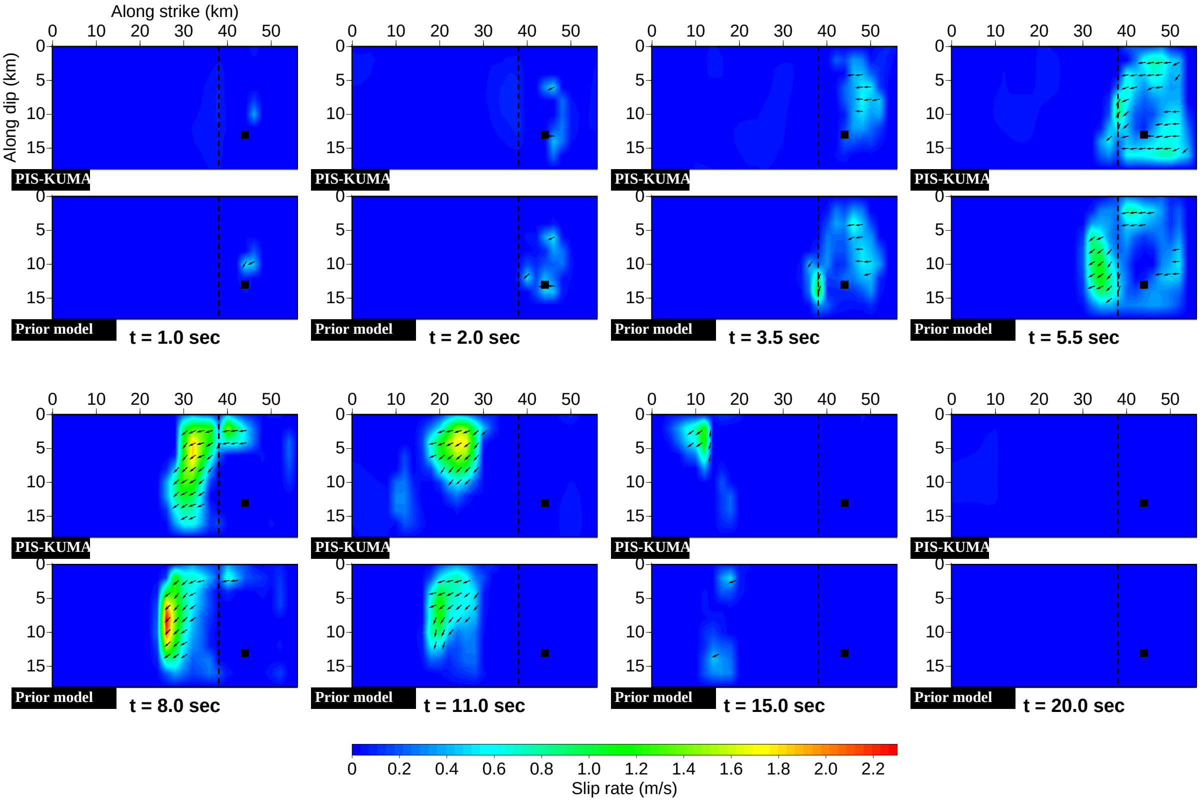

Figure 4.14: Comparison of the slip-rate spatio-temporal distribution obtained from the progressive inversion strategy with regularization (PIS-KUMA) and the prior model. Please note that the solution might differ from the prior model when asked by the data. The time evolution goes from left to right and from top to bottom from 1.0 to 20.0 s. The black square represents the hypocenter location and the dashed vertical black line the boundary between the two fault segments of the assumed fault geometry. Arrows display rake direction of the slip-rate vector.

It is important to mention that, even if the results from SIS-KUMA and PIS-KUMA workflows are different, both fit quite well the data and show plausible rupture evolutions. The difference between SIS-KUMA and PIS-KUMA strategies is one more illustration of the non-uniqueness of the solution, emphasizing the importance of uncertainty quantification in the future. In addition, this difference is also an illustration of how important are the assumed hypothesis governing rupture physics by model preconditioning and regularization. The estimated average rupture speed extracted from the arrival times of the maximum value of the slip-rate functions at each node is ≈ 2.4 km/s. The local values of rake angle that are assumed in this work come from the results from the previous study of Asano and Iwata (2016) and we do not explore the variability of these results with unset rake values. In agreement with these previous studies, the areas that exhibit the maximum slip (≈ 5.1 m for PIS-KUMA case and ≈ 5.3 m for SIS-KUMA case) in this study have a small normal component, around $15^o - 20^o$ from the strike-slip direction, while the other zones exhibit only strike-slip motion. This normal component of the motion at these areas is a coincidence of all the previous studies of this mainshock and we consider that using this information as a prior information is a pertinent assumption.

According to the PIS-KUMA results, taken as the "best" solution, the rupture initiates on the shortest segment of the fault system. The slip near the hypocenter is considerably less (from 0.2 to 0.9 m) than other shallow regions that exhibited a slip of $\approx$ 5 m. The rupture first propagates mostly to the

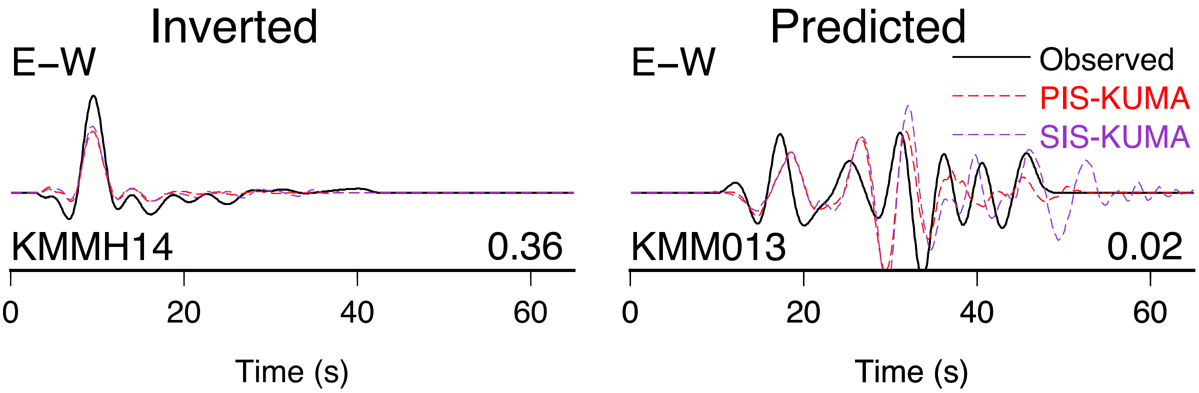

Figure 4.15: Comparison of observed (solid black line) and synthetic seismograms from slip-rate distributions of the SIS-KUMA case (purple dashed line) and the PIS-KUMA case (red dashed line). On the left, the receiver is used in the inversion (similar results in both cases). On the right, the receiver is not used during the inversion but the traces are predicted from the results. SIS-KUMA prediction presents spurious oscillations while PIS-KUMA one does not. Both traces are E-W components. Receiver name and maximum observed velocity (in m/s) are also provided along the time axis. The location of the corresponding station can be seen in Figure 4.1.

south-west of the Hinagu fault at a low speed around 2.0 km/s (see first three snapshots in Figure 4.14). After approximately 5 seconds, the rupture crossed to the Futagawa fault. The rupture across this fault segment propagated from the south-west to the north-east and from deep to shallow zones. The rupture speed accelerated from 2.0 km/s to around 2.6 km/s near the two areas having the maximum slip ($\approx$ 5.1 m). The rupture does not reach the pre-defined fault boundaries, with the exception of the upper boundary that exhibits a maximum slip of $\approx$ 1.4 m. Once the rupture passes the last area of maximum slip (25 km along strike far from the hypocenter), the rupture speed increased until $\approx$ 2.9 km/s (see transitions from snapshot 6 and 7 in Figure 4.14). Apparently, this faster speed does not exceed the local shear wave speed of the medium at this region ($\approx$ 3.2 km/s). However, this increment of the rupture speed could be a consequence of the acceleration that the rupture suffers after breaking the last patch and the lack of resistance to stop the rupture at this furthest region, which could cause a local instantaneous acceleration.

Table 4.2: Summary of the results for the SIS and PIS approaches applied to the 2016 Kumamoto mainshock.

	M_0 $\times 10^{19}$[Nm]	Final data misfit [%]
NIED	4.42 (M_w 7.06)	
SIS2-KUMA	5.52 (M_w 7.12)	32
PIS2-KUMA	4.86 (M_w 7.09)	34

As an overall evaluation, the final slip distributions from SIS-KUMA and PIS-KUMA cases are in agreement with the results from Asano and Iwata (2016), Uchide et al. (2016) and Hao et al. (2017). The hypocentral zone compared to other zones on the fault segments does not provide significant slip contribution. The areas with maximum slip exhibit a normal component of the particle motion. The slip-rate propagates from deep to shallow zones and the maximum slip is around 5 to 6 m. However,

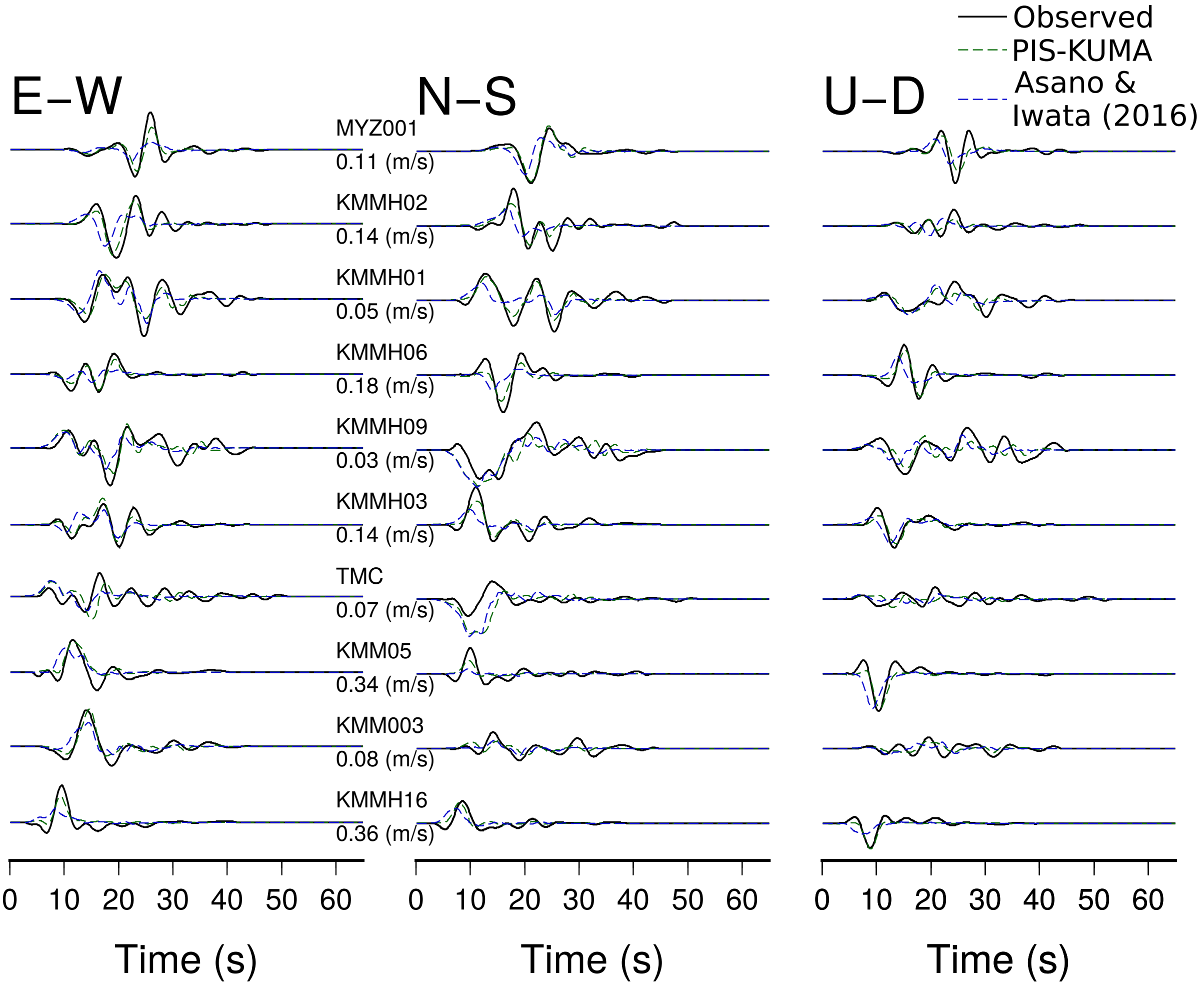

Figure 4.16: Comparison between observed and synthetic wavefields at the inverted sites that are in common for the PIS exercise and the work from Asano and Iwata (2016). Black solid lines represent observed velocity recordings band-pass filtered (0.025-0.25 Hz). Green and blue dashed lines correspond to the synthetic seismograms for stations included in the PIS-KUMA case and for the reconstructed model from Asano and Iwata (2016), respectively. Receiver name and maximum observed velocity at each location are provided next to each E-W trace. Acoording to a normalized L2 norm, where every trace contributes equally to a 100% of misfit, the seismograms from the source model proposed by Asano and Iwata (2016) have a misfit of 82% compared to 54% obtained from the PIS-KUMA.

both solutions show two patches of maximum slip instead of only one as found by others: the diversity of solutions is one key feature of kinematic inversions. The selected fault geometry and the given velocity structure might have an impact and should be investigated. Nevertheless, we have shown that the evolutive linear kinematic inversion can be applied to real datasets. Finally, acoording to a normalized L2 norm, where each of the traces contribute equally to a 100% of misfit, the seismograms estimated from the source model proposed by Asano and Iwata (2016) have an 82% of misfit compared to a 54% from the ones obtained for the preferred model PIS-KUMA (see Figure 4.16).

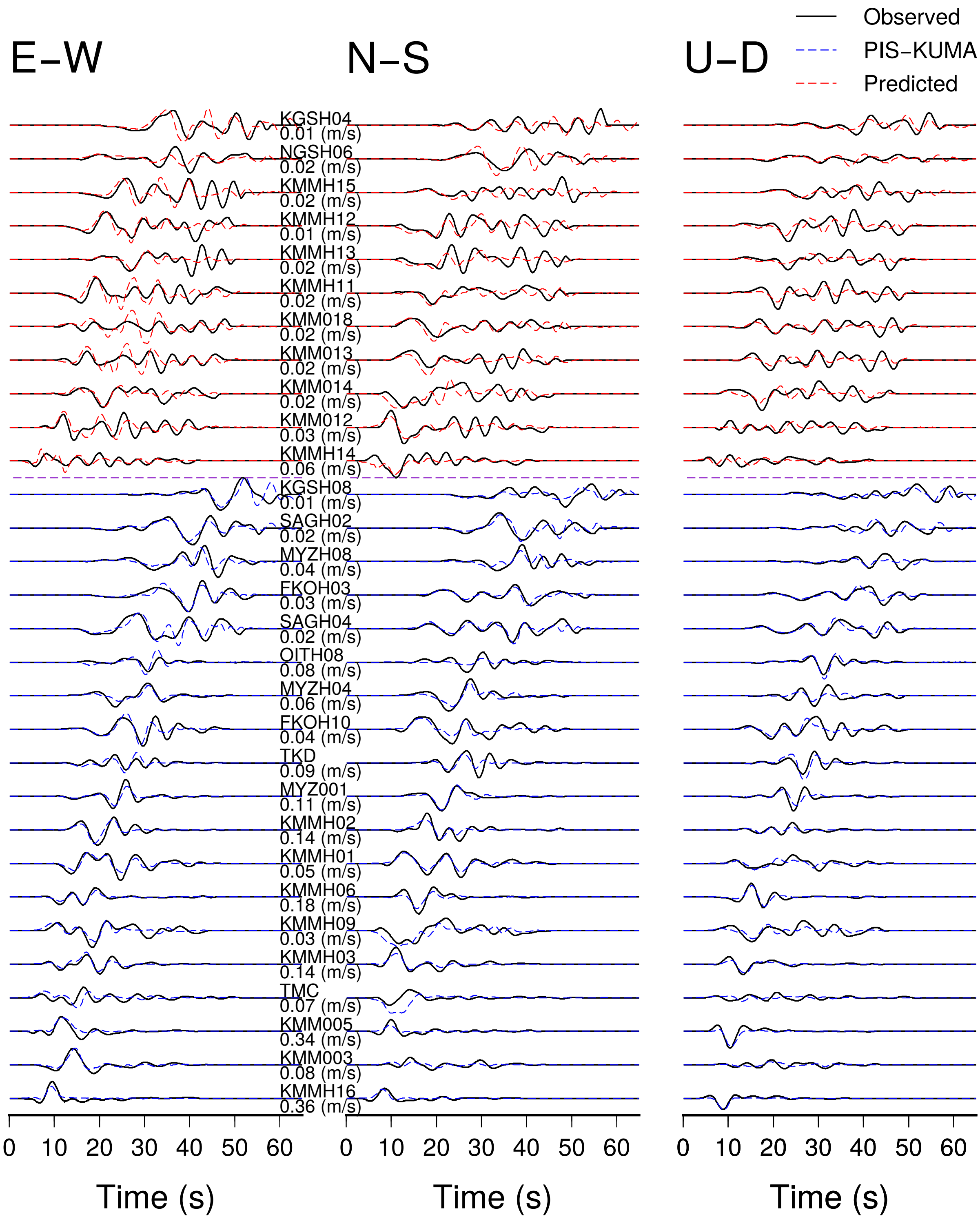

Figure 4.17: Comparison between observed and synthetic wavefields at 30 stations. Black solid lines represent observed velocity recordings band-pass filtered (0.025-0.25 Hz). Blue and red dashed lines correspond to the synthetic seismograms for stations included in the PIS-KUMA case and for those not included but predicted, respectively. Receiver name and maximum observed velocity at each location are provided next to each E-W trace.

4.5 Conclusion

In this chapter, I successfully apply the progressive inversion strategy to the real data set of the 2016 (M_w7.0) Kumamoto earthquake. This strategy is based on a time-domain formulation where the causality feature of the source rupture strongly drives the inversion, mitigating leakage and ambiguity for the reconstruction. By progressively considering increasing time-windows at receivers, slip-rate is carefully built up on the source surface starting from the hypocenter: Later phases delayed by the propagation kernel are removed for later slip-rate reconstruction. This time-domain formulation is based on a linear formulation of the forward problem and an adjoint-state formulation of the optimization (see Chapter 3 for details). In this inversion, the whole time-space history of the slip-rate vector across a 3D grid representing continuously the source geometry and history is reconstructed. Therefore, the source time function is not assumed at each node but is reconstructed. In a very flexible and intuitive way, all basic ingredients, such as regularization, prior information and model preconditioning, are introduced in this approach (see Section 4.3). One may foresee that complex ruptures could be considered for dense acquisition network in the future. Meanwhile, prior information is necessary and is based on expected physical behavior of the seismic rupture. In short, under this linear time-domain formulation, the progressive and limited increment of the time-space samples used to invert the source history according to the increasing data time windows reduces the leakage of the information over a large fixed number of time-space samples. This way of handling simultaneously the data and the unknowns reduces the ambiguity or cross-talk between neighboring time-space nodes preventing them from representing an equivalent rupture history that, to some extent, fits the data as well as the target solution. With this new hierarchical approach on how to extract information from seismic data for source imaging based on causality, there are two important contributions of this work. The first one is the possibility of performing a partial source reconstruction based on available windows, even before the end of the rupture, opening the door for early warning issues. In other words, by analyzing only the first seconds of a given dataset, the nucleation and the beginning of the seismic rupture could be imaged without waiting for the full dataset. This time formulation of slip-rate values, related to a wide model space, should be constrained through data-driven and model-driven strategies. Model-driven component injects soft information on how seismic rupture could physically occur reduces the ill-conditioning of the kinematic reconstruction while still keeping a linear inverse formulation, while alternative reduced-order model strategies in time or in frequency widely used in seismology impose hard constrains on the rupture.

The second main contribution of this work comes with the linearity with respect to model parameters we have preserved in the forward problem. We have shown that the reconstruction is possible in spite of the drastic increase of unknowns by designing prior models and model covariances (covariance build-up has been kept simple as diagonal matrix but could be improved in the future if needed). This linear property opens road for stochastic inversion in a Bayesian approach which has been recognized as very important for uncertainty quantification in source imaging (Minson et al., 2013). Variabilities of kinematic source reconstruction emphasizes the importance of uncertainty quantification and the need of stochastic inversion for which an evolutive inversion approach based on a forward linear problem is quite appealing.

Nowadays, there is a wide variety of strategies to perform a kinematic source inversion. However, to my knowledge, even if most of them are quite fast and efficient, these strategies are using the entire set of records for the investigated event and leave the fitting process to the inversion scheme. In this chapter, I illustrate some important features of this progressive time-domain formulation tackling the real data of the 2016 Kumamoto earthquake: 1) different slip and slip-rate distributions can be obtained from a full-time-window strategy or an increasing-time-window strategy, 2) for both strategies the overall structure of the distributions is recovered, 3) as shown in Section 4.3, physical plausible regularization terms can be expressed in a natural way without a significant increment of the computational cost or any change in the inverse formulation, 4) thanks to a pre-computed database of the stress-state tensor the progressive strategy is able to invert very short data time-windows and the results can be used to provide a rough estimation of delayed phases that are not yet recorded. Thus, this progressive strategy opens the door to quasi-real-time inversions while recording is still occurring. For the current seismic networks surrounding active faults, physical prior models of the seismic rupture are essential for these time-domain formulation: as there are more parameters than unknowns. Nothing prevents us to consider more complex rupture scenarios, especially when more data will be available. It is important as well to highlight that the rake attribute extracted from the two slip-rate components is poorly constrained by current acquisition design. Therefore, slip-rate vector inversion should be cautiously performed in a hierarchical way with prior constraints regarding the variability of the rake angle. In the future, the drastic increase of receivers might reduce this requirement.

Chapter 5

Bayesian inference and kinematic source inversion

> *"La probability est relative en partie à cette ignorance, en partie à nos connaissances."*
>
> — Pierre-Simon Laplace, 1840

Contents

5.1 Introduction

As I show in the previous chapters, the kinematic source inversion problem consists of providing a reconstruction of the time and space history of a seismic rupture which explains, to some degree of accuracy, a given set of observations (seismograms, accelerograms or geodetic data). However, the solution of the ill-posed kinematic inverse problem is non-unique. For instance, it is possible to appreciate the large variability between the kinematic models proposed to explain the rupture of the 2010 (M_w8.8) Maule, Chile, earthquake in Figure 1.10. In addition, according to current acquisition systems surrounding active faults, this problem is highly under-determined, in spite of its rather simple formulation as a linear inverse problem. Regarding all these limitations, it is possible to say that there are as many acceptable kinematic models for a given earthquake as authors working on it. However, accurate kinematic models are fundamental to enhance our knowledge of the seismic cycle as well as to improve surface ground motion prediction. Consequently, because it is impossible (up to now) to give an accurate and unique solution correctly representing a real earthquake source, it is necessary to assess the uncertainties associated to any proposed model.

Optimistically, it can be seen that for some recent earthquakes that present a large set of observations with a significant good azimuthal distribution (reducing the under-determination of the problem) the proposed models provided by different authors are not so different from each other (see for instance the results proposed for the 2016 Kumamoto earthquake from Asano and Iwata, 2016; Uchide et al., 2016; Hao et al., 2017; Sánchez-Reyes et al., 2018). Agreement between solutions might mean that we are all observing solutions in the vicinity of the true solution. Due to uncertainties on the modeling, fault geometry, description of the medium and data accuracy, a closer estimation to the true solution is prevented. However, similar results might be inside the same cloud of probable scenarios, or in other words, they belong to the same probability distribution. Therefore, providing a description of this vicinity of probable solutions seems to be much more suitable to tackle this problem than providing a unique (inaccurate) rupture model for a given earthquake.

Some authors have focused their work to study all the possible sources of uncertainties that are part of this problem. For instance, regarding our poor knowledge of the velocity-density structures and the impact that this limited knowledge has in our inferences of the source parameters, I can mention the work from Yagi and Fukahata (2011) and Hallo and Gallovič (2016). Another important source of uncertainties is related to all the simplistic geometrical assumptions that are used to describe the fault surfaces where the rupture occurs. Usually, simple models with one, two or even three different fault segments with prescribed geometries (strike and dip angles) are used to represent the complex surfaces where the faulting takes place. I might as well mention the fact that opening across a fault is not discarded nowadays, which means that the slip vector is not always in the fault plane. Recently, Ragon et al. (2018) presented a framework which allows to account for the uncertainties of fault geometry into the static source inversion. However, the extension of this strategy to the kinematic inversion problem has not yet been explored. A third source of uncertainties is related to the different possible shapes that the slip-rate functions can take (under non-linear formulations). The work from Razafindrakoto and Mai (2014) presents an investigation regarding the impact of the uncertainties of the assumed source time functions, as well as the unknown velocity-density structure, into the kinematic source inversion problem. Finally, all the available data used to study earthquakes has a significant level of noise that might not be completely removed by the digital filters, which might be another source of uncertainties that can impact our results without mentioning the limited coverage that current acquisition systems provide.

Duputel et al. (2012) and Minson et al. (2013) are some of the pioneering works related to the uncertainty assessment of static and kinematic models in the earthquake source imaging field. To my knowledge, these works are the first to explore in a completely Bayesian framework this problem. Several other works such as Duputel et al. (2014) or Hallo and Gallovič (2016) continue the development of this research field, establishing ways to account for the estimated uncertainties related to the unknown velocity structure into the source inversion strategies. However, most of the works related to this topic still relies on non-linear formulations of the forward problem: the source history is described by a reduced number of parameters such as rise time, rupture velocity, rake angle and slip amplitude. These parameters are not linearly related to the observed seismograms. And, even though such parameters drastically diminishes the dimensionality of the model space where the exploration has to be performed, this parametrization implies drastic assumptions on the rupture history.

In this chapter, I present a Monte Carlo strategy to tackle the kinematic source inversion problem under a linear time-domain formulation. This strategy is based on Hamiltonian dynamics, which can be used to efficiently describe, under a Bayesian framework, the high dimensional probability distribution of solutions to this inverse problem. The development here presented could be used to tackle the following two goals: 1) To make an attempt to obtain the solution to the kinematic source inversion problem together with the associated uncertainties or 2) to assess the uncertainties around a given solution which can come from either a Bayesian or a deterministic approach. In this chapter I present a preliminary investigation focused on the second goal. Under this approach, I provide two synthetic examples under an idealized source-receiver geometry to illustrate the advantages and performance of this promising technique.

Outline Consequently, this chapter is organized as follows:

- In Section 5.2, I mention basic concepts related to Bayesian inference. In this section, I introduce concepts such as the prior, likelihood and data evidence probability distribution functions and how these concepts can be used to infer characteristics of a target function that needs to be explored.
- In Section 5.3, I present two different strategies to perform the exploration of a posterior probability functions: 1) a standard Markov Chain Monte Carlo strategy and 2) a Hamiltonian Monte Carlo approach. Once the fundamental concepts of both strategies are presented, I give two encouraging examples that illustrate some of the advantages of the HMC approach over the standard MCMC.
- In Section 5.4, I reformulate the inverse problem that I present in Chapters 3 and 4 to be able to work with the HMC approach. In this section, I demonstrate the suitability of the HMC strategy to tackle the kinematic source inversion problem applying it to two synthetic case: 1) a simple spike test and 2) a more complex bilateral rupture.
- Finally, in Section 5.5 I discuss some conclusions and perspectives for this new strategy as well as its limitations.

5.2 Bayesian inference

Let me start with a non-exhaustive description of how the Bayesian statistical inference works and what are the fundamental ingredients necessary to infer probable values of the unknown parameters which solve an inverse problem. This section does not offer a rigorous mathematical formulation of the concepts behind Bayesian inference. To have a deeper insight on this topic and its application to geophysical problems, I invite the reader to consult works as Olofsson and Andersson (2005); Sen and Stoffa (2013) and Tarantola (2005).

5.2.1 Bayes Theorem

Let me first state Bayes theorem, which is the mathematical expression that lies behind all what is presented in this chapter.

To do that, let us define two events that are observed to occur independently. The first event is denoted as event $\mathbf{A}$, while the second is $\mathbf{B}$. The probabilities of observing each of these two events are defined as $P(\mathbf{A})$ and $P(\mathbf{B})$. Such probabilities are also known as the *marginal probabilities*. I can now define the conditional probability of observing event $\mathbf{A}$ given that event $\mathbf{B}$ happened as $P(\mathbf{A}|\mathbf{B})$. This conditional probability is also known as the *likelihood* of $\mathbf{A}$ given $\mathbf{B}$. Here, I denote the joint probability of both events occurring as $P(\mathbf{A} \cup \mathbf{B})$. This joint probability of both events occurring is estimated as the product of the marginal probability of $\mathbf{B}$ and the likelihood of $\mathbf{A}$ given $\mathbf{B}$, or vice versa. In other words,

$$P(\mathbf{A} \cup \mathbf{B}) = P(\mathbf{A}|\mathbf{B})P(\mathbf{B}) = P(\mathbf{B}|\mathbf{A})P(\mathbf{A}). \tag{5.1}$$

Thus, the relationship between the two conditional probabilities can be expressed as

$$P(\mathbf{A}|\mathbf{B}) = \frac{P(\mathbf{B}|\mathbf{A})P(\mathbf{A})}{P(\mathbf{B})}. \tag{5.2}$$

In terms of a general inverse problem, such as $\underline{\underline{G}}\,\underline{m} = \underline{d}$, where $\underline{d}$ is the vector of observations, $\underline{m}$ is the vector of unknowns and $\underline{\underline{G}}$ is the mapping operator from the space of unknowns to the space of observables, equation (5.2) can also be written as,

$$P(\underline{m}|\underline{d}) = \frac{P(\underline{d}|\underline{m})P(\underline{m})}{P(\underline{d})}, \tag{5.3}$$

which means that the probability of a certain model $\underline{m}$ given the observed data $\underline{d}$ can be obtained as the product between the marginal probability of the model (i.e. *prior probability of the model*) and the likelihood of the data divided by the marginal probability of the data (i.e. *evidence of the data*). In terms of the kinematic source inversion problem, $P(\underline{m}|\underline{d})$ is the probability of a reconstructed slip-rate time-space history $\underline{m} = \underline{V}(\underline{\xi}, \tau) = [V_\phi(\underline{\xi}, \tau), V_\delta(\underline{\xi}, \tau)]^T$ given a certain set of data (e.g. seismograms) $\underline{d} = \underline{v}(\underline{x}, t) = [v_x(\underline{x}, t), v_y(\underline{x}, t), v_z(\underline{x}, t)]^T$.

I would like to highlight that the main goal of equation (5.3), contrary to the form $\underline{m} = \underline{\underline{G}}^{-1}\underline{d}$, is not to find the most suitable $\underline{m}$ explaining $\underline{d}$. What equation (5.3) aims at doing is to provide an estimate of the probability of $\underline{m}$ given the observed data $\underline{d}$, and nothing more. Consequently, because the most suitable $\underline{m}$ remains unknown, it is our duty to smartly use this estimated probability $P(\underline{m}|\underline{d})$ to infer not only the most suitable solution but also the uncertainties related to it.

5.2.2 Key ingredients of Bayesian statistical inference

As it was mentioned above, Bayes theorem relies on three fundamental probabilities to estimate the suitability and uncertainties of a given model $\underline{m}$. These three ingredients are: 1) $P(\underline{d}|\underline{m})$ the likelihood of the data given a certain model, 2) $P(\underline{m})$ the prior model probability and 3) $P(\underline{d})$ the evidence of the data. It can be seen in equation (5.3) that the evidence of the data acts as a normalization factor. This term is the one in charge of limiting $P(\underline{m}|\underline{d})$ to a range between 0 (unlikely) and 1 (likely). Therefore, the term related to the evidence of the data can be estimated as,

$$P(\underline{d}) = \int_{\underline{m}} P(\underline{m}|\underline{d})P(\underline{m})d\underline{m} \tag{5.4}$$

However, most of the real and complex problems tackled in the real world have large dimensions. These real world problems pose some big obstacles to estimate this data evidence term. For instance, one important reason why $P(\underline{d})$ is often computationally intractable is the fact that for its computation it is required to integrate over the whole model space. Whether a closed form for the prior or the likelihood *pdf*s are known or not, this integration makes the computation of the data evidence prohibitive. Therefore, the evidence of the data is commonly not estimated in practice.

Fortunately, the evidence of the data is only a normalization factor. Consequently, even if this term is not estimated, $P(\underline{m}|\underline{d})$ remains proportional to the product of the prior probability $P(\underline{m})$ and the likelihood $P(\underline{d}|\underline{m})$,

$$P(\underline{m}|\underline{d}) \propto P(\underline{d}|\underline{m})P(\underline{m}). \tag{5.5}$$

This proportionality is the feature used to infer characteristics of the probability distribution function $P(\underline{m}|\underline{d})$, which is the one we are interested in.

Now that the evidence of the data is discarded, it is possible to focus our attention to the other remaining two terms: the prior probability $P(\underline{m})$ and the likelihood $P(\underline{d}|\underline{m})$. These two terms, together with another one, known as the *proposal probability distribution function*, are the principal ingredients of any Bayesian inference technique. Let me then define these terms.

Prior probability distribution function $P(\underline{m})$: In Bayesian statistical inference, this function is the one in charge of reflecting the degree of certainty that we have of a particular model $\underline{m}$ based on the prior knowledge that we have about the possible values that this model can take. This degree of certainty is taken from a probability distribution function that is built based on the available prior knowledge. It is important to notice that the probability that is associated to a certain model $\underline{m}$ by this probability distribution function does not take into account any evidence (such as seismograms in the source reconstruction problem) that can help to support or disapprove our level of confidence on that model. In terms of the kinematic source inversion problem, this function is used to estimate the probability that a particular rupture model based on any prior knowledge in our hands, such as the shape of expected slip-rate functions, rupture velocity, maximum slip, etc. For instance, Schmedes et al. (2010, 2013) propose to use dynamic simulations to build different possible prior models.

Likelihood probability distribution function $P(\underline{d}|\underline{m})$: Contrary to the prior probability distribution function, the likelihood is defined as a particular function in charge of measuring the probability to observe a certain dataset $\underline{d}$ given a known model $\underline{m}$. The associated model $\underline{m}$ in this probability function is believed to well represent the frequency distribution of the population of all the possible models that explain, to some extent, the observed evidence. Once again, in terms of the kinematic source inversion problem, the likelihood is a function that estimates the probability of a given synthetic set of seismograms, associated to a given rupture model, to correctly represent the observed wavefields.

These ingredients, the prior and the likelihood probability distribution functions are at the core of the Bayesian statistical inference field. Let me now introduce two different techniques that have been proposed to infer characteristics of $P(\underline{m}|\underline{d})$ based on the concepts above mentioned.

5.3 Markov Chain Monte Carlo and Hamiltonian Monte Carlo

5.3.1 Markov Chain Monte Carlo (MCMC)

The Markov Chain Monte Carlo methods are a family of computational statistical techniques that employ two concepts: 1) Markov Chains and 2) Monte Carlo simulations to infer, or to estimate, characteristics of complex functions that, without using these numerical strategies, would be extremely difficult to assess. In order to understand the main idea behind these methods, let me explain briefly each of the concepts that form part of these techniques.

Monte Carlo methods: These techniques are direct sampling methods. These techniques are also known with the term *stochastic simulations*, as the sampling of a given function is randomly selected from all the available set of values that the function takes. The principal idea behind these techniques is that characteristics and other estimations of a given function can be obtained based on a repetitive massive random sampling of it.

Markov Chain: Following (Brooks et al., 2011), a sequence $\underline{m}^{(1)}$, $\underline{m}^{(2)}$, ..., $\underline{m}^{(n)}$, of random elements of some set is said to be a *Markov Chain*, if the conditional distribution of $\underline{m}^{(n+1)}$ given $\underline{m}^{(1)}, \ldots, \underline{m}^{(n)}$, depends on $\underline{m}^{(n)}$ only, which is denoted as $P(\underline{m}^{(n)}|\underline{m}^{(n-1)})$. The set in which every $\underline{m}^{(i)}$ takes place is know as the *state space* of the Markov Chain.

In the Bayesian statistical inference field there are several techniques that could be used to make an attempt to retrieve a correct description of $P(\underline{m}|\underline{d})$. One big family of these techniques are related to the Monte Carlo method as well as to the concept of Markov Chains. In order to further detail these techniques and their application to the kinematic source inversion problem, it is first necessary to introduce another important ingredient known as the *proposal probability distribution function*. Most of the Bayesian strategies that incorporate the Monte Carlo technique into their algorithms rely on a systematic evaluation of the conditional probability function $P(\underline{m}|\underline{d})$ of a large number of models (thousands or millions of them). Therefore, for those techniques it is very important to define a way, or a function, to select each of these models to be qualified from the enormous population of all the possible models. This function is known as the *proposal probability distribution function*.

Proposal probability distribution function $P(\underline{m}^{(k)}|\underline{m}^{(k-1)})$: This probability function acts as a conventional transition operator that allows to go from one initial state $\underline{m}^{(k-1)}$ to a next state $\underline{m}^{(k)}$ according to a given probability. Commonly, the new proposed state depends only on the previous state. This characteristic of the proposal distribution is also known as a *memoryless* transition. In terms of the kinematic source problem, this proposal function can be seen as an engine that is able to provide different rupture models (that have to respect some physical constraints) that might depend or not on a previous estimated rupture model.

Markov Chain Monte Carlo methods (MCMC): These strategies combine the Monte Carlo random sampling techniques together with the Markov Chain concepts to perform a more efficient, compared to simple Monte Carlo methods, exploration of a given function. The idea is to construct a particular Markov Chain of K states, $\underline{m}^{(1)}$, ..., $\underline{m}^{(K)}$, using a repetitive random sampling Monte Carlo method described by the proposal probability distribution function. In order to accept a new proposal state $\underline{m}^{(k^*)}$ to form part of the state space, an acceptance/rejection criterion has to be passed by the new proposed state. As the number of random samples grows, $K \to \infty$, the state space constructed by the MCMC technique is expected to converge towards the sampled function (feature known as *stationarity* of the Markov Chain). Consequently, the built Marcov Chain from these strategies can be used to infer characteristics of the *ppd* which is the probability distribution we want to describe.

It is important to highlight that, with the massive use of the ingredients, $P(\underline{m})$, $P(\underline{d}|\underline{m})$, and $P(\underline{m}^{(k)}|\underline{m}^{(k-1)})$, the MCMC methods are able to determine (approximately and fulfilling some requirements) the shape of $P(\underline{m}|\underline{d})$, which is the main goal. When this distribution is sampled enough, the resulting *posterior probability density* (*ppd*), offers a correct representation or a map of the probable solutions to a given problem and how well they are distributed inside the space of probable solutions. For instance, in terms of the source reconstruction problem, the shape of this function will allow us to evaluate the most probable value of the slip-rate function at a position on the fault and at a given time, $\underline{V}(\xi, \tau)$, taking into account the observed seismograms, $\underline{v}(\underline{x}, t)$ and any prior information. Moreover, not only the most probable scenario could be obtained, but also a description of its vicinity, which allows to assess the uncertainties of the most suitable rupture model.

Certainly, many more things can be said about the Monte Carlo simulations, Markov Chains, and the MCMC strategies. The purpose of this chapter, however, is not to detail these strategies. The reader is invited to consult Brooks et al. (2011), and references therein, to have an exhaustive explanation of many of the different properties, and derived techniques related to the MCMC methods.

One of the principal ingredients of the MCMC methods, besides the probability distribution functions that were already mentioned in the previous section (i.e. prior, likelihood and proposal probability distribution functions), is the acceptance/rejection criterion. This criterion has been a complete field of study. Metropolis et al. (1953); Hastings (1970) and Green (1995) are three of the most important publications discussing this criterion, as well the impact that it has on the MCMC strategies, and its generalization to facilitate a correct sampling of the target functions. In this work, however, I keep simple the discussion about this criterion. Therefore, the reader has to know that the acceptance/rejection criterion in this work is always referred to a Metropolis-Hastings (MH) generalization. Which means that, in order to accept a new proposed state $\underline{m}^{(k^*)}$ to be part of the Markov Chain as $\underline{m}^{(k)}$, the ratio of probabilities r, estimated as

$$r = \frac{P(\underline{m}^{(k^*)}|\underline{d})P(\underline{m}^{(k-1)}|\underline{m}^{(k^*)})}{P(\underline{m}^{(k-1)}|\underline{d})P(\underline{m}^{(k^*)}|\underline{m}^{(k-1)})} \tag{5.6}$$

has to be compared to a number u, that is sampled from a uniformly distributed function $u = \text{Unif}(0, 1)$, and the decision to accept or reject the proposal state is based on that comparison as follows,

$$\begin{cases} \underline{m}^{(k)} = \underline{m}^{(k^*)} & \text{if} \quad u < r, \qquad \text{(accept)} \\ \underline{m}^{(k)} = \underline{m}^{(k-1)} & \text{if} \quad u \geq r, \qquad \text{(reject)} \end{cases} \tag{5.7}$$

This acceptance/rejection criterion has the particular characteristic that, for every proposal whose probability $P(\underline{m}^{(k^*)}|\underline{d})$ is larger than $P(\underline{m}^{(k-1)}|\underline{d})$ (being $r > 1$), the proposal $\underline{m}^{(k^*)}$ is always accepted. Therefore, an efficient exploration towards the regions with denser probabilities is ensured. In addition, other proposals whose probabilities $P(\underline{m}^{(k^*)}|\underline{d})$ are less than $P(\underline{m}^{(k-1)}|\underline{d})$ can still be accepted, as long as $u < r$. Such acceptance/rejection criterion is supposed to alleviate the problems that a MCMC exploration can have when dealing with rough functions, in which the chain can be prone to get trapped in certain regions (preventing a complete exploration of the target function).

Based on all the above mentioned: prior, likelihood and proposal distribution functions, as well as Monte Carlo simulations, Markov Chains and the acceptance/rejection criterion, a standard MCMC algorithm based on the Metropolis-Hastings criterion can be set as follows,

Algorithm 3: Standard Monte Carlo Markov Chain algorithm based on MH acceptance criterion.

```
input : Expressions for the estimation of the prior, likelihood and proposal probability
        distribution functions;
Set $k = 0$
Get first state, $\underline{m}^{(k)}$, from the prior probability functions $\underline{m}^{(k)} \sim P(\underline{m})$
while $k < K$ do
    set $k = k + 1$;
    Draw a new state $\underline{m}^{(k^*)}$ using the proposal probability functions $\underline{m}^{(k^*)} \sim P(\underline{m}^{(k^*)}|\underline{m}^{(k-1)})$;
    Estimate the ratio $r = \frac{P(\underline{m}^{(k^*)}|\underline{d})P(\underline{m}^{(k-1)}|\underline{m}^{(k^*)})}{P(\underline{m}^{(k-1)}|\underline{d})P(\underline{m}^{(k^*)}|\underline{m}^{(k-1)})}$ (Metropolis-Hastings algorithm);
    Draw a random number $u$, where $u = \text{Unif}(0, 1)$;
    if $u < r$ then
        accept the proposal state $\underline{m}^{(k^*)}$ and set $\underline{m}^{(k)} = \underline{m}^{(k^*)}$ ;
    else
        reject and set $\underline{m}^{(k)} = \underline{m}^{(k-1)}$ ;
```

Numerous problems can be tackled using the standard MCMC Algorithm here presented. However, this powerful strategy reduces exponentially its efficiency as the dimensionality of the problems tackled increases. This feature is well-known in the related research fields, and its basically due to two things: 1) the exponential growth of the space where the exploration has to be performed and 2) the random walk behavior along high dimensional spaces. To improve the efficiency of the space exploration several different strategies, based on the simplest MCMC algorithm, have been proposed to mitigate these effects. In this chapter, I focus my work on a specific technique based on Hamiltonian dynamics that, in recent years, has called the attention of many researchers working with high-dimensional problems, such as the kinematic source inversion problem that I want to tackle.

5.3.2 Hamiltonian Monte Carlo (HMC)

In the last decades, more sophisticated Monte Carlo strategies have been specifically developed in order to tackle high-dimensional problems. All these strategies are based on an efficient exploration of the high-dimensional space instead of a simple random-walk. Some of these methods, such as the optimal directional Gibbs sampler, relies on a pre-computation of optimal and independent directions where to explore (Christen et al., 2017). Other strategies, as the Langevin and Hamiltonian Monte Carlo rely on physical principles to generate in a more efficient way a new state of the random walk that allows a faster sampling of the target *ppd*.

Standard MCMC algorithms based on Metropolis-Hastings acceptance/rejection criterion are well-known to be hampered by their random-walk behaviors, specially for high-dimensional problems. One way to accelerate the space exploration is to add auxiliary variables that can help the chain to move more rapidly though the target distribution. An interesting family of methods that apply this augmented strategy are the Hamiltonian Monte Carlo methods. These techniques rely on the addition of a momentum term to each component of the target space. Then, both variables are updated together using Hamiltonian dynamics and the MH criterion. In this sense, Hamiltonian dynamics are used in order to get a new proposed state while MH criterion is in charge of accepting or rejecting the proposal. Contrary to the random-walk of the MCMC strategies, the HMC techniques take benefit from a different sampling rule. Such sampling rule, instead of being controlled by the proposal probability function, is based on a physical system known as Hamiltonian dynamics. This algorithm is designed to favor jumps inside the space according to a distance and a direction, which are controlled by the auxiliary variables that are related to the gradient of the target density function being explored. Thus, this different sampling algorithm allows the chain to move rapidly through the space, which allows a faster convergence towards the high density regions of the target distribution. In the following sections of this chapter, I present the fundamental concepts behind the HMC as well as the application of this technique to the kinematic source inversion problem.

Hamiltonian dynamics

Hamiltonian dynamics are a very useful tool to describe the motion of a particle through a system, which is shaped by the misfit landscape of the model space. In this section, I explain how it is possible to use the concepts related to Hamiltonian dynamics to assess the uncertainties of a general inverse problem. Let me then start describing the system that links the position and momentum of a particle and how this system can be linked to the probability distribution function that we want to explore.

Consider first a given particle position $\underline{q}$, which represent the model parameters (e.g. the time-space slip-rate history), and its momentum $\underline{p}$. The vector $\underline{p}$ has the same dimension as $\underline{q}$, and each of its elements represent an auxiliary variable that is used to perturb the corresponding position (i.e. slip-rate value) of the particle. The position and the momentum have an associated potential $U(\underline{q})$ and kinetic $K(\underline{p})$ energies respectively. One can see that, neglecting other forces or interactions in the system, the total energy of the system, hereafter referred as Hamiltonian, at a given time instant t is the sum of these two energies,

$$H(\underline{q},\underline{p}) = U(\underline{q}) + K(\underline{p}). \tag{5.8}$$

Because no external forces are acting in the system, such as friction, the Hamiltonian or total energy $H(\underline{q},\underline{p})$ must remain constant during the evolution of the system. For instance, if there is an increment of the potential energy, the kinetic energy has to be reduced in order to keep constant the total energy of the system. The Hamiltonian equations are a set of differential equations describing this balance between potential and kinetic energies during the time evolution of the system,

$$\frac{\partial q_i}{\partial t} = \frac{\partial H}{\partial p_i} = \frac{\partial K(\underline{p})}{\partial p_i} \tag{5.9}$$

$$\frac{\partial p_i}{\partial t} = -\frac{\partial H}{\partial q_i} = -\frac{\partial U(\underline{q})}{\partial q_i} \tag{5.10}$$

The ensemble of equations (5.9) and (5.10) form a symplectic structure. This set of Oridnary Differential Equations (ODEs) make H to be constant when a proper integration in time is performed. From equations (5.9) and (5.10), it can be seen that having expressions for $\partial U(\underline{q})/\partial q_i$ and $\partial K(\underline{p})/\partial p_i$, and knowing the initial conditions of the system $[\underline{q},\underline{p}]_{t=0}$, it is possible to predict the position and momentum of an object at any time instant by simulating the evolution of this dynamic system.

Let me now establish the link between the total energy $H(\underline{q}, \underline{p})$, which is preserved during integration thanks to the symplectic structure, and the probability distribution function $P(\underline{m}|\underline{d})$ that we want to describe. The energy $H(\underline{q}, \underline{p})$ can be related to $P(\underline{m}|\underline{d})$ through what is known as the *canonical distribution*,

$$\begin{aligned} P(H) = \frac{1}{Z}\exp(-H(\underline{q}, \underline{p})) &= \frac{1}{Z}\exp(-(U(\underline{q}) + K(\underline{p}))) \\ &\propto \exp(-U(\underline{q}))\exp(-K(\underline{p})) \propto P(\underline{q})P(\underline{p}) \end{aligned} \tag{5.11}$$

where $P(\underline{q})$ and $P(\underline{p})$ are independent probability distributions and Z is a normalization constant.

From equation (5.11), it is possible to see that the joint canonical distribution $P(H(\underline{q}, \underline{p}))$ can be factorized into the two independent terms $P(\underline{q})$ (for the position) and $P(\underline{p})$ (for the momentum). As I shall discuss further on, the position, which is related to values of parameters and its related potential energy can be directly linked to the misfit function of an inverse problem.

On the other hand, the momentum, and its associated kinetic energy, can be linked to the perturbations of the model parameters that are being investigated. The independence of both terms is an important property. Thanks to this feature, samples from the joint distribution $P(H(\underline{q}, \underline{p}))$ can be taken and, by ignoring the term related to the momentum (driving the model perturbation), inferences of the shape of the distribution associated to the position (misfit function of the inverse problem) can be done.

Potential energy: Assuming that a direct link between $\underline{q}$ and the unknown model parameters exists $\underline{q} = \underline{m}$, the potential energy $U(\underline{q})$, from equation (5.8), has to be a particular function that can help us to infer the shape of the probability distribution that we are looking for. Therefore, we can define this function in terms of the prior probability and the likelihood as

$$U(\underline{q}) = -\log(P(\underline{q})) = -\log(P(\underline{m}|\underline{d})) \propto -\log(P(\underline{d}|\underline{m})P(\underline{m})). \tag{5.12}$$

Equation (5.12) describes a function of $P(\underline{q})$ that, when negated and run through the exponential function can provide us, at least, a proportional estimation of the target distribution. Using this potential energy function, a straightforward physical interpretation of this function can be observed: a large potential energy, associated to a given model $\underline{m}$, corresponds to very unlikely model parameter values, while a small potential energy is translated into a high probable scenario.

Kinetic energy: Because the probability distribution for $P(\underline{q})$ is independent of the distribution $P(\underline{p})$, we can choose any distribution from which to sample the momentum variables. In this field, several authors (e.g Neal et al., 2011; Betancourt, 2017; Fichtner et al., 2018) suggest to use a zero-mean normal distribution with covariance matrix $\underline{\underline{M}}^{-1}$. The matrix $\underline{\underline{M}}$ is interpreted in the Hamiltonian dynamics as the mass matrix. This matrix must have a symmetric and positive definite structure. Therefore, a simple quadratic kinetic energy function can be defined in terms of the particle momentum as follows,

$$K(\underline{p}) = \frac{\underline{p}^T \underline{\underline{M}}^{-1} \underline{p}}{2}, \tag{5.13}$$

in such a way that

$$P(\underline{p}) \propto \exp(-K(\underline{p})), \tag{5.14}$$

It is worth to mention that it is the structure of the mass matrix which is in charge of controlling the independence (diagonal) or the coupling (non-diagonal) between the momentum of different particles.

The correlation between these momentum variables can be crucial when tackling problems such as the kinematic source inversion problem where we know there is an important trade-off between parameters. In addition, the form of the kinetic energy is chosen to be quadratic due to the fact that this shape allows to use the Hamiltonian dynamics as a transition probability function (proposal engine) with an important feature known as *reversibility*. A reversible transition probability function implies that the constructed Markov Chain, based on this transition function, will also be reversible and stationary. These features are fundamental to infer any characteristic of the target probability function from the Markov Chain.

I would like to point out the following. Because the particle position $\underline{q}$ is related to the model parameters of an inverse problem, the momentum $\underline{p}$ can be seen as the vector of auxiliary variables that ease a faster transition of a Markov Chain towards the regions with denser probabilities. In other words, we have double the number of unknowns, but $\underline{p}$ will serve us only to perturb $\underline{q}$ according to the information of the local estimation of the gradient of the misfit function.

Integration of Hamiltonian system: The main idea of the HMC strategy is to use the Hamiltonian system to accelerate the model space exploration of the Markov Chain. This is performed by using the time evolution of the system as the engine to draw a new sample, that, then should be accepted or rejected according to the MH criterion. Therefore, it is crucial to make evolve in time the Hamiltonian system. To do this, the authors working in this domain suggest to use symplectic integrators[1]. These numerical methods have, among some very useful characteristics, the property to keep (nearly) constant the total energy equal to the Hamiltonian expression. In fact, even though symplectic integrators are associated to Hamiltonian systems, a perfect energy conservation is not computationally mandatory or desired for a good exploration of a target function (e.g. see the detailed explanation provided by Neal et al., 2011). The simplest symplectic integration scheme, and the one I use through all this chapter, is the Leap-Frog integrator. Using this integration scheme, the system described by equations (5.9) and (5.10) is integrated in time in the following way,

$$\begin{aligned} p_i(t+\delta/2) =& p_i(t) - (\delta/2)\frac{\partial U(\underline{q}(t))}{\partial q_i} \\ q_i(t+\delta) =& q_i(t) + \delta\frac{p_i(t+\delta/2)}{m_i} \\ p_i(t+\delta) =& p_i(t+\delta/2) - (\delta/2)\frac{\partial U(\underline{q}(t+\delta))}{\partial q_i}. \end{aligned} \tag{5.15}$$

Before putting in practice the HMC, it is important also to highlight that many other strategies can be coupled with it, among them tempering trajectories (see Neal et al., 2011, and references therein). In addition, HMC can incorporate constraints in the space of solutions that is to be explored. Following Neal et al. (2011), these constraints can be included if the potential energy $U(\underline{q})$ is separated into different parts. For instance, if the parameters $\underline{q}$ are to be found between prescribed lower and upper bounds, a new potential energy can be defined as,

$$U(\underline{q}) = U_*(\underline{q}) + C_r[\underline{m}_{solution}](\Delta q_i), \tag{5.16}$$

---

[1] A symplectic integrator is a numerical integration scheme suitable for Hamiltonian systems. Symplectic integrators form the subclass of geometric integrators which, by definition, are canonical transformations. They are widely used in nonlinear dynamics, molecular dynamics, discrete element methods, accelerator physics, etc.

where $U_*(\underline{q})$ is the previous potential function described in (5.12), and $C_r[\underline{m}_{solution}](\Delta q_i)$ can be any barrier function. For instance, one can use a function of the following form,

$$C_r[\underline{m}_{solution}](\Delta q_i) = \begin{cases} r^{r+1}(l_i - \Delta q_i)^r & \text{if} \quad \Delta q_i < l_i \\ 0 & \text{if} \quad l_i \leq q_i \leq u_i \\ r^{r+1}(\Delta q_i - u_i)^r & \text{if} \quad \Delta q_i > u_i \end{cases}, \tag{5.17}$$

with

$$\Delta q_i = q_i - m_{i_{solution}}. \tag{5.18}$$

In this case, l_i and u_i represent the lower and upper bounds of every q_i. In other words, they act as control quantities, while Δq_i is the distance from which the HMC is allowed to explore far from the given solution $\underline{m}_{solution}$. It is important to recall that the position is linked to the parameters of the current model which probability is being evaluated $\underline{q} = \underline{m}$. In equation (5.17), one can see that $\lim_{r\to\infty} C_r[\underline{m}_{solution}](\Delta q_i)$ is equal to zero for any $l_i \leq \Delta q_i \leq u_i$ and infinity for any $\Delta q_i > u_i$ or $\Delta q_i < l_i$. Moreover, for $r > 1$, $U(\underline{q})$ is differentiable, so we can still use it to define Hamiltonian dynamics. The new total Hamiltonian is then defined as,

$$H(\underline{q}, \underline{p}) = U_*(\underline{q})/2 + [C_r[\underline{m}_{solution}](\Delta q_i) + K(\underline{p})] + U_*(\underline{q})/2. \tag{5.19}$$

Before continuing, it is important to recall that the main goal of using this approach is to be able to assess the uncertainties associated to a given kinematic rupture model. Therefore, the function $C_r[\underline{m}_{solution}](\Delta q_i)$ plays a very important role regarding the allowed amount of perturbation to the solution $\underline{m}_{solution}$ to be considered during the HMC exploration.

The changes that the definition of this new Hamiltonian implies for the symplectic integration are further detailed in Neal et al. (2011). The important thing to keep in mind is that, function $C_r[\underline{m}_{solution}](\Delta q_i)$ acts as a barrier function. This very steep barrier has to be climbed if the value of Δq_i passes the threshold u_i or l_i. Because the barrier is too steep as $r \to \infty$, in practice while the system is being integrated, once the Δq_i passes the prescribed bounds, we fall down the the same q_i we had before passing the constrained boundary but with a negated momentum p_i which will prevent us to move again towards the barrier. This constrained Hamiltonian system is of great importance if we have in mind that in some cases, instead of making the attempt to find a solution to the kinematic source inversion problem together with the associated uncertainties, we would prefer to assess the uncertainties of a given solution in a restricted region around that solution. Therefore upper and lower limits for the slip-rate functions can be set using this constrained version of the HMC.

To end this section, as well as it is done in Section 5.3.1, the steps to perform a Hamiltonian Monte Carlo exploration are provided in the following algorithm.

Algorithm 4: Standard Hamiltonian Monte Carlo (HMC) algorithm.

```
input : Form of gradient of the potential function, the integration step $\delta$, and (optionally) the
        number of integration steps $L$, and the mass matrix $\underline{\underline{M}}$ used to propose the momentum;
    Set $k = 0$;
    Get first state $\underline{m}^{(k)}$, from the prior probability function $\underline{m}^{(k)} \sim P(\underline{m})$;
    while $k < K$ do
        4.1: set $k = k + 1$;
        4.2: sample a momentum variable from the momentum distribution $\underline{p}^{(0)} \sim P(\underline{p})$;
        4.3: set $\underline{q}^{(0)} = \underline{m}^{(k-1)}$;
        4.4: define a number of integration steps $L$
        4.5: run Leap-Frog algorithm starting at $(\underline{q}^{(0)}, \underline{p}^{(0)})$ for $L$ steps and step size $\delta$ to get proposed
             state $(\underline{q}^{(L)}, \underline{p}^{(L)})$;
        4.6: Estimate the ratio $r = \frac{P(\underline{q}^{(L)}, \underline{p}^{(L)})}{P(\underline{q}^{(0)}, \underline{p}^{(0)})} \propto \exp\big(-U(\underline{q}^{(L)}) - K(\underline{p}^{(L)}) + U(\underline{q}^{(0)}) + K(\underline{p}^{(0)})\big)$;
        4.7: Draw a random number $u$, where $u = \mathrm{Unif}(0, 1)$;
        4.8: if $u < r$    (Metropolis-Hastings acceptance criterion) then
                 4.8.1: accept the proposal state $\underline{q}^{(L)}$ and set    $\underline{m}^{(k)} = \underline{q}^{(L)}$
             else
                 4.8.2: reject and set    $\underline{m}^{(k)} = \underline{m}^{(k-1)}$;
```

5.3.3 MCMC vs HMC: encouraging examples

In this section, I present two different examples where some of the advantages of the Hamiltonian Monte Carlo method are illustrated. For both examples, I compare the results obtained from the HMC approach to the ones coming from a standard MCMC strategy. These examples shall encourage us to use HMC to tackle high-dimensional problems such as the kinematic source inversion problem, that is discussed in the following section.

A 2D problem in seismology: Source spectrum estimation

The first example in this section is related to the inference of the two parameters that are used to describe the displacement source spectrum from Brune's model for a real data set. The inference of these two parameters and their uncertainties is carried out using two strategies: 1) a standard MCMC strategy as the one described in Section 5.3.1 and in Algorithm 3 and 2) the HMC approach as described in Section 5.3.2 and in Algorithm 4. The principal objective of this example is to show the applicability of HMC to seismological problems as well as to illustrate its faster convergence and exploration of the model space compared to a standard MCMC approach.

Problem setup: One parameter that has been used for long time to characterize the size of earthquakes and other important features related to these events (such as the stress-drop) is the corner frequency (f_c) of the source spectrum. One of the mathematical models that is commonly used in seismology to represent theoretically the displacement source spectrum is Brune's model (Brune, 1970),

$$u(f) = \frac{\Omega_0}{1 + (f/f_c)^n}, \tag{5.20}$$

or in logarithmic form,

$$\log(u(f)) = \log(\Omega_0) - \log(1 + (f/f_c)^n), \tag{5.21}$$

where the amplitude of the displacement spectrum u at a given frequency f can be determined based on the long-period amplitude (proportional to the seismic moment) Ω_0, the corner frequency f_c and the high-frequency falloff rate n (i.e., $n = 2$ for ω^2 models). Ω_0 and f_c are very important source attributes that can be related to the stress-drop of an earthquake (Madariaga, 1976; Abercrombie, 1995; Shearer et al., 2006; Kaneko and Shearer, 2014). Therefore, it is important to infer these attributes as well as their uncertainties.

For this first exercise, the goal is to retrieve the corner frequency f_c and the long-period amplitude Ω_0, as well as the related uncertainties, of a real recording. For that, I use as dataset the raw (in gain) recording of a foreshock from the 2011 Tohoku earthquake. This event (according to the JMA Catalog) occurred the 10th of March 2011 at 6:23:59.75 (GMT Time) at 38.1722^o North and 143.0448^o East at a depth of approximately 9.3 km. I use the vertical component of receiver KNIH from the Hi-net, that recorded the particle velocity for that earthquake at approximately 200 km from the epicenter. I do not process the recording to account for any instrument correction. The recording was base-line corrected. The signal was cut to account only for the first 40 seconds, and the Fourier amplitude spectrum is estimated from a tapered version of that signal. This spectrum is then smoothed using the Konno-Ohmachi smoothing function (Konno and Ohmachi, 1998). The resulting spectrum is shown in Figure 5.1a (solid black line). The goal in this exercise is to compare the performance of the HMC against a standard MCMC.

In order to apply the standard MCMC strategy as detailed in Algorithm 3, the prior, likelihood and proposal probability distribution functions have to be defined. To do that, the likelihood is designed as a normal distribution function with a standard deviation $\sigma_{likeli} = 2$. Remember that the observed and predicted spectra are compared in a logarithmic scale. Therefore, the standard deviation is related to the logarithmic values of the spectra. On the other hand, I decide to use for each parameter (separately) a non-informative uniform distribution. For the corner frequency the minimum and maximum values of the uniform distribution are -2.3 and 1.6, which correspond to $f_{c_{min}} = \exp(-2.3) = 0.1$ Hz and $f_{c_{max}} = \exp(2.6) = 13.4$ Hz. For the long-period amplitude Ω_0, the minimum and maximum values of the uniform distribution are set to 1 and 13 (logarithm of the amplitude in gain), which corresponds to $\Omega_{0_{min}} = \exp(1) = 2.7183$ and $\Omega_{0_{max}} = \exp(15) = 3.26 \times 10^6$. As it can be noticed, the exploration of the space is performed in a logarithmic space. Therefore, I define a 2D normal distribution centered at the current state and with a diagonal covariance matrix, $\text{diag}(\underline{\underline{\Sigma}})_{proposal} = [0.01, 0.01]^T$, as the proposal distribution function in the logarithmic space. For the MCMC strategy, the total number of iterations is fixed to 2000 iterations. Finally, the first guess is $f_c = 10$ Hz and $\Omega_0 = 1 \times 10^4$ (gain) (blue dashed line in Figure 5.1a). This initial guess is also used by the HMC approach that is detailed in the next paragraph.

In order to apply the HMC strategy to this problem, several things need to be established. The first is to define the potential function that is needed by HMC. For this problem, I decide to define it as the negative logarithm of an exponential whose argument is the L2 norm between the logarithm of the observed, $y(f)$, and estimated, $u(f)$, amplitude spectra. By defining it in such way we obtain the following potential function,

$$\begin{aligned} U(\underline{q}) &= -\log\Bigg(\exp\Bigg(-\frac{1}{2}\Bigg(\log(y(f)) - \log(u(f,[f_c,\Omega_0]))\Bigg)^2\Bigg)\Bigg) \\ &= \frac{1}{2}\Bigg(\log(y(f)) - \log(u(f,[f_c,\Omega_0]))\Bigg)^2, \end{aligned} \tag{5.22}$$

whose partial derivatives with respect to Ω_0 and f_c, that are also required by the HMC strategy, are

$$\begin{aligned} \frac{\partial U(\underline{q})}{\partial \Omega_0} &= -\frac{\log(y) + \log((f/f_c)^n + 1) - \log(\Omega_0)}{\Omega_0} \\ \frac{\partial U(\underline{q})}{\partial f_c} &= -\frac{n(f/f_c)^{(n-1)}(\log(y) + \log((f/f_c)^n + 1) - \log(\Omega_0))f}{((f/f_c)^n + 1)f_c^2}. \end{aligned}$$

Another important parameter to set for the HMC strategy is the mass matrix $\underline{\underline{M}}$. After some initial tests, and regarding the different variability that Ω_0 can have (ranging from 1×10^3 to 1×10^9 (gain)) compared to f_c (ranging from 1×10^{-1} to $1 \times 10^{1.7}$ Hz), I decide to define a smaller mass for Ω_0 than for f_c, so that Ω_0 can vary more freely,

$$\underline{\underline{M}} = \begin{bmatrix} 1 \times 10^{-4} & 0 \\ 0 & 1 \end{bmatrix}.$$

Finally, for the HMC it is necessary to define the time integration step ϵ and the number of steps of integration for the Leap-Frog scheme. For the integration step, I set a small value that prevents the divergence of the integration of this system ($\delta = 0.1$). For the number of steps, I decide to use a generator of random integer numbers (ranging from 1 to 40). Defining L as a random number of integration steps can be seen as another type of perturbation to the parameter exploration. A total number of 2000 iterations is also fixed for the HMC.

The results from this first exercise are summarized in Figure 5.1. According to the data misfit shown in Figure 5.1c and the comparison in Figure 5.1a, both strategies provide a correct estimation of both source attributes. Similar means and covariance matrices are obtained from both strategies. According to the MCMC and HMC explorations, the parameters follow a lognormal probability distribution function. The MCMC reports the mean values as $f_{c_{mean}}^{MCMC} = \exp(1.1953) = 3.3046$ Hz, $\Omega_{0_{mean}}^{MCMC} = \exp(13.720) = 9.0886 \times 10^5$ (gain), while the HMC estimates $f_{c_{mean}}^{HMC} = \exp(1.1931) = 3.2974$ Hz, $\Omega_{0_{mean}}^{HMC} = \exp(13.709) = 8.9938 \times 10^5$ (gain). However, the covariance matrices of the two lognormal distributions that are found, showed that the results from the standard MCMC strategy are more dispersive than the ones from the HMC: feature that is consistent with the behavior observed in Figure 5.1c.

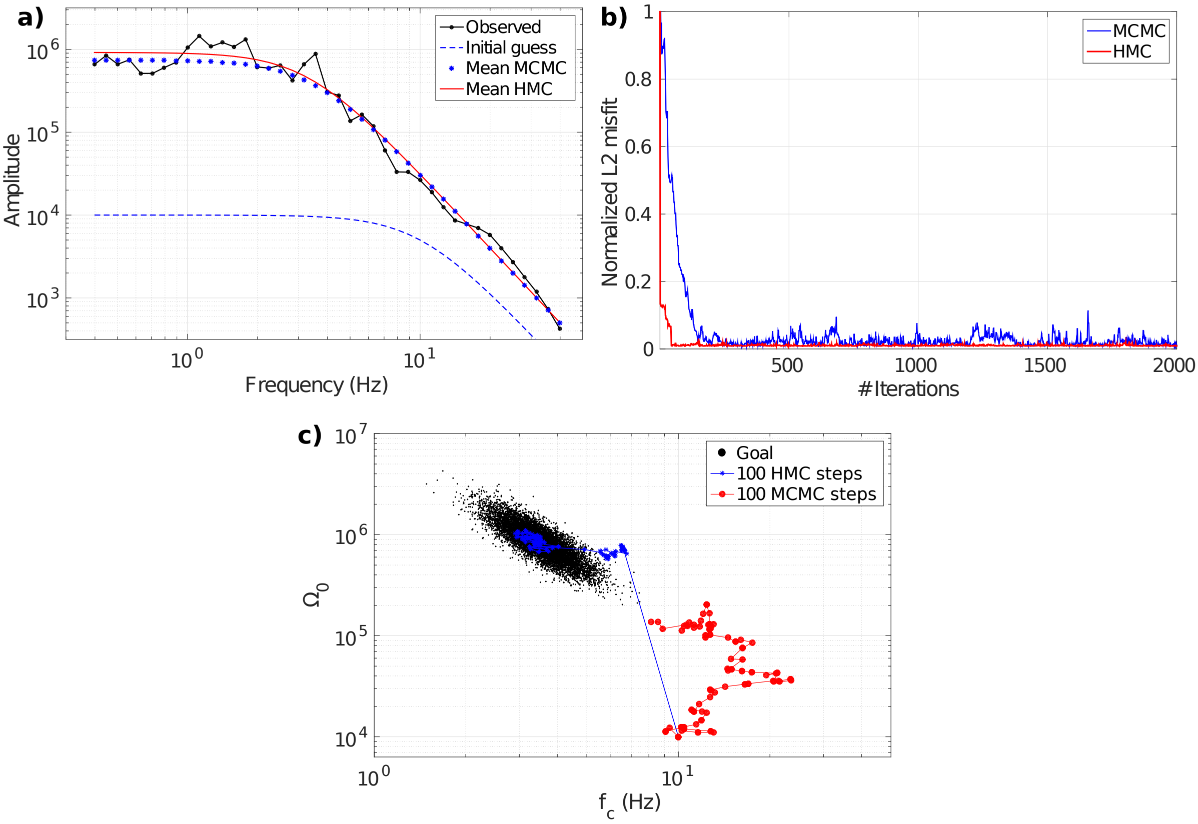

Figure 5.1: Summary of the results from Brune's model exercise. a) compares the observed displacement spectrum (black line) with the initial guess (dashed blue line) and the two spectra estimated based on the mean values of Ω_0 and f_c that were obtained through the MCMC (blue dotted line) and the HMC (red solid line) strategies. b) illustrates the evolution of the normalized data misfit through the iterations of the two approaches. It can be noticed that the burn in phase of the HMC is approximately ten times faster than the MCMC for this 2D example. For this exercise the decay is set as $n = 3$. c) shows the evolution of the two Markov Chains obtained. The first 100 samples of the chains are plotted for both strategies (MCMC in red while HMC is in blue). Notice that in less than 100 steps HMC arrives to the region of denser probability and performs its exploration, while the MCMC has not yet arrived to this region of interest.

$$\text{cov}(\Omega_0, f_c)^{MCMC} = \begin{bmatrix} 0.0426 & -0.0148 \\ -0.0148 & 0.0107 \end{bmatrix}, \qquad \text{cov}(\Omega_0, f_c)^{HMC} = \begin{bmatrix} 0.0322 & -0.0125 \\ -0.0125 & 0.0079 \end{bmatrix}.$$

One of the important results to highlight from this exercise is the faster convergence of the HMC to the region where the most probable scenarios are located in the model space. This faster exploration is represented in Figure 5.1b, where the first 100 members of the constructed Markov chains (MCMC and HMC) are plotted for both strategies. In that figure one can see that, while the MCMC (blue line) has not yet arrived to the dense probable region, the HMC (red line) is already exploring it. This feature can be also noticed in Figure 5.1c, where the normalized misfit function of the HMC (red line) strategy converges much faster than the one for the MCMC (blue line).

A multimodal case

Another well-known difficulty for a standard MCMC (and other techniques) is to deal with multimodal functions. These type of functions mean that, in the space of probable solutions, there might be more than one region with dense probabilities. In other words, more than one solution is likely. The purpose of this second exercise is to compare the performance of the exploration of the model space using the HMC and the standard MCMC in a complex multimodal case. To do that, I define the following multimodal probability distribution as the target function to be described,

$$P(\underline{m}|\underline{d}) = \frac{0.7\exp(-(x_1^2+y_1^2)) + 1.3\exp(-(x_2^2+y_2^2)) + 2\exp(-(x_3^2+y_3^2))}{11.8679} \tag{5.23}$$

with

$$\begin{aligned} x_1 &=(x-2)/0.5; \\ y_1 &=y/2; \\ x_2 &=x/1.8; \end{aligned} \qquad\qquad \begin{aligned} y_2 &=(y-1.8)/0.7; \\ x_3 &=(x+7)/1.2; \\ y_3 &=(y+7)/0.6; \end{aligned}$$

In this exercise, three exponential functions are summed. Therefore, for this problem there are three regions with dense probabilities: 1) at $(x_1 = 2, y_1 = 0)$, 2) at $(x_2 = 0, y_2 = 1.8)$ and 3) at $(x_3 = -7, y_3 = -7)$, as it can be seen in Figure 5.2a.

For the standard MCMC, the setting is simple. I use as proposal function a 2D normal distribution function which mean vector is the current state of the Markov Chain and the covariance matrix is taken as the identity. The estimation of $P(\underline{m}|\underline{d})$ for the current and proposed state is performed as a simple evaluation of equation (5.23). The initial guess for both strategies is $[x, y] = [0, -8]$. The total number of iterations is set to 200,000, in order to ensure a complete exploration of the space of solutions.

In order to apply the HMC strategy, it is necessary to first define a potential function. This function is taken as $U(\underline{q}) = -log(P(\underline{m}|\underline{d}))$, where $P(\underline{m}|\underline{d})$ is given by equation (5.23). The gradient of the potential energy function, also required by the HMC, is analytical,

$$\begin{aligned} \frac{\partial U(\underline{q})}{\partial x} =& -2\left(\frac{25x+175}{18}\right)\exp\left(-\left(\frac{5x+35}{6}\right)^2 - \left(\frac{5y+35}{3}\right)^2\right) \\ &- \frac{7(8x-16)}{10}\exp\left(-(2x-4)^2 - \left(\frac{y}{2}\right)^2\right) - \frac{65x}{81}\exp\left(-\left(\frac{10y-18}{7}\right)^2 - \frac{25x^2}{81}\right), \qquad (5.24) \\ \frac{\partial U(\underline{q})}{\partial y} =& -2\left(\frac{50y+350}{9}\right)\exp\left(-\left(\frac{5x+35}{6}\right)^2 - \left(\frac{5y+35}{3}\right)^2\right) \\ &- \frac{13}{10}\left(\frac{200y-360}{49}\right)\exp\left(-\left(\frac{10y-18}{7}\right)^2 - \frac{25x^2}{81}\right) - \frac{7y}{20}\exp\left(-(2x-4)^2 - \left(\frac{y}{2}\right)^2\right). \qquad (5.25) \end{aligned}$$

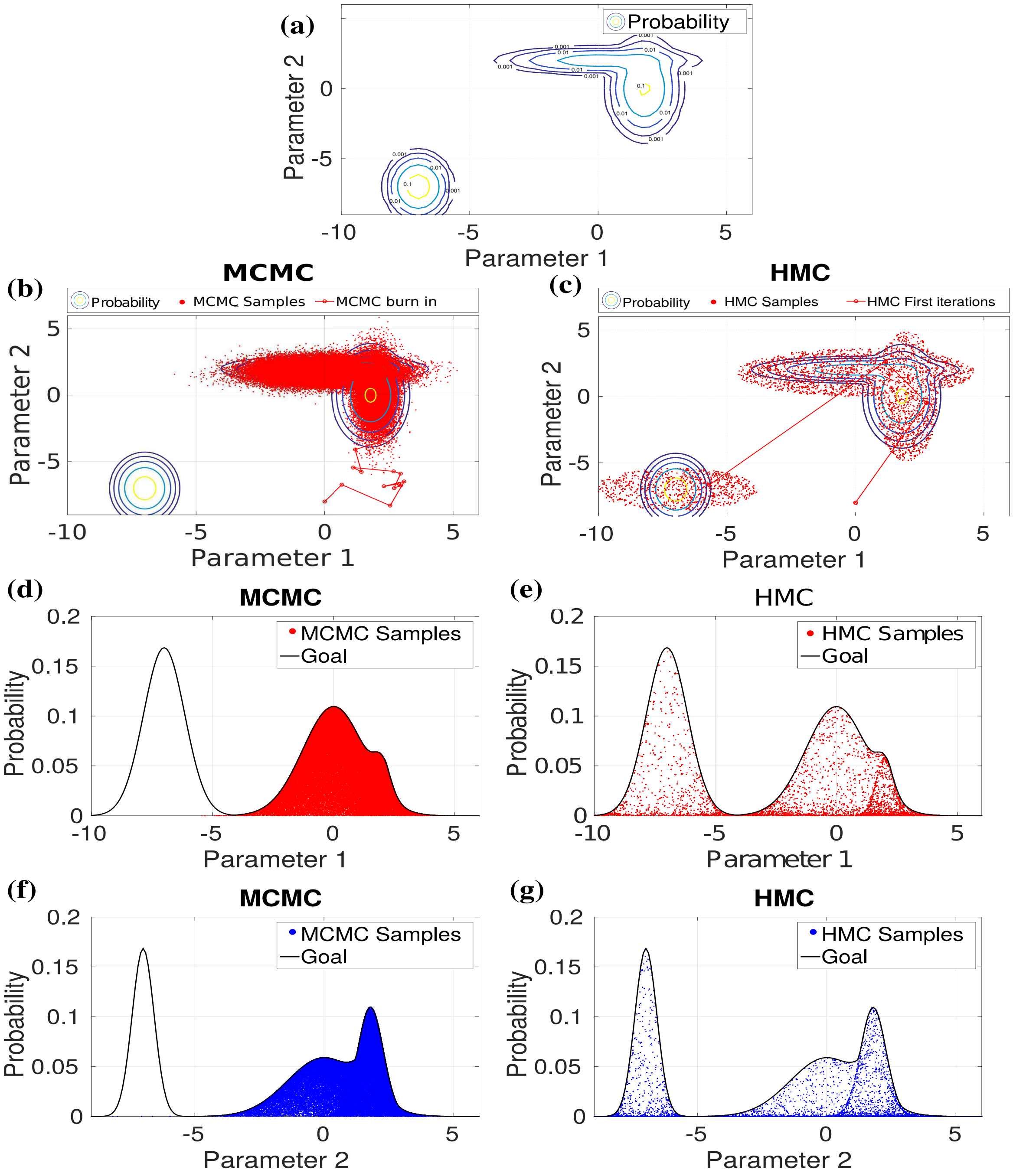

Figure 5.2: Summary of the results from the exercise that explores a multimodal 2D probability function. (a) Illustrates a 2D map of the multimodal probability function (sum of three exponential functions). (b) and (c) show the evolution of the Markov Chains that are obtained using the MCMC (200,000 samples red dots in (b)) and the HMC (30,000 samples red dots in (c)) strategies. Notice that in the first 30 samples of the HMC exploration (red line in (c)) the HMC was able to explore the three denser regions of probability, while the MCMC (red line in (b)) has not yet arrived to the region where it gets stuck. (d) and (f) illustrate in a profile view the exploration that the standard MCMC strategy does after 200,000 iterations. (e) and (g) are the same as (d) and (f) but for the HMC strategy after 30,000 iterations.

For this exercise, the integration step and number of steps for the Leap-Frog scheme are set to $\delta = 0.1$ and $L = 20$. These values are not necessarily optimal, since I did not perform an exhaustive exploration of how to set these parameters for this example. The total number of iterations for the HMC is set to 30,000. The mass matrix is taken as the identity and the probability distribution from which the momentum parameters are sampled is a 2D normal distribution with zero mean. The results from this exercise are summarized in Figure 5.2.

The results from this second exercise illustrate another advantage of the HMC strategy over the standard MCMC approach. As it can be seen in Figure 5.2, HMC is able to explore the three regions with dense probabilities. On the contrary, the MCMC is not able to get away from the first region where it arrived after its burn in phase. Several test were performed, and the results were always the same: either the third region at $(x_3 = -7, y_3 = -7)$ is sampled but not the other two, or the first two are sampled but the third is not. The MCMC approach is not able to move across the three regions because one of them is too far from the other two. As it can be seen in Figure 5.2, MCMC is able to explore the other two regions, because the distance between then is not so large as the one separating them from the third. Certainly, there are other MCMC strategies that could tackle this problem in a better way. Another possibility to overcome this problem using the same MCMC approach would be to set a larger perturbation in the proposal function instead of using the identity as the proposal covariance matrix. The fact is that, without a complex tuning of the parameters involved in the HMC strategy (e.g. step size, number of steps, mass matrix), the HMC strategy is able to visit the three regions and to provide a correct description of the probability function we are interested in even after very few iterations (30 iterations as shown in Figure 5.2c).

Before applying the HMC technique to the kinematic source inversion problem I would like to point out that the application of this method to the two exercises previously presented belong to the most complex approach to each of this problems: the attempt is to retrieve the solution to an inverse problem together with the associated uncertainties. Another approach would be to only investigate the uncertainties associated to a given solution. It is important to point out that in more complex problems (e.g. the source inversion problem) the second approach should be preferred.

5.4 HMC and the Kinematic Source Inversion Problem

Contrary to the goal of Chapters 3 and 4, the purpose of this chapter is not only to provide a rupture model that explains the observations, but to assess also the uncertainties associated to that solution. Therefore, instead of only providing one single rupture model that explains, to some extent, the observed wavefields; my goal is to provide a description of the *posterior probability density* (*ppd*) of a set of parameters, describing the seismic rupture, given the observed evidence (e.g. seismograms, static displacements, etc.). As I mentioned in the beginning of this chapter, the HMC technique can be used to achieve two different goals: 1) obtain a solution to the kinematic source inversion problem and its related uncertainties or 2) assess the uncertainties in the vecinity of a given solution. The preliminary investigation presented in this section is mainly focused on the second goal. Under that approach, it is important to mention that the given solution around which we can describe the related uncertainties can come from the results of the deterministic approach that is presented in the previous chapters, as well as from other strategies. The answer to the first goal, which seems more challenging, is also an interesting approach to be explored.

As it was discussed in the previous chapters, the linear or non-linear formulations of the kinematic source inversion problem involves a large number of parameters (tens of thousands). Therefore, if we want to keep the linearity of the problem - feature that must be promoted for several reasons (e.g.

linear propagation of errors, quadratic convex shape of the misfit function) - we should be aware of the difficulty that this feature implies for the uncertainty assessment. As mentioned before, one of the recent strategies that has been proved to be suitable to tackle such large dimension problems is the Hamiltonian Monte Carlo strategy. Therefore, in this section I investigate the suitability of the HMC strategy to assess the uncertainties of the kinematic source inversion problem under the linear time-domain formulation that was presented in the previous chapters.

5.4.1 Resetting the kinematic source inversion problem

Because there is no closed form of the *ppd* for the source inversion problem, I expect to construct a large enough Markov Chain which stationary distribution tends to the desired *ppd* of the model parameters for a given solution. Therefore, my goal is to describe $P(\underline{m}|\underline{d})$, which is the target *ppd* of the vector of model parameters ($\underline{m}$) given the observations ($\underline{d}$). In this case, the model parameters represent the time-space slip-rate history $\underline{V}(\underline{\xi}, \tau)$ which is discussed in Chapters 3 and 4, while the observations are the particle velocity recordings $\underline{v}(\underline{x}, t)$. In the same sense, the likelihood function from equation (5.2), $P(\underline{d}|\underline{m})$, is the conditional probability related to the forward problem. In addition, $P(\underline{m})$ is the marginal prior probability that takes into account all the prior information that we can have about the expected source model. $P(\underline{m})$ is the term in charge of injecting the physics into the linear kinematic source inversion formulation, as it is done by the regularization term used in the previous chapters. In fact, as discussed by Figueiredo (2003); Aster et al. (2004); Tarantola (2005) and several other authors, considering a likelihood function which includes (besides the data misfit term) a L2 model regularization term, as the one used in previous chapters, is equivalent to assume an independent data misfit likelihood function being multiplied by a normal prior distribution. Therefore, I focus my investigation more on the description of the likelihood function, assuming the following,

$$P(\underline{m}|\underline{d}) \quad \propto \quad \underbrace{P^*(\underline{d}|\underline{m})}_{\text{data likelihood term}} \quad \underbrace{P^*(\underline{m})}_{\text{prior model term}} \quad \propto \quad \underbrace{P(\underline{d}|\underline{m})}_{\text{data + L2 regularization}} \tag{5.26}$$

where $P^*(\underline{d}|\underline{m})$ and $P^*(\underline{m})$ are the independent likelihood and prior *pdf*s respectively, while $P(\underline{d}|\underline{m})$ is the likelihood *pdf* which already incorporates the prior information as a L2 model regularization term.

Because my goal is to use the HMC technique to assess the uncertainties associated to a given solution of the kinematic source inversion problem, it is necessary to first define a potential energy function. In terms of the source inversion problem, this potential energy is set as a negative logarithm of an exponential function whose argument is the regularized misfit function. This misfit function is in charge of measuring the difference between the observed and the synthetic seismograms (in a least-squares sense). The regularization term of that misfit function injects any available prior information that can be used to constrain the problem. The time-space slip-rate history on the prescribed fault geometry represents the model parameters $\underline{m} = \underline{V}(\underline{\xi}, \tau)$, while the target *ppd* is the set of physically plausible rupture scenarios surrounding a given solution which explain, to some extent, the observations $\underline{d} = \underline{v}(\underline{x}, t)$. Therefore, the potential energy can be defined as

$$U(\underline{q}) = -\log(P(\underline{m}|\underline{d})) \propto -\log(P(\underline{d}|\underline{m})) = -\log(\exp(-C(\underline{V}))) = C(\underline{V}). \tag{5.27}$$

From equation (5.27), it can be seen that the potential energy of the Hamiltonian system, to be used to explore the space of solutions, is exactly the same as the expression of the misfit function $C(\underline{V})$ that is used in Chapter 3 and 4. Therefore, under the HMC approach,

$$U(\underline{q}) = -\log(P(\underline{m}|\underline{d}))$$

$$
\begin{aligned}
&\propto -\log(P(\underline{d}|\underline{m})) \\
&\propto -\log\Bigg(\exp\Bigg(-\frac{1}{2}\sum_{\underline{x}}\int_t \Delta\underline{d}[\underline{V}]^T\underline{\underline{W}}_{\underline{d}}^T\underline{\underline{W}}_{\underline{d}}\Delta\underline{d}[\underline{V}]\,dt\Bigg)\Bigg) \\
&\quad -\log\Bigg(\exp\Bigg(-\frac{\epsilon}{2}\int_{\underline{\xi}}\int_{\tau} \Delta\underline{m}[\underline{V}]^T\underline{\underline{W}}_{\underline{m}}^T\underline{\underline{W}}_{\underline{m}}\Delta\underline{m}[\underline{V}]\,d\tau d\underline{\xi}\Bigg)\Bigg)
\end{aligned}
\tag{5.28}
$$

where it is possible to identify from equation (5.28), the data misfit term (equation (3.11)) and the model misfit term (equation (3.13)), which are exhaustively discussed in Section 3.2.2. As a brief summary, $\Delta\underline{d}[\underline{V}]$ represents the residuals between the observed, $\underline{u}(\underline{x},t) = [u_x(\underline{x},t), u_y(\underline{x},t), u_z(\underline{x},t)]^T$ and the calculated seismograms, $\underline{v}[\underline{V}](\underline{x},t) = [v_x[\underline{V}](\underline{x},t), v_y[\underline{V}](\underline{x},t), v_z[\underline{V}](\underline{x},t)]^T$, where $[\underline{V}]$ is used to denote the dependence of $\Delta\underline{d}$ on a given rupture model $\underline{V}$, while $\Delta\underline{m}[\underline{V}]$ represents the model residual between a current rupture model $\underline{V}(\underline{\xi},\tau)$ and the prior model $\hat{\underline{V}}(\underline{\xi},\tau)$. In addition, $\underline{\underline{W}}_{\underline{d}}$ and $\underline{\underline{W}}_{\underline{m}}$ are used to denote the data and model weighting matrices respectively. Notice that, both matrix multiplications can be directly linked to the covariance of the probability functions, being $\underline{\underline{W}}_{\underline{m}}^T\underline{\underline{W}}_{\underline{m}} = \underline{\underline{C}}_{\underline{m}}^{-1}$ and $\underline{\underline{W}}_{\underline{d}}^T\underline{\underline{W}}_{\underline{d}} = \underline{\underline{C}}_{\underline{d}}^{-1}$.

Equations (5.27) and (5.28) imply that the gradient of the chosen potential energy is also the same as the gradient of the misfit function (equation (3.18)) that is presented in Section 3.2.2,

$$
\begin{aligned}
(\nabla_{q_i}U(\underline{q}))_k =&\mathcal{G}_k[\underline{V}](\underline{\xi},\tau) \\
=&\sum_{\underline{x}}\int_{t_1}^{t_2} \underline{\underline{W}}_{\underline{d}}^T\underline{\underline{W}}_{\underline{d}}\Delta d_n[\underline{V}](\underline{x},t)\mathcal{T}_{ni}(\underline{\xi},\tau-t;\underline{x},0)\,\mathcal{P}_{ik}^T dt \\
&+\epsilon\left[\underline{\underline{W}}_{\underline{m}}^T\underline{\underline{W}}_{\underline{m}}\Delta m[\underline{V}](\underline{\xi},\tau)\right]_k, \\
&n,i\in[x,y,z]\ \text{ and }\ k\in[\phi,\delta]\text{ or }k\in[\lambda],
\end{aligned}
\tag{5.29}
$$

where I use the same index and Einstein summation convention as for equations (3.7), (3.16) and (3.18). As in equation (3.18), the first term in equation (5.29) is the data term (or likelihood *pdf*), which is the sum of the projections of the unexplained residues at all the receivers onto the fault plane through the stress-state tensor, while the second term incorporates the prior model information (prior *pdf*). In this case where we are interested in describing the *ppd* around a given solution, it is the prior model which takes the role of that given solution, which can come from the deterministic approach previously presented.

From equations (5.27) and (5.29) we can see the advantage of choosing the potential energy described in equation (5.28). It is possible to use all the development presented in the previous chapters to assess the uncertainties of the proposed rupture models using the HMC strategy.

A standard MCMC scheme is based on three principal steps. However, the definition of the proposal transition function, which is required by that scheme, appears to be not a easy engine to build in order to assess the uncertainties associated to the source reconstruction problem (under the linear formulation where thousands of unknowns have to be perturbed simultaneously). Certainly, this proposal transition function can be designed in terms of perturbations of physical parameters of the expected shape of the slip-rate time histories, rupture velocity, rake angle, etc. However, somehow, this model perturbation bring us back to the non-linear formulation of the problem. On the contrary, the HMC strategy has the ability to move rapidly through the high-dimensional model space based on perturbations to the model that take into account the gradient of the misfit function, that is computed with respect to every single time and space slip-rate sample describing the rupture history. I shall recall the reader that, thanks to the precomputed stress-state tensors that are presented in Chapter 2, the computation of the gradient is a rather efficient operation.

As mentioned in Section 5.3, the HMC also requires to define a mass matrix. The inverse of this matrix, as pointed out by several authors (Neal et al., 2011; Betancourt, 2017), and as it is briefly described in the first example from Section 5.3.3, acts as the covariance matrix of the *pdf* used to draw the auxiliary momentum variables that serve us to perturb the unknown parameters. Therefore, the definition of its structure is directly linked to the speed in which the exploration of the desired *ppd* is performed. Some authors, for instance Fichtner et al. (2018), propose that an optimal mass matrix for linear forward problems with Gaussian priors (least-squares misfit functions) can be the inverse posterior covariance matrix, $\underline{\underline{M}} = \underline{\underline{C}}^{-1}_{\text{posterior}}$. In other words, an optimal choice of the inverse of the mass matrix is the Hessian. However, for high-dimensional problems, the access to the exact inverse of the covariance matrix, can be intractable. Nevertheless, strategies such as lBFGS can offer an approximation estimate of the Hessian through an iterative optimization process (Nocedal and Wright, 2006). Furthermore, knowing beforehand the posterior covariance matrix turns meaningless the purpose of performing the sampling. Other studies, such as Biswas and Sen (2017) or K. and Reetam (2017), assume as mass matrix the identity, and leave without tunning this matrix that could help improving the efficiency of the exploration. This rather simple assumption might be due to the complexity that the tunning of this matrix can represent.

In this work, I propose a block diagonal mass matrix (symmetric positive definite), whose structure is based on the estimated gradient of the initial guess and a 2D (e.g. time and space) correlation distance between parameters. The value of each element in the matrix has to be assigned according to the absolute value of the gradient with respect to that parameter and its correlation with its neighbors. It is very important to point out that, in this sense, there are two possible scenarios that depend on the quality of the illumination of the seismic source given the monitoring receiver acquisition configuration. The first is related to good or perfect illuminations (not realistic scenarios). In this scenario, the elements of the mass matrix that correspond to parameters with a large absolute value of the gradient, have to take small values, which will promote large perturbations and a faster exploration. On the contrary, very large values will be given for the elements of the matrix that correspond to small absolute values of the gradient (i.e. the exploration is freezed for these parameters). The second case, and the more common one, is when there is lack of illumination. In that case, the mass needs to be large for the parameters with relative high gradient values, while small mass values have to be given to the parameters with relative low gradient values. This important change of the definition of the mass matrix when there is lack of illumination is due to the fact that we are interested in exploring more rapidly the places where the gradient is low and where the uncertainties are expected to be large. Finally, by defining the mass matrix in terms of the first initial gradient can be seen as a prescribed constrain to the exploration: depending on the values of the first gradient some parameters are permanently forced to be largely perturbed, while others remain frozen.

5.4.2 HMC kinematic source inversion examples

The two examples presented in this section are focused on the understanding of the HMC exploration in a synthetic configuration with simple geometry and assuming perfect illumination. More complex ruptures with realistic source-receiver geometries remain as perspectives of my research work and are not part of what is presented here.

A simple line source well illuminated

For the following two exercises, the source-receiver geometry is composed by a line source located at a depth of $z = 2$ km. The line source is represented by 21 spatial nodes distributed every 0.5 km along the x-direction, from $x_{min} = 12$ km to $x_{max} = 22$ km, with a constant location along y-direction. 420 receivers monitoring this line source are deployed surrounding it. Every fault spatial node is surrounded by 20 receivers (following a circular array). The distance between each spatial fault node and the 20 receivers around it is of 2 km. This type of idealized tube-like source-receiver geometry is illustrated in Figure 5.3. The velocity-density structure is a homogeneous half-space with $\alpha = 4.8$ km/s, $\beta = 2.6$ km/s and $\rho = 2.3$ g/cm^3, as the P and S wave velocities and density respectively.

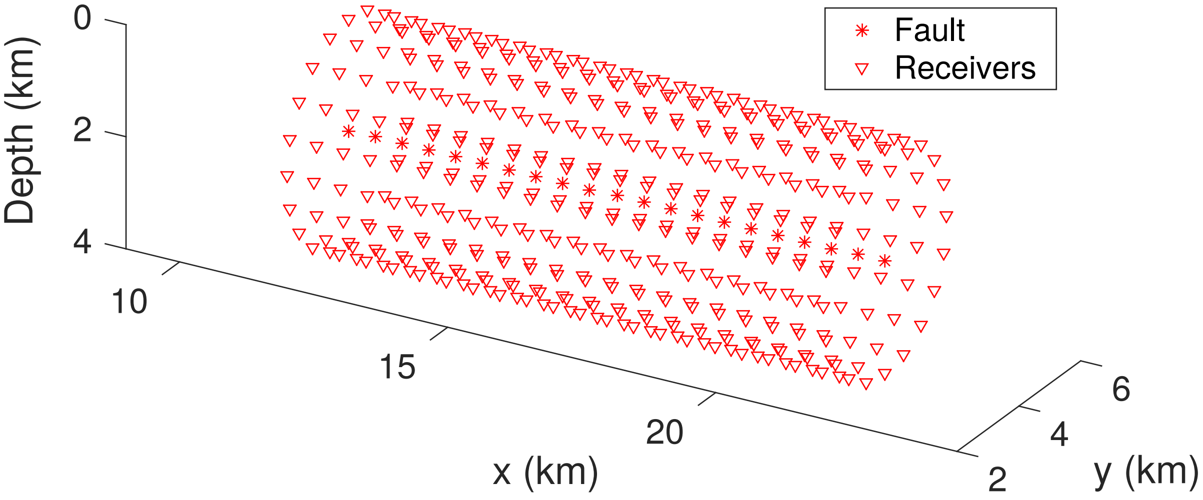

Figure 5.3: Idealistic tube-like source-receiver geometry assumed for the first two examples presented in Section 5.4.2. 21 spatial nodes (asterisks) separated every 0.5 km along the x-direction (from $x_{min} = 12$ to $x_{max} = 22$ km) at a constant depth of $z = 2$ km and at $y = 4$ km formed the line source to be monitored. 420 receivers (triangles) surrounding the line source represented the acquisition system. Every spatial node is surrounded by 20 receivers equally separated from the fault node by 2 km (forming circular arrays around the nodes).

A spike test

The goal of this first exercise is to assess the uncertainties of a simple spike test. For that purpose, I assume that, at the center of the line source (fault node 11 at $x = 17$ km) a sudden slip-rate impulse takes place. Therefore, $\underline{V}(\underline{\xi}, \tau) = 1$ m/s at $\underline{\xi} = [17, 4, 2]$ km and at $\tau = 1$ s. This sudden slip-rate impulse is illustrated in Figure 5.4a. The focal mechanism is fixed to strike 90^o, dip 90^o and rake 90^o for all the nodes on the fault. The time-space slip history is fixed to last 10 s and to have a sampling rate of $\Delta t = 0.25$ s. Therefore, the total number of unknowns (dimensions where to search) is 41 [time samples] $\times$ 21 [fault nodes] = 861 [unknowns]. The exact solution to this problem requires that the unknown #415 is equal to 1.0 m/s while all the other remaining unknowns are equal to zero. Using all this information, the 3 components (E-W, N-S and U-D) at the 420 receivers are estimated and then they are assumed as the available observations. Notice that these "observed“ recordings are noise-free and that the velocity-density structure is perfectly known.

In this example, I do not investigate uncertainties related to the source geometry, or the influence that noisy data can have on the source reconstruction. My main focus is related to assess the uncertainties inside this fixed time-space-amplitude slip-rate grid. Because, the illumination is perfect for this case, and the source is rather simple, I do not use any prior model information (the model term in equation (5.27) is equal to zero) as well as the hyper-parameter ϵ. Therefore, in this case, the desired *ppd* is assumed to be proportional to the data likelihood. Knowing the form of the potential energy (equation (5.28)) and its gradient (equation (5.29)), the only missing terms that need to be defined before running the HMC exploration are the integration step δ, the number of steps L and the mass matrix.

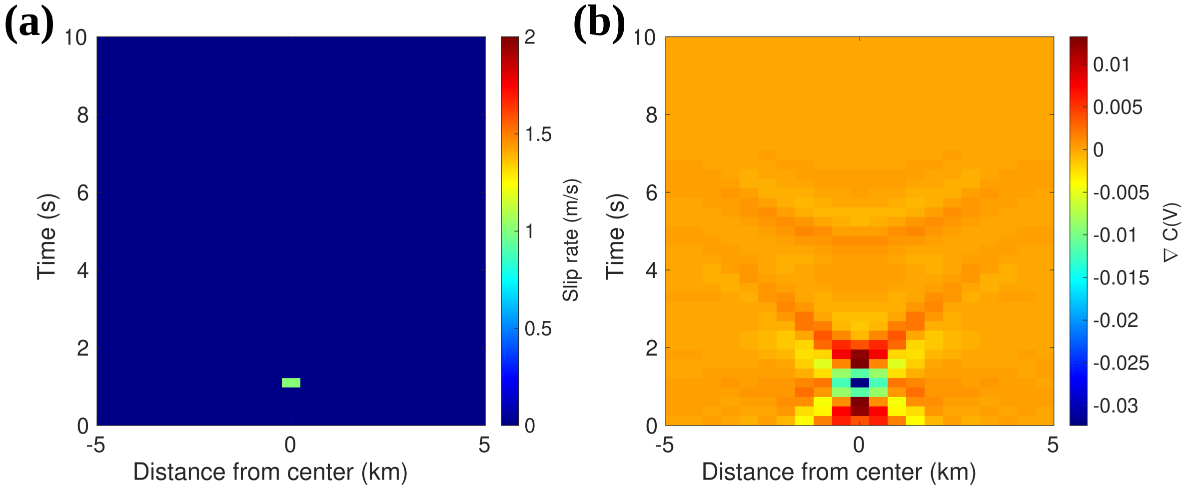

Figure 5.4: Illustration of the spike test model and gradient of the misfit function at first iteration. (a) illustrates a slip-rate sudden impulse ($\underline{V}(\underline{\xi}, \tau) = 1$ m/s) at the center of the source array ($\underline{\xi} = [17, 4, 2]$ km) from Figure 5.3 at $\tau = 1$ s. (b) illustrates the gradient of the misfit function at the first iteration. The misfit is computed taking into account the 3 components of the 420 receivers. The initial guess is a rupture model with no slip-rate values anywhere. It can be seen in (b), that the gradient is pointing out where the slip-rate from the first guess has to be incremented to better explain the data (yellow region in (b)). The elongated artifacts are due to the low frequency approximation of the source.

Due to the rather simple source time-space history to be reconstructed, δ, L and $\underline{\underline{M}}$ do not require very sophisticated tuning to ensure a correct behavior of the exploration and convergence to the desired *ppd*. The integration step is chosen to be $\delta = 0.1$, which ensures a correct integration of the Hamiltonian system. The number of integration steps is randomly selected for each HMC iteration from a uniformly distributed probability distribution of integer numbers ranging from 1 to 100 steps. The first guess, slip-rate values at the first HMC iteration, is zero slip-rate values everywhere.

According to this first guess, the gradient of the misfit function is computed (see Figure 5.4b). Then, the mass matrix is determined based on the gradient from the first guess. Thanks to the information provided by the gradient, I decide only to perform an exploration of the parameter #415 (out of the 861 unknowns), where the gradient presents the maximum absolute value. Therefore, because I decide not to perturb other parameters, the mass matrix is designed as a diagonal matrix, with very large values for the elements that are not the #415 and the unit for the parameter #415. In other words, this mass matrix allows the HMC strategy to explore the dimension related to the parameter #415 and the other unknowns remain freezed (decision based on the initial guess). The way this mass matrix is desighed can be understood in the scope that was previously defined: asseess the uncertainties related to a given solution. In this case, thanks to the gradient from the first guess, we know that the most probable solution is to have an important slip-rate value at unknown #415 and the chosen mass matrix will help us to determine the *ppd* associated to that solution. This simple design is due to the shape of the source to be reconstructed as well as the good illumination, circunstances that are usually not common in realistic problems.

The results from this first exercise are summarized in Figure 5.5. Thanks to the restrictions imposed by the mass matrix (which is designed based on the gradient), the evolution of the Hamiltonian system (illustrated in Figure 5.5a) is well-behaved and the particle trajectories resemble concentric circles which center is the expected slip-rate value $(q = 1, p = 0)$. It is exactly at this point where the probability is maximum as the slip-rate value takes the corresponding value of the solution and the momentum is equal to zero (no need to perturb more the parameter).

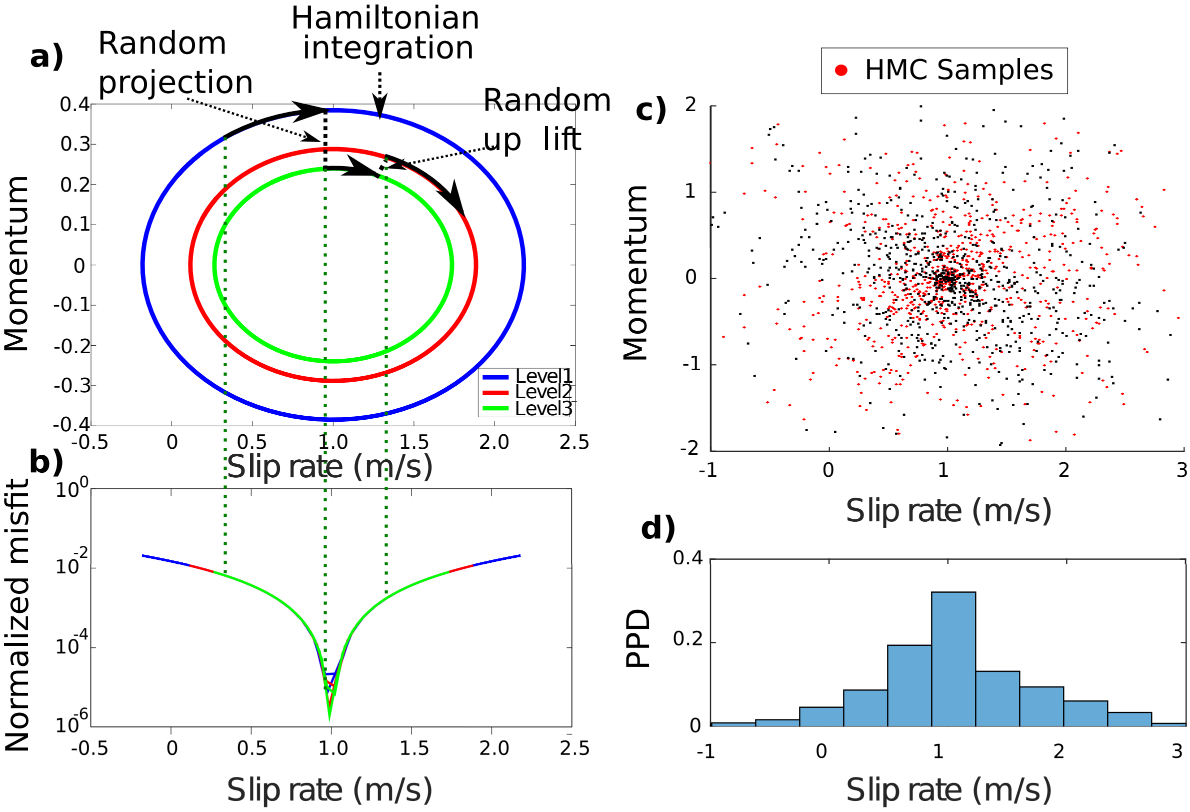

Figure 5.5: Summary of the results from the HMC exploration related to the spike test. a) illustrates the random projection and uplift produced by the auxiliary momentum variable. In a) the duration of the Hamiltonian integration is represented by the length of the arc circles along the contour lines representing different energy levels. b) shows how the trajectories of the three levels of energy from a) map the misfit function (convex quadratic). c) illustrates the samples forming the constructed Markov Chain after 1,000 iterations. In c) the black dots represent the beginning and the end of the Hamiltonian trajectories that are accepted to form part of the Markov Chain after passing the acceptance/rejection criterion. d) represents the *ppd* inferred from the HMC exploration for the slip-rate values of parameter #415. Notice that, ignoring the part related to the momentum variable from c) we can infer the *ppd* of the slip-rate which is shown in d).

It is interesting to see how the perturbation introduced by the auxiliary variable allows to map the geometry of the misfit function even when random projections and uplifts to different energy levels are done (Figure 5.5a,b). The energy levels (solid colored lines in Figure 5.5a) represent the constant value of the Hamiltonian (total energy of the system) for a given value of the slip-rate and momentum for the particle #415. During the evolution of the system, which starts at some initial slip-rate value with a random momentum, the Hamiltonian remains constant and, as a consequence, the balance between the slip-rate and the momentum creates the circular trajectory around the solution. After, 1,000 iterations of the HMC exploration (keeping only the starting and ending points of the Hamiltonian trajectories) together with the MH criterion we obtain a Gaussian-shape *ppd* that can be seen in Figure 5.5c. This Gaussian-shape is in agreement with the quadratic convex shape of the misfit function that we expected and that is shown in Figure 5.5b.

In reality the HMC requires very few iterations to solve this simple problem (there is only 1 unknown). For instance, after 500 HMC iterations I obtain already a mean equal to 1.0006 m/s with a $\sigma = 0.64$ m/s for this problem. The 1,000 iterations illustrated in Figure 5.5 were carried out only for illustration and research purposes.

The results from this simple exercise help us to validate the reformulation of the problem that I presented in the previous chapters and to get familiar with the behavior of the HMC exploration for this problem. This spike test serve us only for two main purposes: 1) to validate the formulation and numerical methods and 2) to assess the amplitude uncertainty of a well-located point source. Let me then move on to a more complex exercise.

A bilateral rupture

This exercise is several steps further in complexity from the previous exercise. In the previous example the ambiguity related to time and space was discarded thanks to the information provided by the gradient at the first iteration (based on a good illumination). In this second exercise I keep the same source-receiver configuration but instead of assuming a punctual impulsive source as the target, I assume a small bilateral rupture. This rupture starts at the center of the line source and propagates to both sides of the line source. The total duration of this source is 2.5 seconds. Only three out of the 21 spatial nodes (the central one and two nodes beside) exhibit significant slip-rate values (see Figure 5.6a). The slip-rate time history of each of the three fault nodes involved in this rupture are exactly the same: each time history is just delayed according to a rupture velocity of 2 km/s. The representation of this synthetic bilateral rupture is shown in Figure 5.6a. In total, this rupture represents 8 [time samples] × 3 [spatial nodes] = 24 [unknowns] out of the total 861 dimensions of the model.

Let me recall the two different approaches where the HMC technique can be used: 1) to obtain a solution and the associated uncertainties or 2) to assess the uncertainties of a given solution. In this exercise, I propose four different configurations where these two different approaches can be illustrated. The first configuration assumes a simple diagonal mass matrix whose elements in the diagonal are either large ($1e10$) or small (equal to 1). The elements which values are small are the ones related to the 24 unknowns that are easy to identified thanks to the values of the first gradient (due to the good illumination and the noise-free data). The other parameters are set to have very large mass values. For the other two exercises, the inverse of the mass matrix (covariance of the momentum probability distribution function) is designed based on a 2D anisotropic Gaussian-shape correlation function (as described in equation (4.1)), which block diagonal structure allows to take into account an expected time and space coherence of the rupture model (see Figure 5.8c). Therefore, for these two HMC explorations the 24 auxiliary momentum variables related to the 24 unknown are drawn from a probability distribution which covariance matrix is linked to that mass matrix. For the other remaining dimensions the mass is assumed to be very large ($1e10$). The integration step is set as $\delta = 0.1$ and the number of integrations steps is selected from a uniform distribution of integer numbers ranging from 1 to 50 for the four HMC runs. The initial guess for the four runs is the same, a rupture model with zero slip-rate values everywhere. The total number of HMC iterations is set as 2700 for the all explorations. Notice that the first two explorations belong to the first approach: a solution to the problem and the associated uncertainties have to be determined.

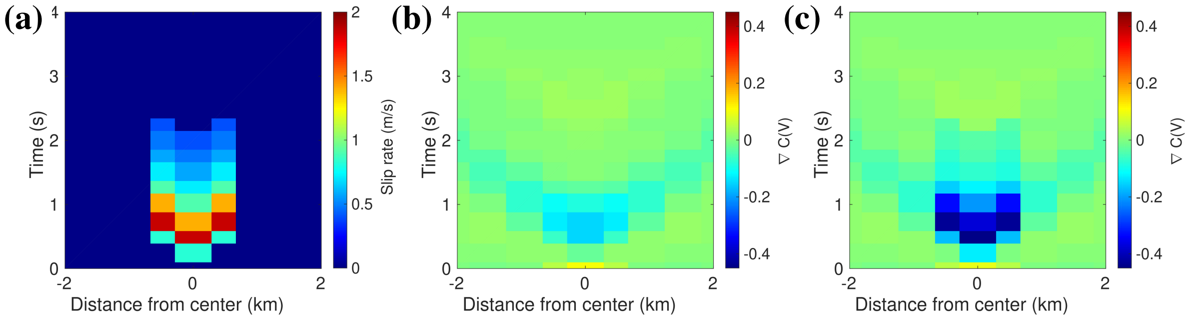

Figure 5.6: Illustration of the a) synthetic bilateral rupture model, and the gradient of the misfit function at the first iteration b) without considering prior information and c) considering it. The gradients here shown are computed taking into account the 3 components of the 420 receivers. The initial guess is a rupture model with no slip-rate values anywhere. The model used as a prior model (affecting the gradient) is shown in Figure 5.8b. It can be seen in (b), that the gradient is pointing out where the slip-rate from the first guess has to be incremented to better explain the data. In c) the shape of the gradient is improved and its shape is much closer to the expected rupture model.

On the contrary, the third and fourth configurations belong to the second approach: the assessment of the uncertainties have to be determined based on a given solution. For the third HMC exploration the regularization information is incorporated. Therefore, the prior model (a given solution), which is close to the target (compare Figures 5.6a and 5.8b) is considered. This prior model (which is very close to the target) is chosen in order to evaluate the effect of including accurate prior information into the HMC exploration. The prior model is just a small modification of the target model, Figure 5.7, compares the two different slip-rate functions from the target and the prior models. In realistic cases, however, the prior model might be far from the true solution, which can prevent us from looking close to the vicinity of the target solution. The hyper-parameter ϵ from the regularization term is set in such a way that the prior information is equally balanced with the data misfit term. This third case, however, considers the identity matrix as the mass matrix of the auxiliary momentum variables. Therefore, we are interested in looking at the impact of the prior information even when the mass matrix is poorly tuned. Finally, the fourth case considers exactly the same configuration as the third, but instead of considering an identity mass matrix it uses the time-spatial coherence matrix (Figure 5.8c).

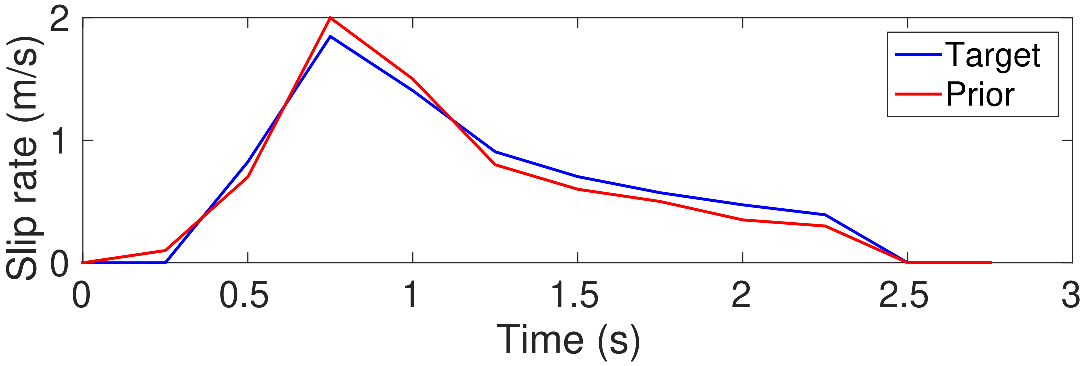

Figure 5.7: Comparison of the slip-rate time functions of the target (blue line) and the prior (red line) models respectively.

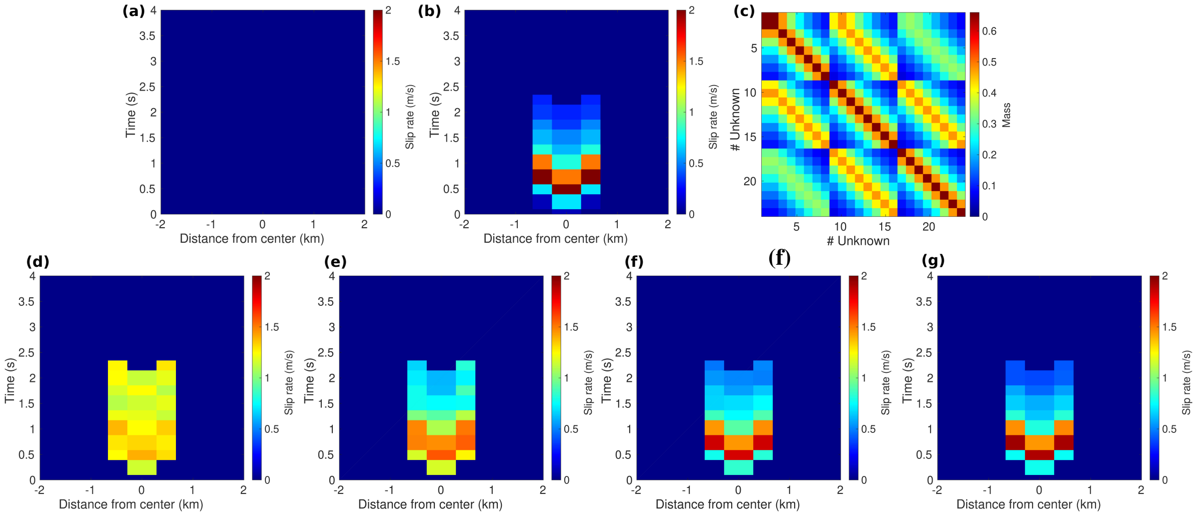

Figure 5.8: Summary of the resulting mean rupture models obtained from the four different HMC explorations. (a) initial guess used for the four explorations. (b) prior model used only for the third and fourth exercises ((f) and (g)). (c) mass matrix used for the second and fourth ((e) and (g)) explorations to draw the auxiliary momentum variables. On the bottom, a comparison between the resulting mean rupture models obtained from the four explorations: (d) without taking into account prior information and with the identity as the mass matrix, (e) only using the mass matrix showed in (c) and no prior information, (f) using the prior information from (b) and with an identity mass matrix, and (g) using the mass matrix shown in (c) plus the prior model illustrated in (b). Notice that by tuning the mass matrix to account for time-space coherence the resulting mean model (e) improves significantly. Results from (f) where the prior information is considered are also quite improved even if the mass matrix considered is diagonal.

Notice that these four different explorations are also helpful to see the influence of the mass matrix and the prior information into the HMC exploration. In addition, these four HMC explorations incorporate upper and lower limits (constraints as described in equation (5.17), which force the exploration to be in a range from -1 to 2.5 m/s. Finally, as in the previous exercise, I use the synthetic bilateral rupture to compute the exact seismograms that are then used as the noise-free observations at the 3 components of the 420 receivers around the line source.

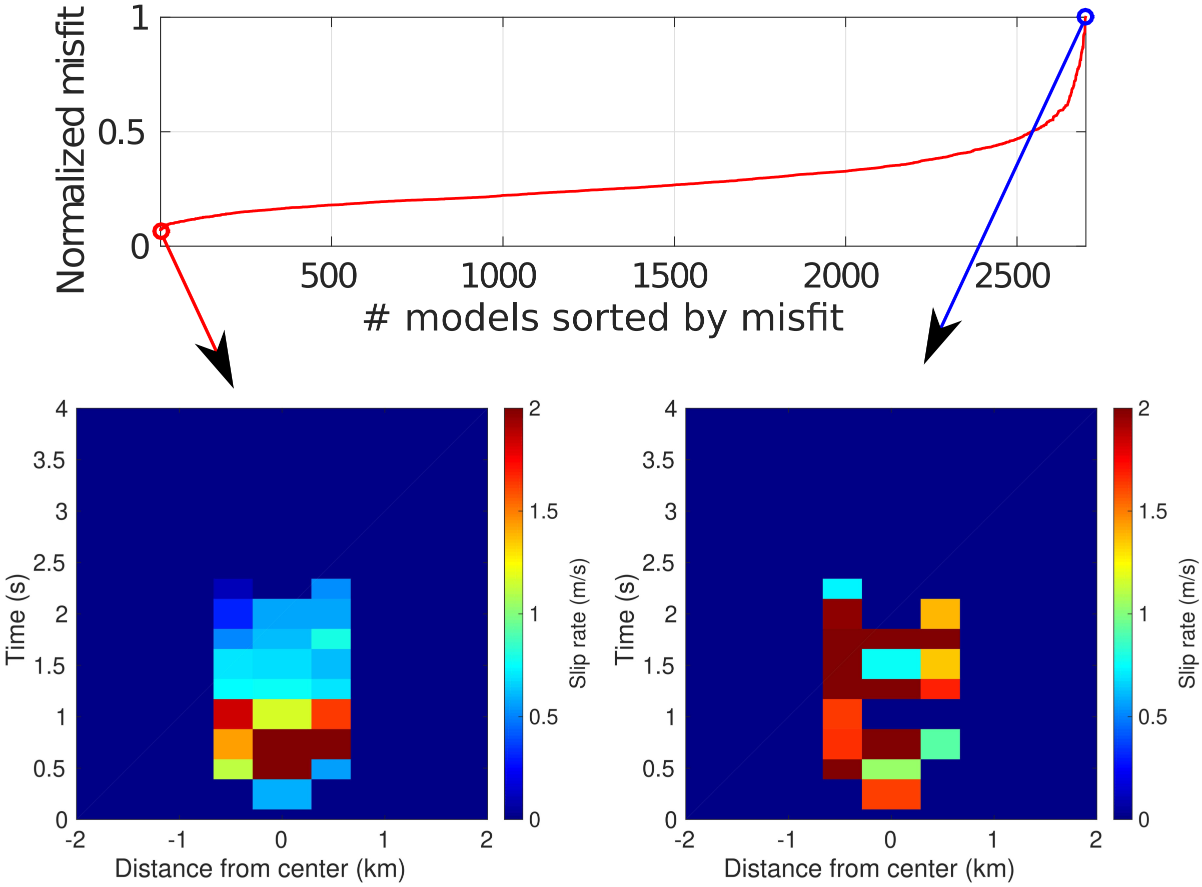

Figure 5.9: a) Misfit of the 2,700 models explored by the HMC strategy sorted from the minimum (most likely scenario) to the maximum (most unlikely). In a) the red and blue circles represent the misfit of the minimum and maximum misfit scenarios respectively. b) and c) illustrate the rupture models with the minimum and maximum misfits (according to the red and blue arrows). These plots correspond to the third HMC exploration, which considers prior information and a block diagonal mass matrix to account for time-space coherence.

On the contrary, the results from the second and third exercises are much better than the first case. It is evident that, for the second case the enforced spatial coherence (due to the non-diagonal mass matrix) allows to account for a coherent perturbation of the parameters. Therefore, the HMC exploration is able to focused only on the models that respect this time-space coherence and the resulting *ppd* exhibits a Gaussian-shape (see Figure 5.10b). Notice also that the mean model from that second exploration is less smooth that the one from the first case (compare Figures 5.8e with 5.8d). Finally, the best case is the third one, which includes the prior information besides the tunning of the mass matrix. For that case, the exploration is driven closer to the real solution. The mean model from this last case is the closest to the target solution (see the mean model from Figure 5.8f). The *ppd* is the less similar to a uniform distribution and its Gaussian-shape is better defined (compare Figures 5.10a,b,c).

The results from the four runs above described are summarized from Figures 5.9 to 5.13. The first run, which does not consider any prior information or time-space coherence (enforced by the mass matrix) provides a mean model very smooth and far from the real target model to be reconstructed (Figure 5.8d). Looking at the 24-dimensional *ppd* that is found by this run, it is clear that, when no pior information is incorporated into the potential energy (misfit function) and a simple diagonal mass matrix is assumed, it is not enough to determine correctly the expected solution and the estimated *ppd* behaves as a uniform distribution (see the uniform behavior of Figure 5.10a). The shape of the posterior distribution shows a small evidence of where the most probable might be, but in general, exhibits a uniform-shape *ppd*. This resulting *ppd* means that any slip-rate value ranging from -1 to 2.5 m/s randomly organized in this 24-dimensional model are equally accepted to explain, to some extent, the available data. It is important to highlight that this is a striking result if we recall that this exercise is carried out in a unrealistic perfect illumination configuration. Therefore, to get simultaneously an accurate approximation to the solution to the problem together with the associated *ppd* without using any information or tuned mass matrix (first approach) appears to be very difficult even in perfect illumination conditions.

Regarding the evolution of the Hamiltonian system, I can say the following. The individual trajectories (perturbations of the slip-rate parameters) are completely chaotic if the mass matrix is assumed as diagonal (no correlation between parameters) and/or if no prior information is used. For the case that assumes no prior information and the identity as the mass matrix, each auxiliary variable is independent from the others. Therefore, the parameters are randomly perturbed in all possible directions without any link between them. The fact is that, this random independent perturbation is not a correct assumption as we might expect that parameters close in time and space have to act similarly. The consequence that can be seen from this random independent perturbation is that the chaotic behavior of the particle proposes scenarios where all the parameters interact in such a way that their responses sum or cancel the effect of the others with the only goal to fit the data. These interactions provide scenarios that are very far from the target solution but that produce seismograms that are not completely far from the observations (belonging to the null space). As a consequence, most of these scenarios are accepted, fact that is reflected by the uniform-like shape of the *ppd* obtained from the first exercise (Figure 5.10a).

It is important to notice that, when the prior information is considered (Figures 5.8f,g), the resulting mean model remains close to the assumed prior model, regardless of the shape of the mass matrix (either diagonal or non-diagonal). Therefore, the prior model is able to enforce the time and space coherence that is not taken into account by the diagonal matrix. However, for this exercises, which might not be realistic, the prior model is very close from the target solution.

The Figure 5.11, 5.12 and 5.13 form the corner plot of the 24-dimensional *ppd* found by the fourth HMC exploration. In those figures, it is clear that thanks to the prior information and enforced coherence between parameters, the shape of the *ppd* tends to a Gaussian-shape. As a final illustration, in Figure 5.9 I provide a plot of the misfit values for all the 2700 models explored by the third HMC exploration. The values of the misfit are sorted in an incremental fashion. Below that plot, I provide the models with the minimum and maximum value of misfit from the the whole population of the 2700 models.

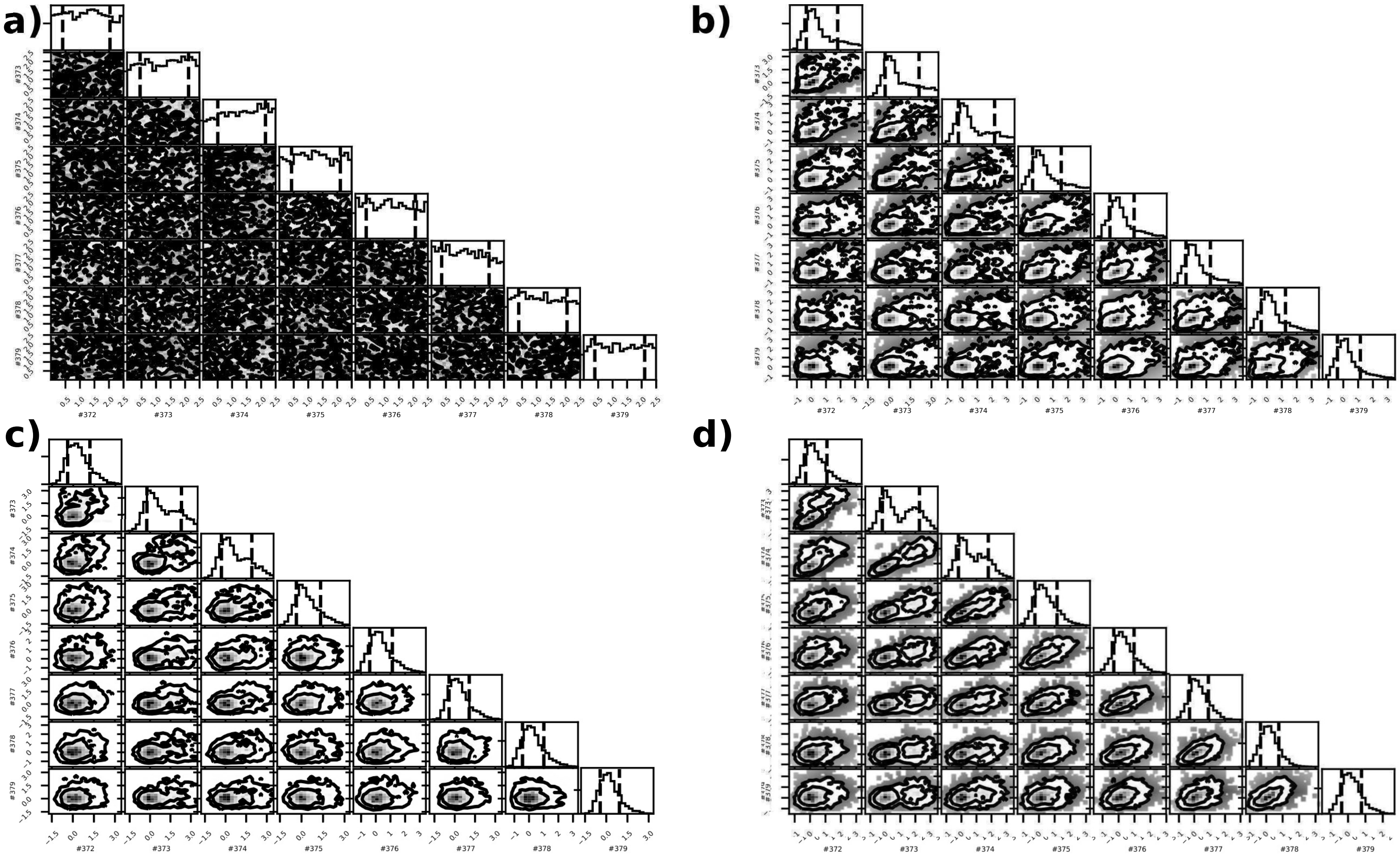

Figure 5.10: Comparison of the first 7 dimensions of the obtained *ppd*s from the four HMC explorations after 2,700 iterations. a) No regularization and diagonal mass matrix, b) using a non-diagonal mass matrix and no prior information and c) accounting for prior information and a diagonal mass matrix and d) using a non-diagonal mass matrix and accounting for prior information. Only the first 7 dimensions out of the 24 explored are presented in this figure. The 24 dimension of d) are illustrated in Figures 5.11 5.12 and 5.13. In (a), (b) (c) and (d) quantiles 0.16 and 0.84 are represented by the vertical dashed lines in the 1D plots, while the levels of confidence 0.68 and 0.95 are shown as the contour lines in the 2D plots. The seven dimensions here illustrated represent the slip-rate time history of the node at the left of the center of the line source.

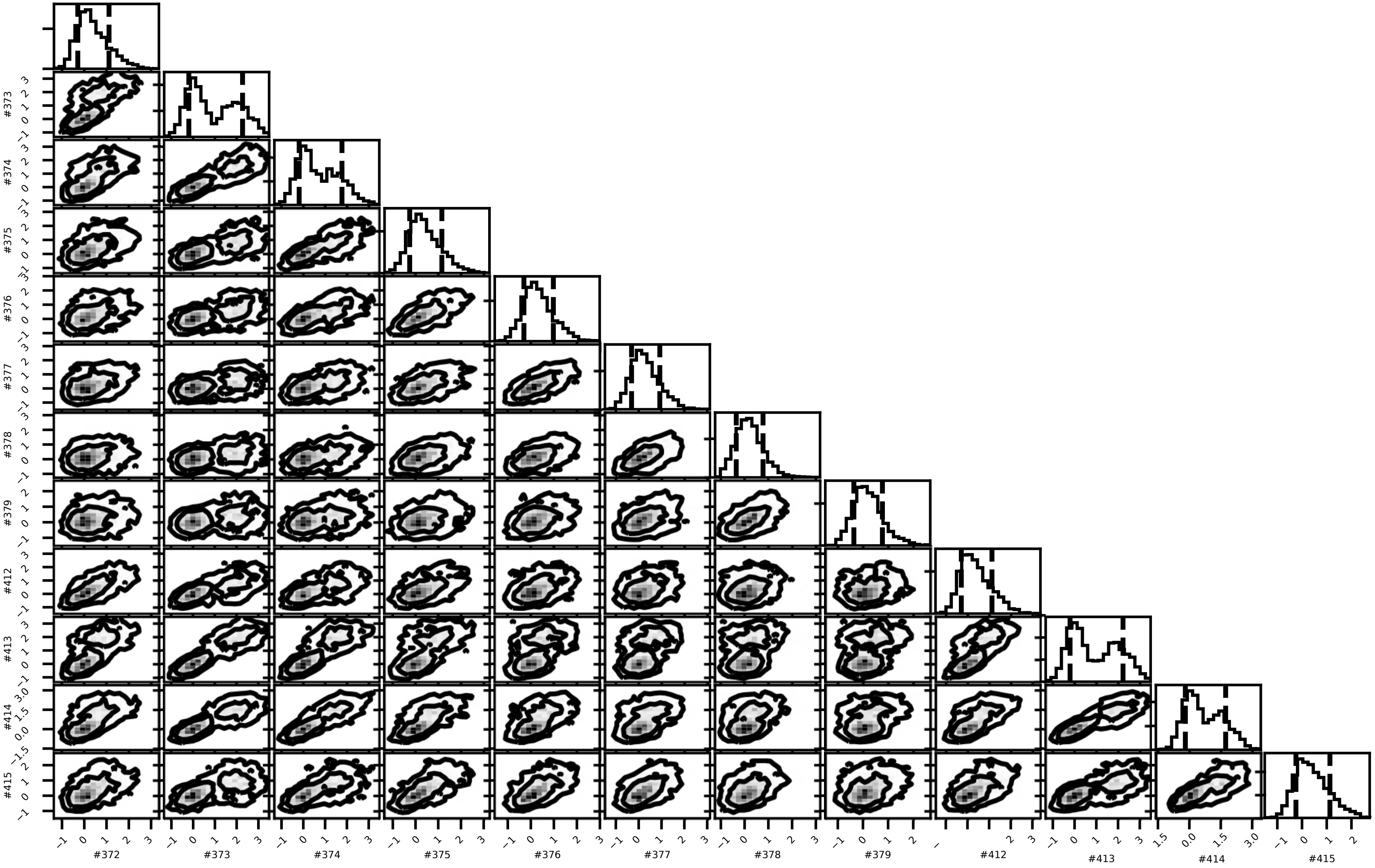

Figure 5.11: Corner plot illustrating the 24-dimensional *ppd* obtained for the bilateral rupture exercise from the third HMC exploration, which accounts for time-space coherence (i.e. non-diagonal mass matrix) and prior information. In this plot, quantiles 0.16 and 0.84 are represented by the vertical dashed lines in the 1D plots, while the levels of confidence 0.68 and 0.95 are shown as the contour lines in the 2D plots. The 24 dimensions here illustrated represent the slip-rate time history of the 3 spatial nodes located at the center of the line source. This *ppd* is obtained after 2,700 HMC iterations.

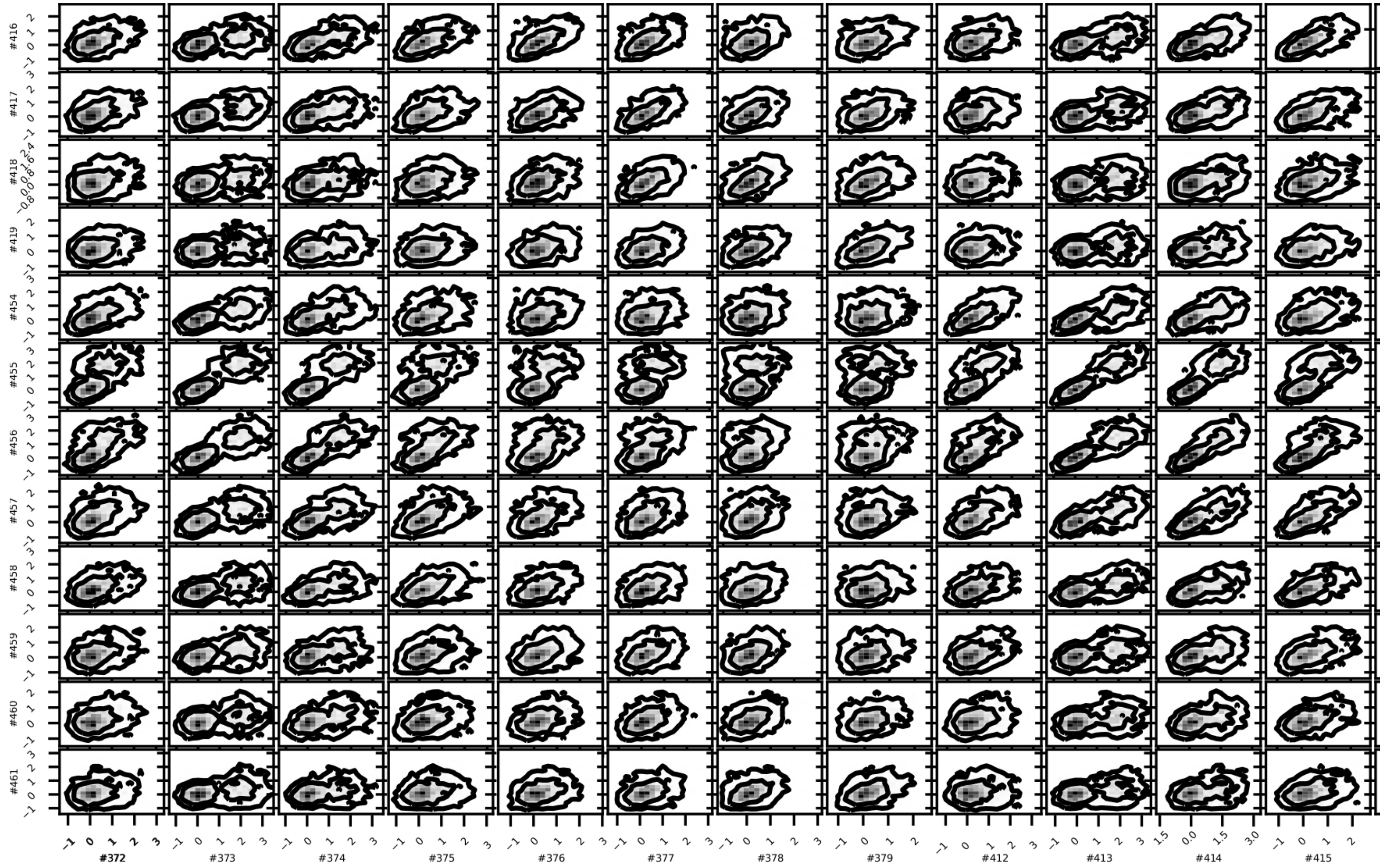

Figure 5.12: Continuation of Figure 5.11

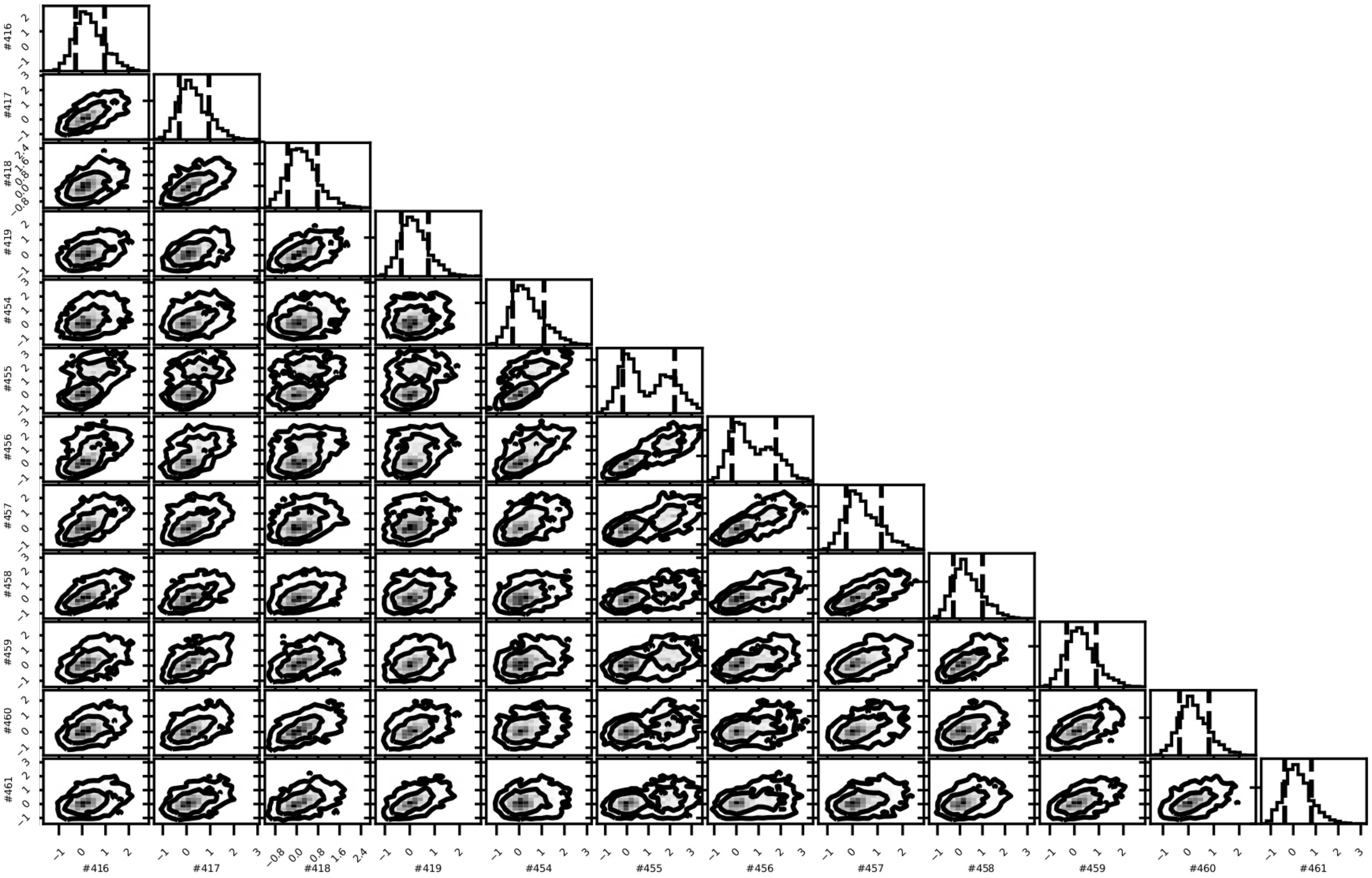

Figure 5.13: Continuation of Figure 5.11 and 5.12.

5.5 Conclusion

In this chapter, I present the basic theory of Bayesian inference as well as the fundamental concepts behind a standard Markov Chain Monte Carlo (MCMC) strategy and the Hamiltonian Monte Carlo (HMC) approach. I provide simple examples where some of the advantages of the HMC strategy are illustrated. Then, I apply the HMC strategy to the kinematic source inversion problem taking into account all the previous development presented in Chapters 3 and 4.

The HMC technique can be applied to the kinematic source reconstruction problem in order to achieve two different goals: 1) to obtain a solution to the problem together with the related uncertainties or 2) to assess the uncertainties given a prescribed solution. In this chapter, the preliminary investigation presented is focused on the second goal. The investigation related to the first goal remains as a very interesting and challenging perspective of this work. Taking into account that the HMC technique is able to describe multimodal functions (like in the second exercise of Section 5.3), its application to the source inversion problem under a non-linear formulation seems as a very interesting approach to be explored. Under the linear formulation of the problem, the HMC exploration around a given solution appears to be more logical and consistent: once a solution is found the HMC strategy serves as an efficient variational technique to describe the closest vicinity. The importance of the linear formulation under this approach relies on the fact that a small perturbation of the slip-rate time space history maps directly into small changes in the estimated seismograms. This feature is not ensured under the non-linear formulation of the problem. Therefore, a more general exploration (first approach) would be more pertinent if a non-linear formulation of the problem is to be used.

According to this preliminary investigation, the HMC approach seems to be pertinent and compatible to perform the exploration of the space of solutions around a given solution under the linear time-domain formulation of the source reconstruction problem. However, the tuning of some fundamental parameters of the technique appears to be crucial for a correct exploration. In the hierarchy of importance, I should point out that the incorporation of prior information (injecting the physics to the problem) as well as the tuning of the mass matrix (controlling the time-space coherence) seem to be the most relevant. It is clear that, when dealing with problems such as the source inversion where a significant trade-off between parameters is present, these ingredients play a very important role. While the prior information allows us not to explore very far from the desired physical scenarios, the mass matrix (used to draw the auxiliary momentum variables) allows to account for the existing interaction between parameters. Under the linear time-domain formulation of the kinematic source inversion problem we know that the number of unknowns is quite large, however, these parameters have to be somehow linked physically. It is the task of this matrix to control the level of perturbation of all the parameters together taking into account this physical interaction. Certainly, a more detailed investigation of a correct way to choose the mass matrix has to be done for this type of problems, the identity matrix is completely far from the optimal to tackle high correlated parameters. In a second level of importance, I would mention the randomness pattern of the integration step δ and the number of steps L, which seem to be less important than the mass matrix, at least for the exercises explored.

Prior information plays an important role. The chaotic behavior that the HMC exploration exhibited in the non-regularized case which used a diagonal mass matrix of the simple bilateral exercise is certainly not only due to the incorrect choice of the mass matrix. In fact, this behavior is also related to the lack of physics of the problem (even when a good illumination is available). From the results of the two exercises where the prior information is incorporated (based on the model regularization term), it can be seen that the chaotic behavior is mitigated and the exploration starts to focus its attention in the regions surrounding the most probable scenarios. This can be interpreted in the following way: the misfit function of this problem is convex and quadratic, however, without prior information its shape in the high-dimensional space of solutions is very flat at its minimum (many scenarios are possible and equivalent). The prior information, that injects to the problem the necessary physics to be honored, allows us to focus our attention only at a determined region of interest of that immense space of solution. Then, including the prior information into the problem allows us to pass from a misfit function with a very flat U-shape to a more defined V-shape. Even though this effect of the prior model can be risky, this is certainly less risky than assuming a different (reduced) parameter design of the slip-rate function, which can consider few parameters such as starting time, rise time, and final slip. In that sense, if the assumed prior model is quite far from the true solution, a closer look to the vicinity where the true solution lies will be far from the region where we are performing our exploration.

The application to the HMC to much more complex cases with realistic source-receivers configurations and with a significant increment of the number of unknowns (dimensions) remains as a challenging opportunity. In particular, the progressive time-domain strategy, that is presented in Chapters 3 and 4, seems to be a very interesting technique to be coupled with the HMC strategy. The coupling of both strategies would allow the HMC exploration to progressively determine the regions of interest in the large dimension space of solutions, in a similar way to the importance sampling technique or the particle filter strategy.

Conclusions and perspectives

Conclusion & Perspectives

Conclusion

Theoretical and computational development

The work presented in this PhD dissertation provides a different and innovative way to tackle the kinematic source inversion problem, as well as a promising technique to assess the associated uncertainties. First, the strategy presented in Chapters 3 and 4 are based on a linear time-domain formulation of the problem, which allows to take into account the causality of the physical phenomenon by progressively inverting increasing data time-windows to reconstruct the whole rupture history. In addition, this strategy is able to incorporate different prior information as well as preconditioning strategies which can help, for instance, to mitigate the loss of resolving power with depth. Moreover, this progressive inversion technique keeps the linearity between observed data and the parameters describing the seismic rupture. This is an important feature which plays a crucial role to assess the uncertainties of a given reconstructed model.

Another important conclusion from this work is the suitability of the HMC technique to assess the uncertainties of the kinematic source inversion problem. Even though the examples presented in this manuscript remain as a preliminary investigation under idealized configurations, the results show that the HMC strategy is with the adjoint-based inversion scheme. This is basically due to the fact that the HMC exploration, contrary to a standard MCMC exploration, relies on random-walks which take into account the local gradient direction. Thanks to the whole development presented in Chapter 3, this local gradient estimation was already a part of the available information in our hands and therefore the implementation of the HMC technique was possible. In order to tackle real datasets, however, a more careful design of the mass matrix (used to perturb coherently the slip-rate parameters) would be required as well as a careful construction of the prior information and the uncertainties related to that information.

Regarding the computational development, three main products are derived from the work here presented. The first is the modified version of the well-known code AXITRA (Coutant, 1989). This modified version is able to compute the stress-state tensors (described in Chapter 2), which are required as inputs by any of the kinematic inversion strategies that I presented.

The second product is the first version of the kinematic source inversion code, which is based on the deterministic approach that is explained in Chapters 3 and 4. This first version is able to perform the source inversion either considering the whole recorded data (Standard Inversion Strategy) or the progressive data time-windowing approach (Progressive Inversion Strategy). As mentioned before, this technique includes the depth preconditioning strategy, which tries to mitigate the loss of resolution at depth. In addition, this code is also able to account for any prior information and for an isotropic or anisotropic smoothing operator.

The third product is the code which is based on the Bayesian formulation and the Hamiltonian Monte Carlo strategy presented in Chapter 5. This version also includes the tools incorporated by the deterministic one.

The modified version of AXITRA (named AXISTRESS) and the deterministic version of the source inversion strategy (INV3DKIN) are freely available and can be downloaded from my GitHub repository. The toy HMC examples from Section 5.3 can be also obtained from that repository. The HMC version of the kinematic source inversion technique is currently in process of being released in the same way.

Applications

In order to validate all the development here presented, the strategies presented in Chapter 3 were applied to well-known benchmarks. Two exercises from the Source Inversion Validation project were tackled, and significantly good results were obtained. In addition, such validation exercises evidenced some of the advantages of the hierarchical time progressive approach.

In terms of real applications, the different strategies here presented were also successfully applied to the real dataset of the 2016 (M_w7.0) Kumamoto earthquake. The results obtained from our approach were able to correctly explain the data while being coherent with the solutions proposed by other authors, who apply well-established strategies in the source reconstruction community.

Regarding the HMC kinematic source inversion technique, only simple synthetic exercises are investigated and presented in this manuscript. However, a more complex application to the Source Inversion Validation exercises are seen as future synthetic cases to be explored.

Perspectives

Certainly, one of the most interesting perspectives of this work is the possible analysis of real earthquake datasets using the HMC approach that is presented in Chapter 5. The next step is to apply this strategy to more complex synthetic cases (e.g. the SIV2b), and then to a real datasets. Many real datasets might be interesting to tackle using this approach, however, I plan to use this strategy to analyze the 2015 (M_L5.5) Orkney, South Africa, earthquake (Moyer et al., 2017), whose source-receiver configuration and knowledge of the medium of propagation appear to be ideal for the application of this strategy. In addition, this strategy could be also apply to the 2016 Kumamoto earthquake in order to estimate the associated uncertainties related not only to model presented in Chapter 4 but also to other solutions proposed by other authors. To me it would be very interesting to be able to provide a posterior probability density function related to a given rupture model together with the location of other different solutions according to their corresponding confidence level inside that *ppd*. As mentioned in the conclusions of Chapter 5, another interesting perspective of this work would be the application of the HMC technique to the kinematic source inversion problem under a non-linear formulation. The HMC approach appears to be a good strategy to describe multimodal functions (cases with multiple local minima). Therefore, a global search using the HMC technique under the non-linear formulation of the problem can be very attractive.

In addition, some of the foreseen work is to assess the uncertainties related to the number of parameters used to describe the slip-rate time space history. In this sense, I believe that the fundamental development presented here shall allow the use of the HMC strategy together with techniques, such as the trans-dimensional exploration, to be able to provide a statistical analysis of the most suitable number of parameters required to correctly describe the seismic rupture (as done in seismic exploration by K. and Reetam, 2017). This future work is not only linked to the way to describe the temporal and spatial grid defining the total number of parameters. From my point of view, this has to be also linked to the causality of the problem and, therefore, to the progressive inversion scheme that is presented in this dissertation.

Another possible application to the linear time-domain formulation here presented is a three-step kinematic source inversion strategy. Following the strategy presented by Hernandez et al. (1999), I believe that the inclusion of the progressive time-domain source reconstruction technique, here presented, as the third step of the source inversion process can enrich the proposed kinematic models. The linear time-domain formulation can use the results provided by any non-linear (time- or frequency-domain) approach as prior model, and the hard constraints imposed on the shape of the time history and rupture velocities can be relaxed. Such relaxation might help us to see more complex rupture models that might explain better the data. In addition, it might be possible also to use HMC approach either to assess the uncertainties around the models proposed by the non-linear formulations or by the linear time progressive approach using as prior information the results from the non-linear strategies (which are based on a more physical parametrization of the problem). Beside this, another interesting perspective of this work, is the possible application of the deterministic progressive inversion strategy to study more earthquakes. In particular, I believe that this different way of assimilating and inverting the data should ease the analysis of the initial phase of earthquakes. Thanks to the progressive time-domain formulation of the problem, a detailed study of the first seconds of the available recordings, less contaminated by propagating effects, might shade light on what happens at the very first seconds of the rupture.

Finally, another interesting perspective of this work is the fact that, thanks to the precomputed stress-state tensors, it is possible to estimate a rough prediction of some wave packets that have not been yet recorded by analyzing very few data (e.g. 1 or 2 seconds). To me, this specific feature can be of great importance to early disaster response systems when dealing with large earthquakes. Certainly, there are some high-performance computating challenges to solve before thinking in the application of these techniques to either synthetic and/or real earthquakes. Some of these challenges are related to implement an efficient reading of the precomputed data bank of stress-state tensors, as well as to perform the necessary convolutions as fast as possible on a distributed architecture. These challenges are difficult but not unfeasible.

Appendix A: Was the 9 October 1995 Mw8 Jalisco, Mexico, Earthquake a Near-Trench Event?

ADVANCING EARTH AND SPACE SCIENCE

Journal of Geophysical Research: Solid Earth

RESEARCH ARTICLE
10.1029/2017JB014899

Was the 9 October 1995 M_w 8 Jalisco, Mexico, Earthquake a Near-Trench Event?

Vala Hjörleifsdóttir[1], H. S. Sánchez-Reyes[2], Angel Ruiz-Angulo[3], Maria Teresa Ramírez-Herrera[4], Rocio Castillo-Aja[5], Shri Krishna Singh[1], and Chen Ji[6]

[1]Departamento de Sismología, Instituto de Geofísica, Universidad Nacional Autónoma de México, Ciudad de México, México, [2]University Grenoble Alpes, CNRS, ISTerre, Grenoble, France, [3]Centro de Ciencias de la Atmósfera, Universidad Nacional Autónoma de México, Ciudad de México, Mexico, [4]Laboratorio Universitario de Geofísica Ambiental, IGG, Universidad Nacional Autónoma de México, Ciudad Universitaria, Ciudad de México, Mexico, [5]Posgrado en Geografía, Universidad Nacional Autónoma de México, Ciudad Universitaria, Ciudad de México, Mexico, [6]Department of Earth Science, University of California, Santa Barbara, CA, USA

Abstract The behavior of slip close to the trench during earthquakes is not well understood, and observations of large earthquakes breaking the near trench fault surface are rare. The 1995 M_w 8.0 Jalisco earthquake seems to have broken the near-trench area, as evidenced by large M_s-M_w disparity, small high-frequency radiated energy compared to total energy, and low E_r/M_0 ratios, in addition to several finite slip models showing large slip near the trench. However, slip models obtained using campaign Global Positioning System data suggest slip near shore. In this study we try to answer whether this event was a near-trench event or not, by inverting teleseismic *P*, *S*, Rayleigh, and Love waves, as well as campaign Global Positioning System static offsets, either separately or jointly, to obtain the slip distribution on the fault as a function of time. We find two possible end-member scenarios consistent with observed data: (1) coseismic slip distributed between coast and trench and no (or very little) postseismic slip and (2) coseismic slip principally near the trench with large (up to 1.8 m) aseismic slip occurring in the first 5–10 days after the earthquake, with a total moment corresponding to 16% of that of the event. We are unable to distinguish between these two end-member scenarios by tsunami modeling and finally are neither able to conclude or exclude that the event was a typical near trench event.

Key Points:

- The event nucleated at ~20-km depth and broke a >150-km-long segment of the Mesoamerican Subduction Zone, rupturing toward the NW
- There may have been a slip between the trench and coast as suggested by joint inversion of teleseismic records and near-field static offsets
- Another possibility is that there was coseismic slip near the trench and postseismic slip near the coast

Supporting Information:

- Supporting Information S1

Correspondence to:
V. Hjörleifsdóttir,
vala@igeofisica.unam.mx

Citation:
Hjörleifsdóttir, V., Sánchez-Reyes, H. S., Ruiz-Angulo, A., Ramírez-Herrera, M. T., Castillo-Aja, R., Singh, S. K., & Ji, C. (2018). Was the 9 October 1995 M_w 8 Jalisco, Mexico, earthquake a near-trench event? *Journal of Geophysical Research: Solid Earth*, *123*. https://doi.org/10.1029/2017JB014899

Received 25 AUG 2017
Accepted 12 SEP 2018
Accepted article online 15 SEP 2018

1. Introduction

The shallowest portion of the mega thrust interface in subduction zones has lower seismicity than the interface further downdip and has been thought to accommodate the relative plate motion by creep (Byrne et al., 1988). However, in some regions, this portion of the interface breaks in so-called tsunami earthquakes (Kanamori, 1972; Lay et al., 2012), such as the Sanriku 1896 (Tanioka & Satake, 1996), Nicaragua 1992 (Kanamori & Kikuchi, 1993), Java 1994 (Polet & Thio, 2003), and Mentawai 2010 (Hill et al., 2012; Newman et al., 2011) earthquakes or participates in large megathrust events, with exceptionally large slip, as in the 2011 Tohoku earthquake (Ito et al., 2011; Sato et al., 2011; Shao et al., 2011; Simons et al., 2011).

There are many unanswered questions about the relative behavior of the friction on the fault between this shallowest portion of the subduction zone interface and the further downdip segment typically considered seismogenic, for example, what controls the apparent downdip segmentation? How does it vary between different subduction zones? Is the updip segment aseismically creeping in some zones? Can the updip portion break by itself, or do earthquakes have to nucleate and/or involve important slip in the downdip zone as well? The answers to these questions are important for the estimates of tsunami hazard as large slip in the updip zone produces a much larger tsunami than similar slip in the downdip zone. However, due to the long recurrence interval of large earthquakes and short time span of historical records, there are only a few regions where large earthquakes breaking the shallow parts of the interface have been observed.

Arguably, the clearest example of downdip segmentation is in the Japan Trench. Several earthquakes have broken the subduction interface during the last 150 years, notably by the 1896 Sanriku earthquake that is considered to have broken only the shallow part of the interface (Tanioka & Satake, 1996); the 1978 and 2005 Miyagi-Oki earthquakes, which broke the further downdip segment (Okada et al., 2005; Seno et al., 1980; Yamanaka & Kikuchi, 2004); and the 2011 Tohoku earthquake, which broke both the shallow and the

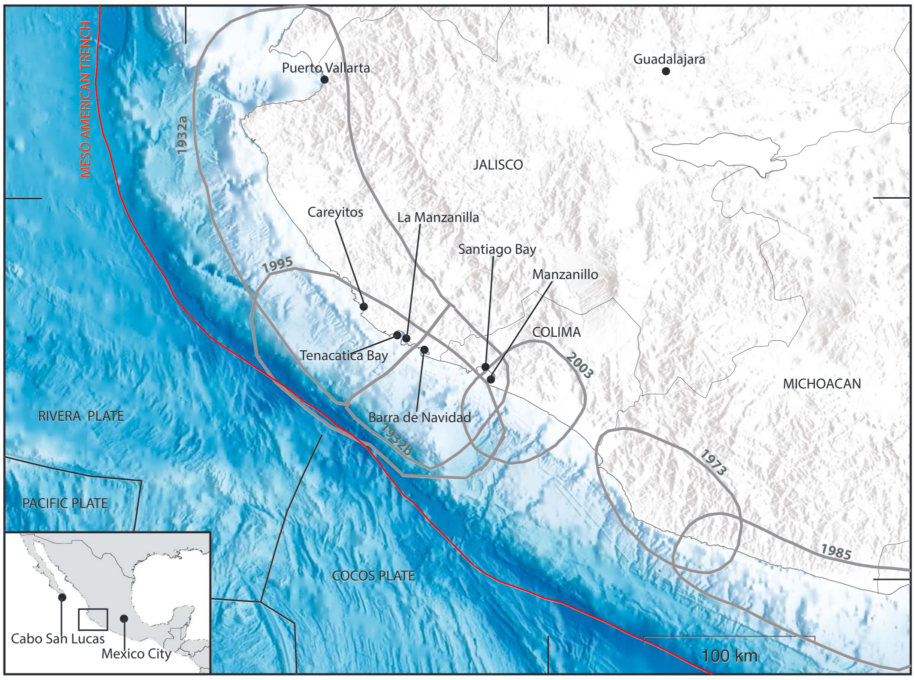

Figure 1. Tectonic context of the 1995 earthquake, as well as rupture areas of large earthquakes in the region (gray circles; 1973, Reyes et al., 1979; 1932, 2003, Singh et al., 1985, 2003; 1985, UNAM Seismology Group, 1986; 1995, Pacheco et al., 1997), localities referred to in text and plate boundaries (Bird, 2003).

deep parts of the subduction interface (Ammon et al., 2011; Simons et al., 2011) with an extraordinarily large slip of up to 60 m (Ito et al., 2011; Sato et al., 2011; Shao et al., 2011) on the shallow part. In this region, the near-trench area has also been observed to slip in episodic slow-slip events (Ito et al., 2015).

Not only can the updip portion of the fault accommodate relative motion across it by creep or episodic slow slip but so can the downdip portion, as well as some areas in the traditionally seismogenic zone (see, for example, Lay et al., 2012). The interpretation is that the friction on the fault interface varies from place to place (Pacheco et al., 1993).

In Mexico, the two largest subduction interface events recorded in the last 100 years, those of 3 June 1932, M_S 8.2 (Abe, 1981), and 9 October 1995, M_w 8.0 (GlobalCMT), broke the same lateral segment of the Mesoamerican Trench (Figure 1). Additionally, another large earthquake, the 18 June 1932, M_S 7.8 (Abe, 1981) event, broke the same segment. Several observations suggest that the 1932 and 1995 events were very different (Pacheco et al., 1997). High intensities and similar M_S (8.2) versus M_w (8.0) values were reported for the 1932 event (Anderson et al., 1989; Singh et al., 1985), whereas low intensities and a large discrepancy between m_b/M_S (6.6/7.4, U.S. Geological Survey [USGS]) versus M_w (8.0, GlobalCMT) for the 1995 event (Ortiz et al., 1998, 2000). These differences suggest that perhaps the 1995 event broke the shallower segment of the fault interface, whereas the 1932 event the deeper.

There is conflicting evidence from seismic (Mendoza & Hartzell, 1999; Mendoza et al., 2011; Ye et al., 2016, USGS Finite fault source model) and geodetic data (Hutton et al., 2001; Melbourne et al., 1997) on the location of the large slip during the 1995 event; the slip distributions obtained from seismic data show much shallower slip than those obtained from Global Positioning System (GPS) data. Both types of models have their uncertainties and resolution issues, but the question remains, can both data sets be predicted by the same model?

In this study we aim to reconcile the different locations of large slip areas obtained by inverting seismic and geodetic data for the Jalisco 1995 earthquake. To do so, we invert seismic and geodetic recordings separately, as well as jointly. We find two possible scenarios: (1) a joint model with fairly uniform and purely coseismic slip

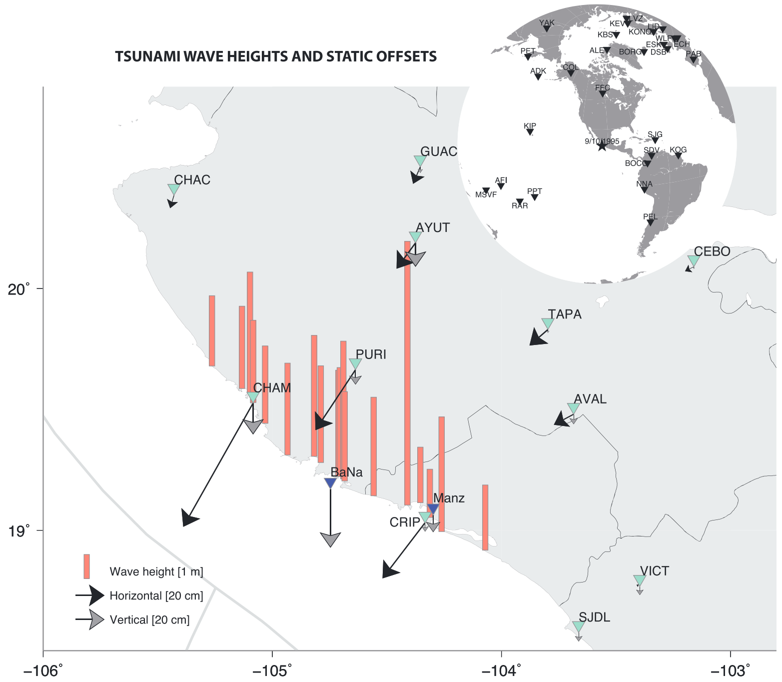

Figure 2. Data used in this study observed static displacements measured at Global Positioning System stations (aquamarine triangles), subsidence measured at pressure gauges (blue triangles), post tsunami field survey runup height estimates (peach bars), and seismic stations (black triangles on inset).

between coast and trench and (2) coseismic slip principally near the trench and aseismic slip (slow slip or afterslip) in the 6 months before or 5–10 days after the event, downdip of the coseismic slip. The tsunami wave height expected for each of the models is calculated and compared with tsunami observations in an attempt to set further constraints on the source model.

2. Seismic Source Modeling: Data and Methods

2.1. Teleseismic Data

Several digital, teleseismic, broadband recordings of the 1995 Jalisco earthquake are available. In this study we used *P* and *S* waves registered at 27 and 17 stations, respectively, with a relatively good azimuthal distribution, given the lack of high-quality stations in the Pacific basin (Figure 2). Furthermore, we use Rayleigh and Love waves registered at 17 and 13 stations, respectively. The stations are located at angular distances of 32 to 89° from the hypocenter.

The *P* and *S* wave arrival times are picked manually, to remove the effect of 3-D structure along their trajectories on the traveltime of the waves. Considerable care was taken in this step to assure that all stations were aligned on the same phase. We deconvolved the instrument responses from the original records, resulting in displacement seismograms, which we subsequently band-passed between 1–100 s for the body wave records and 170–250 s for the surface-wave seismograms.

2.2. Static Displacements

The 1995 Jalisco earthquake is one of the first large earthquakes for which coseismic displacements were measured by GPS instruments. A campaign survey that measured locations of 11 sites in the Jalisco-Colima area was carried out in March/April of 1995. The sites were reoccupied 5–10 days after the 9 October earthquake (Melbourne et al., 1997), roughly 6 months after the initial measurement. Coseismic displacement vectors were calculated by Melbourne et al. (1997) and Hutton et al. (2001). Both studies included 5–10 days of postseismic displacement in their estimates of coseismic displacement, due to the time spent to reoccupy the stations, as well as the aforementioned 6 months of preseismic displacements. In this study we mostly use the displacement vectors estimated by the second group Hutton et al. (2001) as they considered more precise orbits for the calculations; however, the differences are not large between the two sets of estimated displacement vectors, and we will show that our results are minimally affected by this choice.

2.3. Subsidence and Strong Motion Records

The observed subsidence at a tide gauge in Manzanillo harbor and on pressure sensors slightly offshore Barra de Navidad show subsidence of 11.8 ± 1.3 cm and 40 ± 2 cm, respectively (Ortiz et al., 2000). We note that these observations were not used in previous geodetic studies and the subsidence estimate from the tide gauge corresponds to deformation during a different time window than the GPS data, making a direct comparison difficult. For these reasons we have not included the data points in the inverse modeling, but rather forward predicted the subsidence values at the Barra de Navidad site, to compare with our models for reference. The Manzanillo harbor site is very close to the CRIP GPS site.

Records from five accelerographic stations are available for this earthquake. Unfortunately, none of the stations are located within a fault length of the earthquake, and they were located on or near dams, with near-station effects heavily influencing the movements. Therefore, we do not use these stations for the modeling.

2.4. Inversion Method

We invert the observed motions for the distribution of slip on the fault plane during the earthquake. The inversion is performed using the Fast Finite Fault (FFF) inversion algorithm (Ji et al., 2002a, 2002b). The algorithm uses a simulated annealing method, which minimizes the weighted difference between wavelet coefficients of observed and simulated seismograms. The slip on each subfault has an asymmetric time function (Ji et al., 2003), and smoothing is applied both to the slip distribution and to the rupture contours (Shao et al., 2011). Static offsets cannot be modeled by wavelets and are included in the misfit function by a simple difference between observed and modeled displacements.

Several subjective choices of input parameters are necessary for the modeling. First, the size and orientation of the fault plane have to be fixed. The strike is relatively well determined by the orientation of the subduction zone, but an error in the dip angle can have an important effect on the solution. We use the dip of 13° in this study, as an intermediate between the dip of the GlobalCMT solution (9°) and the dip of the slab model Slab1.0, which is 10–20° in this region (Hayes et al., 2012). The rake is allowed to vary within ±45° from an average rake of 90°. The weights put on the misfit of scalar moment, and the solution roughness is also important. However, amplitudes of surface waves are very sensitive to the scalar moment and when included in the inversion the weight on the scalar moment becomes unimportant. For reference we compare to the moment of the GlobalCMT solution, $M_{0_ref} = 1.15 * 10^{21}$Nm.

The slip on the fault plane is determined relative to the hypocenter. Therefore, the location of the hypocenter used has an effect on the geographical locations of the slip patches. Furthermore, the depth can have an effect on the observed pattern of slip. In Mexico it has been noticed that hypocenters estimated from global data tend to be mislocated toward the northeast by on the order of 20 km (Hjörleifsdóttir et al., 2016; Singh & Lermo, 1985), and we therefore use the hypocentral location reported by a local network (Red Sísmica del Estado de Colima, RESCO) (lat. 18.81°N, lon. 104.54°W, and depth 17.0 km); however, we set the hypocenter depth to 20 km so that the fault plane does not reach the surface far from the trench.

Other subjective choices are the weight on each wavelet coefficient (the relative importance of different periods) and the relative weight of static, long-period, and body wave data. Here we use the wavelet coefficients typically used in the FFF algorithm (Ji et al., 2002a, 2002b). We use the same weight on body and surface waves but vary the relative importance of the static data. Furthermore, the reference rupture velocity has an important impact on the slip distribution. We will invert the data assuming both nearly fixed and variable rupture velocities.

Journal of Geophysical Research: Solid Earth 10.1029/2017JB014899

3. Seismic Source Modeling; Results

3.1. Teleseismic Body and Surface-Wave Inversion

First, we perform an inversion of body and surface waves together. The seismograms used are chosen based on station noise level, as well as to obtain a satisfactory azimuthal coverage. We then assign the strike of the fault plane to best match the orientation of the trench, and based on initial test inversions, we select a fault plane sufficiently large as to contain all the slip in the earthquake. In this set of inversions, we do not constrain the moment, as it is well constrained by the surface-waves. We use the Crust2.0 (Bassin et al., 2000) velocity structure to describe the local structure at the source.

We inverted the observed seismograms for the slip distribution, assuming different values of nearly fixed rupture speeds v_r = 1.5, 2.0, 2.5, and 3.0 km/s, allowing the speed to vary locally from the average value by ±0.1 km/s (Figures 3a–3d). Then we performed two more inversions, with average values of v_r = 2.0 and 2.5 km/s, respectively, but permitting larger variations in the rupture speed of ±0.8 km/s (Figures 3e and 3f). All the resulting slip models have several things in common. They all rupture two patches that are more or less connected, one near the hypocenter and one to the NW, reaching up to the trench. For small values of the rupture speed, the second patch is closer to the hypocenter than for higher values of the rupture speed. Larger slip is observed over a smaller area for smaller rupture speeds and vice versa. The comparison of observed and modeled seismograms for our best fitting model (v_r = var2.5; Figure 3f) is shown in Figure 4.

The predicted static displacements for all models are close to or larger than the observed in the SE, near CRIP, but only about half the observed near CHAM in the NW. We note that the higher rupture velocities, v_r = 2.0 or 2.5 km/s, generate better matches to the static data, which was not used in the modeling.

We find that the misfit to the various data sets and constraints decreases with increasing rupture speed. This observation should be taken with caution, as increasing the rupture speed effectively allows for a larger fault plane or more free parameters. However, visibly poor fits for rupture velocity of 1.5 km/s indicates that an average rupture speed of 2 km/s or larger is required (waveforms and discussion are presented in section S1 and Figures S1–S6). Furthermore, we find that the synthetic surface waves show a larger directivity effect than observed for v_r = 3.0 km/s. Allowing a variable rupture speed increases the number of free parameters further, so predictably the misfit is lower in the inversions with a larger range of allowed rupture speeds. However, we note that the slip distribution is very similar to the fixed rupture velocity model. Based on the mismatch between observed and predicted seismograms for rupture speeds of 1.5 and 3.0 km/s, we estimate an average rupture speed of 2.0–2.5 km/s.

However, the most notable result from these experiments is that all the models show that most of the slip occurs near the trench, with the amount of slip and size of fault patches varying only slightly with rupture speed. We performed various tests, varying the dip and the relative importance of the waveform misfit and the smoothness constraint in the inversion, and by large they show the same pattern.

3.2. Static Inversion

We invert the 11 static displacement vectors estimated by Hutton et al. (2001) and Melbourne et al. (1997) (Figure 5), using our preferred fault geometry. We find that there is little difference between the two. For each data set, we perform two inversions: (1) weight on each measurement is based on its error ($w = 1/\sigma$, where σ is the displacement uncertainty reported in each of the studies) and (2) same weight on all measurements.

The results from these inversions agree in several characteristics with the slip distributions presented by Melbourne et al. (1997) and Hutton et al. (2001). We observe most of the slip northwest from the hypocenter. We also found that the rupture is described by more than one slip patch even though we constrained the solution to be smooth. The large offsets measured at the nearest stations (CHAM, CRIP, and PURI) have the largest effect on the static solutions, as previously pointed out by Melbourne et al. (1997). The maximum slip obtained in our inversion is somewhat smaller than the results from Melbourne et al. (1997) and Hutton et al. (2001), who suggest a maximum slip of 4–5 m. However, we found that the location of the maximum slip along strike and dip are quite similar to those previously presented.

The majority of slip is located deeper and closer to the coast in this model than in the seismic models presented in the previous section. This is consistent with results of the previous studies, which suggest

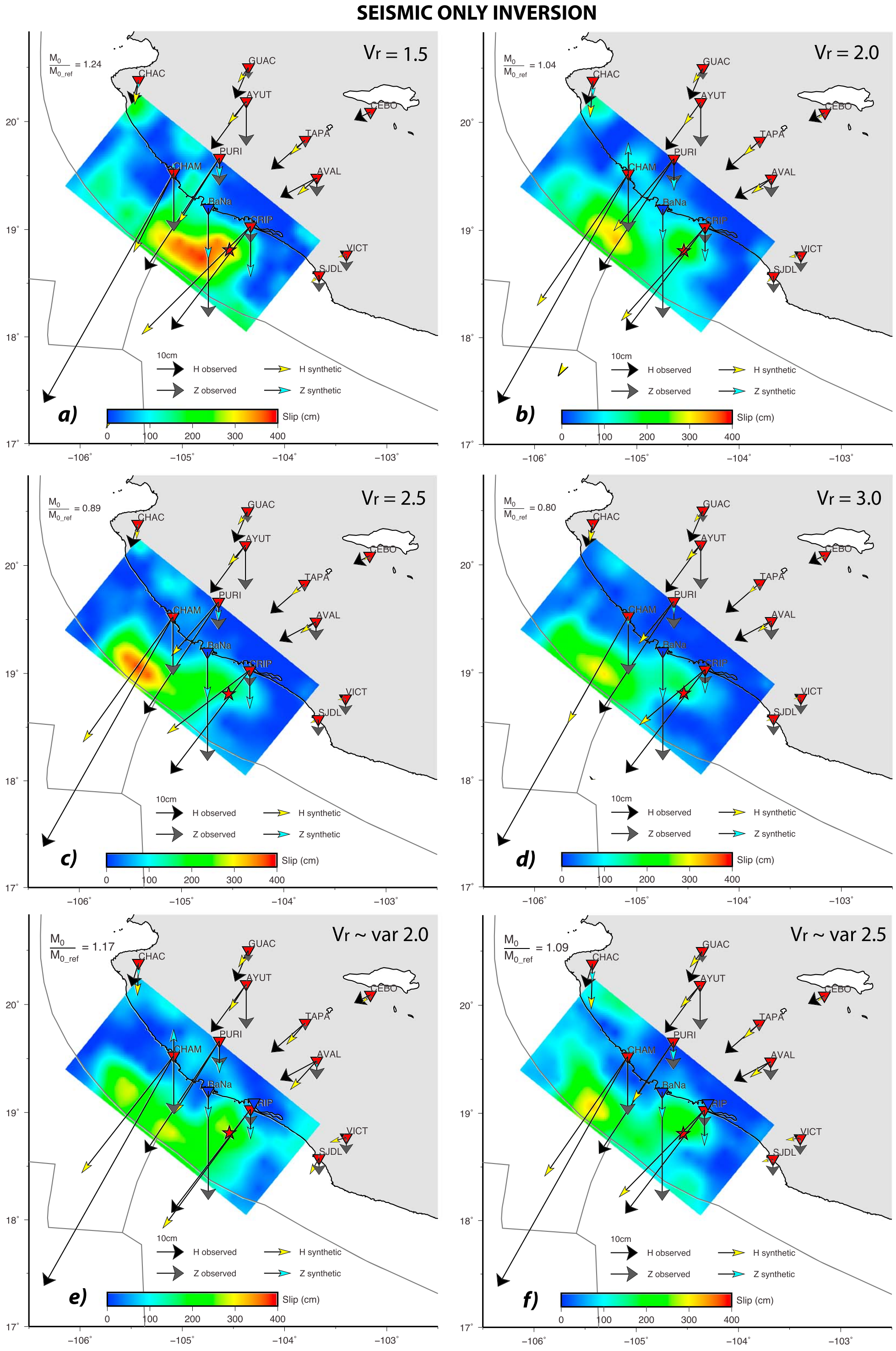

Figure 3. Slip distributions obtained from seismic data (body and surface waves). Observed horizontal and vertical displacements (Hutton et al., 2001) are shown with black and gray vectors, whereas horizontal and vertical displacements predicted by the slip model are shown with yellow and blue vectors. The slip distributions in panels (a)–(d) are obtained by fixing the rupture speed to values of 1.5, 2.0, 2.5, and 3.0 km/s. In the last two panels, the rupture speed was allowed to vary from a range of (e) 1.2–2.8 and (f) 1.7–3.2. We do not invert for the subsidence observed at the pressure sensor at Barra de Navidad (BaNa).

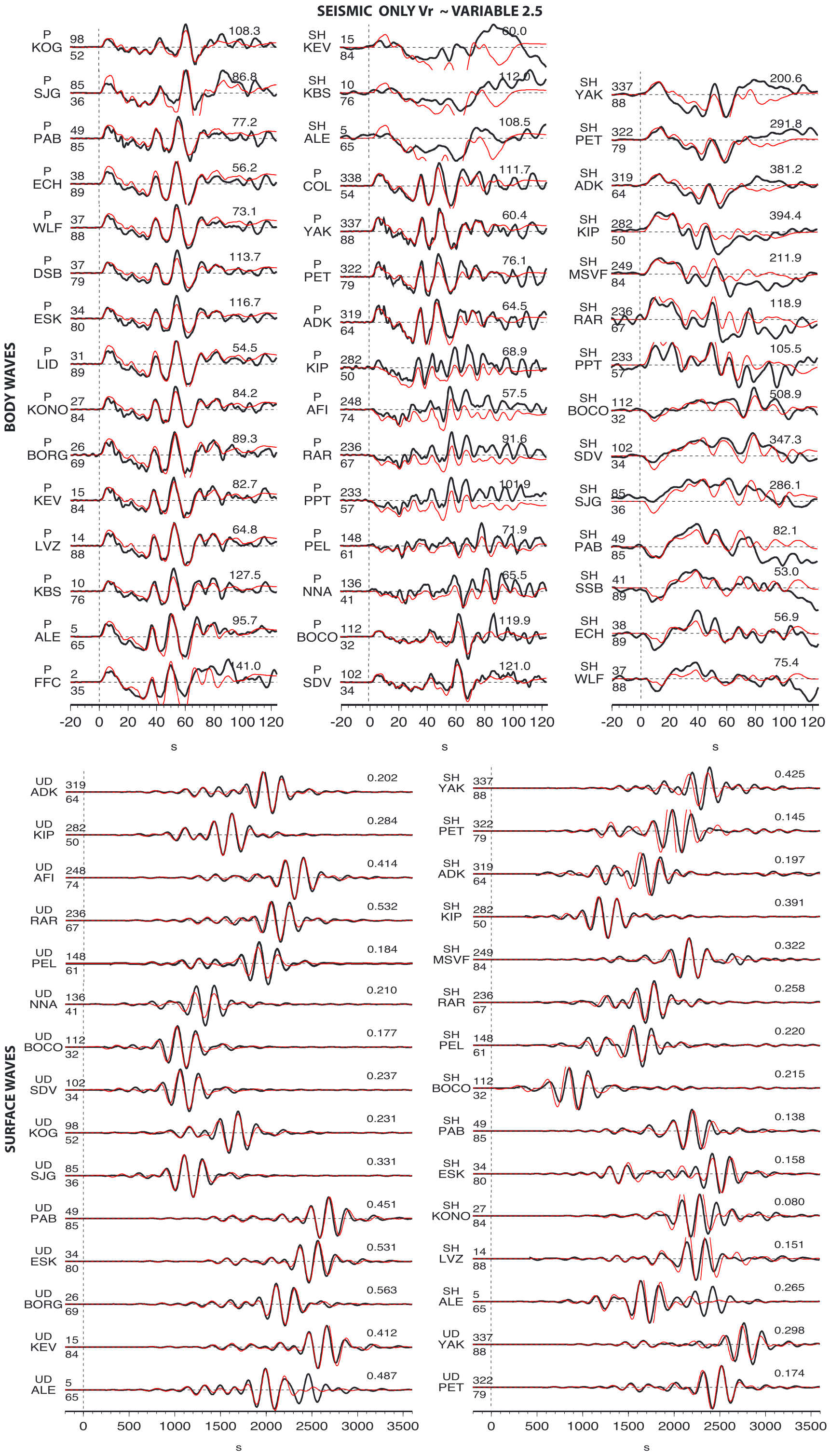

Figure 4. Observed (black) and synthetic (red) teleseismic (a) body waves, (b) surface waves for the model shown in Figure 3f. Labels on each station indicate from top to bottom, left to right. Vertical (P/UD) and transverse (SH) component, the station name, azimuth from the source, angular distance, and relative amplitude of each trace.

Journal of Geophysical Research: Solid Earth 10.1029/2017JB014899

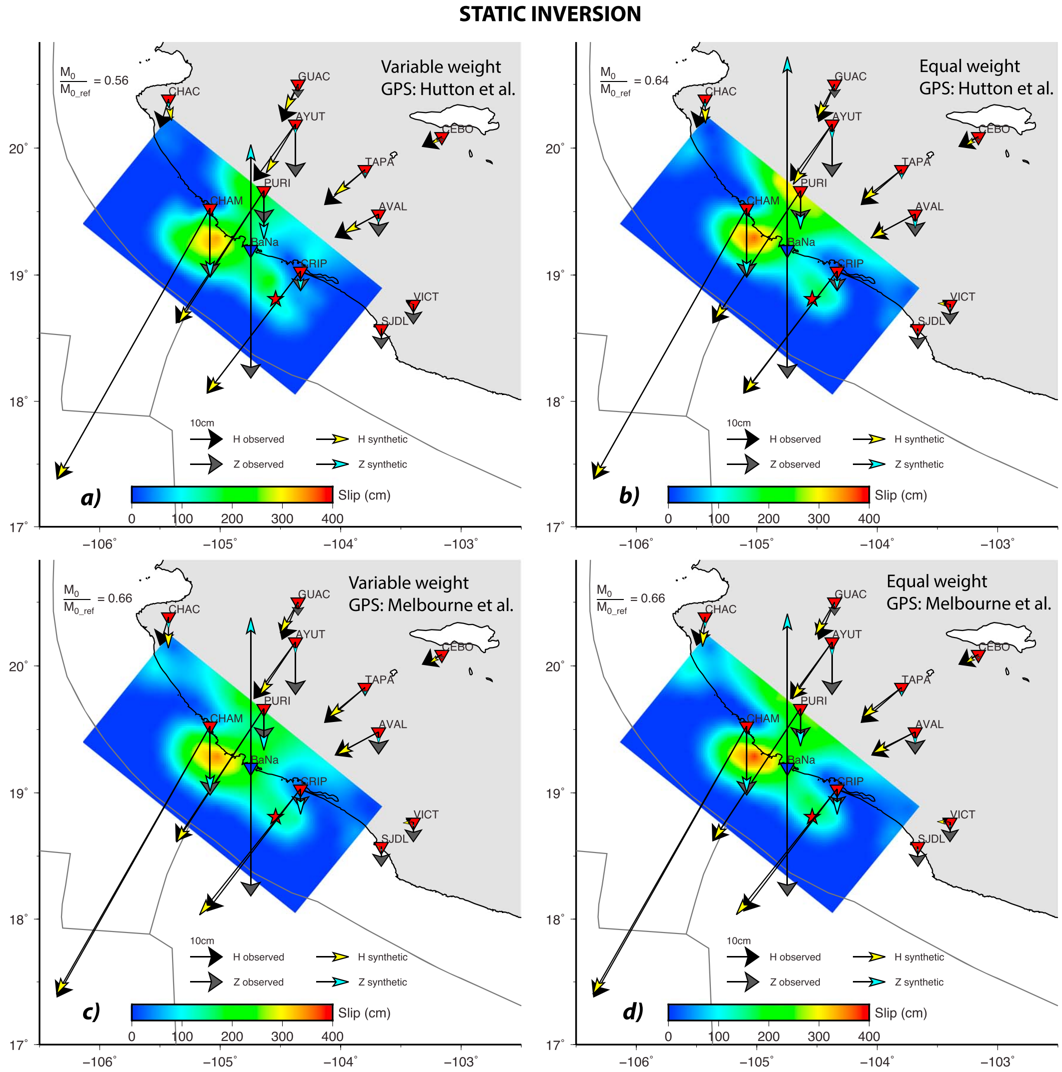

Figure 5. Slip distributions obtained from geodetic data (static offsets obtained from repeat campaign Global Positioning System measurements). Observed horizontal and vertical displacements are shown with black and gray vectors, whereas horizontal and vertical displacements predicted by the slip model are shown with yellow and blue vectors. The slip distributions in panels (a) and (b) are obtained for displacements estimated by Hutton et al. (2001) and those in panels (c) and (d) from Melbourne et al. (1997). Panels (a) and (c) have weights on the individual stations that depend on the errors, whereas for panels (b) and (d) all stations have equal weights. We do not invert for the subsidence observed at the pressure sensor at Barra de Navidad (BaNa).

that the depth of the patch may reflect the incapacity of this network to resolve slip near the trench. We performed various tests to evaluate whether the depth of the slip was an artifact of the model parameters, and how it could be reconciled with the seismic models. We tried various dips of the faults plane, different weighting of the GPS vectors relative to each other, and weighting the horizontal components more strongly relative to the vertical component. However, all of the resulting models had the majority of slip much deeper than the seismic models.

We notice an unexpected trend in the change in the vertical component as a function of distance from the trench; from PURI to AYUT and GUAC. The typical pattern would be diminishing vertical motions with distance from the end of the slip model; however, out of these three stations, we find the largest subsidence at AYUT, more than 150 km from the trench, indicating that perhaps the data at this station are erroneous. However, removing this station from the inversions does not show any significant changes in the slip pattern.

The static model predicts large uplift offshore Barra de Navidad (BaNa), contrasting with the large subsidence observed there by a moored pressure sensor. The modeled uplift/subsidence is controlled by the spatial gradient of slip below the station, or in this case the mooring. As the model predicts artificial large slip at the bottom of the fault, due to anomalously large subsidence at AYUT, the spatial gradient is small close to BaNa and large uplift is predicted. By including this site in the inversion, it is relatively easy to produce large subsidence there, simply by concentrating the slip contours near it. However, we chose not to include this station in the inversion for two main reasons: (1) It does not cover the same time period as the GPS data. (2) Strong currents due to the tsunami may have moved the mooring, in a similar way as they moved large sunken ships in the nearby lagoon (Filonov, 1997).

3.3. Joint Inversion

Finally, we invert the body waves, surface waves, and static displacements together, combining the data sets of the previous two sections. In these inversions we do not constrain the moment and we apply the same smoothing as for the seismic inversions. As one might guess from looking at the relatively different solutions in Figures 3 and 5, both data sets are not very well matched by either of the single-data set slip models. We perform several inversions, with increasing relative weights on the GPS-data set (Figure 6) compared to the seismic data. Note that the absolute weight is not meaningful; however, as we increase it from 0.001 to 1.0 the effect goes from barely considering the GPS data to requiring it to be almost exactly matched.

We find that when the weight is small on the GPS data set, the slip distributions are very similar to the seismic only models, and that the GPS vectors at the eastern section of the fault (CRIP) are well fit, whereas the displacement vector at CHAM is relatively poorly fit, especially the vertical component. Increasing the weight on the GPS data set predictably improves the match between observed and predicted static offset vectors, whereas the match to the seismic data deteriorates somewhat, when the weight rises above 0.1 (waveforms for weight of 0.1 are shown in Figure 7). Decreasing fit to the seismograms with increasing weight on the GPS data is not so easily observed by eye in the waveforms; however, the overall scalar moment increases (from $M_0/M_{0\_ref} = 1.08$ for weight 0.001 on GPS to $M_0/M_{0\_ref} = 1.28$ for weight 1.0 on GPS), resulting in the surface waves being on average a bit too large (section S2 and Figures S7–S12). We also see a slightly increased misfit to the first 20 s of the records at stations toward the north and northeast (for example stations FFC and LID) for a weight on GPS of 1.0. The slip models with large weight of the seismic data have large slip close to the trench, whereas the slip models with large weight on the static data have large slip near the coast, consistent with the results of previous sections. Intermediate results show relatively uniform slip between the coast and the trench.

Based on this analysis, we find that the models with weights on the static data of 0.1 or below provide predictions that can match the seismic data reasonably well, whereas weights on GPS data of 0.05 or higher give good matches to the static offsets (Figure 6). We note that there is therefore a range of models that give reasonably good matches to both data sets simultaneously.

3.4. Comparison With Previous Slip Models

Several studies have presented kinematic seismic source models of the 1995, Jalisco earthquake. Some characteristics of this earthquake appear in all the models; the rupture propagated to the north west of the hypocenter and the approximate length of the rupture was between 150 and 200 km. However, there is an important disagreement in the slip distributions obtained from the different types of data used in the analysis. Inversions for the rupture history based on inversion of broadband recordings of teleseismic body waves (Mendoza et al., 2011; Mendoza & Hartzell, 1999; Ye et al., 2016) as well as joint inversion of body and surface waves (USGS *finite fault solution*) show slip near the hypocenter followed by shallow slip, with maximum values of 3–4 m at a distance between 70 and 130 km NW of the hypocenter and at distances of 10–40 km from the trench. In contrast, the models presented by Melbourne et al. (1997) and Hutton et al. (2001) from the inversion of the available geodetic data, maximum slip values of 4–5 m were located at 55 km away from the trench in the downdip direction.

The slip models obtained when matching static and seismic data in this study are very similar to those obtained by other researchers using the corresponding data sets; the seismic slip model is similar to those presented by Mendoza and Hartzell (1999), Mendoza et al. (2011), and Ye et al. (2016) and the USGS Finite fault slip model, whereas the static slip model resembles the models by Melbourne et al. (1997) and

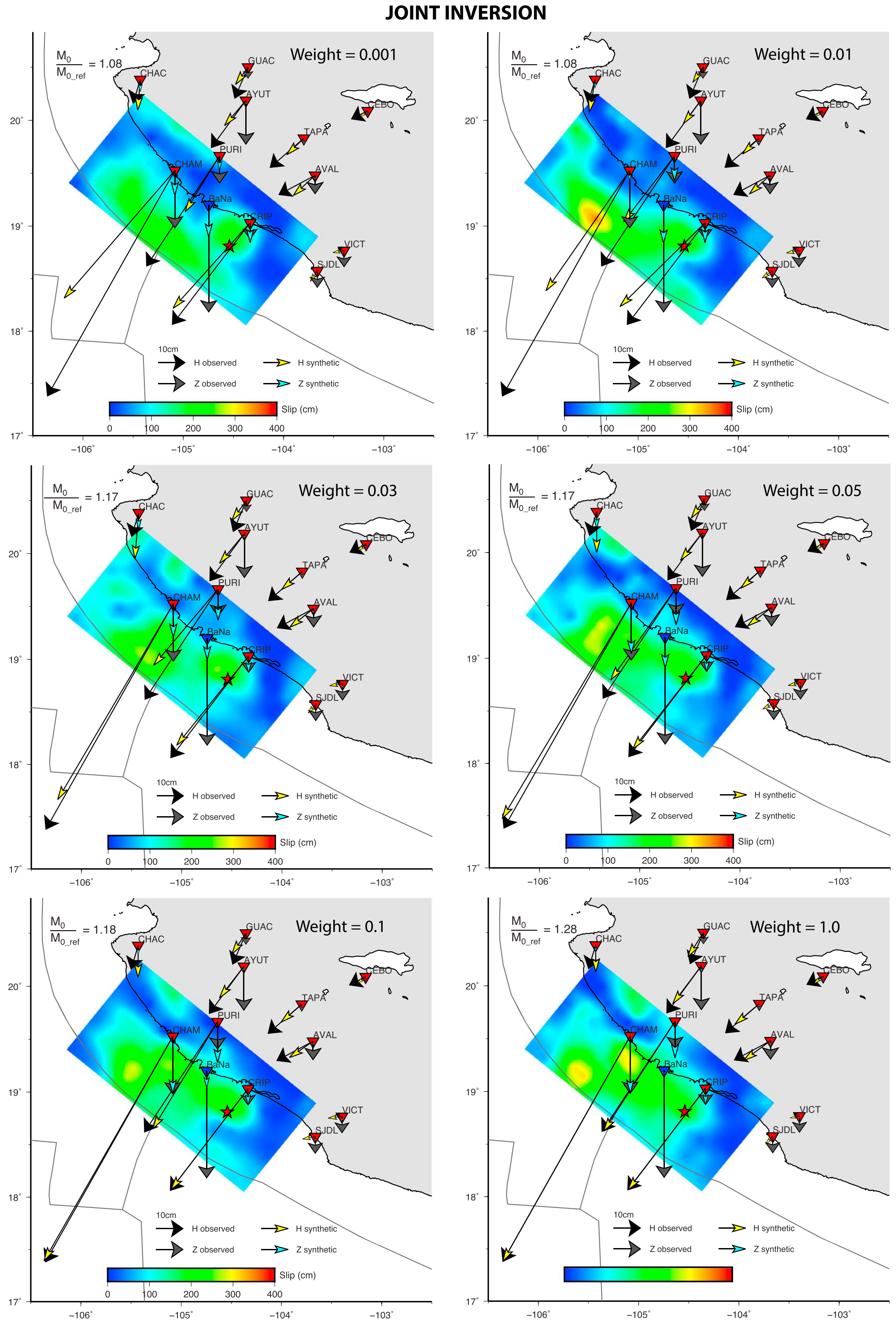

Figure 6. Slip distributions obtained from seismic (body and surface waves) together with geodetic data, displacement vectors same as in Figure 3. The panels (a) to (f) have increasing weight on the Global Positioning System data set relative to the seismic, as marked. We do not invert for the subsidence observed at the pressure sensor at Barra de Navidad (BaNa).

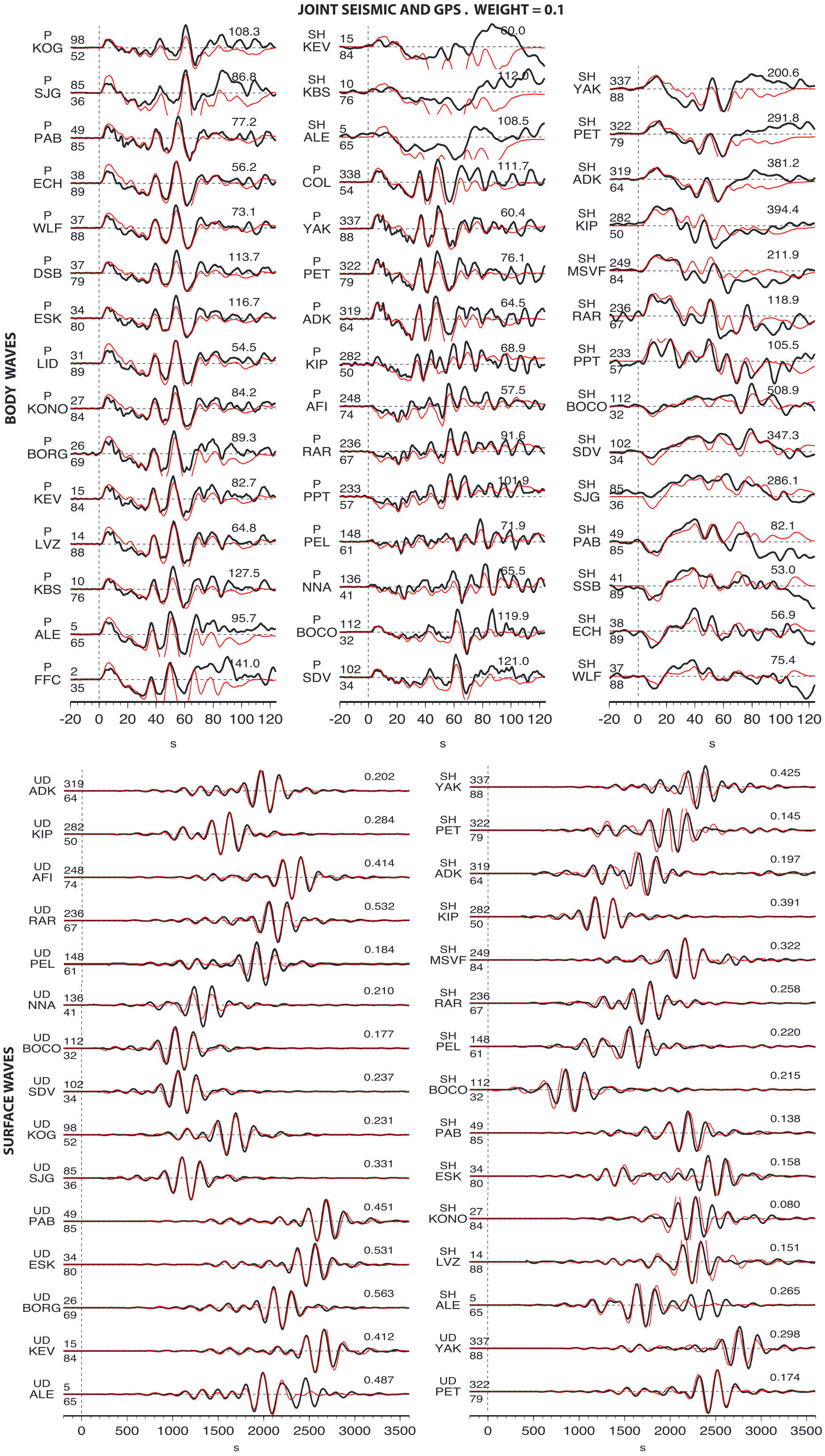

Figure 7. Teleseismic waveforms for joint seismic and geodetic slip model, with weight 0.1 (Figure 6e). Labels same as Figure 4.

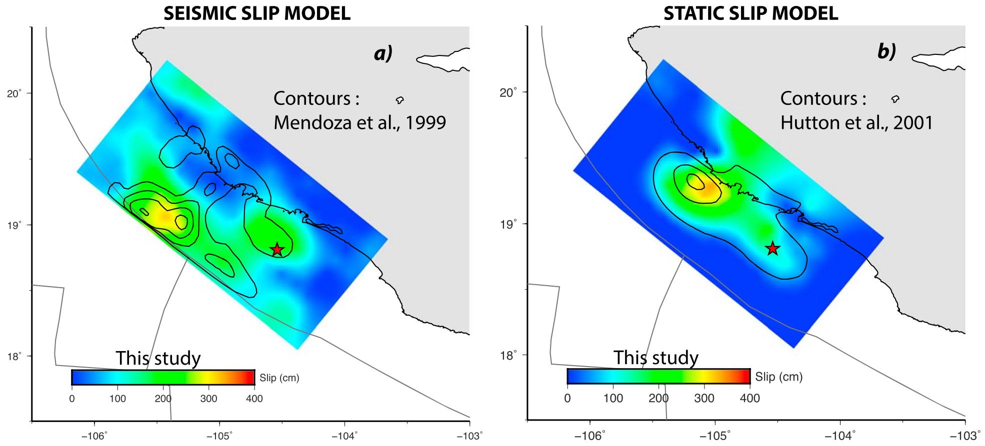

Figure 8. Comparison of slip models obtained in this study (colors) to those obtained by other researchers (contours). (a) Our seismic only model (variable rupture velocity, v_r = 1.9–3.1), versus the seismic only model of Mendoza et al. (1999), contour lines every 0.5 m. (b) Comparison of our geodetic only model, to the geodetic only model by Hutton et al. (2001), contour lines every 1 m.

Hutton et al. (2001) obtained using the same data set (Figure 8). On one hand these results are reassuring, as using the same data leads to similar models, regardless of the details of the methods used. On the other hand the differences between the static and seismic models are disconcerting, as there can only be one true coseismic slip model.

4. Discussion

4.1. Alternative Model: Afterslip

There are several indications that the 1995 Jalisco event produced small high-frequency radiation compared to other earthquakes: (1) ratios of total radiation to high-frequency radiation in Mexico City (at about 500 km distance) are high compared to other Mexican earthquakes and similar to ratios of events that are located near the trench (Shapiro et al., 1998); (2) estimated energy-to-moment ratio, E_S/M_0 = 4.2e−6, is smaller than the ratios for other subduction zone events nearby (Pérez-Campos et al., 2003; Pérez-Campos & Beroza, 2001), and similar to that of tsunami earthquakes (Ye et al., 2016); (3) moreover, the 9 October 1995 earthquake exhibited the largest disparity along the Mexican Subduction Zone between the estimated M_S (7.4) and the M_w (8.0) (Pacheco et al., 1997).

The small high-frequency radiation by this event has grouped it together with tsunami or near-trench earthquakes. However, the joint model, presented in the previous section, breaks (at least almost) all the way to the coast, making this event only partially a *near-trench* event.

We will now show that there is an alternative model. Perhaps one of the most critical assumptions we have made up to this point is that the measured static displacement vectors include only the coseismic displacements and that no other slip occurred during the rest of the measurement period. However, rapid afterslip following this earthquake has been suggested, based on the daily averages of the tidal record in Manzanillo (a few kilometers northeast of GPS station CRIP), compared to tidal records in Acapulco and Puerto Vallarta. This comparison shows a coseismic subsidence of 14 cm in Manzanillo, contrasting with 7 ± 2 cm of uplift in the following 4 days (Melbourne et al., 2002). Given that the static offsets used in this study were measured 5–10 days after the event, this type of large early afterslip could significantly influence them.

We therefore hypothesize that there was a significant contribution to the measured geodetic offsets from aseismic slip and further assume that the coseismic slip is well described by the seismic only models. As the tide gauge records suggest large afterslip, we will assume that the aseismic slip occurs after the event, although we cannot exclude that a significant part of it occurs in a slow-slip event in the 6 months before

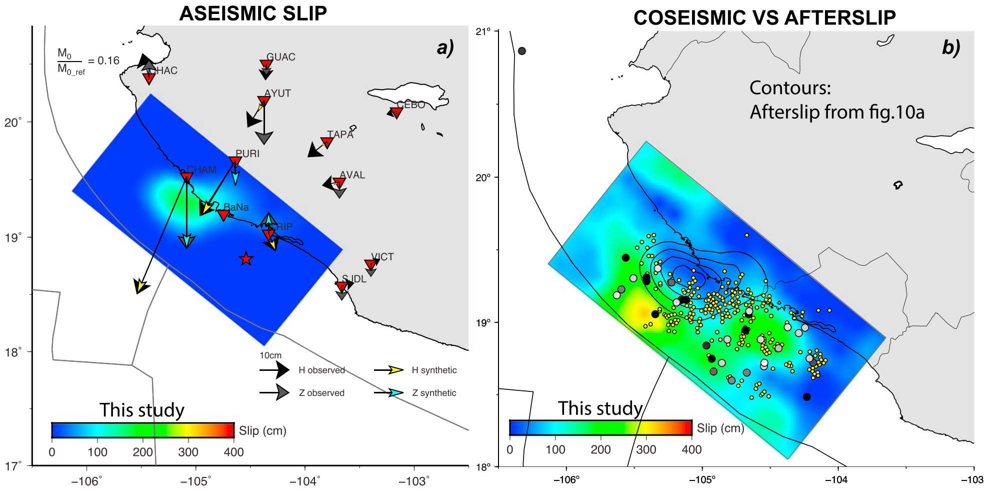

Figure 9. Modeling the displacements not predicted by the seismic only model. (a) The black vectors show residual between the observed displacements (Hutton et al., 2001) and those predicted by our preferred seismic only model (variable rupture velocity, $v_r = 1.9–3.1$). The slip model shown is that which best predicts the differences, and the colored vectors are the displacements predicted by this model. (b) Our preferred seismic model shown with colors, overlain with the contours (every 0.5 m) of the slip model shown in Figure 9a, together with aftershock locations from a local network (small yellow circles, Pacheco et al., 1997), as well as corrected aftershock locations (see text) from global networks (larger circles). Timing of aftershocks is shown with progression from white (first day after earthquake) to black (5 days after earthquake and later) circles.

the earthquake. Furthermore, we do not consider the possibility of viscoelastic rebound causing postseismic motion, due to the short timescales involved. We can then pose the question of how much afterslip is required to match the difference between the predicted offsets for the seismic only model and the observed static offsets.

Next we assume that the difference in the seismic and geodetic models is due to afterslip. We can then estimate the static deformation due to the aseismic slip by subtracting the contribution of the coseismic slip, as predicted by our best coseismic model, from the observed static displacements. We use the coseismic slip model with a variable rupture velocity, centered on 2.5 km/s (Figure 3f). We now invert for the slip distribution of the aseismic event that best predicts the residual static deformation (Figure 9a). We find highly localized slip of up to 1.8 meters offshore station CHAM, with slip above 1 m in an elliptical area of about 40 × 60 km. Comparing the slip in the aseismic event to that during the seismic event (Figure 9b), we see that the aseismic slip has little overlap with the coseismic slip and is nestled in the corner downdip of the shallower asperity and northwest of the deeper asperity of the coseismic slip distribution. It should be emphasized that the details of the slip distribution of the aseismic slip depends heavily on the coseismic slip model chosen for the modeling. However, all of the seismic only models show a large underestimate of the static offset of GPS station CHAM, indicating that most of the aseismic slip would have to occur near that station.

Interestingly, the seismic only models predict larger subsidence at CRIP (13.3 cm) than observed by the GPS station 6 days after the earthquake (6.2 cm; Hutton et al., 2001; Figure 3f), leading to a positive residual (7.1 cm), which requires uplift in the postseismic period. These predictions are consistent with observed tide gauge records (Melbourne et al., 2002), which suggest 14.2 ± 2 cm subsidence during the earthquake and a gradual uplift of 7 ± 2 cm during the following 6 days. We note that the close agreement between the subsidence and subsequent uplift predicted by our analysis and the tide gauge may be a coincidence, as both estimates have large errors. The subsidence values predicted by our modeling depend heavily on the choice of coseismic model and those estimated by the tide gauge measure the difference in sea level between two stations, which may depend on other factors than just the ground deformation, such as sea condition. However, we conclude that their overall agreement supports the general pattern of our model.

We find that the aftershocks located by a regional network (Pacheco et al., 1997) are concentrated in the area between the maximums of the coseismic and afterslip (Figure 9b). Unfortunately, the timing information of these aftershocks has been lost. Locations of earthquake in this part of the Mesoamerican subduction zone by global networks are biased on average by 21 km toward 62° (Hjörleifsdóttir et al., 2016; Singh & Lermo, 1985), but correcting for that bias, we can get an approximate location of the largest aftershocks from global networks (Figure 9b). Of the 35 aftershocks reported by NEIC during the first month after the earthquake, 7 of them occur within the first day after the earthquake and 23 within 5 days of the event. We do not see a time progression in the location of the aftershocks within this time period.

The afterslip inferred in this study is very rapid and large. The maximum afterslip (~1.8 m) within 5–10 days of the event is about half the maximum coseismic slip (~3.5 m). However, the scalar moment of the afterslip in the first 5–10 days is only 16% of the coseismic moment. Similar rapid afterslip in the first day has been seen after other events: 20% of coseismic displacements in first day after the M_w 6.3, 2009, L'Aquila, Italy, earthquake (Yano et al., 2014); 7% in the first 3 hr after the M_w 7.6, 2012, Nicoya, Costa Rica, earthquake (Malservisi et al., 2015); and 30% in the first 24 hr after both the M_w 7.6 1994 Sanriku-Haruka-Oki, Japan, earthquake (Heki and Tamura, 1997) and the M_w 7.8, 2010, Mentawai, Indonesia event (Hill et al., 2012). Furthermore, large afterslip to coseismic slip ratios have been observed for several other earthquakes in the Middle America Trench, such as the Pinotepa-Nacional/Ometepec M_w 7.5 earthquake in 2012 (Graham et al., 2014), the M_w7.2, 2012, El Salvador earthquake, and the M_w 6.9, 2004, 9 October, Nicaragua earthquake (Geirsson et al., 2015).

It has been suggested that large afterslip relative to coseismic slip may be characteristic of tsunami type events, weakly coupled regions, as well as regions on the boundary between fault areas with velocity strengthening and weakening friction (Geirsson et al., 2015). This would suggests a transition from a more highly coupled region in the southeastern part of the fault plane slipping in the 1995 Jalisco event, to a fault patch with smaller coupling or conditionally stable creep in the northwestern part of the fault plane.

4.2. Tsunami Modeling

In previous sections, we have obtained substantially different slip models that can predict observed seismic and/or static displacements. Some models show large slip near the trench, and others near the coast. These models could be expected to generate very different tsunamis. In order to test whether we can use the tsunami observations to distinguish between the different models, we carried out simulations for three representative slip models based on the joint inversions: (a) adjusted to fit principally the seismic data (weight on GPS 0.001; Figure 3a), (b) joint model (weight on GPS 0.1; Figure 3e), and (c) adjusted to fit mostly the GPS data (weight on GPS 1; Figure 3f). The tsunami numerical simulations were carried out with GeoClaw, a validated tsunami propagation model that solves the nonlinear shallow water equations (LeVeque et al., 2011). A table of observed runup and details of the methodology used to calculate the tsunami wave height and propagation are presented in Table S1 and section S2 (Becker et al., 2009; Borerro et al., 1997; Carrillo-Martinez, 1997; Černý et al., 2016; Geist, 1998, 2002; Jarvis et al., 2008; Lander et al., 2003; Ramírez-Herrera et al., 2016; Synolakis, 1991). Snapshots of the predicted wave height at 9 min after the earthquake initiation time show that the crest of the seismic only model (model a) is higher but has not arrived at the coast at this time. On the other hand, the joint (model b) and static-only model (model c) has wider crests that have already arrived at the coast at this time (Figures 10a–10c). Looking at other time frames, we find that the simulated arrival time for the first waves vary between 10 and 20 min, consistent with the reported times (Filonov, 1997). We also note that in the region between Chola, Jalisco to Caleta de Campos, Michoacán (between 75 and 100 km along the trench), the seismic model predicts larger wave heights than the static model, whereas the joint inversion predicts an intermediate value. All three models show peaks of local amplification at two locations along the coast that are not related to the arrival of the first wave, with the maximum amplitude occurring more than 40 min after the first arrival.

A similar observation can be made by comparing the modeled tsunami waveforms with pressure recorded by a conductivity-temperature-depth mooring deployed at 30-m depth offshore Barra de Navidad (Ortiz et al., 2000). We find that the timing of the first arrivals for the seismic only and joint models (models a and b) are later than observed, whereas the first arrival for the static only model (model c) are slightly earlier. The amplitude of the waveforms cannot be directly compared, as the pressure sensor is not moored at the bottom but at 20 m above the seafloor, which induces pendular movements as the mooring moves horizontally

Journal of Geophysical Research: Solid Earth 10.1029/2017JB014899

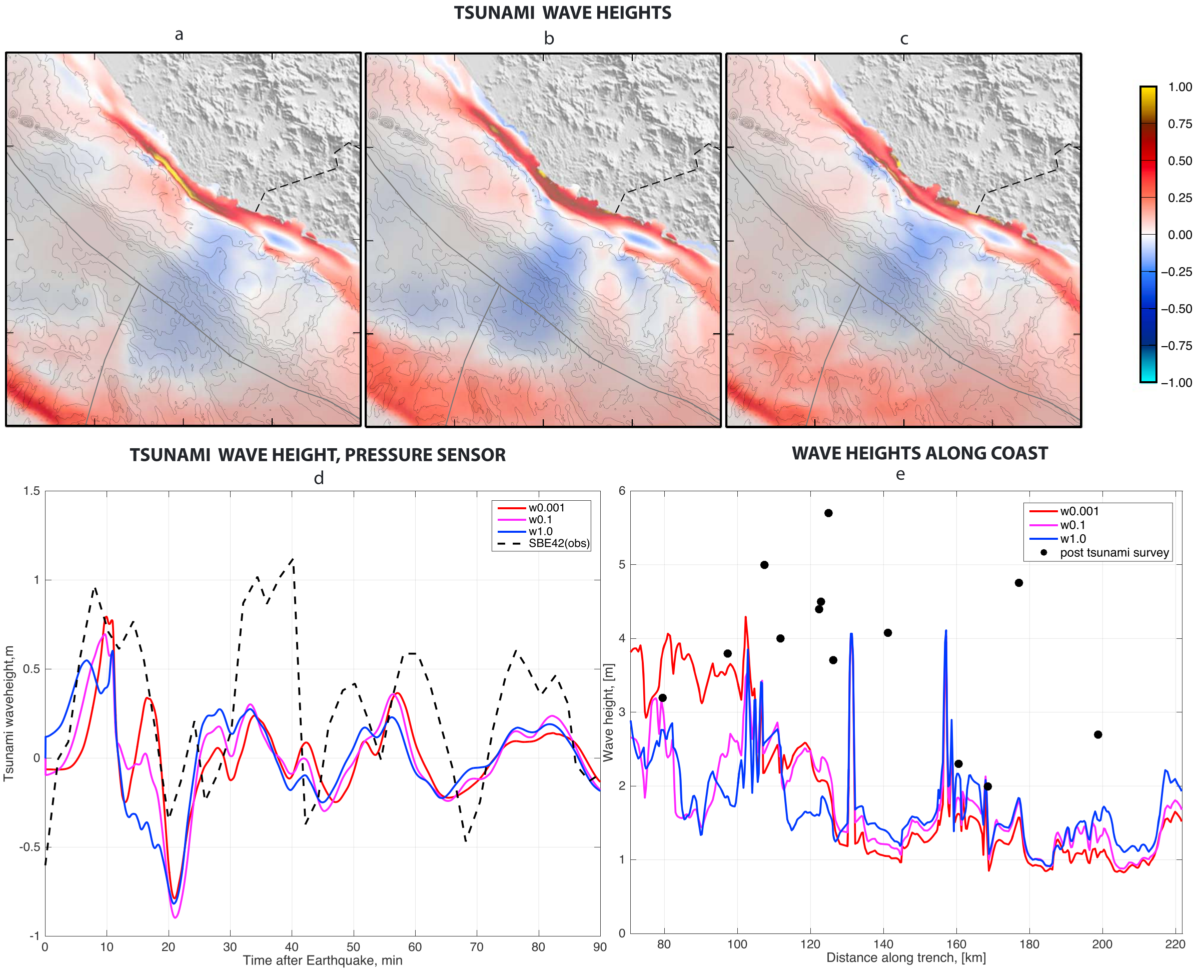

Figure 10. Predicted tsunami wave height 9 min after earthquake for three different models: (a) Seismic (w0.001). (b) Joint Seismic and GPS (w0.1). (c) GPS (w1.0). (d) Corresponding estimated waveforms compared to the conductivity-temperature-depth mooring/pressure sensor offshore Barra de Navidad (amplitude scaled by 0.5). (e) Calculated tsunami wave heights along the coast compared to the posttsunami survey observations.

and down with the tsunami waves, inducing additional pressure. We have scaled the observed waveform by 0.5 for comparison. The maximum difference in the arrival time of the first tsunami wave between models is on the order of 5 min.

We find that only few of the runup observations show a fair agreement with the tsunami simulations (Figure 10e). In particular, the middle section of the domain does not have a good agreement between observed and simulation. This is consistent with recent work by Mori et al. (2017), who model the tsunami produced by a seismic only slip model for this event and find that the predicted tsunami is much smaller than observed. The morphology of the Manzanillo area is relatively complex as it has several bays that are known to be prone to resonance effects (see for example Okal & Synolakis, 2015). The largest observed runup occurs in one of the bays of the Manzanillo region, consistent with our simulations. Furthermore, most of the measurements are made in bays, where the waves can amplify, possibly biasing the observations to larger values. Unfortunately, the resolution of the available bathymetry data limits the possibility of proper simulations including runup and inundation areas. This could be resolved by future work that includes higher resolution bathymetry and topography, allowing for more accurate simulations. We therefore conclude that we are not able to use the tsunami modeling to distinguish between the end-member scenarios.

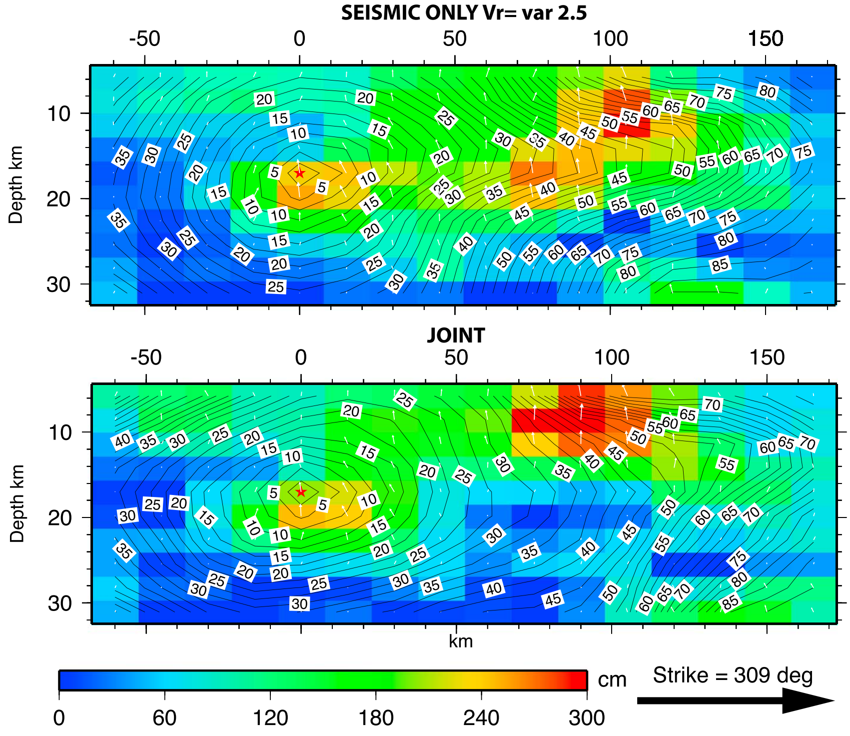

Figure 11. Slip on fault for the best fit seismic only model (Figure 3f) and for the joint model with weight 0.1 (Figure 6e). Slip amplitude is shown with colors, direction with white arrows, and timing of rupture at each point with black rupture contours. The contours are very dense in the large slip or red patch, suggestive of a slower rupture velocity.

4.3. Relatively High Average Rupture Speed

Typically, earthquakes that break the near-trench area have slow rupture speeds, which can be as low as 1.0 km/s (Ammon et al., 2006; Kanamori & Kikuchi, 1993). On the contrary, the 1995 event had an average rupture speed of 2–2.5 km/s, which is typical for subduction zone earthquakes at traditionally seismogenic depths. This is a relatively robust result, as models with average rupture speeds of as high as 1.5 km/s generate substantially poorer fits to the observed seismograms than the more rapid ones. This may be explained in at least two ways: (1) the shallow fault plane properties in the Jalisco area are more similar to those at greater depth than in other subduction zones and (2) the earthquake ruptured both the shallow and the deeper part, as suggested by the joint models that have similar relative weights on the seismic and static observations (Figurec 6c and 6d) and the average speed is a combination of a faster rupture at depth and a slower rupture near the trench. Analyzing the rupture contours for the inversions where variable rupture speed was allowed, we find that indeed the rupture speed in the shallow large-slip patches is as low as 1–1.5 km/s for both the seismic only and joint solutions (Figure 11), consistent with the second explanation above. However, the variations in rupture speed along the fault plane are not well resolved, and although this finding is suggestive, it is not robust. Furthermore, we cannot resolve systematic variations in the risetime along the rupture plane.

4.4. Recurrence Times

The M_w 8.0 1995 Jalisco event, together with the M_w 8.2 1932 Jalisco and M_w 8.0 1985 Michoacán earthquakes, is the three largest events to break the Mexican subduction interface in the last 100 years. It is somewhat surprising that two of these events break the same segment of the subduction zone. When should we expect the next event in this segment? The answer to this question depends on whether there was significant overlap between the rupture areas in the two events or not. Based on high seismic intensities, it has been suggested that the 1932 earthquake broke the fault surface near the coast (Singh et al., 1985).

Comparing the slip in the 1995 earthquake, of about 2 m over a large part of the rupture area (although reaching 3.5 m in the large slip patches), to the convergence rate between the Rivera and the North American plate, of about 3.3 cm/year (DeMets et al., 2010) or increasing from 3.9–4.8 cm/year going southeast along the rupture (Bandy, 1992; Kostoglodov & Bandy, 1995), and supposing that the plates are fully coupled, we would expect this type of event every 45–60 years or so.

The recurrence interval of the 1932 3 June event, supposing it had a coseismic slip of 3–5 m (somewhat larger than the 1995 event) and that there was little spatial overlap between that and the 1995 events may be on the order of 100–200 years. This recurrence interval suggests that we could expect another 1932 Jalisco earthquake in the next 100 years, with possibly severe consequences for this now much more populated area. However, the two end-member scenarios have slip (either coseismic or seismic) close to the cost, suggesting a possible overlap between the 1932 and 1995 rupture. This would indicate that the some of the accumulated slip deficit was released in this event, which may delay the next event in this segment.

5. Conclusions

We invert for the slip during the 1995 M_w 8.0 Jalisco, Mexico, earthquake, using seismic and geodetic (campaign GPS) data. We find that the slip distribution depends heavily on the data set used, slip in a deeper patch near the hypocenter and in a shallower patch toward the trench when using seismic data and slip in two patches close to the coast when using geodetic data. These results are very similar to those of other authors using the same data sets. Joint inversions of both data sets simultaneously show relatively uniform slip between the coast and the trench. The 1995 earthquake has macroseismic properties, such as the ratio between radiated energy to moment, typical for tsunami or near-trench earthquakes. However, although the joint inversion shows larger slip close to the trench than typical for Mexican earthquakes, there is substantial slip deep into the zone typically considered seismogenic. This is atypical for earthquakes with macroseismic properties similar to those of tsunami earthquakes.

Alternatively, we obtain a different model by allowing for rapid postseismic slip affecting the observed static offsets. With this assumption we find that more than 1 m of aseismic slip occurs in an elliptical area of about 40 × 60 km, most likely as afterslip during the 5–10 days after the earthquake. The afterslip fits into a *gap* in the coseismic slip model, downdip of the shallower slip patch, and to the northwest of the deeper slip patch. Most of the aftershocks occur on the boundary between the coseismic and aseismic slip areas. Slow-slip events have been observed in the same region as the afterslip reported in this study. The aseismic slip could significantly increase the expected recurrence interval of earthquakes in this zone.

We model the tsunami resulting from three representative models, but we were not able to discriminate between them based on the comparison of observed and modeled tsunami wave height. We find that the average rupture speed (2–2.5 km/s) is more similar to that of typical subduction earthquakes than the tsunami earthquakes that often break the near-trench area, although this average may be a combination of a faster rupture at depth and a slower shallower rupture speed.

The assumptions that there is no postseismic motion (joint inversion) or that all the difference between seismic and geodetic models are due to postseismic motions can be seen as two permissible end-member models. It is plausible that the true model is somewhere in between these two scenarios and that the Jalisco earthquake was only partially a *near-trench* earthquake.

Acknowledgments
We thank Ryota Hino for helpful discussions. All data used in this paper have either been previously published or are publically available. Seismograms were obtained from the open access database of the Incorporated Research Institutions for Seismology (IRIS), networks II, IU, and G, and geodetic and tsunami data from published literature as explained in text. Graphics were prepared using the Generic Mapping Tools (GMT, Wessel, and Smith). Hjörleifsdóttir thanks UNAM/DGAPA/PAPIIT grants IB101812 and IN111316, Ramírez-Herrera thanks PASPA-DGAPA-2015 and SEP-CONACYT grant 129456. Castillo-Aja thanks for CONACYT PhD scholarship. Slip models can be accessed on the finite-source rupture model database (SRCMOD).

References

Abe, K. (1981). Magnitudes of large shallow earthquakes from 1904 to 1980. *Physics of the Earth and Planetary Interiors*, *27*(1), 72–92. https://doi.org/10.1016/0031-9201(81)90088-1

Ammon, C., Lay, T., Kanamori, H., & Cleveland, M. (2011). A rupture model of the 2011 off the Pacific coast of Tohoku earthquake. *Earth, Planets and Space*, *63*(7), 693–696. https://doi.org/10.5047/eps.2011.05.015

Ammon, C. J., Kanamori, H., Lay, T., & Velasco, A. A. (2006). The 17 July 2006 Java tsunami earthquake. *Geophysical Research Letters*, *33*, L24308. https://doi.org/10.1029/2006GL028005

Anderson, J., Singh, S., Espindola, J. M., & Yamamoto, J. (1989). Seismic strain release in the Mexican subduction thrust. *Physics of the Earth and Planetary Interiors*, *58*(4), 307–322. https://doi.org/10.1016/0031-9201(89)90102-7

Bandy, W. (1992). *Geological and geophysical investigation of the Rivera-Cocos plate boundary: Implications for plate fragmentation*. Mexico City, Mexico: Universidad Nacional Autonoma de Mexico.

Bassin, C., Laske, G., & Masters, G. (2000). The current limits of resolution for surface wave tomography in North America. *Eos, Transactions American Geophysical Union*, *81*(48), F897.

Becker, J. J., Sandwell, D. T., Smith, W., Braud, J., Binder, B., Depner, J., et al. (2009). Global bathymetry and elevation data at 30 arc seconds resolution: SRTM30_PLUS. *Marine Geodesy*, *32*(4), 355–371. https://doi.org/10.1080/01490410903297766

Bird, P. (2003). An updated digital model of plate boundaries. *Geochemistry, Geophysics, Geosystems*, *4*(3), 1027. https://doi.org/10.1029/2001GC000252

Borerro, J., Ortiz, M., Titov, V., & Synolakis, C. (1997). Field survey of Mexican tsunami produces new data, unusual photos. *Eos, Transactions American Geophysical Union*, *78*(8), 85–88. https://doi.org/10.1029/97EO00054

Byrne, D., Davis, D., & Sykes, L. (1988). Loci and maximum size of thrust earthquakes and the mechanics of the shallow region of subduction zones. *Tectonics*, *7*(4), 833–857. https://doi.org/10.1029/TC007i004p00833

Carrillo-Martinez, M. (1997). Isosistas Locales del Sismo de Manzanillo del 9 de Octubre de 1995, 9:36 a.m., Estados de Colima y Jalisco, Mexico. *Revista Mexicana de Ciencias Geologicas*, *14*(1), 110–113.

Černý, J., Ramírez-Herrera, M.-T., Bógalo, M.-F., Goguitchaichvili, A., Castillo-Aja, R., Morales, J., et al. (2016). Magnetic record of extreme marine inundation events at Las Salinas site, Jalisco, Mexican Pacific coast. *International Geology Review*, *58*(3), 342–357. https://doi.org/10.1080/00206814.2015.1075230

DeMets, C., Gordon, R., & Argus, D. (2010). Geologically current plate motions. *Geophysical Journal International*, *181*(1), 1–80. https://doi.org/10.1111/j.1365-246x.2009.04491.x

Filonov, A. (1997). Researchers study tsunami generated by Mexican earthquake. *Eos*, *78*(3), 21–25. https://doi.org/10.1029/97EO00014

Geirsson, H., LaFemina, P., DeMets, C., Hernandez, D., Mattioli, G., Rogers, R., et al. (2015). The 2012 August 27 Mw 7.3 El Salvador earthquake: Expression of weak coupling on the Middle America subduction zone. *Geophysical Journal International*, *202*(3), 1677–1689. https://doi.org/10.1093/gji/ggv244

Geist, E. (1998). Local tsunamis and earthquake source parameters. *Advances in Geophysics*, *39*, 117–209. https://doi.org/10.1016/S0065-2687(08)60276-9

Geist, E. (2002). Complex earthquake rupture and local tsunamis. *Journal of Geophysical Research*, *107*(B5), 2086. https://doi.org/10.1029/2000JB000139

Graham, S. E., DeMets, C., Cabral-Cano, E., Kostoglodov, V., Walpersdorf, A., Cotte, N., et al. (2014). GPS constraints on the 2011-2012 Oaxaca slow slip event that preceded the 2012 March 20 Ometepec earthquake, southern Mexico. *Geophysical Journal International*, *197*(3), 1593–1607. https://doi.org/10.1093/gji/ggu019

Hayes, G. P., Wald, D. J., & Johnson, R. L. (2012). Slab1.0: A three-dimensional model of global subduction zone geometries. *Journal of Geophysical Research*, *117*, B01302. https://doi.org/10.1029/2011JB008524

Heki, K., & Tamura, Y. (1997). Short term afterslip in the 1994 Sanriku-Haruka-Oki earthquake. *Geophysical Research Letters*, *24*(24), 3285–3288.

Hill, E. M., Borrero, J. C., Huang, Z., Qiu, Q., Banerjee, P., Natawidjaja, D. H., et al. (2012). The 2010 Mw 7.8 Mentawai earthquake: Very shallow source of a rare tsunami earthquake determined from tsunami field survey and near-field GPS data. *Journal of Geophysical Research*, *117*, B06402. https://doi.org/10.1029/2012JB009159

Hjörleifsdóttir, V., Singh, S., & Husker, A. (2016). Differences in epicentral location of Mexican earthquakes between local and global catalogs: An update. *Geofisica Internacional*, *55*(1), 79–93.

Hutton, W., DeMets, C., Sánchez, O., Suárez, G., & Stock, J. (2001). Slip kinematics and dynamics during and after the 1995 October 9 Mw = 8.0 Colima-Jalisco earthquake, Mexico, from GPS geodetic constraints. *Geophysical Journal International*, *146*(3), 637–658. https://doi.org/10.1046/j.1365-246X.2001.00472.x

Ito, Y., Hino, R., Suzuki, S., & Kaneda, Y. (2015). Episodic tremor and slip near the Japan Trench prior to the 2011 Tohoku-Oki earthquake. *Geophysical Research Letters*, *42*, 1725–1731. https://doi.org/10.1002/2014gl062986

Ito, Y., Tsuji, T., Osada, Y., Kido, M., Inazu, D., Hayashi, Y., et al. (2011). Frontal wedge deformation near the source region of the 2011 Tohoku-Oki earthquake. *Geophysical Research Letters*, *38*, LO0G05. https://doi.org/10.1029/2011gl048355

Jarvis, A., Reuter, H. I., Nelson, A., and Guevara, E. (2008). Hole-filled SRTM for the globe version 4. Available from the CGIAR-CSI SRTM 90m Database,

Ji, C., Helmberger, D. V., Wald, D. J., & Ma, K. (2003). Slip history and dynamic implications of the 1999 Chi-Chi, Taiwan, earthquake. *Journal of Geophysical Research*, *108*(B9), 2412. https://doi.org/10.1029/2002jb001764

Ji, C., Wald, D., & Helmberger, D. (2002a). Source description of the 1999 Hector Mine, California, earthquake. Part I: Wavelet domain inversion theory and resolution analysis. *Bulletin of the Seismological Society of America*, *92*(4), 1192–1207. https://doi.org/10.1785/0120000916

Ji, C., Wald, D. J., & Helmberger, D. V. (2002b). Source description of the 1999 Hector Mine, California, earthquake. Part II: Complexity of slip history. *Bulletin of the Seismological Society of America*, *92*(4), 1208–1226. https://doi.org/10.1785/0120000917

Kanamori, H. (1972). Mechanism of tsunami earthquakes. *Physics of the Earth and Planetary Interiors*, *6*(5), 346–359. https://doi.org/10.1016/0031-9201(72)90058-1

Kanamori, H., & Kikuchi, M. (1993). The 1992 Nicaragua earthquake: A slow tsunami earthquake associated with subducted sediments. *Nature*, *361*(6414), 714–716. https://doi.org/10.1038/361714a0

Kostoglodov, V., & Bandy, W. (1995). Seismotectonic constraints on the convergence rate between the Rivera and North American plates. *Journal of Geophysical Research*, *100*(B9), 17977–17989. https://doi.org/10.1029/95JB01484

Lander, J. F., Whiteside, L. S., & Lockridge, P. A. (2003). Two decades of global tsunamis 1982-2002. *Science of Tsunami Hazards*, *21*(1), 1–88.

Lay, T., Kanamori, H., Ammon, C. J., Koper, K. D., Hutko, A. R., Ye, L., et al. (2012). Depth-varying rupture properties of subduction zone megathrust faults. *Journal of Geophysical Research*, *117*, B04311. https://doi.org/10.1029/2011JB009133

LeVeque, R., George, D., & Berger, M. (2011). Tsunami modelling with adaptively refined finite volume methods. *Acta Numerica*, *20*, 211–289. https://doi.org/10.1017/S0962492911000043

Malservisi, R., Schwartz, S. Y., Voss, N., Protti, M., Gonzalez, V., Dixon, T. H., et al. (2015). Multiscale postseismic behavior on a megathrust: The 2012 Nicoya earthquake, Costa Rica. *Geochemistry, Geophysics, Geosystems*, *16*, 1848–1864. https://doi.org/10.1002/2015GC005794

Melbourne, T., Carmichael, I., DeMets, C., Hudnut, K., Sanchez, O., Stock, J., et al. (1997). The geodetic signature of the M8.0 Oct. 9,1995, Jalisco Subduction earthquake. *Geophysical Research Letters*, *24*(6), 715–718. https://doi.org/10.1029/97GL00370

Melbourne, T. I., Webb, F. H., Stock, J. M., & Reigber, C. (2002). Rapid postseismic transients in subduction zones from continuous GPS. *Journal of Geophysical Research*, *107*(B10), 2241. https://doi.org/10.1029/2001JB000555

Mendoza, C., & Hartzell, S. (1999). Fault-slip distribution of the 1995 Colima-Jalisco, Mexico, earthquake. *Bulletin of the Seismological Society of America*, *25*(15), 2857–2860. https://doi.org/10.1029/98GL02059

Mendoza, C., Torres, C., & Gonzalez, G. (2011). Moment-constrained finite-fault analysis using teleseismic P waves: Mexico Subduction Zone. *Bulletin of the Seismological Society of America*, *101*(6), 2675–2684. https://doi.org/10.1785/0120100126

Mori, N., Muhammad, A., Goda, K., Yasuda, T., & Ruiz-Angulo, A. (2017). Probabilistic tsunami hazard analysis of the pacific coast of Mexico: Case study based on the 1995 Colima earthquake tsunami. *Frontiers in Built Environment*, *3*, 34.

Newman, A., Hayes, G., Wei, Y., & Convers, J. (2011). The 25 October 2010 Mentawai tsunami earthquake, from real-time discriminants, finite-fault rupture, and tsunami excitation. *Geophysical Research Letters*, *38*, L05302. https://doi.org/10.1029/2010GL046498

Okada, T., Yaginuma, T., Umino, N., Kono, T., Matsuzawa, T., Kita, S., & Hasegawa, A. (2005). The 2005 M7.2 MIYAGI-OKI earthquake, NE Japan: Possible rerupturing of one of asperities that caused the previous M7.4 earthquake. *Geophysical Research Letters*, *32*, L24302. https://doi.org/10.1029/2005GL024613

Okal, E. A., & Synolakis, C. E. (2015). Sequencing of tsunami waves: Why the first wave is not always the largest. *Geophysical Journal International*, *204*(2), 719–735. https://doi.org/10.1093/gji/ggv457

Ortiz, M., Kostoglodov, V., Singh, S. K., & Pacheco, J. (2000). New constraints on the uplift of October 9, 1995 Jalisco-Colima earthquake (M). *Geofísica Internacional*, *39*(4), 349–357.

Ortiz, M., Singh, S., Pacheco, J., & Kostoglodov, V. (1998). Rupture length of the October 9, 1995 Colima-Jalisco earthquake (Mw 8) estimated from tsunami data. *Geophysical Research Letters*, *25*(15), 2857–2860. https://doi.org/10.1029/98GL02059

Pacheco, J., Singh, S. K., Domínguez, J., Hurtado, A., Quintanar, L., Jiménez, Z., et al. (1997). The October 9, 1995 Colima-Jalisco, Mexico earthquake (Mw 8): An aftershock study and a comparison of this earthquake with those of 1932. *Geophysical Research Letters*, *24*(17), 2223–2226. https://doi.org/10.1029/97GL02070

Pacheco, J. F., Sykes, L. R., & Scholz, C. H. (1993). Nature of seismic coupling along simple plate boundaries of the subduction type. *Journal of Geophysical Research*, *98*(B8), 14,133–14,159. https://doi.org/10.1029/93JB00349

Pérez-Campos, X., & Beroza, G. C. (2001). An apparent mechanism dependence of radiated seismic energy. *Journal of Geophysical Research*, *106*(B6), 11,127–11,136. https://doi.org/10.1029/2000jb900455

Pérez-Campos, X., Singh, S., & Beroza, G. (2003). Reconciling teleseismic and regional estimates of seismic energy. *Bulletin of the Seismological Society of America*, *93*(5), 2123–2130. https://doi.org/10.1785/0120020212

Polet, J., & Thio, H. (2003). The 1994 Java tsunami earthquake and its "normal" aftershocks. *Geophysical Research Letters*, *30*(9), 1474. https://doi.org/10.1029/2002GL016806

Ramírez-Herrera, M., Bógalo, M., Černý, J., Goguitchaichvili, A., Corona, N., Machain, M., et al. (2016). Historic and ancient tsunamis uncovered on the Jalisco-Colima Pacific coast, the Mexican subduction zone. *Geomorphology*, *259*, 90–104. https://doi.org/10.1016/j.geomorph.2016.02.011

Reyes, A., Brune, J. N., & Lomnitz, C. (1979). Source mechanism and aftershock study of the Colima, Mexico earthquake of January 30, 1973. *Bulletin of the Seismological Society of America*, *69*(6), 1819–1840.

Sato, M., Ishikawa, T., Ujihara, N., Yoshida, S., Fujita, M., Mochizuki, M., & Asada, A. (2011). Displacement above the hypocenter of the 2011 Tohoku-Oki earthquake. *Science*, *332*(6036), 1395–1395. https://doi.org/10.1126/science.1207401

Seno, T., Shimazaki, K., Somerville, P., & Sudo, K. (1980). Rupture process of the Miyagi-Oki, Japan, earthquake of June 12, 1978. *Physics of the Earth and Planetary Interiors*, *23*(1), 39–61. https://doi.org/10.1016/0031-9201(80)90081-3

Shao, G., Li, X., Ji, C., & Maeda, T. (2011). Focal mechanism and slip history of the 2011 mw 9.1 off the Pacific coast of Tohoku earthquake, constrained with teleseismic body and surface waves. *Earth, Planets and Space*, *63*(7), 9. https://doi.org/10.5047/eps.2011.06.028

Shapiro, N., Singh, S., & Pacheco, J. (1998). A fast and simple diagnostic method for identifying tsunamigenic earthquakes. *Geophysical Research Letters*, *25*(20), 3911–3914. https://doi.org/10.1029/1998GL900015

Simons, M., Minson, S. E., Sladen, A., Ortega, F., Jiang, J., Owen, S. E., et al. (2011). The 2011 magnitude 9.0 Tohoku-Oki earthquake: Mosaicking the megathrust from seconds to centuries. *Science*, *332*(6036), 1421–1425. https://doi.org/10.1126/science.1206731

Singh, S., Pacheco, J., Alcántara, L., Reyes, G., Ordaz, M., Iglesias, A., et al. (2003). A preliminary report on the Tecomán, Mexico earthquake of 22 January 2003 (Mw 7.4) and its effects. *Seismological Research Letters*, *74*(3), 279–289. https://doi.org/10.1785/gssrl.74.3.279

Singh, S., Ponce, L., & Nishenko, S. (1985). The great Jalisco, Mexico, earthquakes of 1932: Subduction of the Rivera plate. *Bulletin of the Seismological Society of America*, *75*(5), 1301–1313.

Singh, S. K., & Lermo, J. (1985). Mislocation of Mexican earthquakes as reported in international bulletins. *Geofísica Internacional*, *24*(2).

Synolakis, C. (1991). Tsunami runup on steep slopes: How good linear theory really is. *Natural Hazards*, *4*(2-3), 221–234. https://doi.org/10.1007/BF00162789

Tanioka, Y., & Satake, K. (1996). Fault parameters of the 1896 Sanriku tsunami earthquake estimated from tsunami numerical modeling. *Geophysical Research Letters*, *23*(13), 1549–1552. https://doi.org/10.1029/96GL01479

UNAM Seismology Group (1986). The September 1985 Michoacán earthquakes: Aftershock distribution and history of rupture. *Geophysical Research Letters*, *13*(6), 573–576. https://doi.org/10.1029/GL013i006p00573

Yamanaka, Y., & Kikuchi, M. (2004). Asperity map along the subduction zone in northeastern Japan inferred from regional seismic data. *Journal of Geophysical Research*, *109*, B07307. https://doi.org/10.1029/2003JB002683

Yano, T. E., Shao, G., Liu, Q., Ji, C., & Archuleta, R. J. (2014). Coseismic and potential early afterslip distribution of the 2009 Mw 6.3 L'Aquila, Italy earthquake. *Geophysical Journal International*, *199*(1), 23–40. https://doi.org/10.1093/gji/ggu241

Ye, L., Lay, T., Kanamori, H., & Rivera, L. (2016). Rupture characteristics of major and great (Mw $\geq$ 7.0) megathrust earthquakes from 1990 to 2015: 1. Source parameter scaling relationships. *Journal of Geophysical Research: Solid Earth*, *121*, 826–844. https://doi.org/10.1002/2015jb012426

Appendix B: Kinematic study of Iquique 2014 M_w 8.1 earthquake: Understanding the segmentation of the seismogenic zone

Earth and Planetary Science Letters 503 (2018) 131–143

Contents lists available at ScienceDirect

Earth and Planetary Science Letters

www.elsevier.com/locate/epsl

Kinematic study of Iquique 2014 M_w 8.1 earthquake: Understanding the segmentation of the seismogenic zone

Jorge Jara [a,*,1], Hugo Sánchez-Reyes [a], Anne Socquet [a], Fabrice Cotton [b,c], Jean Virieux [a], Andrei Maksymowicz [d], John Díaz-Mojica [e], Andrea Walpersdorf [a], Javier Ruiz [c], Nathalie Cotte [a], Edmundo Norabuena [f]

[a] *Univ. Grenoble Alpes, Univ. Savoie Mont Blanc, CNRS, IRD, IFSTTAR, ISTerre, F-38000 Grenoble, France*
[b] *German Research Centre for Geosciences, GFZ Helmholtz Centre Potsdam, Potsdam, Germany*
[c] *Institute for Earth and Environmental Sciences, University of Potsdam, Potsdam, Germany*
[d] *Departamento de Geofísica, Facultad de Ciencias Físicas y Matemáticas, Universidad de Chile, Santiago, Chile*
[e] *Instituto de Geofísica, Universidad Nacional Autónoma de México, México, Mexico*
[f] *Instituto Geofísico del Perú, Lima, Peru*

ARTICLE INFO

Article history:
Received 28 February 2018
Received in revised form 15 September 2018
Accepted 19 September 2018
Available online xxxx
Editor: J.P. Avouac

Keywords:
high-rate GPS
strong Motion
megathrust earthquakes
kinematic inversion
subduction segmentation

ABSTRACT

We study the rupture processes of Iquique earthquake M_w 8.1 (2014/04/01) and its largest aftershock M_w 7.7 (2014/04/03) that ruptured the North Chile subduction zone. High-rate Global Positioning System (GPS) recordings and strong motion data are used to reconstruct the evolution of the slip amplitude, rise time and rupture time of both earthquakes. A two-step inversion scheme is assumed, by first building prior models for both earthquakes from the inversion of the estimated static displacements and then, kinematic inversions in the frequency domain are carried out taken into account this prior information. The preferred model for the mainshock exhibits a seismic moment of 1.73×10^{21} Nm (M_w 8.1) and maximum slip of ~9 m, while the aftershock model has a seismic moment of 3.88×10^{20} (M_w 7.7) and a maximum slip of ~3 m. For both earthquakes, the final slip distributions show two asperities (a shallow one and a deep one) separated by an area with significant slip deficit. This suggests a segmentation along-dip which might be related to a change of the dipping angle of the subducting slab inferred from gravimetric data. Along-strike, the areas where the seismic ruptures stopped seem to be well correlated with geological features observed from geophysical information (high-resolution bathymetry, gravimetry and coupling maps) that are representative of the long-term segmentation of the subduction margin. Considering the spatially limited portions that were broken by these two earthquakes, our results support the idea that the seismic gap is not filled yet.

1. Introduction

On 1 April 2014, a M_w 8.1 subduction earthquake struck the North of Chile offshore Iquique. This earthquake is of interest for two main reasons. First, the megathrust rupture was preceded by a long precursory phase characterized by a slow slip event that lasted several months (Kato et al., 2016; Socquet et al., 2017), and interactions between shallow and intermediate-depth seismicities (Bouchon et al., 2016; Jara et al., 2017) that ended into an intense foreshock sequence, which origin remains debated in terms of slip behavior (Ruiz et al., 2014; Meng et al., 2015; Kato et al., 2016). This precursory phase has been the focus of many studies, while the present paper targets another interesting questions raised by Iquique earthquake. The mainshock occurred in a mature seismic gap, where a moment deficit equivalent to ~M 8.6 has been accumulating since the 1877 historical earthquake (e.g., Métois et al., 2016) (Fig. 1). With a moment magnitude M_w 8.1, Iquique earthquake was therefore significantly smaller than what could be feared in this area, and the different published slip models show that the earthquake together with its largest aftershock of M_w 7.7 broke a spatially limited area (~200 km along the subduction) (e.g., Hayes et al., 2014; Lay et al., 2014; Ruiz et al., 2014; Duputel et al., 2015; Liu et al., 2015), leaving two regions with the potential capability to generate earthquakes of $M_w \geq 8.0$ (Hayes et al., 2014; Ruiz et al., 2014; Duputel et al., 2015). However, the reason why this earthquake together with its largest aftershock broke

---

* Corresponding author.
E-mail address: jara@geologie.ens.fr (J. Jara).

[1] Now at Laboratoire de Géologie, Département de Géosciences, ENS, CNRS, UMR8538, PSL Research University, Paris, France.

https://doi.org/10.1016/j.epsl.2018.09.025
0012-821X/© 2018 Elsevier B.V. All rights reserved.

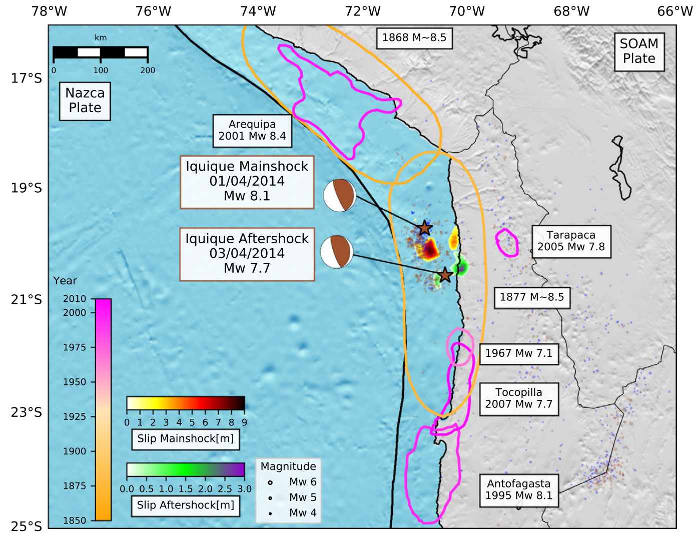

Fig. 1. (a) Seismotectonic Context of North Chile–South Peru subduction zone. Historical and instrumental rupture areas are color coded as a function of their date of occurrence. Dates and magnitudes of all earthquakes $M > 7.0$ in the area are indicated in squared boxes. Mainshock (M_w 8.1 2014/04/01) and aftershock (M_w 7.7 2014/04/03) focal mechanisms from Duputel et al. (2015) are color coded by time. Stars symbolize the mainshock and aftershock epicenters from CSN catalog, as well as the seismicity since 2013/07/01 up to 2014/12/31 with magnitudes over 4.0, color coded by time (blue dots denote events before the mainshock and dark brown events after it) and scaled by magnitude. Preferred slip models for the mainshock and aftershock are plotted with colors depending on the slip. (For interpretation of the colors in the figure(s), the reader is referred to the web version of this article.)

only this specific limited portion of the seismic gap remains elusive. What are the physical conditions (slip deficit, state of stress, friction or structural complexity) that contributed to enhance the ruptures, to end it? Do these earthquakes contribute to fill the slip deficit derived from interseismic geodetic coupling? Are the mechanisms that trigger the mainshock similar to the ones that initiate the aftershock? Is the ruptured area structurally peculiar? Here we explore these questions by studying the rupture process of the Iquique earthquake and its biggest aftershock (M_w 7.7, 2014/04/03), and then by comparing our results with complementary geophysical data that describe the interseismic coupling and the structural complexity in the area.

This earthquake has been well recorded by geodetic and strong motion networks (including co-located stations), providing a unique opportunity to explore the compatibility of both datasets and to show how high-rate GPS can help to better constrain the kinematic rupture processes. We perform a two-step inversion in the frequency domain proposed by Hernandez et al. (1999), that consists in carrying out a static inversion, used as prior information in the kinematic models to explore the source of both earthquakes. Inverting in the frequency domain presents the advantage of evaluating how each frequency is explained (or not) by the inverted slip model. This approach offers the opportunity to have a continuum (in the frequency domain) between the static and kinematic solution. However, frequency domain inversions have not been improving so much these last years and there is then a need to take into account the recent development and ideas of the slip inversion community (multigrid analysis (Bunks et al., 1995), sensitivity analysis (Duputel et al., 2015), better control of the smoothing process (Wellington et al., 2017)), that are explored during this work.

2. Data analysis

2.1. High-rate continuous GPS

High-rate GPS (HRGPS, 1 Hz) data from different networks located in South Peru–North Chile (IPOC, LIA "Montessus de Ballore", CAnTO, ISTerre, IGP and CSN, Fig. S1) are processed using TRACK software (Herring et al., 2016). We use the LC combination and IGS precise orbits, employing the atmospheric delay estimated from daily GPS processing each 2 hours (see Supplementary Material for further details). TRACK computes a relative position with respect to a reference station supposed to be fixed. Here, we have chosen as a reference UCNF station (Fig. S1), located ∼150 km from the epicenters. When the seismic waves reach the reference station, its movement is reflected in the computed displacements of the whole network. This effect, together with orbital errors, is corrected by removing a common mode from the original signal and a sidereal filtering is applied to dismiss the multipath effects (Figs. S2 and S3). The static coseismic offsets are then estimated by fitting a step function in the HRGPS signal, 500 s before and after the earthquake (Fig. S4 and Table S1).

2.2. Strong motion versus HRGPS seismograms

Strong motion stations located in North Chile from different networks are employed in this study (IPOC, LIA "Montessus de Ballore" and CSN, Figs. 4 and 6b). The signals are twice integrated to obtain the ground displacements, and then filtered between 0.01–0.5 Hz. These signals are compared to those from collocated HRGPS. HRGPS signals are filtered in the same frequency band as strong-motion ones. The superposition of both signals shows an excellent consistency in waveform (Fig. S5). This procedure confirms the relevance of using HRGPS for the kinematic inversion of displacements, avoiding the double integration procedure of the strong motion data which induces some uncertain amplifications.

3. Static and kinematic inversion procedures

Let us first consider procedures for this two-step inversion where both the spatial discretization and the model covariance matrices play crucial roles for reducing the intrinsic ill-posedness of this inversion problem. To deal with this problem and because we do not apply any slip positivity constrain (thus allowing larger slip variability), we have imposed several regularization schemes as explained below.

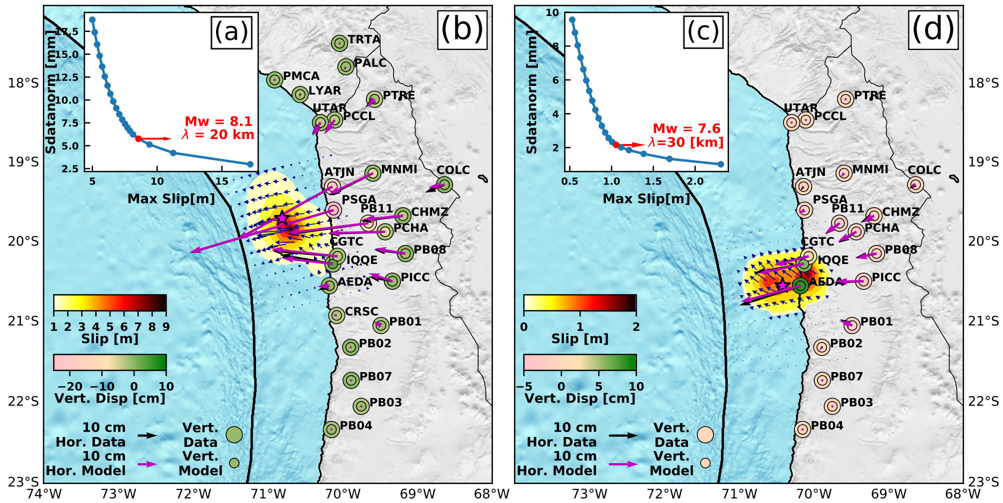

Fig. 2. Static inversion results obtained using HRGPS for the mainshock and the aftershock. (a), (c) Normalized misfit as a function of the maximum slip, showing the correlation length of the preferred slip model for mainshock ((a) $\lambda = 20$ km) and aftershock ((c) $\lambda = 30$ km). Slip model and comparison between data and model (horizontal in arrows and vertical in circles) for the mainshock (b) and aftershock (d). Pink stars symbolize the epicenter of the events reported by the CSN catalog. The dark blue arrows denote the slip direction for both earthquakes, scaled by the slip amplitude.

3.1. Static inversion

GPS static displacements are inverted for the mainshock (M_w 8.1, 2014/04/01, Fig. 2b) and for the biggest aftershock (M_w 7.7, 2014/04/03, Fig. 2d) to get the final slip distribution associated with both earthquakes. A fault of 210 km × 175 km is discretized into 12 subfaults of 17.5 km along-strike and 14 subfaults of 12.5 km along-dip. The dip of the fault progressively increases with depth (the shallower segment dips at 5°, followed by a segment at 9°, 3 segments at 15°, 4 at 20° and finally the 5 deepest segments at 23°). A constant strike is considered (346° for the mainshock and 352° for the aftershock). The rake angle is allowed to vary within the two perpendicular directions to the convergence angle of N77°E. In both cases, the fault plane is fixed to a geometry compatible with the one of Slab 1.0 (Hayes et al., 2012) (Fig. S6). The static Green's functions are calculated through the discrete-wave-number method (Bouchon, 1981) in an elastic stratified medium with AXITRA program (Coutant, 1989), employing the velocity model proposed by Peyrat et al. (2010) (Table S2). This procedure allows us to calculate the complete Green's functions, therefore the static displacement is given by the zero-frequency, expressed as a linear function of the static slip through the expression Gm.

For each station, the three components of the displacement field, compactly designed as d, are inverted altogether in a least-squares sense (Tarantola, 2005), where the misfit function S is defined as:

$$S(m) = \frac{1}{2}[(Gm-d)^t C_d^{-1}(Gm-d) + (m-m_0)^t C_m^{-1}(m-m_0)], \quad (1)$$

where the data and the model covariances are noted respectively C_d and C_m, and m_0 is the initial or prior model. The expected slip model m is defined by:

$$m = m_0 + C_m G^t (G C_m G^t + C_d)^{-1}(d - Gm), \quad (2)$$

where the prior model m_0 is defined as zero static slip for both events. Data covariance matrix C_d is assumed to contain only diagonal terms with variances (σ_d^2) associated with estimated errors during the coseismic offsets calculation (Table S1). The model covariance matrix C_m is going to play an important role in building the slip, requiring a band-diagonal structure given by

$$C_m(\mathbf{x},\mathbf{x}') = \left(\frac{\lambda_0}{\lambda_{dip}\lambda_{strike}}\right)\sigma(\mathbf{x})\mathcal{F}(\mathbf{x},\mathbf{x}'), \quad (3)$$

where the scaling factor λ_0 is usually taken as the size of an individual subfault (Radiguet et al., 2011) (here 15 km for both events). This band-limited structure of the covariance matrix reduces its model-square complexity down to a more manageable model-like complexity. The model correlation between two different positions $\mathbf{x} = (dip, strike)$ and $\mathbf{x}' = (dip', strike')$ on the fault plane is expressed by the operator $\mathcal{F}$. Its expression with a laplacian decay

$$\mathcal{F}(\mathbf{x},\mathbf{x}') = \exp\left(-\frac{|dip - dip'|}{\lambda_{dip}} - \frac{|strike - strike'|}{\lambda_{strike}}\right), \quad (4)$$

will provide more coupling than the often used Gaussian decay (Wellington et al., 2017): a key point for mitigating trade-off between parameter values for this static reconstruction. For static slip inversion, this relatively slow decay behavior has been found to behave better than the often used Gaussian decay (Radiguet et al., 2011). The correlation lengths λ_{dip} and λ_{strike} are considered as homogeneous in this work, although they can be tuned to vary with the fault position, especially when fault points are moving away from acquisition network. Correlation length λ_{dip} has been tested between 5–100 km, with a step each 5 km. Following the L-curve criterion (Hansen, 1992), we have chosen the best compromise between the maximum slip and the normalized misfit (Fig. 2 a and c): optimal values are 20 km (mainshock) and 30 km (aftershock).

The operator $\sigma(x)$ (with a model complexity) expresses the prior expected local variability or sensitivity of the static slip: small values will prevent the static slip reconstruction to move away from the prior model value which is zero in our case. The operator $\sigma(x)$ compensates for poor geometry of the acquisition with respect to the active fault. The lack of sensitivity with depth can also be controlled by this operator. Moreover, we may increase the sensitivity of zones where we expect high values when fitting the data. The following operator

$$\sigma(x) = \sigma_{min} + (\sigma_{max} - \sigma_{min}) \times \exp\left(-\frac{|dip - dip_0|}{\lambda_{dip_0}} - \frac{|strike - strike_0|}{\lambda_{strike_0}}\right) \quad (5)$$

has been selected where the position $(dip_0, strike_0)$ is the zone with the most expected variation of the static slip for the mainshock. We have assumed a circular shape through the choice for quantities λ_{dip_0} and λ_{strike_0} equal to 40 km and 40 km respectively, with values ranging from 0.01 to 2.5 m. For the aftershock, such single-shape operator has been considered in a first trial: the data gradient still drives us toward two zones of maximum slip. Therefore, we have considered in a second trial two joint prior shapes with σ values ranging from 0.01 to 1.0 m around these expected high-slip zones: the data gradient has built up a solution coherent with this second sensitivity design. In both cases λ_{dip_0} and λ_{strike_0} are equal to 25 km and 52.5 km.

For the final solution, the model resolution is evaluated following the resolution matrix proposed by Tarantola and Valette (1982), given by

$$R = C_m G^t (G C_m G^t + C_d)^{-1} G, \qquad (6)$$

gives us low resolution for all subfaults (Fig. S7 for mainshock and Fig. S8 for the aftershock, a and b): for a perfectly resolved model, the matrix should be the identity. On the other hand, the data sensitivity defined by Duputel et al. (2015) through

$$Sen = diag(G^t C_d^{-1} G) \qquad (7)$$

shows the ability of the network to detect slip at a given location on the fault (Fig. S7 for mainshock and Fig. S8 for the aftershock, c and d).

3.2. Kinematic inversion

The kinematic reconstruction of the rupture process is an even more ill-posed problem because of possible leakages between space and time: we have followed the two-step strategy proposed by Hernandez et al. (1999) for a reconstruction in the frequency domain building the solution by sweeping from low to high frequencies. At each frequency, the static solution obtained from inversion of geodetic data will be used as the prior model in the kinematic inversion. The synthetic displacement waveform in the frequency domain is computed following the sparse parameterization proposed by Cotton and Campillo (1995), given by

$$\begin{aligned} V_i(w) = &\sum_{k=1}^{n} G_{ski}(w)\ [slip_{sk}\ \exp(-iwt_k) S_k(R_k, w)] \\ &+ \sum_{k=1}^{n} G_{dki}(w)\ [slip_{dk}\ \exp(-iwt_k) S_k(R_k, w)], \end{aligned} \qquad (8)$$

where the Green's function (i.e. the displacement for a unit constant slip on the k-th subfault for the frequency w) is denoted by the symbol G_{ski} for the strike component and by G_{dki} for the dip. The slip is parametrized depending on the component as well: slip along-strike by $slip_{sk}$ and slip along-dip by $slip_{dk}$. The rupture time is indicated by t_k, while the source time function (STF) is given by the following analytical expression $S_k(t) = 0.5(1 + tanh(t + R_k/2.0)^2)$, depending on the rise time R_k. Therefore, only four parameters have to be reconstructed for each subfault. Each subfault is represented by an array of point sources, separated by distances of less than one sixth of the shortest wavelength to be considered locally. For these point sources, Green's functions are computed and then, the sum of all point sources response delayed in time to include the travel-time difference, due to the rupture front propagation across each subfault (Cotton and Campillo, 1995). The Green's functions are calculated using the same strategy as for the static inversion with the program AXITRA (Coutant, 1989), but keeping the whole frequency range. We do not consider variable rupture velocity inside each subfault which is allowed to slip once. The velocity model is the same as the one used during the static inversion for both events.

The four parameters, namely strike slip, dip slip, rise time and rupture time in each subfault, are inverted using the non-linear least-squares formulation proposed by Tarantola and Valette (1982). A non-linear operator f relates the model parameters m to the data vector d through the general expression $d = f(m)$. The model solution is obtained through an repetitive procedure based on a linearized approximation where the next model m_{l+1} is obtained from the current model m_l following the iterative algorithm

$$\begin{aligned} m_{l+1} = m_l + b(&A_l^t C_d^{-1} A_l + C_m^{-1})^{-1} \\ &\times (A_l^t C_d^{-1}(d - f(m_l)) + C_m^{-1}(m_0 - m_l)), \end{aligned} \qquad (9)$$

which minimizes the least-squares data misfit. At each frequency, the initial model m_0 will be used also as a prior model. For the lowest frequency, the static solution will be considered as the initial/prior model and the final solution at this frequency will be used as the initial/prior model for the next frequency. The Jacobian matrix A_l are obtained by taking the closed-form derivative of the Equation (8) with respect to the related parameter. The damping factor b between 0 and 1 prevents any divergence. The data covariance C_d has a diagonal matrix filled with ones, for simplicity considering the stations' spatial distribution, while the model covariance requires more attention as we see in the multigrid approach we associate with the frequency sweeping.

Based on a multigrid approach, the inversion starts with a Large Subfault Size (LSS) discretization sweeping over frequencies, obtaining a final solution (Bunks et al., 1995). The final solution is interpolated in a Small Subfault Size (SSS) discretization, repeating again the inversion scheme with another set of frequency windows still sweeping from low to high frequencies. By combining this dynamic frequency sampling and a recursive spatial sampling, we are able to improve the data fit and to increase the model resolution with still stable results. For the LSS sampling, we have adopted the same subfault geometry employed during the static inversion (168 subfaults). The SSS sampling is obtained by dividing each subfault in four subsequent subfaults, so that the total fault encompasses 672 subfaults (24 along-strike with 8.75 km and 28 along-dip with 6.25 km) for both events.

The inversion procedure is performed by using a progressively broadened frequency range for both events for fixed spatial sampling. The LSS model is initiated with a frequency range of 0.01–0.02 Hz using the static solution as the initial/prior model. The obtained solution is then used as the new initial/prior model for the new frequency range of 0.01–0.03 Hz. This procedure is repeated until the frequency range of 0.01–0.25 Hz is reached (24 models in total). The last LSS model is then interpolated and used as the initial/prior model for the SSS sampling, considering the first frequency range of 0.01–0.02 Hz. The same iterative procedure is repeated for the small-subfaults configuration until the frequency range of 0.01–0.3 Hz is reached (29 models in total).

For both events, the model covariance matrix C_m is defined as a matrix, following Radiguet et al. (2011). The variances σ_{strike} and σ_{dip} are defined following the Equation (5) with the same strategy employed during the static inversion. The σ_{rup_time} is defined with the same idea as in Equation (5), but increasing the values from the epicenter of the earthquakes, because the rupture time may be better estimated near the epicenter, but not far from it. We have started by allowing a considerable variability through σ_{dip} (main slip direction) and σ_{rup_time}, but a lower one in the strike slip component (Table S3). When the seismic moment reported for the earthquakes is reached, we keep the same proportion mentioned to define σ in terms of variability, but reducing the values between which parameters are allowed to move, in order to hold the seismic moment (Table S3). There is no physical reason to constrain the rise time, so we have assigned the same σ_{rise_time} value to all subfaults in both models and events (LSS and SSS, Table S3).

In order to avoid spurious jumps in the model parameters (slip along-dip and strike, rise time), we introduce a correlation length of 17.5 km in LSS model and 8.75 km in SSS model, for both events. It allows to connect the adjacent subfaults providing a smooth rupture process. To evaluate the fit to the data, we compute the variance reduction proposed by Cohee and Beroza (1994). The sensitivity is also analyzed (Equation (7)) for the mainshock (Fig. S15) and the aftershock (Fig. S16).

4. Results

4.1. Static inversion

The mainshock (Fig. 2a) has broken an asperity localized between 15–40 km depth with a maximum slip of ∼9 m. It is located South of the epicenter reported by CSN (∼40 km). The seismic moment obtained is 1.52 × 10^{21} Nm, equivalent to M_w 8.1. The dominant slip direction is on the dip-slip component, observing some strike-slip component at the south-east of the rupture plane. The aftershock (Fig. 2b) is composed of two asperities localized on each side of the epicenter, with a maximum slip of ∼1.2 m. The shallower asperity (close to the trench) is confined between 15–30 km depth, and the deeper one between 40–50 km depth. The seismic moment obtained from the inversion is 3.68 × 10^{20} Nm, associated with an earthquake magnitude M_w 7.6. The main dominant slip direction is in the north-west component, which is not the convergence direction. We find as an interesting point the fact the slip vectors of the aftershock point towards the mainshock asperity. Our hypothesis is that this feature might be related to the stress generated by the mainshock, producing a particular behavior of the slip vectors (increasing the amount of its strike-slip component). Comparing those slip models to the resolution analysis (resolution matrix and sensitivity), we find that the data can better resolve the slip close to the coast than close to the trench (Fig. S7 for the mainshock and Fig. S8 for the aftershock). The poor resolution obtained at the trench vicinity is typical for subduction zones lacking offshore instrumentation, due to the lack of data close to the trench. The results are good enough to be used as our prior model in the kinematic inversion, especially because the spatial distribution is well resolved where the slip is located.

4.2. Kinematic inversion

4.2.1. Mainshock

Some differences can be appreciated between the resulting kinematic and static slip distributions. The final slip obtained during the kinematic inversion shows a very concentrated asperity South of the epicenter (∼43 km) with a maximum slip of ∼9 m and confined between 15–35 km depth. Conversely to the static solution, less slip is seen North of the epicenter and the emergence of a second deep asperity is observed between 40 and 55 km depths (Fig. 3a) with a maximum slip of 5 m. The main slip direction is on the dip-slip component.

The rupture is characterized by a very slow moment rate during the first 25 s, leading to an abrupt acceleration at the moment liberation at 30 s (Fig. 3 e and f). After that, the moment rate decreases to reach the final rupture time at 125 s (Fig. 3 e and f). The total seismic moment obtained is 1.73 × 10^{21} Nm (Fig. 3e), equivalent to a magnitude M_w 8.1 and a stress drop of 7.8 MPa. The difference between data and synthetics corresponds to a mean variance reduction of 82.37% (see Table 1), fitting better the lower frequencies 0.01–0.15 Hz (Fig. 3d). At higher frequencies, a limited variance reduction up to 0.2 Hz is obtained. This is also visible in the data fit, where the low frequencies are better fitted (Fig. 4a, see Supplementary Information for not normalized and frequency domain fit, Figs. S11 and S13), while the high frequencies are not well solved. Some complexity in the rupture time (Fig. 3b) and rise time (Fig. 3c) are required to the South of the rupture to fit the signal of Southern stations. This complexity is also reflected in the STF after the 75 s (Fig. 3f). To the North, the rupture propagates at a much more constant rate than to the South (Fig. 3b). This variation in complexity might be associated with changes in the lithology that are not reflected in the velocity model. To evaluate the kinematic solution in terms of the static model, a forward static model is performed (Fig. S17a). A large misfit is found for stations ATJN and PSGA indicating that a significant portion of slip is missed by the kinematic inversion in the northern part of the rupture. Interestingly, this amount of slip that is missed by the kinematic inversion is located in an area where the rise time is high and rupture time is rather slow compared to the main peaks of slip, which may explain a tiny signal in the accelerometer data that mostly cover this portion of the rupture. To solve this inconsistency, we have performed another static inversion of coseismic displacements keeping the same values for lambda and data covariance matrix as those described in section 3.1, but using the final kinematic slip distribution as prior model and constant covariance matrix defined as 10% of the maximum slip. This is meant to test whether it is possible to obtain static solution that remains close to our kinematic model (Fig. 7 and Fig. S17c). It allows us to improve the solution of static displacements, holding the slip features that appeared during the kinematic inversion and fitting well the measured coseismic offsets. We have performed the same procedure for the aftershock case (Fig. 7b and Fig. S17d), although there is not a big discrepancy between the final kinematic slip model and the static displacements obtained during the forward mode (Fig. S17b).

Table 1
Mainshock and Aftershock moment estimations and data fit using different parameterizations.

No of subfaults	Starting rup. front vel. (km/s)	Moment $\times 10^{21}$ (Nm)	Mean variance reduction (%)
Mainshock			
168	1.2	1.92	76.65
168	1.3	1.74	78.53
168	1.4	1.71	79.73
168	1.5	1.62	79.15
168	1.6	1.57	79.20
168	1.7	1.52	77.71
672	1.4	1.73	82.37
Aftershock			
168	2.4	0.423	81.56
168	2.5	0.428	81.75
168	2.6	0.404	83.26
168	2.7	0.430	82.15
168	2.8	0.432	81.96
672	2.6	0.388	85.74

4.2.2. Aftershock

The slip distribution of the largest aftershock is characterized by two asperities located on both sides of the epicenter (Fig. 5a). The shallow asperity is confined between 15–30 km depths with a maximum slip of 1.5 m, while the deeper one is located between 30–50 km depths with a maximum slip of ∼3 m (Fig. 5a, see Supplementary Information for not normalized and frequency domain fit, Figs. S12 and S14). The calculated seismic moment is 3.88 × 10^{20} Nm, equivalent to a magnitude M_w 7.7 (Fig. 5 e and f) and a stress drop of 1.8 MPa. The main slip direction for the

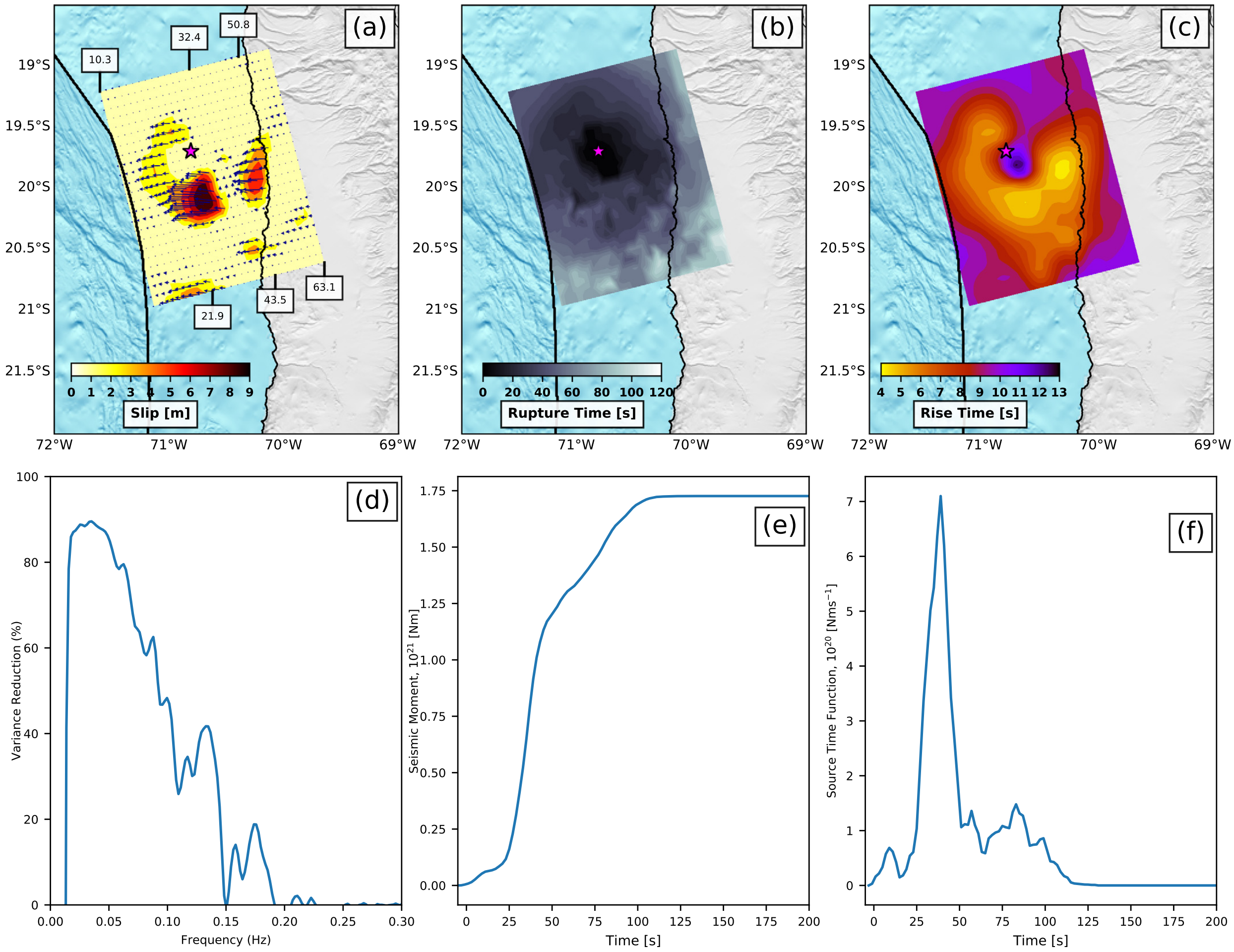

Fig. 3. Mainshock kinematic inversion results. Preferred slip model (a), rupture time (b) and rise time (c). Plane depths are indicated inside white boxes in (a). The pink star indicates the epicenter location reported by CSN catalog and the dark blue arrows denote the slip direction, scaled by the slip amplitude. (d) Mean variance reduction computed for each frequency between data of all the stations and synthetics. (e) Cumulative seismic moment and (f) and STF.

shallower asperity is on the dip-slip component, while the deeper one is oriented in the north-west component. The result obtained during the kinematic inversion is similar to the static one, but provides further details in the asperities location and the slip distribution.

The rupture has begun with an acceleration during the first 18 s (Fig. 5e), breaking the asperity close to the trench. Then, the second deeper asperity has slipped during 20 s (Fig. 5e). The STF is simpler than the mainshock (Fig. 5f), and lasts 60 s. The fit to the data corresponds to a mean variance reduction of 85.74%, solving the frequency range of 0.01–0.3 Hz (Fig. 5d). Although not significant differences are found in the static forward model obtained using the final kinematic slip model (Fig. S17b), we have repeated the strategy described above to obtain the final aftershock static model (Fig. 7b).

4.2.3. Comparison between LSS and SSS models

LSS and SSS models have been compared in order to explore the differences and advantage of SSS model for the mainshock (Fig. S9) and the aftershock (Fig. S10). For both earthquakes, the spatial resolution of the model discretization is increased. Rupture time (Figs. S9 and S10c, d) and rise time (Figs. S9 and S10e, f) show the same variation as the slip, but do not change the general pictures of their behaviors are not changed, thanks to the multigrid approach. One important change between LSS and SSS models is the increase in the frequency range resolution. For the mainshock (Fig. S9g), the resolution is improved by about 40% in the frequency range of 0.1–0.15 Hz. At higher frequencies, the resolution still slightly increases (∼15%), but not significantly. For the aftershock (Fig. S10, g) the SSS models improves significantly the mean variance reduction in the frequency range 0.1–0.25 Hz. The seismic moment obtained with both models is of the same order (Figs. S9 and S10h, i). The STF show some differences between LSS and SSS models (Figs. S9 and S10i): the STF is slightly more smoothed in the SSS models due to the change in the subfault size, avoiding any large change of the parameters between the adjacent subfaults. The resolution of the kinematic models (Figs. S15 for the mainshock and S16 for the aftershock) is similar between LSS and SSS models.

The number of parameters inverted during the inversion increases from 672 in the LSS model to 2688 parameters in the SSS model. For both earthquakes the model resolution close to the trench is quite low because the stations are located inland. The increase of the number of parameters seems to reduce the local resolution on each subfault, but the spatial pattern of the resolution is kept (well resolved close to the epicenter, and poorly resolved by the trench, Figs. S15 and S16).

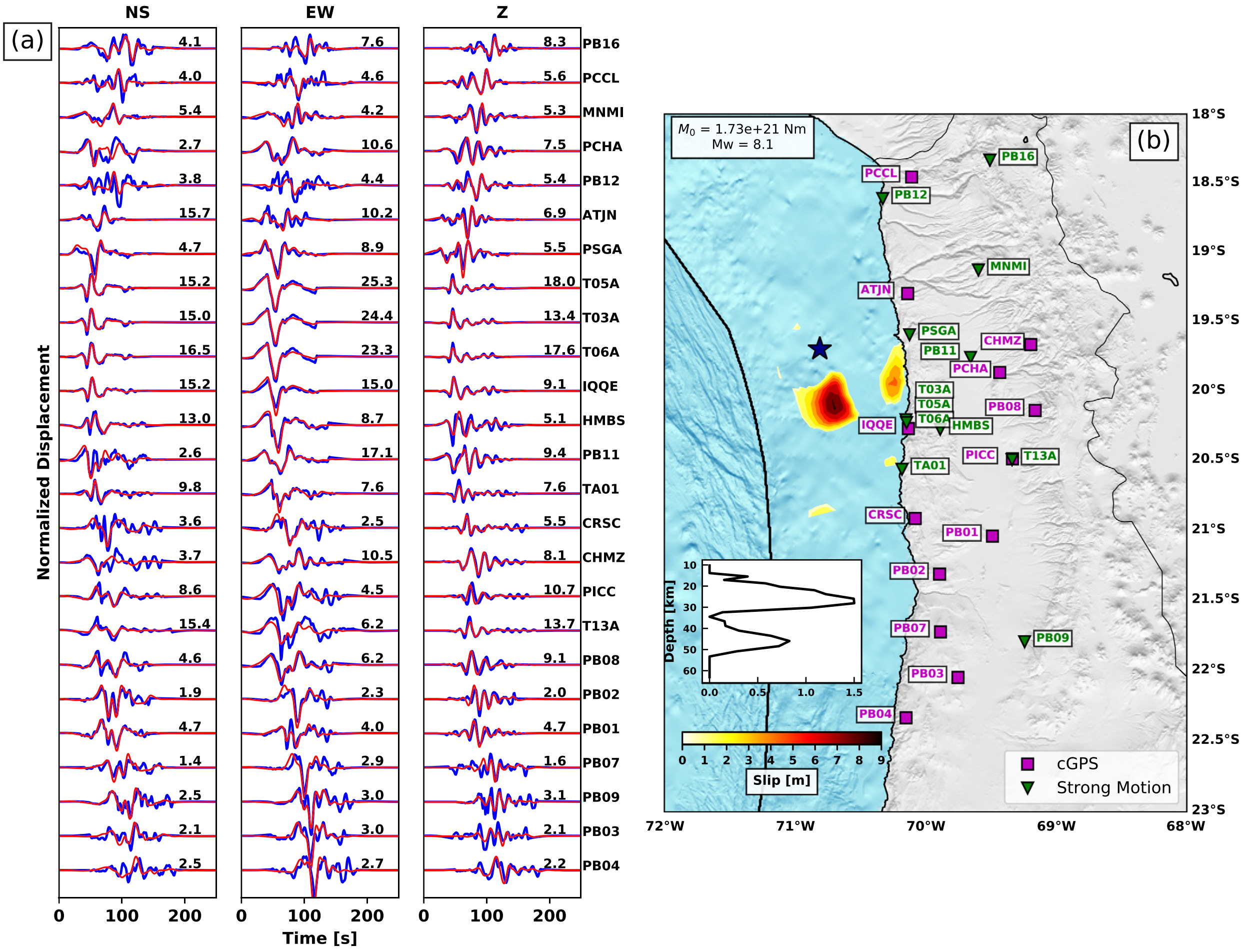

Fig. 4. (a) Mainshock normalized Strong Motion – HRGPS (blue) and synthetic seismograms (red). For each station and component, the maximum data displacement is shown in [cm]. (b) Final preferred slip model and stations map used during the kinematic inversion. Green triangles symbolize strong motion location and magenta squares HRGPS. Star indicates the epicenter of the event by CSN catalog. Also, at the bottom left is shown the slip averaged along-strike as a function of depth.

5. Discussion

5.1. Along-strike segmentation of the seismogenic zone

Our results confirm that 2014 M_w 8.1 Iquique earthquake together with its largest aftershock ruptured a limited portion of the seismic gap (Fig. 1). Moreover, the obtained slip distributions show that both earthquakes ruptured into two distinct asperities, quite spatially concentrated (Fig. 8).

Following Aki (1979), it is therefore likely that the earthquake stopped because it encountered a geometric or inhomogeneous barrier. It has been proposed that large earthquakes rupture areas that are strongly coupled, while aseismic slip is seen in poorly coupled zones and it has been proposed to act as a barrier for seismic ruptures. This might be supported by the occurrence of preseismic slow slip surrounding the main slip patches of the mainshock (Socquet et al., 2017) (Fig. 9d). Our coseismic slip distribution compared to the interseismic slip distribution obtained by Métois et al. (2016) tends to confirm this finding, at least for the mainshock (Fig. 9c). The mainshock was initiated in an area at the transition between low and high coupling, prone to high stresses, possibly even further loaded by the 8-month slow slip that preceded the rupture. The earthquake has then propagated Southward and ruptured a highly locked patch, and eventually stopped at the Southern termination of this highly coupled patch (Fig. 9c). The mainshock has therefore contributed to release the slip deficit accumulated in this locked asperity during the interseismic period.

On the contrary, the largest aftershock has broken areas that were poorly coupled in the interseismic period (Fig. 9c). In order to understand this apparent contradiction, we have calculated the stress change produced by the mainshock on the subduction plane (Fig. 8a). The aftershock is located in areas with positive Coulomb Stress change (Fig. 8a), suggesting that it has been triggered by the mainshock stress increase. Fig. 8a shows towards the north of the epicenter, the CSC is more heterogeneous than the southern region. Towards the north, the slab is changing the strike because of the Arica bend, which is not represented in our geometry employed in the inversion procedures (dip variable and strike constant on the fault plane). It might explain the positives values of the CSC in the northern region not observing large aftershocks. Also, Fig. 9 (c and d) shows the region struck by the mainshock is surrounded by preseismic slip. The region where the aftershock is emplaced is the only place where not coseismic slip is observed, that combined with the positives values of the CSC, it might explain the triggering of this event by the mainshock.

To further understand the parameters that control the location of such a seismic asperity and high coupling patch, we compared our findings with the bathymetry and the free-air gravity anomaly

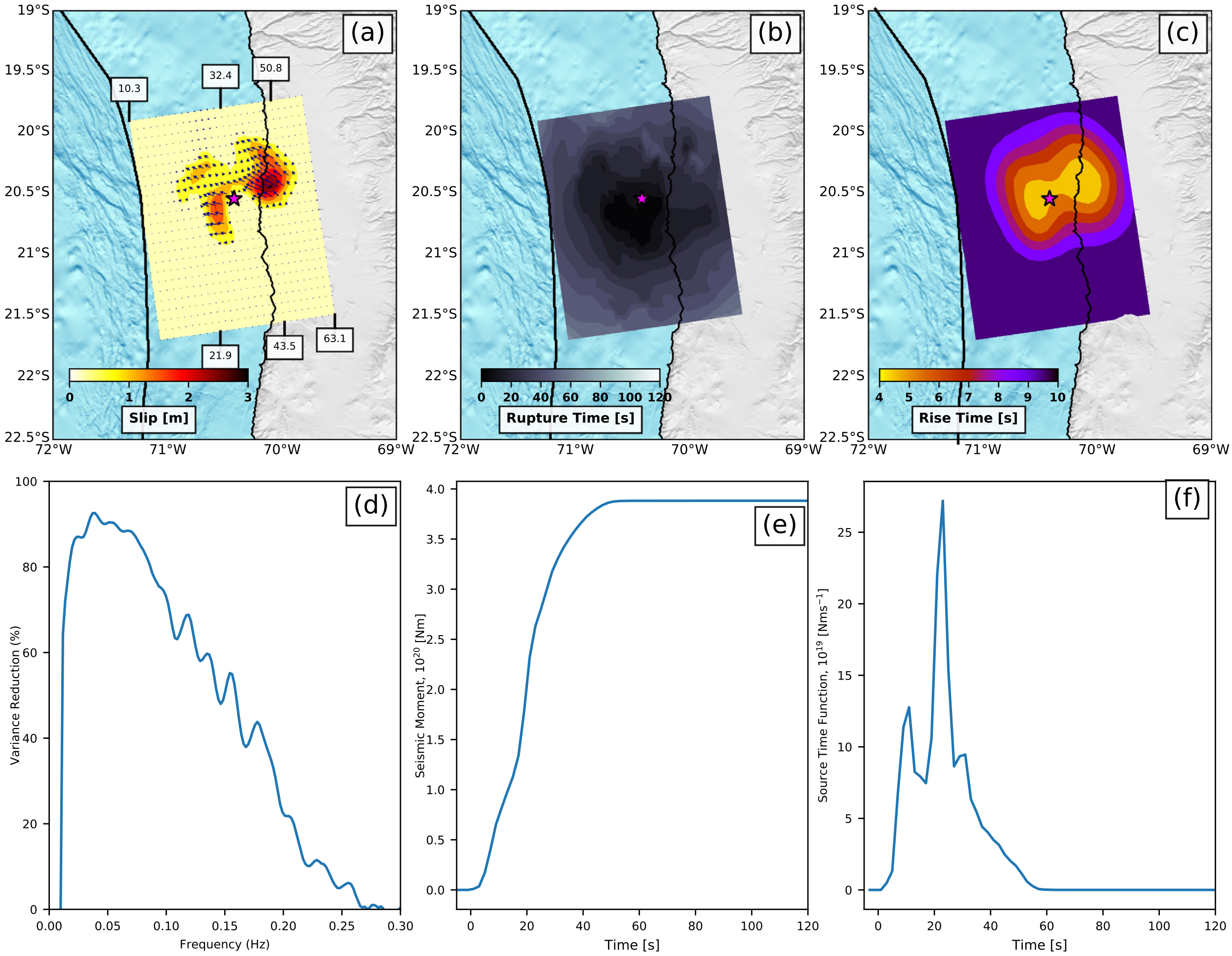

Fig. 5. Same caption as in Fig. 3, but for the aftershock case.

(Fig. 9 a and b). Geological features affecting the subducting slab or the overriding plate (such as fracture zones, ridges, changes in the slab geometry, peninsulas, fault systems and marine basins) have been shown to correlate with low coupling zones and the arrest of seismic rupture (e.g., Armijo and Thiele, 1990; Song and Simons, 2003; Wells et al., 2003; Audin et al., 2008; Béjar-Pizarro et al., 2010; Contreras-Reyes et al., 2012; Maksymowicz et al., 2015), and can be interpreted as a structural complexity that acts as a geometrical barrier for the seismic rupture (Aki, 1979; King, 1986). Using seismic velocity profiles and gravity data, Wells et al. (2003) evidenced a spatial correlation between forearc basins and the peak of slip of several great earthquakes, suggesting that the basin is an indicator of a long-term seismic moment release. Song and Simons (2003) have proposed another way to analyse the gravity data through the definition of the Trench Parallel Gravity Anomaly (TPGA), where areas of negatives values correlate with the coseismic slip in subduction zones.

The asperity with highest slip value of 2014 Iquique mainshock is centered in the Iquique basin (Armijo et al., 2015), inferred from high resolution bathymetry (Fig. 9a) and free-air gravity anomaly (Fig. 9b). This is in agreement with the results shown and discussed by Meng et al. (2015), who demonstrated that the main asperity is located in an area with negative value of TPGA. The Southern limit of the main rupture is characterized by an important change in the gravity reported by Maksymowicz et al. (2018), who have modeled the free-air anomaly (Fig. 9b) and the local gravity data in the northern Chile region. Probably, this feature is associated with a change in the lithology, fracturing and fluid content inside the continental wedge. Considering that tectonic erosion is characteristic along the Northern Chile margin, the distance between the deformation front and the shelf break increases in the northern segment of the study area and the lower slope decreases. This feature suggests the presence of a wider frontal sedimentary prism to the north, and in general, a latitudinal tectonic segmentation of the continental wedge, which is supported by velocity models (Comte et al., 2016) and density gravity models (Maksymowicz et al., 2018). This strong gravity change is associated with a geological change that could explain the complexity observed in the Southern part of the rupture and the heterogeneities in the tail of the STF (Fig. 3b and f).

The North limit of the aftershock also seems related to the gravity changes discussed above. This sharp change marks an E–W line that separates both earthquakes. The Southern limit of the aftershock is not associated with any clear change in the gravity, but might be related to geological features of the overriding plates responsible to stop the rupture. Audin et al. (2008) have pointed out the relationship between the Chololo coastal fault system and the Southern end of Arequipa coseismic rupture in Peru (M_w 8.4, 2001, Fig. 1). The tectonic map of González et al. (2003) indicates that the region where the aftershock stops at 21°S is characterized by

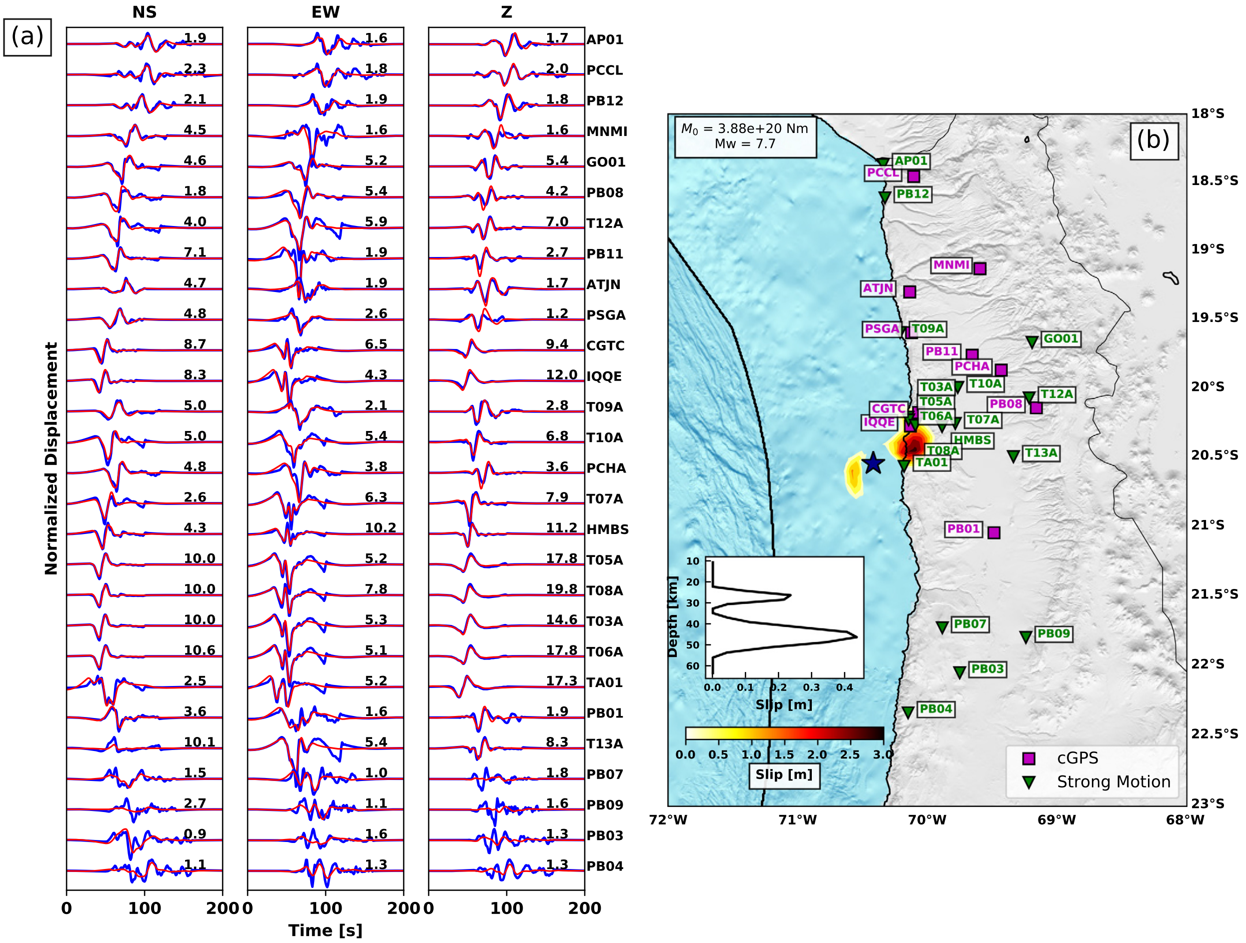

Fig. 6. Same caption as in Fig. 4, but for the aftershock case.

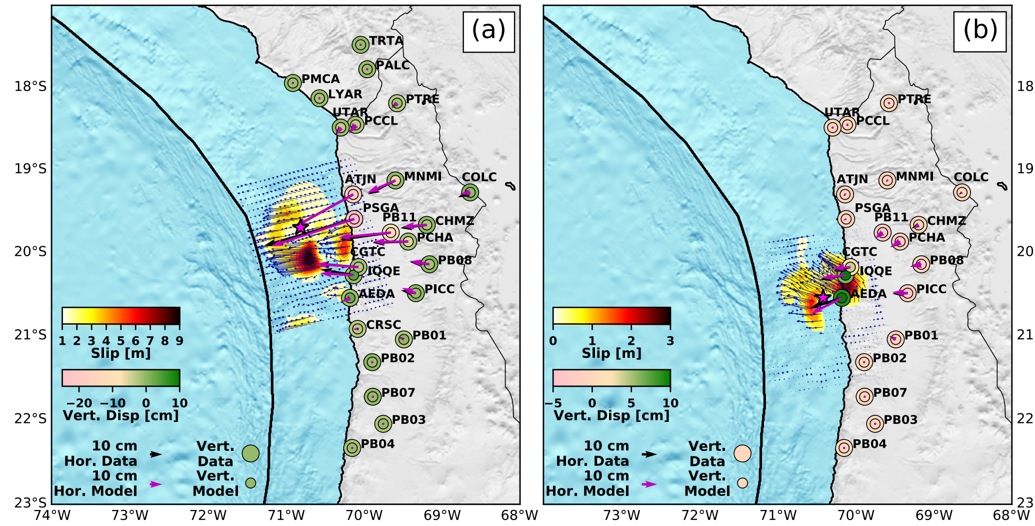

Fig. 7. (a) Mainshock ((b) Aftershock) static inversion results obtained using the kinematic slip model as the prior model. A small value for the model covariance (C_m) is used to perform the inversion (10% of the maximum slip for each event). Slip model and comparison between data and model (horizontal in arrows and vertical in circles) are plotted and color coded. Pink stars symbolize the epicenter of the events reported by the CSN catalog. The dark blue arrows denote the slip direction for both earthquakes, scaled by the slip amplitude.

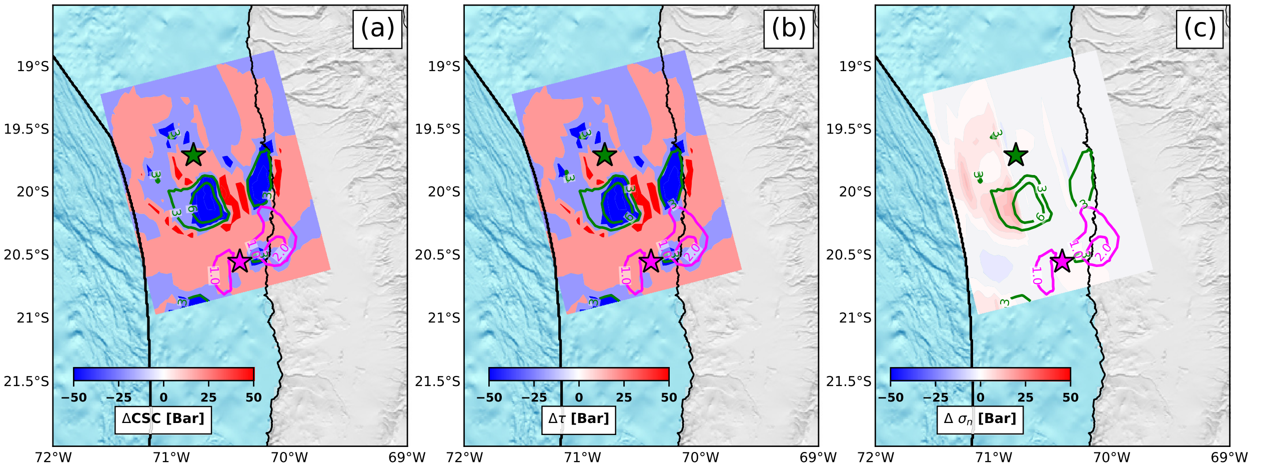

Fig. 8. Coulomb stress change (a), shear stress change (b) and normal stress change (c) on the fault plane calculated using the mainshock preferred slip model. Green (pink) star and contours denote the epicenter of the mainshock (aftershock) reported by CSN catalog and the slip produced by the event (see Supplementary Material for further information about the calculation).

an increased complexity in the faults system. South of 21°S almost all the faults are parallel to the trench and the coastal scarp (mainly normal faults), but North to this limit, the area of the Salar Grande is affected by a series of E–W thrust faults combined with conjugated strike-slip faults (González et al., 2003). This tectonic difference might be related to the Southern termination of the aftershock rupture.

5.2. Along-dip segmentation of the seismogenic zone

Both the mainshock and the large aftershock show an interesting bimodal pattern along-dip (Fig. 4b and Fig. 6b). In both cases, the shallow patch of slip extends from 15 km and 30 km depths, while the deep patch of slip is confined between 35 and 50 km depths. The upper limit at 15 km depth corresponds to the deformation front extracted from gravity (Maksymowicz et al., 2018) and seismic velocity models (Comte et al., 2016). The downdip limit at ∼50 km depth is in agreement with other seismological (Comte and Suárez, 1995) and geodetic (Béjar-Pizarro et al., 2010; Chlieh et al., 2011; Métois et al., 2016) definitions of the lower extent of the seismogenic zone in North Chile subduction.

The most intriguing aspect of the observed along-dip segmentation is the separation between shallow and deep asperities. Indeed both earthquakes present almost no slip at 30–35 km depths. Armijo and Thiele (1990) proposed that the coastal scarp could be a west-dipping normal fault reaching the subduction zone at depth. A change in the slab dip has been inferred from wide-angle seismic refraction and reflection data, complemented with relocated aftershock seismicity in the Tocopilla area (∼22°S) (Contreras-Reyes et al., 2012) (M_w 7.7, 2007, Fig. 1). Based on a correlation with the coastal scarp and following the idea proposed by Armijo and Thiele (1990), the authors suggest that this change in dip from 10° to 22° affects a wide portion of the slab. Maksymowicz et al. (2018) have modeled the gravimetry in the region observing the same change in dip proposed by Contreras-Reyes et al. (2012) in the Tocopilla area. Employing those results, we have inferred the location towards the North of this change in the dip (purple line in Fig. 9 a and b), observing that in the area affected by Iquique earthquake, this feature seems to delimit a separation between the deep and shallow asperities. This change in slab geometry may therefore act as a barrier for the rupture by slowing its velocity and reducing the amount of slip between the shallow and deep asperities. Such an along-dip segmentation had already been observed in the area during the 2007 Tocopilla earthquake that ruptured the deeper part of the seismogenic interface (Béjar-Pizarro et al., 2010).

This along-dip segmentation is also associated with a change in the frequency content of the seismic rupture. The deeper asperities both rupture into a pulse of slip that is much shorter than the slippage of the shallower asperities (as shown from the rise time and the rupture time, Fig. 3 b and c and Fig. 5 b and c). Meng et al. (2015) and Lay et al. (2014) have shown a compatible observation: back-projected high-frequency energy is radiated in the deeper portion of the rupture, close the to deep asperity. Although the structural complexity might be invoked, numerical simulations also provide the simple explanation that the base of the coupled area is a zone of high prestress that tends to keep partial ruptures confined, producing pulse-like ruptures that propagate along-strike (Michel et al., 2017). Such observations are compatible with the along-dip segmentation of the megathrust described in North Chile from the analysis of the frequency content of moderate magnitude earthquakes (Piña-Valdés et al., 2018). Also, Lay (2015) characterizes the segmentation of the subduction zone through four domains (A, B, C and D), based on the radiated energy generated by the earthquakes, using teleseismic data. Domain A corresponds to depths less than 15 km, experiencing either aseismic deformation or large coseismic displacement in tsunami earthquakes. Domain B is located between 15 and 35 km, observing the nucleation of megathrust earthquakes that generate large slip and high amount of low-frequency radiation. Domain C is localized between 35–60 km depths, where a large amount of high-frequency radiation is emitted and asperities much smaller than region B are seen. Finally, the Domain D is placed deeper than 60 km and is where slow slip events, low-frequency events, and seismic tremor have been reported, and it is not reported in all subduction zones. Following the model proposed by Lay (2015), our results show that the shallow asperities for the mainshock such as the aftershock, are located at depths between 15 and 35 km, suggesting they would break the Domain B. Also, for both events, the deeper asperities are emplaced at depths between 35 and 60 km, suggesting they would break the Domain C, depicting the heterogeneity of the seismogenic zone. This segmentation along dip in terms of frequency content during the earthquake ruptures has been already reported in Chile. After the Maule earthquake (M_w 8.8, 2010), Kiser and Ishii (2011) and Wang and Mori (2011) show that high-frequency radiation is predominant in the deeper part of the

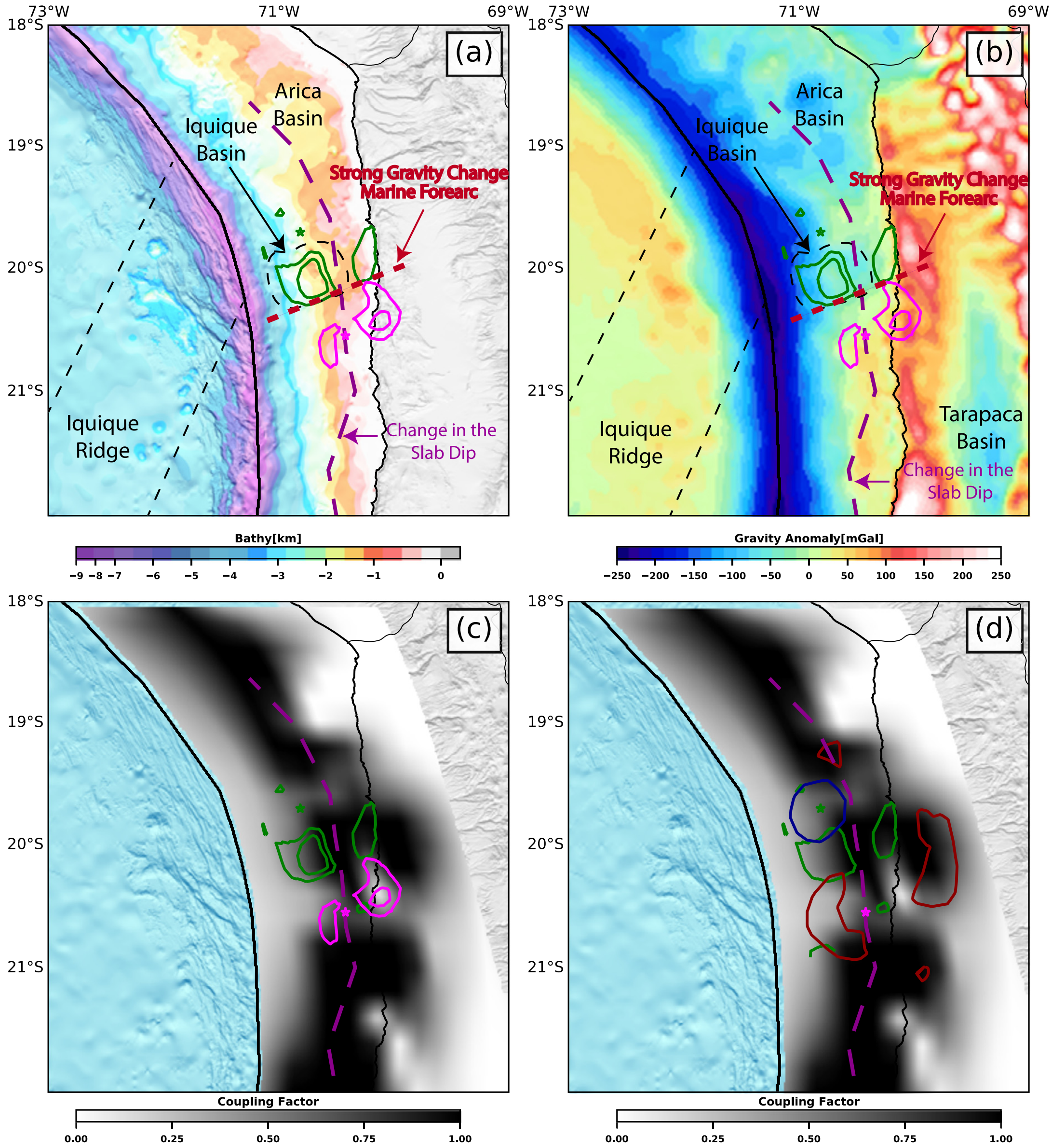

Fig. 9. (a) High-resolution topography (Contreras-Reyes et al., 2012), (b) free air gravity anomaly (Sandwell et al., 2014) and (c) and (d) coupling distribution (Métois et al., 2016) on the study area. Mainshock (green) and aftershock (pink) slip contour of 2.0 m and 0.5 m are plotted. Violet line parallel to the trench represents the abrupt change on dip proposed by Contreras-Reyes et al. (2012) interpolated to the North, extracted from gravity models. (d) Coupling map with the mainshock contours (green), the 8-month SSE (red) and the 2-week preseismic slip (dark blue) shown by Socquet et al. (2017) contoured in mm.

seismogenic zone. Similar results have been observed after the occurrence of Illapel earthquake (M_w 8.4, 2015) (Melgar et al., 2016; Ruiz et al., 2016).

5.3. Differences between our results and previous works

Our results are very consistent with those presented by Duputel et al. (2015) for the mainshock as well for the aftershock, although we use a different methodology. The main difference between their work and ours is the emergence of a previously unnoticed deep slip asperity. Our initial static slip model is not able to see this feature, because GPS data are poorly sensitive to deep slip (see for instance the predicted displacement generated by the deep asperity only as dark blue arrows in Fig. S17a). Also, it seems this deep feature is resolved by waveforms of frequencies over 0.05 Hz (Fig. S18). In the kinematic result, this deep slip is needed to fit the maximum amplitude of displacement, notably at the closest stations that are less well fit by Duputel et al. (2015) or Liu et al. (2015) (Fig. S19). Another difference between their work and ours, is the number of stations used in near-field range for the kinematic inversion. We have employed 25 HRGPS and strong motion while they have used 19 HRGPS and strong motion (plus all the other data set). We have found a rupture with 125 s of duration, they have used just 80 s. This longer rupture allows us to observe the second deep asperity and the complexity of the rupture process to the South. We have found a similar static patch as Duputel et al. (2015) for the aftershock, but our results are clearer because we have included more data. Comparing our mainshock results with those of Liu et al. (2015), we obtain the same shallow asperity, but their slip is closer to the trench and further North with respect to the epicenter. The difference in the obtained slip can be attributed to the simpler geometry used by Liu et al. (2015) that does not follow a realistic slab geometry. We conclude that the parametrization of the fault plane is a first-order characteristic input required to perform kinematics inversions. For both events, we have used more near-field data than Liu et al. (2015), allowing to get a better resolution and the apparition of the second deep asperity. The use of HRGPS therefore seems to improve the resolution of the rupture process, filling the data gap in areas where strong motion instruments are not installed.

When authors have used teleseismic data to invert the rupture process (Lay et al., 2014; Hayes et al., 2014), the differences are due to the lack of resolution of those datasets to resolve details that the near-field data can distinguish, although obtaining similar values for the seismic moment, maximum slip and mean stress drop (e.g., Lay et al., 2014; Hayes et al., 2014; Ye et al., 2016; Hayes, 2017). Also, our models present more details in terms of the rupture process than the static inversions (e.g., Socquet et al., 2017) because modeling the waveforms provides details occurring during the rupture that a static change cannot see. The results obtained by Meng et al. (2015) seem to move all asperities landward, using repetitive earthquakes and backprojection. As they do not have any prior information of where the asperities provided by the static inversion or teleseismic data are located, we suspect that their results are affected by a shift in the asperity localization, providing a general picture about the slip, but incrementing the resolution in terms of the frequency content generation through back-projection technique.

6. Conclusions

The kinematic rupture process of Iquique earthquake M_w 8.1 and its biggest aftershock M_w 7.7 provides interesting insights about the segmentation of the seismogenic zone. Both ruptures are confined within 15–50 km depths, with a low slip zone that separates shallow and deep asperities, which may be related to a change of dip in the subducting slab (or bending of it). We show that the segmentation along-strike depends on several factors. The mainshock is centered on a forearc basin associated with an important gravity change in the area of $\sim$20.5°S, limiting the rupture to the South. The aftershock rupture might have stopped in the vicinity of a fault system dissecting the overriding plate. Several aseismic processes may affect the rupture extension, including the long precursory slow slip surrounding the mainshock area, and the spatial distribution of interseismic coupling before the earthquake. The mainshock contributed to fill the slip deficit in the area, but changed the stresses in the region and likely triggered the biggest aftershock that ruptured a poorly coupled zone. An along-dip segmentation is also observed, notably in the frequency content of the earthquakes, in agreement with previous works in the area (Meng et al., 2015; Piña-Valdés et al., 2018). These results are very important in the perspective of the seismic hazard studies, where the segmentation is a primordial element of the models.

Acknowledgements

The authors thank the International Plate Boundary Observatory Chile (IPOC, www.ipoc-network.org), Laboratoire International Associé “Montessus de Ballore” (www.lia-mb.net), Central Andean Tectonic Observatory Geodetic Array (CAnTO, http://www.tectonics.caltech.edu/resources/continuous_gps.html), Instituto Geofísico del Perú (www.igp.gob.pe) and Centro Sismológico Nacional de Chile (CSN, www.csn.uchile.cl) for making the raw GPS and strong motion data available. Jorge Jara acknowledges a Ph.D. scholarship granted by Chilean National Science Cooperation (CONICYT) through “Becas Chile” Program. Hugo Sanchez-Reyes thanks the Centre National de la Recherche Scientifique (CNRS) for a Ph.D. scholarship. This work has been supported by grants from Labex OSUG@2020 (Investissement d'avenir – ANR10 LAB56), IRD AO-Sud, and by ANR-17-CE31-0002-01 AtypicSSE. This work was partially supported by funding from the European Research Council (ERC) under the European Union's Horizon 2020 research and innovation program (grant agreement 758210, project Geo4D). The authors would like to thank E. Contreras-Reyes, M. Radiguet, M. Causse, L. Audin, J. Pina-Valdes, R. Jolivet, H. Bhat, C. Vigny and M. Bouchon for all the constructive discussions about this work. Finally, the authors thank Z. Duputel, an anonymous reviewer, and the Editor J.P. Avouac for their constructive comments.

Appendix A. Supplementary material

Supplementary material related to this article can be found online at https://doi.org/10.1016/j.epsl.2018.09.025.

References

Aki, K., 1979. Characterization of barriers on an earthquake fault. J. Geophys. Res., Solid Earth 84 (B11), 6140–6148.

Armijo, R., Lacassin, R., Coudurier-Curveur, A., Carrizo, D., 2015. Coupled tectonic evolution of Andean orogeny and global climate. Earth-Sci. Rev. 143, 1–35.

Armijo, R., Thiele, R., 1990. Active faulting in Northern Chile: ramp stacking and lateral decoupling along a subduction plate boundary? Earth Planet. Sci. Lett. 98 (1), 40–61.

Audin, L., Lacan, P., Tavera, H., Bondoux, F., 2008. Upper plate deformation and seismic barrier in front of Nazca subduction zone: the Chololo fault system and active tectonics along the coastal Cordillera, Southern Peru. Tectonophysics 459 (1), 174–185.

Béjar-Pizarro, M., Carrizo, D., Socquet, A., Armijo, R., Barrientos, S., Bondoux, F., Bonvalot, S., Campos, J., Comte, D., De Chabalier, J., et al., 2010. Asperities and barriers on the seismogenic zone in North Chile: state-of-the-art after the 2007 M_w 7.7 Tocopilla earthquake inferred by GPS and InSAR data. Geophys. J. Int. 183 (1), 390–406.

Bouchon, M., 1981. A simple method to calculate Green's functions for elastic layered media. Bull. Seismol. Soc. Am. 71 (4), 959–971. http://www.bssaonline.org/content/71/4/959.abstract.

Bouchon, M., Marsan, D., Durand, V., Campillo, M., Perfettini, H., Madariaga, R., Gardonio, B., 2016. Potential slab deformation and plunge prior to the Tohoku, Iquique and Maule earthquakes. Nat. Geosci. 9 (5), 380–383.

Bunks, C., Saleck, F.M., Zaleski, S., Chavent, G., 1995. Multiscale seismic waveform inversion. Geophysics 60 (5), 1457–1473.

Chlieh, M., Perfettini, H., Tavera, H., Avouac, J.-P., Remy, D., Nocquet, J.-M., Rolandone, F., Bondoux, F., Gabalda, G., Bonvalot, S., 2011. Interseismic coupling and seismic potential along the Central Andes subduction zone. J. Geophys. Res., Solid Earth 116 (B12).

Cohee, B.P., Beroza, G.C., 1994. Slip distribution of the 1992 landers earthquake and its implications for earthquake source mechanics. Bull. Seismol. Soc. Am. 84 (3), 692–712.

Comte, D., Carrizo, D., Roecker, S., Ortega-Culaciati, F., Peyrat, S., 2016. Three-dimensional elastic wave speeds in the Northern Chile subduction zone: variations in hydration in the supraslab mantle. Geophys. Suppl. Mon. Not. R. Astron. Soc. 207 (2), 1080–1105.

Comte, D., Suárez, G., 1995. Stress distribution and geometry of the subducting Nazca plate in Northern Chile using teleseismically recorded earthquakes. Geophys. J. Int. 122 (2), 419–440.

Contreras-Reyes, E., Jara, J., Grevemeyer, I., Ruiz, S., Carrizo, D., 2012. Abrupt change in the dip of the subducting plate beneath North Chile. Nat. Geosci. 5 (5), 342–345.

Cotton, F., Campillo, M., 1995. Frequency domain inversion of strong motions: application to the 1992 Landers earthquake. J. Geophys. Res., Solid Earth 100 (B3), 3961–3975.

Coutant, O., 1989. Program of numerical simulation AXITRA. Res. Rep. LGIT (in French), Universite Joseph Fourier, Grenoble.

Duputel, Z., Jiang, J., Jolivet, R., Simons, M., Rivera, L., Ampuero, J.-P., Riel, B., Owen, S., Moore, A., Samsonov, S., et al., 2015. The Iquique earthquake sequence of April 2014: Bayesian modeling accounting for prediction uncertainty. Geophys. Res. Lett. 42 (19), 7949–7957.

González, G., Cembrano, J., Carrizo, D., Macci, A., Schneider, H., 2003. The link between forearc tectonics and Pliocene–Quaternary deformation of the Coastal Cordillera, Northern Chile. J. South Am. Earth Sci. 16 (5), 321–342.

Hansen, P.C., 1992. Analysis of discrete ill-posed problems by means of the L-curve. SIAM Rev. 34 (4), 561–580.

Hayes, G.P., 2017. The finite, kinematic rupture properties of great-sized earthquakes since 1990. Earth Planet. Sci. Lett. 468, 94–100.

Hayes, G.P., Herman, M.W., Barnhart, W.D., Furlong, K.P., Riquelme, S., Benz, H.M., Bergman, E., Barrientos, S., Earle, P.S., Samsonov, S., 2014. Continuing megathrust earthquake potential in Chile after the 2014 Iquique earthquake. Nature 512 (7514), 295–298.

Hayes, G.P., Wald, D.J., Johnson, R.L., 2012. Slab1.0: a three-dimensional model of global subduction zone geometries. J. Geophys. Res., Solid Earth 117 (B1).

Hernandez, B., Cotton, F., Campillo, M., 1999. Contribution of radar interferometry to a two-step inversion of the kinematic process of the 1992 Landers earthquake. J. Geophys. Res., Solid Earth 104 (B6), 13083–13099.

Herring, T., King, R.W., Floyd, M.A., McClusky, S.C., 2016. GAMIT, Reference Manual. Department of Earth, Atmospheric, and Planetary Sciences, Massachusetts Institute of Technology.

Jara, J., Socquet, A., Marsan, D., Bouchon, M., 2017. Long-term interactions between intermediate depth and shallow seismicity in North Chile subduction zone. Geophys. Res. Lett. 44 (18), 9283–9292. https://doi.org/10.1002/2017GL075029. 2017GL075029.

Kato, A., Fukuda, J., Kumazawa, T., Nakagawa, S., 2016. Accelerated nucleation of the 2014 Iquique, Chile Mw 8.2 earthquake. Sci. Rep. 6.

King, G., 1986. Speculations on the geometry of the initiation and termination processes of earthquake rupture and its relation to morphology and geological structure. Pure Appl. Geophys. 124 (3), 567–585.

Kiser, E., Ishii, M., 2011. The 2010 Mw 8.8 Chile earthquake: triggering on multiple segments and frequency-dependent rupture behavior. Geophys. Res. Lett. 38 (7).

Lay, T., 2015. The surge of great earthquakes from 2004 to 2014. Earth Planet. Sci. Lett. 409, 133–146.

Lay, T., Yue, H., Brodsky, E.E., An, C., 2014. The 1 April 2014 Iquique, Chile, Mw 8.1 earthquake rupture sequence. Geophys. Res. Lett. 41 (11), 3818–3825.

Liu, C., Zheng, Y., Wang, R., Xiong, X., 2015. Kinematic rupture process of the 2014 Chile Mw 8.1 earthquake constrained by strong-motion, GPS static offsets and teleseismic data. Geophys. J. Int. 202 (2), 1137–1145.

Maksymowicz, A., Ruiz, J., Vera, E., Contreras-Reyes, E., Ruiz, S., Arraigada, C., Bonvalot, S., Bascuñan, S., 2018. Heterogeneous structure of the Northern Chile marine forearc and its implications for megathrust earthquakes. Geophys. J. Int. 215 (2), 1080–1097.

Maksymowicz, A., Tréhu, A.M., Contreras-Reyes, E., Ruiz, S., 2015. Density-depth model of the continental wedge at the maximum slip segment of the Maule Mw 8.8 megathrust earthquake. Earth Planet. Sci. Lett. 409, 265–277.

Melgar, D., Fan, W., Riquelme, S., Geng, J., Liang, C., Fuentes, M., Vargas, G., Allen, R.M., Shearer, P.M., Fielding, E.J., 2016. Slip segmentation and slow rupture to the trench during the 2015, Mw 8.3 Illapel, Chile earthquake. Geophys. Res. Lett. 43 (3), 961–966.

Meng, L., Huang, H., Bürgmann, R., Ampuero, J.P., Strader, A., 2015. Dual megathrust slip behaviors of the 2014 Iquique earthquake sequence. Earth Planet. Sci. Lett. 411, 177–187.

Métois, M., Vigny, C., Socquet, A., 2016. Interseismic coupling, megathrust earthquakes and seismic swarms along the Chilean subduction zone (38°–18°S). Pure Appl. Geophys. 173 (5), 1431–1449.

Michel, S., Avouac, J.-P., Lapusta, N., Jiang, J., 2017. Pulse-like partial ruptures and high-frequency radiation at creeping-locked transition during megathrust earthquakes. Geophys. Res. Lett. 44 (16), 8345–8351. https://doi.org/10.1002/2017GL074725. 2017GL074725.

Peyrat, S., Madariaga, R., Buforn, E., Campos, J., Asch, G., Vilotte, J., 2010. Kinematic rupture process of the 2007 Tocopilla earthquake and its main aftershocks from teleseismic and strong-motion data. Geophys. J. Int. 182 (3), 1411–1430.

Piña-Valdés, J., Socquet, A., Cotton, F., Specht, S., 2018. Spatiotemporal variations of ground motion in Northern Chile before and after the 2014 Mw 8.1 Iquique megathrust event. Bull. Seismol. Soc. Am. 108 (2), 801–814.

Radiguet, M., Cotton, F., Vergnolle, M., Campillo, M., Valette, B., Kostoglodov, V., Cotte, N., 2011. Spatial and temporal evolution of a long term slow slip event: the 2006 Guerrero slow slip event. Geophys. J. Int. 184 (2), 816–828.

Ruiz, S., Klein, E., del Campo, F., Rivera, E., Poli, P., Metois, M., Christophe, V., Baez, J.C., Vargas, G., Leyton, F., et al., 2016. The seismic sequence of the 16 September 2015 Mw 8.3 Illapel, Chile, earthquake. Seismol. Res. Lett. 87 (4), 789–799.

Ruiz, S., Metois, M., Fuenzalida, A., Ruiz, J., Leyton, F., Grandin, R., Vigny, C., Madariaga, R., Campos, J., 2014. Intense foreshocks and a slow slip event preceded the 2014 Iquique Mw 8.1 earthquake. Science 345 (6201), 1165–1169.

Sandwell, D.T., Müller, R.D., Smith, W.H., Garcia, E., Francis, R., 2014. New global marine gravity model from Cryosat-2 and Jason-1 reveals buried tectonic structure. Science 346 (6205), 65–67.

Socquet, A., Valdes, J.P., Jara, J., Cotton, F., Walpersdorf, A., Cotte, N., Specht, S., Ortega-Culaciati, F., Carrizo, D., Norabuena, E., 2017. An 8 month slow slip event triggers progressive nucleation of the 2014 Chile megathrust. Geophys. Res. Lett. 44 (9), 4046–4053. https://doi.org/10.1002/2017GL073023. 2017GL073023.

Song, T.-R.A., Simons, M., 2003. Large trench-parallel gravity variations predict seismogenic behavior in subduction zones. Science 301 (5633), 630–633.

Tarantola, A., 2005. Inverse Problem Theory and Methods for Model Parameter Estimation. SIAM.

Tarantola, A., Valette, B., 1982. Generalized nonlinear inverse problems solved using the least squares criterion. Rev. Geophys. 20 (2), 219–232.

Wang, D., Mori, J., 2011. Frequency-dependent energy radiation and fault coupling for the 2010 Mw 8.8 Maule, Chile, and 2011 Mw 9.0 Tohoku, Japan, earthquakes. Geophys. Res. Lett. 38 (22).

Wellington, P., Brossier, R., Hamitou, O., Trinh, P., Virieux, J., 2017. Efficient anisotropic dip filtering via inverse correlation functions. Geophysics 82 (4), A31–A35. https://doi.org/10.1190/geo2016-0552.1.

Wells, R.E., Blakely, R.J., Sugiyama, Y., Scholl, D.W., Dinterman, P.A., 2003. Basin-centered asperities in great subduction zone earthquakes: a link between slip, subsidence, and subduction erosion? J. Geophys. Res., Solid Earth 108 (B10).

Ye, L., Lay, T., Kanamori, H., Rivera, L., 2016. Rupture characteristics of major and great (Mw ≥ 7.0) megathrust earthquakes from 1990 to 2015: 1. Source parameter scaling relationships. J. Geophys. Res., Solid Earth 121 (2), 826–844.

Appendix C: Discrete forward modeling and gradient computation

Unstructured grids

The principal idea behind this discrete representation is to deploy across the fault surface, which length and orientation are previously defined, a finite number of point sources. Each of these point sources has its own slip and slip-rate time history. The ensemble of all the slip or slip-rate time histories across the whole spatial distribution forms the time-space history that we want to reconstruct. Ideally, the time history of each spatial node (point source) should exhibit a similar behavior than its neighbors, condition that implies spatial coherence. Therefore, first order polynomial approximations of the surface integrals (equation (1.3)) must be preferred over the zero order approximations. However, as mentioned by Somala et al. (2018), the use of higher order approximations (> 1) can affect the solution (e.g. unphysical negative slip or slip-rate values can appear) and should be avoided, unless some specific interpolation (such as b-spline) is used.

The point sources representing the fault surface can be equally separated along the strike and dip directions of the surface: defining a standard structured grid. However, nothing prevents the use of unstructured grids, as long as a correct representation of the surface integral is preserved: the wave and rupture propagation must be well represented through the assumed spatial discretization. For instance, in Figure C.1 I illustrate that the synthetic seismograms computed (Figure C.1a,b,c) using either a structured or an unstructured grid (Figure C.1d,e) are equivalent. However, the use of unstructured grids is less often in the literature, and when used, its design is rather subjected to empirical tests that try to improve the resolution of the problem by reducing the number of unknowns (Simons et al., 2002). In recent years, Barnhart and Lohman (2010) presented a strategy to automatically determine the optimal fault model discretization to be used for static slip inversions, but the extension of this work to the kinematic source inversion problem might not be straightforward.

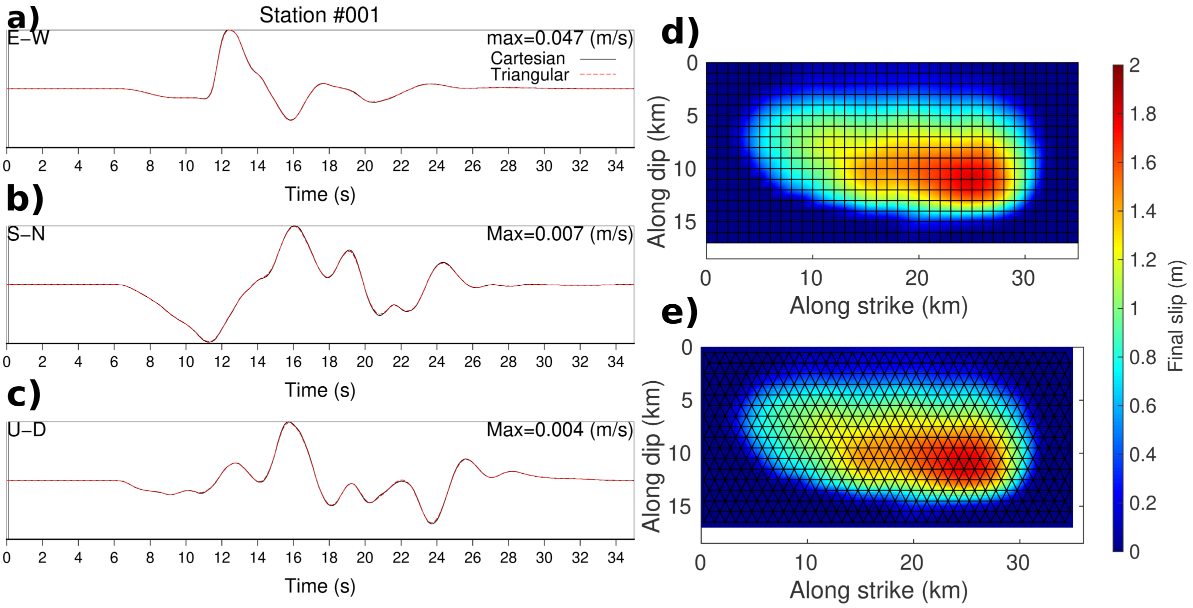

Figure C.1: Illustration showing that the synthetic seismograms, shown in panels a), b) and c), computed using a structured grid (solid black line), from panel d), or an unstructured grid (dashed red line), from panel e), are equivalent. Panels a), b) and c) show the three components of the particle velocity recorded at a receiver location near the source. Panels d) and e) show the final slip distribution of the Source Inversion Validation exercise 1 (SIV1) using a structured and an unstructured grid of point sources. The location of the point sources in panels d) and e) are represented at the junction of the lines. See Chapter 3 for more details about the SIV1.

Fortunately, the discrete representation of extended finite sources does not change the structure of the equations representing the forward (seismograms computation) and inverse (time-space source reconstruction) problems. In fact, it is possible to include the contribution of each of the fault nodes. However, the inclusion of the spatial dimensions (along strike and dip directions) into the problem arises the ambiguity between time, space and slip amplitude. Such ambiguity is further discussed in Section 1.4.

Bibliography

Abercrombie, R. E. (1995). Earthquake source scaling relationships from- 1 to 5 ml using seismograms recorded at 2.5-km depth. *Journal of Geophysical Research: Solid Earth*, 100(B12):24015–24036.

Aki, K. (1968). Seismic displacements near a fault. *Journal of Geophysical Research*, 73(16):5359–5376.

Aki, K. and Larner, L. (1970). Surface motion of a layered medium having an irregular interface due to incident plane SH waves. *Journal Geophysical Research*, 75:1921–1941.

Aki, K. and Richards, P. G. (2002). *Quantitative seismology, theory and methods, second edition*. University Science Books, Sausalito,California.

Archuleta, R. J. (1984). A faulting model for the Imperial Valley earthquake. *Journal Geophysical Research*, 89:4559–4585.

Asano, K. and Iwata, T. (2016). Source rupture processes of the foreshock and mainshock in the 2016 kumamoto earthquake sequence estimated from the kinematic waveform inversion of strong motion data. *Earth, Planets and Space*, 68(1):147.

Asnaashari, A. (2013). *Quantitative 4D seismic imaging in complex media using 2D full waveform inversion*. PhD thesis, ISTerre, Université Joseph Fourier.

Asnaashari, A., Brossier, R., Garambois, S., Audebert, F., Thore, P., and Virieux, J. (2013). Regularized seismic full waveform inversion with prior model information. *Geophysics*, 78(2):R25–R36.

Aster, R. C., Borchers, B., and Thurber, C. H. (2004). *Parameter Estimation and Inverse Problems*. Academic Press.

Barnhart, W. and Lohman, R. (2010). Automated fault model discretization for inversions for coseismic slip distributions. *Journal of Geophysical Research: Solid Earth*, 115(B10).

Ben Jemaa, M., Glinsky-Olivier, N., Cruz-Atienza, V. M., and Virieux, J. (2009). 3D Dynamic rupture simulations by a finite volume method. *Geophysical Journal International*, 178:541–560.

Beresnev, I. A. (2003). Uncertainties in finite-fault slip inversions: to what extent to believe? (a critical review). *Bulletin of the Seismological Society of America*, 93(6):2445–2458.

Bernard, P. and Madariaga, R. (1984). A new asymptotic method for the modelling of near-field accelerograms. *Bulletin of the Seismological Society of America*, 74:539–559.

Berteussen, K.-A. (1977). Moho depth determinations based on spectral-ratio analysis of norsar long-period p waves. *Physics of the Earth and Planetary Interiors*, 15(1):13–27.

Betancourt, M. (2017). A conceptual introduction to hamiltonian monte carlo. *arXiv preprint arXiv:1701.02434*.

Biswas, R. and Sen, M. (2017). 2d full-waveform inversion and uncertainty estimation using the reversible jump hamiltonian monte carlo. In *SEG Technical Program Expanded Abstracts 2017*, pages 1280–1285.

Bodin, T., Sambridge, M., Tkalčić, H., Arroucau, P., Gallagher, K., and Rawlinson, N. (2012). Transdimensional inversion of receiver functions and surface wave dispersion. *Journal of Geophysical Research: Solid Earth*, 117(B2).

Bouchon, M. (1981). A simple method to calculate Green's functions for elastic layered media. *Bulletin of the Seismological Society of America*, 71(4):959–971.

Bouchon, M. (2003). A review of the discrete wavenumber method. *Pure and applied Geophysics*, 160(3-4):445–465.

Bouchon, M. and Aki, K. (1977). Discrete wave-number representation of seismic-source wave fields. *Bulletin of the Seismological Society of America*, 67(2):259–277.

Bouchon, M., Bouin, M. P., Karabulut, H., Toksoz, M. N., Dietrich, M., and Rosakis, A. J. (2001). How fast is rupture during an earthquake? new insights from the 1999 Turkey earthquakes. *Geophysical Research Letters*, 28:2723–2726.

Bouchon, M., Campillo, M., and Gaffet, S. (1989). A boundary integral equation - discrete wavenumber representation method to study wave propagation in multilayered media having irregualr interfaces. *Geophysics*, 54:1134–1140.

Brebbia, C. A. (1980). *The boundary element method for engineers*. Number BOOK. Pentech press.

Brooks, S., Gelman, A., Jones, G., and Meng, X.-L. (2011). *HandBook of markov chain monte carlo*. CRC press.

Brune, J. N. (1970). Tectonic stress and the spectra of seismic shear waves from earthquakes. *Journal Geophysical Research*, 75:4997–5009.

Burridge, R. and Knopoff, L. (1964). Body force equivalents for seismic dislocations. *Bulletin of the Seismological Society of America*, 56(6):1875–1888.

Capdeville, Y. and Cance, P. (2015). Residual homogenization for elastic wave propagation in complex media. *Geophysical Journal International*, 200(2):986.

Capdeville, Y. and Guillot, L. (2009). 2D/3D Elastic model up-scaling for the wave equation based on non-periodic homogenization. In *Expanded Abstracts, 79th Annual Society of Exploration Geophysics Conference & Exhibition, Houston*. Society of Exploration Geophysics.

Capdeville, Y., Guillot, L., and Marigo, J.-J. (2010). 2-D non-periodic homogenization to upscale elastic media for P-SV waves. *Geophysical Journal International*, 182:903–922.

Capdeville, Y. and Marigo, J.-J. (2013). A non-periodic two scale asymptotic method to take account of rough topographies for 2D elastic wave propagation. *Geophysical Journal International*, 192:163–189.

Capdeville, Y. and Métivier, L. (2018). Elastic full waveform inversion based on the homogenization method: theoretical framework and 2-d numerical illustrations. *Geophysical Journal International*, 213(2):1093–1112.

Cara, M. (1978). Regional variations of higher rayleigh-mode phase velocities: a spatial-filtering method. *Geophysical Journal International*, 54(2):439–460.

Červený, V. (1985a). The application of ray tracing to the numerical modeling of seismic wavefields in complex structures. In Helbig, K. and Treitel, S., editors, *Handbook of geophysical exploration, section I: Seismic exploration*, volume 15, pages 1–124. G. Dohr, Geophysical Press, London.

Červený, V. (1985b). Ray synthetic seismograms for complex two-dimensional and three-dimensional structures. *J. geophys*, 58(2):26.

Červený, V. (2001). *Seismic Ray Theory*. Cambridge University Press, Cambridge.

Chapman, C. (2004). *Fundamentals of seismic waves propagation*. Cambridge University Press, Cambridge, England.

Christen, J. A., Fox, C., and Santana-Cibrian, M. (2017). Optimal direction gibbs sampler for truncated multivariate normal distributions. *Communications in Statistics-Simulation and Computation*, 46(4):2587–2600.

Claerbout, J. (1971). Towards a unified theory of reflector mapping. *Geophysics*, 36:467–481.

Claerbout, J. F. (1992). *Earth Sounding Analysis*. Blackwell Scientific Publications.

Cohee, B. P. and Beroza, G. C. (1994). Slip distribution of the 1992 Landers earthquake and its implications for earthquake source mechanics. *Bulletin of the Seismological Society of America*, 84:692–712.

Cotton, F. and Campillo, M. (1995). Frequency domain inversion of strong motions: Application to the 1992 landers earthquake. *Journal of Geophysical Research: Solid Earth*, 100(B3):3961–3975.

Coutant, O. (1989). Program of Numerical Simulation AXITRA. *Research report, LGIT, Grenoble*.

Delouis, B., Nocquet, J.-M., and Vallée, M. (2010). Slip distribution of the february 27, 2010 mw= 8.8 maule earthquake, central chile, from static and high-rate gps, insar, and broadband teleseismic data. *Geophysical Research Letters*, 37(17).

Diao, F., Wang, R., Aochi, H., Walter, T. R., Zhang, Y., Zheng, Y., and Xiong, X. (2016). Rapid kinematic finite-fault inversion for an mw 7+ scenario earthquake in the marmara sea: an uncertainty study. *Geophysical Journal International*, 204(2):813–824.

Dufumier, H. and Rivera, L. (1997). On the resolution of the isotropic component in moment tensor inversion. *Geophysical Journal International*, 131(3):595–606.

Duputel, Z., Agram, P. S., Simons, M., Minson, S., and Beck, J. L. (2014). Accounting for prediction uncertainty when inferring subsurface fault slip. *Geophysical Journal International*, 197(1):464–482.

Duputel, Z., Rivera, L., Fukahata, Y., and Kanamori, H. (2012). Uncertainty estimations for seismic source inversions. *Geophysical Journal International*, 190(2):1243–1256.

Emolo, A. and Zollo, A. (2005). Kinematic source parameters for the 1989 loma prieta earthquake from the nonlinear inversion of accelerograms. *Bulletin of the Seismological Society of America*, 95(3):981–994.

Etienne, V., Chaljub, E., Virieux, J., and Glinsky, N. (2010). An hp-adaptive discontinuous Galerkin finite-element method for 3D elastic wave modelling. *Geophysical Journal International*, 183(2):941–962.

Fan, W., Shearer, P. M., and Gerstoft, P. (2014). Kinematic earthquake rupture inversion in the frequency domain. *Geophysical Journal International*, 199(2):1138.

Fehmers, G. C. and Höcker, C. F. W. (2003). Fast structural interpretation with structure-oriented filtering. *Geophysics*, 68(4):1286–1293.

Fichtner, A., Zunino, A., and Gebraad, L. (2018). Hamiltonian monte carlo solution of tomographic inverse problems. *Geophysical Journal International*, 216(2):1344–1363.

Figueiredo, M. A. (2003). Adaptive sparseness for supervised learning. *IEEE transactions on pattern analysis and machine intelligence*, 25(9):1150–1159.

Fink, M. (1993). Time-reversal mirrors. *Journal of Physics D: Applied Physics*, 26(9):1333–1350.

Fink, M. (2008). Time-reversal waves and super resolution. In *Journal of Physics: Conference Series*, volume 124(1), page 012004. IOP Publishing.

Fomel, S. (2002). Applications of plane-wave destruction filters. *Geophysics*, 67(6):1946–1960.

Gaffet, S. and Bouchon, M. (1991). Source location and boundary shape effects on the P-SV near displacement field using a boundary integral equation - discrete wavenumber representation method. *Geophysical Journal International*, 106:341–355.

Gajewski, D. and Tessmer, E. (2005). Reverse modelling for seismic event characterization. *Geophysical Journal International*, 163(1):276–284.

Gallovic, F. and Imperatori, W. (2014). Effect of lateral velocity heterogeneities and topography on slip inversions: case study of the mw6. 3 2009 l'aquila earthquake. In *EGU General Assembly Conference Abstracts*, volume 16, page 2573.

Gauthier, O., Virieux, J., and Tarantola, A. (1986). Two-dimensional nonlinear inversion of seismic waveform : numerical results. *Geophysics*, 51:1387–1403.

Green, P. J. (1995). Reversible jump markov chain monte carlo computation and bayesian model determination. *Biometrika*, 82(4):711–732.

Guitton, A., Ayeni, G., and Díaz, E. (2012). Constrained full-waveform inversion by model reparameterization. *Geophysics*, 77(2):R117–R127.

Gutemberg, B. and Richter, C. F. (1956). Earthquake magnitude, intensity, energy, and acceleration: (second paper). *Bulletin of the seismological society of America*, 46(2):105–145.

Hale, D. (2007). Local dip filtering with directional laplacians. Technical report, Centre for Wave Phenomena, Colorado School of Mines.

Hallo, M. and Gallovič, F. (2016). Fast and cheap approximation of green function uncertainty for waveform-based earthquake source inversions. *Geophysical Journal International*, 207(2):1012–1029.

Hanks, T. C. and Kanamori, H. (1979). A moment magnitude scale. *Journal of Geophysical Research: Solid Earth*, 84(B5):2348–2350.

Hansen, P. C. (1992). Analysis of discrete ill-posed problems by means of the l-curve. *SIAM Review*, 34(4):561–580.

Hao, J., Ji, C., and Yao, Z. (2017). Slip history of the 2016 mw 7.0 kumamoto earthquake: Intraplate rupture in complex tectonic environment. *Geophysical Research Letters*, 44(2):743–750.

Hartzell, S. (1989). Comparison of seismic waveform inversion results for the rupture history of a finite fault: Application to the 1986 north palm springs, california, earthquake. *Journal of Geophysical Research: Solid Earth*, 94(B6):7515–7534.

Hartzell, S. and Helmberger, D. V. (1982). Strong-motion modeling of the imperial valley earthquake of 1979. *Bulletin of the Seismological Society of America*, 72(2):571–596.

Hartzell, S. H. and Heaton, T. H. (1983). Inversion of strong ground motion and teleseismic waveform data for the fault rupture history of the 1979 imperial valley, california, earthquake. *Bulletin of the Seismological Society of America*, 73(6A):1553–1583.

Haskell, N. (1964). Total energy and energy spectral density of elastic wave radiation from propagating faults. *Bulletin of the Seismological Society of America*, 54(6A):1811–1841.

Haskell, N. (1966). Total energy and energy spectral density of elastic wave radiation from propagating faults. part ii. a statistical source model. *Bulletin of the Seismological Society of America*, 56(1):125–140.

Haskell, N. A. (1969). Elastic displacements in the near-field of a propagating fault. *Bulletin of the Seismological Society of America*, 59(2):865–908.

Hastings, W. K. (1970). Monte carlo sampling methods using markov chains and their applications.

Heaton, T. H. (1990). Evidence for and implications of self-healing pulses of slip in earthquake rupture. *Physics of the Earth and Planetary Interiors*, 64(1):1–20.

Hernandez, B., Cotton, F., and Campillo, M. (1999). Contribution of radar interferometry to a two-step inversion of kinematic process of the 1992 Landers earthquake. *Journal Geophysical Research*, 104:13083–13099.

Herrera, I. and Gourgeon, H. (1982). Boundary methods, c-complete systems for stokes problems. *Computer Methods in Applied Mechanics and Engineering*, 30(2):225–241.

Hesthaven, J. S. and Warburton, T. (2008). *Nodal Discontinuous Galerkin Method. Algorithms, Analysis, and Application*. Springer, New York.

Horikawa, H., Hirahara, K., Umeda, Y., Hashimoto, M., and Kusano, F. (1996). Simultaneous inversion of geodetic and strong-motion data for the source process of the hyogo-ken nanbu, japan, earthquake. *Journal of Physics of the Earth*, 44(5):455–471.

Hsieh, M.-C., Zhao, L., Ji, C., and Ma, K.-F. (2016). Efficient inversions for earthquake slip distributions in 3d structures. *Seismological Research Letters*, 87(6):1342–1354.

Ide, S. (2007). Slip inversion. In Kanamori, H., editor, *Treatise on Geophysics*, volume 4, pages 193–223. Elsevier BV.

Ide, S., Baltay, A., and Beroza, G. C. (2011). Shallow dynamic overshoot and energetic deep rupture in the 2011 mw 9.0 tohoku-oki earthquake. *Science*, 332(6036):1426–1429.

Igel, H. (2017). *Computational seismology: a practical introduction*. Oxford University Press.

Ishii, M., Shearer, P. M., Houston, H., and Vidale, J. E. (2007). Teleseismic p wave imaging of the 26 december 2004 sumatra-andaman and 28 march 2005 sumatra earthquake ruptures using the hi-net array. *Journal of Geophysical Research*, 112:B11307.

Ji, C., Wald, D. J., and Helmberger, D. V. (2002a). Source description of the 1999 hector mine, california, earthquake, part i: Wavelet domain inversion theory and resolution analysis. *Bulletin of the Seismological Society of America*, 92(4):1192–1207.

Ji, C., Wald, D. J., and Helmberger, D. V. (2002b). Source description of the 1999 hector mine, california, earthquake, part ii: Complexity of slip history. *Bulletin of the Seismological Society of America*, 92(4):1208–1226.

K., S. M. and Reetam, B. (2017). Transdimensional seismic inversion using the reversible jump hamiltonian monte carlo algorithm. *Geophysics*, 82(3):R119–R134.

Kanamori, H. (1977). The energy release in great earthquakes. *Journal of geophysical research*, 82(20):2981–2987.

Kaneko, Y. and Shearer, P. (2014). Seismic source spectra and estimated stress drop derived from cohesive-zone models of circular subshear rupture. *Geophysical Journal International*, 197(2):1002–1015.

Kennett, B. L. N. and Kerry, N. J. (1979). Seismic waves in a stratified half space. *Geophysical Journal of the Royal Astronomical Society*, 57:557–583.

Kikuchi, M. and Fukao, Y. (1985). Iterative deconvolution of complex body waves from great earthquakes—the tokachi-oki earthquake of 1968. *Physics of the earth and planetary interiors*, 37(4):235–248.

Kikuchi, M. and Kanamori, H. (1982). Inversion of complex body waves. *Bulletin of the Seismological Society of America*, 72(2):491–506.

Kikuchi, M. and Kanamori, H. (1986). Inversion of complex body waves-ii. *Physics of the earth and planetary interiors*, 43(3):205–222.

Kikuchi, M. and Kanamori, H. (1991). Inversion of complex body waves—iii. *Bulletin of the Seismological Society of America*, 81(6):2335–2350.

Kolb, P., Collino, F., and Lailly, P. (1986). Prestack inversion of 1-D medium,. In *Extended Abstracts*, volume 74, pages 498–508.

Konno, K. and Ohmachi, T. (1998). Ground-motion characteristics estimated from spectral ratio between horizontal and vertical components of microtremor. *Bulletin of the Seismological Society of America*, 88(1):228–241.

Koper, K. D., Hutko, A. R., Lay, T., Ammon, C. J., and Kanamori, H. (2011). Frequency-dependent rupture process of the 2011 m w 9.0 tohoku earthquake: Comparison of short-period p wave backprojection images and broadband seismic rupture models. *Earth, planets and space*, 63(7):16.

Kubo, H., Asano, K., Iwata, T., and Aoi, S. (2016). Development of fully bayesian multiple-time-window source inversion. *Geophysical Journal International*, 204(3):1601–1619.

Lailly, P. (1983). The seismic inverse problem as a sequence of before stack migrations. In Bednar, R. and Weglein, editors, *Conference on Inverse Scattering, Theory and application, Society for Industrial and Applied Mathematics, Philadelphia*, pages 206–220.

Larmat, C., Montagner, J. P., Fink, M., and Capdeville, Y. (2006). Time-reversal imaging of seimic sources and appplication to the great Sumatra earthquake. *Geophysical Research Letters*, 33:L19312.

Lay, T., Ammon, C. J., Kanamori, H., Xue, L., and Kim, M. J. (2011). Possible large near-trench slip during the 2011 m w 9.0 off the pacific coast of tohoku earthquake. *Earth, planets and space*, 63(7):32.

Lee, J.-J. and Langston, C. A. (1983). Wave propagation in a three-dimensional circular basin. *Bulletin of the Seismological Society of America*, 73(6A):1637–1653.

Liu, P. and Archuleta, R. J. (2004). A new nonlinear finite fault inversion with three-dimensional green's functions: Application to the 1989 loma prieta, california, earthquake. *Journal of Geophysical Research: Solid Earth*, 109(B2).

Longbotham, H. G. and Bovak, A. C. (1989). Theory of order statistics filters and their relationship to linear fir filters. *IEEE Transactions on Acoustics Speech and Signal Processing*, 37:275–287.

Lorito, S., Romano, F., Atzori, S., Tong, X., Avallone, A., McCloskey, J., Cocco, M., Boschi, E., and Piatanesi, A. (2011). Limited overlap between the seismic gap and coseismic slip of the great 2010 chile earthquake. *Nature Geoscience*, 4(3):173.

Madariaga, R. (1976). Dynamics of an expanding circular fault. *Bulletin of the Seismological Society of America*, 66:639–666.

Madariaga, R. (1977). High-frequency radiation from crack (stress drop) models of earthquake faulting. *Geophysical Journal International*, 51(3):625–651.

Madariaga, R. (1984). Gaussian beam synthetic seismograms in a vertically varying medium. *Geophysical Journal International*, 79(2):589–612.

Mai, P. M., Schorlemmer, D., Page, M., Ampuero, J.-P., Asano, K., Causse, M., Custodio, S., Fan, W., Festa, G., Galis, M., et al. (2016). The earthquake-source inversion validation (siv) project. *Seismological Research Letters*.

Marcial, C.-Z. (2017). *Optimación del método indirecto de elementos de contorno para aplicaciones de ingeniería sismológica y geotécnica*. PhD thesis, Universidad Nacional Autónoma de México.

Mendoza, C. and Hartzell, S. H. (1988). Inversion for slip distribution using teleseismic p waveforms: North palm springs, borah peak, and michoacan earthquakes. *Bulletin of the Seismological Society of America*, 78(3):1092–1111.

Mendoza, C. and Hartzell, S. H. (1989). Slip distribution of the 19 september 1985 michoacan, mexico, earthquake: Near-source and teleseismic constraints. *Bulletin of the Seismological Society of America*, 79(3):655–669.

Metropolis, N., Rosenbluth, A. W., Rosenbluth, M. N., Teller, A. H., and Teller, E. (1953). Equation of state calculations by fast computing machines. *The journal of chemical physics*, 21(6):1087–1092.

Mikumo, T. and Yagi, Y. (2003). Slip-weakening distance in dynamic rupture of in-slab normal-faulting earthquakes. *Geophysical Journal International*, 155:443–455.

Minson, S., Simons, M., and Beck, J. (2013). Bayesian inversion for finite fault earthquake source models i—theory and algorithm. *Geophysical Journal International*, 194(3):1701–1726.

Moyer, P. A., Boettcher, M. S., Ellsworth, W. L., Ogasawara, H., Cichowicz, A., Birch, D., and van Aswegen, G. (2017). Call for models—a test case for the source inversion validation: The 2014 ml 5.5 orkney, south africa, earthquake. *Seismological Research Letters*, 88(5):1333–1338.

Muller, G. (1985). The reflectivity method: a tutorial. *Journal of Geophysics*, 58:153–174.

Neal, R. M. et al. (2011). Mcmc using hamiltonian dynamics. *HandBook of markov chain monte carlo*, 2(11):2.

Nocedal, J. (1980). Updating Quasi-Newton Matrices With Limited Storage. *Mathematics of Computation*, 35(151):773–782.

Nocedal, J. and Wright, S. J. (2006). *Numerical Optimization*. Springer, 2nd edition.

Nolet, G. (1987). *Seismic tomography with applications in global seismology and exploration geophysics*. D. Reidel publishing Company.

Nolet, G. (2008). *A Breviary of Seismic Tomography*. Cambridge University Press, Cambridge, UK.

Ohnaka, M. and Yamashita, T. (1989). A cohesive zone model for dynamic shear faulting based on experimentally inferred constitutive relation and strong motion source parameters. *Journal of Geophysical Research: Solid Earth*, 94(B4):4089–4104.

Okuwaki, R. and Yagi, Y. (2017). Rupture process during the mw 8.1 2017 chiapas mexico earthquake: Shallow intraplate normal faulting by slab bending. *Geophysical Research Letters*, 44(23).

Olofsson, P. and Andersson, M. (2005). *Probability, statistics, and stochastic processes*, volume 504. Wiley Online Library.

Olson, A. H. and Anderson, J. G. (1988). Implications of frequency-domain inversion of earthquake ground motions for resolving the space-time dependence of slip on an extended fault. *Geophysical Journal International*, 94(3):443–455.

Olson, A. H. and Apsel, R. J. (1982). Finite faults and inverse theory with applications to the 1979 imperial valley earthquake. *Bulletin of the Seismological Society of America*, 72(6A):1969–2001.

Ozgun Konca, A., Kaneko, Y., Lapusta, N., and Avouac, J.-P. (2013). Kinematic inversion of physically plausible earthquake source models obtained from dynamic rupture simulations. *Bulletin of the Seismological Society of America*, 103(5):2621–2644.

Pérez Solano, C. (2013). *Two-dimensional near-surface seismic imaging with surface waves: alternative methodology for waveform inversion*. PhD thesis, École Nationale Supérieure des Mines de Paris.

Perton, M., Contreras-Zazueta, M. A., and Sánchez-Sesma, F. J. (2016). Indirect boundary element method to simulate elastic wave propagation in piecewise irregular and flat regions. *Geophysical Journal International*, 205(3):1832–1842.

Peyrat, S., Olsen, K., and Madariaga, R. (2004). Which dynamic rupture parameters can be estimated from strong ground motion and geodetic data? *Pure and Applied Geophysics*, 161:2155–2169.

Plessix, R. E. (2006). A review of the adjoint-state method for computing the gradient of a functional with geophysical applications. *Geophysical Journal International*, 167(2):495–503.

Plessix, R. E. and Mulder, W. A. (2008). Resistivity imaging with controlled-source electromagnetic data: depth and data weighting. *Inverse Problems*, 24:034012.

Podvin, P. and Lecomte, I. (1991). Finite difference computation of traveltimes in very contrasted velocity model : a massively parallel approach and its associated tools. *Geophysical Journal International*, 105:271–284.

Pollitz, F. F., Brooks, B., Tong, X., Bevis, M. G., Foster, J. H., Bürgmann, R., Smalley Jr, R., Vigny, C., Socquet, A., Ruegg, J.-C., et al. (2011). Coseismic slip distribution of the february 27, 2010 mw 8.8 maule, chile earthquake. *Geophysical Research Letters*, 38(9).

Radiguet, M., Cotton, F., Vergnolle, M., Campillo, M., Valette, B., Kostoglodov, V., and Cotte, N. (2011). Spatial and temporal evolution of a long term slow slip event: the 2006 guerrero slow slip event. *Geophysical Journal International*, 184(2):816–828.

Ragon, T., Sladen, A., and Simons, M. (2018). Accounting for uncertain fault geometry in earthquake source inversions–i: theory and simplified application. *Geophysical Journal International*, 214(2):1174–1190.

Razafindrakoto, H. N. and Mai, P. M. (2014). Uncertainty in earthquake source imaging due to variations in source time function and earth structure. *Bulletin of the Seismological Society of America*, 104(2):855–874.

Richter, C. F. (1935). An instrumental earthquake magnitude scale. *Bulletin of the Seismological Society of America*, 25(1):1–32.

Romano, F., Trasatti, E., Lorito, S., Piromallo, C., Piatanesi, A., Ito, Y., Zhao, D., Hirata, K., Lanucara, P., and Cocco, M. (2014). Structural control on the tohoku earthquake rupture process investigated by 3d fem, tsunami and geodetic data. *Scientific reports*, 4:5631.

Rothman, D. H. (1986). Automatic estimation of large residual statics corrections. *Geophysics*, 51(2):332–346.

Sánchez-Reyes, H., Tago, J., Métivier, L., Cruz-Atienza, V., and Virieux, J. (2018). An evolutive linear kinematic source inversion. *Journal of Geophysical Research: Solid Earth*, 123.

Sánchez-Sesma, F. J. and Campillo, M. (1991). Diffraction of p, sv, and rayleigh waves by topographic features: a boundary integral formulation. *Bulletin of the Seismological Society of America*, 81(6):2234–2253.

Sánchez-Sesma, F. J., Chávez-García, F. J., and Bravo, M. A. (1988). Seismic response of a class of alluvial valleys for incident sh waves. *Bulletin of the Seismological Society of America*, 78(1):83–95.

Sanchez-Sesma, F. J. and Luzon, F. (1995). Seismic response of three-dimensional alluvial valleys for incident P, S and Rayleigh waves. *Bulletin of the Seismological Society of America*, 85:269–284.

Satake, K., Fujii, Y., Harada, T., and Namegaya, Y. (2013). Time and space distribution of coseismic slip of the 2011 tohoku earthquake as inferred from tsunami waveform data. *Bulletin of the seismological society of America*, 103(2B):1473–1492.

Schmedes, J., Archuleta, R. J., and Lavallée, D. (2010). Correlation of earthquake source parameters inferred from dynamic rupture simulations. *Journal of Geophysical Research: Solid Earth*, 115(B3).

Schmedes, J., Archuleta, R. J., and Lavallée, D. (2013). A kinematic rupture model generator incorporating spatial interdependency of earthquake source parameters. *Geophysical Journal International*, 192(3):1116–1131.

Sen, M. and Stoffa, P. (1991). Non-linear one-dimensional seismic waveform inversion using simulated annealing. *Geophysics*, 56:1624–1638.

Sen, M. K. and Stoffa, P. L. (2013). *Global Optimization Methods in Geophysical Inversion (second edition)*. Elsevier Science Publishing Co.

Shao, G., Li, X., Ji, C., and Maeda, T. (2011). Focal mechanism and slip history of the 2011 m w 9.1 off the pacific coast of tohoku earthquake, constrained with teleseismic body and surface waves. *Earth, planets and space*, 63(7):9.

Shearer, P. M., Prieto, G. A., and Hauksson, E. (2006). Comprehensive analysis of earthquake source spectra in southern california. *Journal of Geophysical Research: Solid Earth*, 111(B6).

Simons, M., Fialko, Y., and Rivera, L. (2002). Coseismic deformation from the 1999 m w 7.1 hector mine, california, earthquake as inferred from insar and gps observations. *Bulletin of the Seismological Society of America*, 92(4):1390–1402.

Somala, S. N., Ampuero, J.-P., and Lapusta, N. (2014). Resolution of rise time in earthquake slip inversions: Effect of station spacing and rupture velocity. *Bulletin of the Seismological Society of America*.

Somala, S. N., Ampuero, J.-P., and Lapusta, N. (2018). Finite-fault source inversion using adjoint methods in 3-d heterogeneous media. *Geophysical Journal International*, 214(1):402–420.

Steidl, J. H., Archuleta, R. J., and Hartzell, S. H. (1991). Rupture history of the 1989 loma prieta, california, earthquake. *Bulletin of the Seismological Society of America*, 81(5):1573–1602.

Stein, S. and Wysession, M. (2003). *An Introduction to Seismology, Earthquakes and Earth Structure*. Blackwell Publishing.

Suzuki, W., Aoi, S., Sekiguchi, H., and Kunugi, T. (2011). Rupture process of the 2011 Tohoku-Oki mega-thrust earthquake (m9. 0) inverted from strong-motion data. *Geophysical Research Letters*, 38(7).

Tago, J., Cruz-Atienza, V. M., Virieux, J., Etienne, V., and Sánchez-Sesma, F. J. (2012). A 3D hp-adaptive discontinuous Galerkin method for modelling earthquake dynamics. *Journal of Geophysical Research*, 117:B09312.

Tape, W. and Tape, C. (2013). The classical model for moment tensors. *Geophysical Journal International*, 195(3):1701–1720.

Tarantola, A. (1984). Inversion of seismic reflection data in the acoustic approximation. *Geophysics*, 49(8):1259–1266.

Tarantola, A. (2005). *Inverse Problem Theory and Methods for Model Parameter Estimation*. Society for Industrial and Applied Mathematics, Philadelphia.

Tarantola, A. and Valette, B. (1982). Generalized nonlinear inverse problems solved using the least square criterion. *Reviews of Geophysical and Space Physics*, 20:219–232.

Thio, H., Graves, R., Somerville, P., Sato, T., and Ishii, T. (2004). A multiple time window rupture model for the 1999 chi-chi earthquake from a combined inversion of teleseismic, surface wave, strong motion, and gps data. *Journal of Geophysical Research: Solid Earth*, 109(B8).

Tinti, E., Fukuyama, E., Piatanesi, A., and Cocco, M. (2005). A kinematic source-time function compatible with earthquake dynamics. *Bulletin of the Seismological Society of America*, 95(4):1211–1223.

Trinh, P. T., Brossier, R., Métivier, L., Virieux, J., and Wellington, P. (2017). Bessel smoothing filter for spectral element mesh. *Geophysical Journal International*, 209(3):1489–1512.

Uchide, T., Horikawa, H., Nakai, M., Matsushita, R., Shigematsu, N., Ando, R., and Imanishi, K. (2016). The 2016 kumamoto–oita earthquake sequence: aftershock seismicity gap and dynamic triggering in volcanic areas. *Earth, Planets and Space*, 68(1):180.

Udías, A. (1991). Source mechanism of earthquakes. In *Advances in Geophysics*, volume 33, pages 81–140. Elsevier.

Virieux, J. (1986). P-SV wave propagation in heterogeneous media: Velocity-stress finite difference method. *Geophysics*, 51:889–901.

Virieux, J. (1991). Fast and accurate ray tracing by hamiltonian perturbation. *Journal of Geophysical Research*, 96(B1):579–594.

Virieux, J. and Operto, S. (2009). An overview of full waveform inversion in exploration geophysics. *Geophysics*, 74(6):WCC1–WCC26.

Wald, D. J. and Heaton, T. H. (1994). Spatial and temporal distribution of slip for the 1992 Landers, California, earthquake. *Bulletin of the Seismological Society of America*, 84:668–691.

Wald, D. J., Heaton, T. H., and Hudnut, K. W. (1996). A dislocation model of the 1994 northridge, california, earthquake determined from strong-motion, gps, and leveling-line data. *Bull. Seism. Soc. Am*, 86:S49–S70.

Wald, D. J., Helmberger, D. V., and Hartzell, S. H. (1990). Rupture process of the 1987 Superstition Hills earthquake from the inversion of strong-motion data. *Bulletin of the Seismological Society of America*, 80(5):1079–1098.

Wang, R., Martın, F. L., and Roth, F. (2003). Computation of deformation induced by earthquakes in a multi-layered elastic crust—fortran programs edgrn/edcmp. *Computers and Geosciences*, 29(2):195–207.

Wellington, P., Brossier, R., Hamitou, O., Trinh, P., and Virieux, J. (2017). Efficient anisotropic dip filtering via inverse correlation functions. *Geophysics*, 82(4):A31–A35.

Yagi, Y. and Fukahata, Y. (2011). Introduction of uncertainty of green's function into waveform inversion for seismic source processes. *Geophysical Journal International*, 186(2):711–720.

Yomogida, K. (1994). Detection of anomalous seismic phases by the wavelet transform. *Geophysical Journal International*, 116(1):119–130.

Zhao, L., Chen, P., and Jordan, T. H. (2006). Strain green's tensors, reciprocity, and their applications to seismic source and structure studies. *Bulletin of the Seismological Society of America*, 96(5):1753–1763.